Nonlinear Analysis and Performance Based Design Methods for Reinforced Concrete Coupled Shear Walls

Danya S. Mohr

A thesis submitted in partial fulfillment
of the requirements for the degree of

Master of Science in Civil Engineering

University of Washington

2007

Program Authorized to Offer Degree: Civil & Environmental Engineering

University of Washington
Graduate School

This is to certify that I have examined this copy of a master's thesis by

Danya S. Mohr

and have found that it is complete and satisfactory in all respects,
and that any and all revisions required by the final
examining committee have been made.

Committee Members:

_____
Laura Lowes

_____
Dawn Lehman

_____
Greg Miller

Date: _____

In presenting this thesis in partial fulfillment of the requirements for a master's degree at the University of Washington, I agree that the Library shall make its copies freely available for inspection. I further agree that extensive copying of this thesis is allowable only for scholarly purposes, consistent with "fair use" as prescribed in the U.S. Copyright Law. Any other reproduction for any purpose or by any means shall not be allowed without my written permission.

Signature_____

Date_____

University of Washington

Abstract

Nonlinear Analysis and Performance Based Design Methods
for Reinforced Concrete Coupled Shear Walls

Danya S. Mohr

Co-Chairs of the Supervisory Committee:
Professor Laura Lowes
Department of Civil and Environmental Engineering

Professor Dawn Lehman
Department of Civil and Environmental Engineering

Recent advances in structural engineering have lead to an increased interest in performance-based design of structural systems. Here the performance of reinforced concrete coupled wall systems, designed in accordance with current practice, is investigated.

Current design methods, including the plastic-design method recommended by the IBC Structural/Seismic Design Manual (2007) were employed to design a 10-story reference coupled wall for use in the study.

Linear and nonlinear analysis were conducted to assess the expected performance of the reference coupled wall. Linear elastic modeling was done using SAP2000 (2006), while nonlinear analysis were conducted using VecTor2 (2006). Nonlinear finite element models and analysis methods were validated against a set of experimental coupling beam tests. Additionally, the effects of confinement reinforcement on diagonally reinforced coupling beams designed per the current ACI 318-05 code versus the proposed full confinement method of the 318-08 code were investigated.

The results of these analysis suggest that current design methods can lead to coupled shear walls that may not behave as desired in a significant seismic event.

TABLE OF CONTENTS

Page

List of Figures v

List of Tables xiii

Glossary xv

Chapter 1: Introduction 1
1.1 Objectives 2
1.2 Outline of Thesis 2

Chapter 2: Background Research 4
2.1 Building Inventory 4
2.2 Coupling Beams 4
2.3 Previous Experimental Coupling Beam Studies 8
2.3.1 Galano & Vignoli 9
2.3.2 Kwan & Zhao 9
2.3.3 Tassios, Maretti, and Bezas 10
2.3.4 Compiled Experiment Coupling Beam Data 13
2.4 Previous Analyses 21
2.4.1 Oyen 21
2.4.2 Brown 21
2.4.3 Zhao et. al. 21

Chapter 3: Coupling Beam Performance and Damage Patterns 24
3.1 Behavior Mode Definition 24
3.2 Experimental Behavior Modes 25
3.3 Comparison Plots 33

Chapter 4: Nonlinear Finite Element Analysis of Coupling Beam Experiments . . 42
4.1 VecTor2 . . . 42
4.2 Modeling Decisions . . . 43
4.2.1 Material Properties . . . 43
4.2.2 Constitutive Models . . . 43
4.2.3 Element Mesh . . . 45
4.2.4 Types of Reinforcement . . . 48
4.2.5 Boundary Conditions . . . 49
4.2.6 Loading Parameters . . . 49
4.3 Description of Evaluation Method . . . 49
4.4 Reduced Data Set for Illustration of VecTor2 Capabilities . . . 55
4.5 Description of Results . . . 55
4.5.1 Galano P01 . . . 55
4.5.2 Galano P02 . . . 57
4.5.3 Tasssios CB2B . . . 58
4.6 Data Analysis and Trends . . . 68
4.7 Discussion and Comparison of Results . . . 89
4.8 Model Parameter Study . . . 90
4.8.1 Vecchio and Palermo Parameters . . . 90

Chapter 5: Evaluation of Transverse Reinforcement of Coupling Beams . . . 92
5.1 Introduction . . . 92
5.1.1 Approach . . . 92
5.1.2 Organization of Chapter . . . 93
5.2 Design Requirements . . . 93
5.2.1 ACI 318-05 Current Code . . . 93
5.2.2 ACI 318H-CH047d Proposal . . . 94
5.3 Description of Models . . . 94
5.3.1 CBR-ACI: ACI318-05 Reference Model . . . 95
5.3.2 CBR-ACI-S: Reference model with additional slab steel . . . 95
5.3.3 CBR-318H: Confinement to meet the ACI 318H proposal . . . 95
5.3.4 CBR-318H-F: Confinement of the entire section to meet ACI 318H proposal . . . 96

5.3.5 CBR-318H-M: Confinement of the entire section with reduced trans. reinf. . . . 96
5.4 Finite Element Modeling . . . 96
5.5 Description of Evaluation Method . . . 97
5.6 Simulation Results . . . 98
5.6.1 Load Drift Plots . . . 98
5.6.2 Stiffness . . . 104
5.6.3 Shear Force . . . 105
5.6.4 Displacement and Drift . . . 108
5.7 Comparison of Confinement Variations . . . 110
5.7.1 CBR-ACI vs. CBR-318H . . . 110
5.7.2 CBR-ACI vs CBR-318H-F . . . 112
5.7.3 CBR-ACI and CBR-318H-M . . . 115
5.8 Conclusions . . . 115

Chapter 6: Coupled Wall Design and Analysis . . . 119
6.1 Objective . . . 119
6.2 Current Design Methods Background . . . 119
6.2.1 Code Design . . . 119
6.2.2 2006 IBC Structural/Seismic Design Recommendations . . . 120
6.3 Design of Coupled Wall Specimen . . . 122
6.4 Strength Design . . . 124
6.5 Recommended Plastic Design . . . 127
6.6 Coupling Beam Reinforcement Details . . . 129
6.7 Coupled Wall Model Variations . . . 131
6.8 Modeling Decisions . . . 134
6.8.1 Constitutive Models . . . 134
6.8.2 Element Mesh . . . 134
6.8.3 Reinforcement Model . . . 138
6.8.4 Boundary Conditions . . . 138
6.8.5 Loading Parameters . . . 138
6.8.6 Summary of Coupled Wall Model Variations . . . 141
6.9 Description of Evaluation Method . . . 143
6.10 Displacement Control Results . . . 144

6.11 Load Control Results . . . 146
6.11.1 Deformed Shape and Crack Patterns . . . 146
6.11.2 Base Reactions . . . 157
6.11.3 Degree of Coupling . . . 160
6.11.4 Displacement and Drift at Yield and Maximum . . . 161
6.11.5 Base Shear vs. Drift Comparisons . . . 162
6.11.6 Inter-story Drift . . . 164
6.11.7 Coupling Beam Rotation . . . 165
6.11.8 Reinforcement Yield . . . 166
6.12 Conclusions . . . 172

Chapter 7: Summary and Conclusions . . . 174
7.1 Summary . . . 174
7.2 Conclusions . . . 175
7.3 Recommendations for Further Work . . . 176

Bibliography . . . 177

Appendix A: Experimental Coupling Beam Load Displacement Plots . . . 180

Appendix B: Coupling Beam Plots . . . 213

LIST OF FIGURES

Figure Number — Page

2.1 Coupling Beam Reinforcement Layouts (Galano and Vignoli 2000) 5
2.2 Galano & Vignoli Experimental Test Setup 10
2.3 Kwan & Zhao Experimental Test Setup 11
2.4 Tassios, Maretti, and Bezas Experimental Test Setup 12

3.1 CB1A - Ductile Flexure 27
3.2 CB1B - Preemptive Diagonal Tension 28
3.3 CB1C - Flexure/Diagonal Tension 29
3.4 CB1D - Flexure/Sliding Shear 30
3.5 CB2F - Flexure Compression 31
3.6 CB2G - Diagonal Compression 32
3.7 Conv. Reinf. Coupling Beams - Displacement Ductility vs. Aspect Ratio . . 34
3.8 Conv. Reinf. Coupling Beams - Displacement Ductility vs. Ultimate Displacement 34
3.9 Conv. Reinf. Coupling Beams - Displacement Ductility vs. Longitudinal Reinforcement Ratio 35
3.10 Conv. Reinf. Coupling Beams - Displacement Ductility vs. Vertical Reinforcement Ratio 35
3.11 Conv. Reinf. Coupling Beams - Displacement Ductility vs. Shear Stress Demand 36
3.12 Conv. Reinf. Coupling Beams - Displacement Ductility vs. Bond Stress Demand 36
3.13 Conv. Reinf. Coupling Beams - Ultimate Displacement vs. Longitudinal Reinforcement Ratio 37
3.14 Conv. Reinf. Coupling Beams - Ultimate Displacement vs. Vertical Reinforcement Ratio 37
3.15 Diag. Reinf. Coupling Beams - Displacement Ductility vs. Aspect Ratio . . . 38
3.16 Diag. Reinf. Coupling Beams - Displacement Ductility vs. Ultimate Displacement 38

3.17 Diag. Reinf. Coupling Beams - Displacement Ductility vs. Diagonal Reinforcement Ratio . . . 39
3.18 Diag. Reinf. Coupling Beams - Displacement Ductility vs. Vertical Reinforcement Ratio . . . 39
3.19 Diag. Reinf. Coupling Beams - Displacement Ductility vs. Shear Stress Demand . . . 40
3.20 Diag. Reinf. Coupling Beams - Displacement Ductility vs. Bond Stress Demand . . . 40
3.21 Diag. Reinf. Coupling Beams - Ultimate Displacement vs. Diagonal Reinforcement Ratio . . . 41
3.22 Diag. Reinf. Coupling Beams - Ultimate Displacement vs. Vertical Reinforcement Ratio . . . 41

4.1 Effect of Mesh Refinement . . . 47
4.2 VecTor2 Predicted Response of Galano P01 . . . 59
4.3 Experimental Response of Galano Specimens . . . 59
4.4 Displaced Shape and Crack Pattern at V_y of Galano P01 . . . 60
4.5 Displaced Shape and Crack Pattern at V_u of Galano P01 . . . 60
4.6 Displaced Shape and Crack Pattern at $0.8V_u$ of Galano P01 . . . 61
4.7 Experimental Failure of Galano P01 . . . 61
4.8 VecTor2 Predicted Response of Galano P02 . . . 62
4.9 Experimental Response of Galano P02 . . . 62
4.10 Displaced Shape and Crack Pattern at V_y of Galano P02 . . . 63
4.11 Displaced Shape and Crack Pattern at V_u of Galano P02 . . . 63
4.12 Displaced Shape and Crack Pattern at $0.8V_u$ of Galano P02 . . . 64
4.13 Experimental Failure of Galano P02 . . . 64
4.14 VecTor2 Predicted Response of Tassios CB2B . . . 65
4.15 Experimental Response of Tassios CB2B . . . 65
4.16 Displaced Shape and Crack Pattern at V_y of Tassios CB2B . . . 66
4.17 Displaced Shape and Crack Pattern at V_u of Tassios CB2B . . . 66
4.18 Displaced Shape and Crack Pattern at Δ_{max} of Tassios CB2B . . . 67
4.19 Experimental Failure of Tassios CB2B . . . 67
4.20 Mono. Coupling Beams - Yield Strength vs. Aspect Ratio . . . 69
4.21 Mono. Coupling Beams - Yield Strength vs. Vertical Reinforcement Ratio . . . 69
4.22 Mono. Coupling Beams - Yield Strength vs. Shear Demand Capacity Ratio . . . 70

4.23 Mono. Coupling Beams - Yield Strength vs. Shear Stress Demand 70
4.24 Mono. Coupling Beams - Ultimate Strength vs. Aspect Ratio 71
4.25 Mono. Coupling Beams - Ultimate Strength vs. Vertical Reinforcement Ratio 71
4.26 Mono. Coupling Beams - Ultimate Strength vs. Shear Demand Capacity Ratio 72
4.27 Mono. Coupling Beams - Ultimate Strength vs. Shear Stress Demand 72
4.28 Mono. Coupling Beams - Ultimate Displacement vs. Aspect Ratio 73
4.29 Mono. Coupling Beams - Ultimate Displacement vs. Vertical Reinforcement Ratio 73
4.30 Mono. Coupling Beams - Ultimate Displacement vs. Shear Demand Capacity Ratio 74
4.31 Mono. Coupling Beams - Ultimate Displacement vs. Shear Stress Demand . . 74
4.32 Mono. Coupling Beams - Yield Stiffness vs. Aspect Ratio 75
4.33 Mono. Coupling Beams - Yield Stiffness vs. Vertical Reinforcement Ratio . . 75
4.34 Mono. Coupling Beams - Yield Stiffness vs. Shear Demand Capacity Ratio . 76
4.35 Mono. Coupling Beams - Yield Stiffness vs. Shear Stress Demand 76
4.36 Mono. Coupling Beams - Ultimate Stiffness vs. Aspect Ratio 77
4.37 Mono. Coupling Beams - Ultimate Stiffness vs. Vertical Reinforcement Ratio 77
4.38 Mono. Coupling Beams - Ultimate Stiffness vs. Shear Demand Capacity Ratio 78
4.39 Mono. Coupling Beams - Ultimate Stiffness vs. Shear Stress Demand 78
4.40 Cyclic Coupling Beams - Yield Strength vs. Aspect Ratio 79
4.41 Cyclic Coupling Beams - Yield Strength vs. Vertical Reinforcement Ratio . . 79
4.42 Cyclic Coupling Beams - Yield Strength vs. Shear Demand Capacity Ratio . 80
4.43 Cyclic Coupling Beams - Yield Strength vs. Shear Stress Demand 80
4.44 Cyclic Coupling Beams - Ultimate Strength vs. Aspect Ratio 81
4.45 Cyclic Coupling Beams - Ultimate Strength vs. Vertical Reinforcement Ratio 81
4.46 Cyclic Coupling Beams - Ultimate Strength vs. Shear Demand Capacity Ratio 82
4.47 Cyclic Coupling Beams - Ultimate Strength vs. Shear Stress Demand 82
4.48 Cyclic Coupling Beams - Ultimate Displacement vs. Aspect Ratio 83
4.49 Cyclic Coupling Beams - Ultimate Displacement vs. Vertical Reinforcement Ratio 83
4.50 Cyclic Coupling Beams - Ultimate Displacement vs. Shear Demand Capacity Ratio 84
4.51 Cyclic Coupling Beams - Ultimate Displacement vs. Shear Stress Demand . . 84
4.52 Cyclic Coupling Beams - Yield Stiffness vs. Aspect Ratio 85

4.53 Cyclic Coupling Beams - Yield Stiffness vs. Vertical Reinforcement Ratio . . 85
4.54 Cyclic Coupling Beams - Yield Stiffness vs. Shear Demand Capacity Ratio . 86
4.55 Cyclic Coupling Beams - Yield Stiffness vs. Shear Stress Demand 86
4.56 Cyclic Coupling Beams - Ultimate Stiffness vs. Aspect Ratio 87
4.57 Cyclic Coupling Beams - Ultimate Stiffness vs. Vertical Reinforcement Ratio 87
4.58 Cyclic Coupling Beams - Ultimate Stiffness vs. Shear Demand Capacity Ratio 88
4.59 Cyclic Coupling Beams - Ultimate Stiffness vs. Shear Stress Demand 88
4.60 Zhao MCB2 Model Comparisons 91
4.61 Zhao MCB2 Model Comparisons 91

5.1 MCBR-ACI Load-Drift Response 99
5.2 CBR-ACI Load-Drift Response 99
5.3 MCBR-ACI-S Load-Drift Response 100
5.4 CBR-ACI-S Load-Drift Response 100
5.5 MCBR-318H Load-Drift Response 101
5.6 CBR-318H Load-Drift Response 101
5.7 MCBR-318H-F Load-Drift Response 102
5.8 CBR-318H-F Load-Drift Response 102
5.9 MCBR-318H-M Load-Drift Response 103
5.10 CBR-318H-M Load-Drift Response 103
5.11 MCBR-ACI vs. MCBR-318H Load-Drift Response 111
5.12 CBR-ACI vs. CBR-318H Load-Drift Response 111
5.13 MCBR-ACI vs. MCBR-318H-F Load-Drift Response 113
5.14 CBR-ACI vs. CBR-318H-F Load-Drift Response 113
5.15 CBR-ACI Crack Distribution at 5.25 % drift 114
5.16 CBR-318H-F Crack Distribution at 5.25 % drift 114
5.17 MCBR-ACI vs. MCBR-318H-M Load-Drift Response 116
5.18 CBR-ACI vs. CBR-318H-M Load-Drift Response 116

6.1 Assumed Coupled Wall Plastic Mechanism 121
6.2 Coupled Wall Dimensions 123
6.3 Geometry of coupling beam diagonal bars (ICC 2007) 126
6.4 Coupled Wall Reinforcement from Plastic Design 132
6.5 Coupling Beam Details 133

6.6 CW-ACI Coupled Wall Mesh . . . 136
6.7 CW-318HF and CW-318HFR Coupled Wall Mesh . . . 137
6.8 Coupled Wall Applied Displaced Shapes . . . 140
6.9 Coupling Beam Rotations . . . 143
6.10 Coupled Wall Story Force . . . 145
6.11 Coupled Wall Response with Applied Elastic Displacement . . . 146
6.12 Coupled Wall Response with Applied Plastic Displacement . . . 147
6.13 CW-ACI Displacement Comparisson . . . 148
6.14 CW-318HF Displacement Comparisson . . . 149
6.15 CW-318HFR Displacement Comparison . . . 150
6.16 Displacement Comparison at First Yield - Inverted Triangular Load . . . 151
6.17 Displacement Comparison at Maximum Base Shear - Inverted Triangular Load 152
6.18 Displacement Comparison at First Yield - Uniform Load . . . 153
6.19 Displacement Comparison at Maximum Base Shear - Uniform Load . . . 154
6.20 Displacement Comparison at First Yield - 0.3H Effective Height Load . . . 155
6.21 Displacement Comparison at Maximum Base Shear - 0.3H Effective Height Load . . . 156
6.22 CW-318HF - Effect of Load Distribution . . . 158
6.23 CW-318HFR - Effect of Load Distribution . . . 158
6.24 CW-ACI - Effect of Load Distribution . . . 159
6.25 Base Shear vs. Roof Drift - Triangular Load . . . 162
6.26 Base Shear vs. Roof Drift - Uniform Load . . . 163
6.27 Base Shear vs. Roof Drift - 0.3H Effective Height Load . . . 163
6.28 CW-ACI-T Roof Drift vs. Base Shear Response . . . 167
6.29 Coupled Wall ACI-U Roof Drift vs. Base Shear Response . . . 167
6.30 Coupled Wall ACI-3H Roof Drift vs. Base Shear Response . . . 168
6.31 CW-318HF-T Roof Drift vs. Base Shear Response . . . 168
6.32 CW-318HF-U Roof Drift vs. Base Shear Response . . . 169
6.33 CW-318HF-3H Roof Drift vs. Base Shear Response . . . 169
6.34 CW-318HFR-T Roof Drift vs. Base Shear Response . . . 170
6.35 CW-318HFR-U Roof Drift vs. Base Shear Response . . . 170
6.36 CW-318HFR-3H Roof Drift vs. Base Shear Response . . . 171

A.1 Galano P01 - Vector2 Force-Disp. Smeared Reinf. . . . 181

A.2 Galano - Experimental Force-Disp. Plot 181
A.3 Galano P01 - Vector2 Force-Disp. Truss Reinf. 182
A.4 Galano - Experimental Force-Disp. Plot 182
A.5 Galano P02 - Vector2 Force-Disp. Smeared Reinf. 183
A.6 Galano P02 - Experimental Force-Disp. Plot 183
A.7 Galano P02 - Vector2 Force-Disp. Truss Reinf. 184
A.8 Galano P02 - Experimental Force-Disp. Plot 184
A.9 Galano P05 - Vector2 Force-Disp. Smeared Reinf. 185
A.10 Galano - Experimental Force-Disp. Plot 185
A.11 Galano P05 - Vector2 Force-Disp. Truss Reinf. 186
A.12 Galano - Experimental Force-Disp. Plot 186
A.13 Galano P07 - Vector2 Force-Disp. Smeared Reinf. 187
A.14 Galano P07 - Experimental Force-Disp. Plot 187
A.15 Galano P07 - Vector2 Force-Disp. Truss Reinf. 188
A.16 Galano P07 - Experimental Force-Disp. Plot 188
A.17 Galano P10 - Vector2 Force-Disp. Smeared Reinf. 189
A.18 Galano - Experimental Force-Disp. Plot 189
A.19 Galano P10 - Vector2 Force-Disp. Truss Reinf. 190
A.20 Galano - Experimental Force-Disp. Plot 190
A.21 Galano P12 - Vector2 Force-Disp. Smeared Reinf. 191
A.22 Galano P12 - Experimental Force-Disp. Plot 191
A.23 Galano P12 - Vector2 Force-Disp. Truss Reinf. 192
A.24 Galano P12 - Experimental Force-Disp. Plot 192
A.25 Tassios CB1A - Vector2 Force-Disp. Smeared Reinf. 193
A.26 Tassios CB1A - Experimental Force-Disp. Plot 193
A.27 Tassios CB1A - Vector2 Force-Disp. Truss Reinf. 194
A.28 Tassios CB1A - Experimental Force-Disp. Plot 194
A.29 Tassios CB1B - Vector2 Force-Disp. Smeared Reinf. 195
A.30 Tassios CB1B - Experimental Force-Disp. Plot 195
A.31 Tassios CB1B - Vector2 Force-Disp. Truss Reinf. 196
A.32 Tassios CB1B - Experimental Force-Disp. Plot 196
A.33 Tassios CB2A - Vector2 Force-Disp Smeared Reinf. 197
A.34 Tassios CB2A - Experimental Force-Disp. Plot 197

A.35 Tassios CB2A - Vector2 Force-Disp Truss Reinf. 198
A.36 Tassios CB2A - Experimental Force-Disp. Plot 198
A.37 Tassios CB2B - Vector2 Force-Disp Smeared Reinf. 199
A.38 Tassios CB2B - Experimental Force-Disp. Plot 199
A.39 Tassios CB2B - Vector2 Force-Disp Smeared Reinf. 200
A.40 Tassios CB2B - Experimental Force-Disp. Plot 200
A.41 Kwan & Zhao MCB1 - Vector2 Force-Disp Smeared Reinf. 201
A.42 Kwan & Zhao - Experimental Force-Disp. Plot 201
A.43 Kwan & Zhao MCB1 - Vector2 Force-Disp Truss Reinf. 202
A.44 Kwan & Zhao - Experimental Force-Disp. Plot 202
A.45 Kwan & Zhao MCB2 - Vector2 Force-Disp Smeared Reinf. 203
A.46 Kwan & Zhao - Experimental Force-Disp. Plot 203
A.47 Kwan & Zhao MCB2 - Vector2 Force-Disp Truss Reinf. 204
A.48 Kwan & Zhao - Experimental Force-Disp. Plot 204
A.49 Kwan & Zhao MCB3 - Vector2 Force-Disp Smeared Reinf. 205
A.50 Kwan & Zhao - Experimental Force-Disp. Plot 205
A.51 Kwan & Zhao MCB3 - Vector2 Force-Disp Truss Reinf. 206
A.52 Kwan & Zhao - Experimental Force-Disp. Plot 206
A.53 Kwan & Zhao MCB4 - Vector2 Force-Disp Smeared Reinf. 207
A.54 Kwan & Zhao - Experimental Force-Disp. Plot 207
A.55 Kwan & Zhao MCB4 - Vector2 Force-Disp Truss Reinf. 208
A.56 Kwan & Zhao - Experimental Force-Disp. Plot 208
A.57 Kwan & Zhao CCB2 - Vector2 Force-Disp Smeared Reinf. 209
A.58 Kwan & Zhao CCB2 - Vector2 Force-Disp Truss Reinf. 209
A.59 Kwan & Zhao CCB4 - Vector2 Force-Disp Smeared Reinf. 210
A.60 Kwan & Zhao CCB4 - Experimental Force-Disp. Plot 210
A.61 Kwan & Zhao CCB4 - Vector2 Force-Disp Truss Reinf. 211
A.62 Kwan & Zhao CCB4 - Experimental Force-Disp. Plot 211
A.63 Kwan & Zhao CCB11 - Vector2 Force-Disp Smeared Reinf. 212
A.64 Kwan & Zhao CCB11 - Vector2 Force-Disp Truss Reinf. 212

B.1 MCBR1.ACI Displacement- VecTor2 214
B.2 MCBR2.318H Displacement - VecTor2 214
B.3 MCBR1.ACI-SN Displacement- VecTor2 215

B.4 MCBR1.ACI-SP Displacement - VecTor2 215
B.5 MCBR2.318H-F Displacement- VecTor2 216
B.6 MCBR3.318H-M Displacement - VecTor2 216
B.7 MCBR1.ACI Drift - VecTor2 217
B.8 MCBR2.318H Drift - VecTor2 217
B.9 MCBR2.318H-F Drift- VecTor2 218
B.10 MCBR3.318H-M Drift - VecTor2 218
B.11 CBR1.ACI Displacement- VecTor2 219
B.12 CBR2.318H Displacement - VecTor2 219
B.13 CBR2.318H-F Displacement- VecTor2 220
B.14 CBR3.318H-M Displacement - VecTor2 220
B.15 CBR1.ACI-S Displacement- VecTor2 221
B.16 CBR1.ACI Drift- VecTor2 222
B.17 CBR2.318H Drift - VecTor2 222
B.18 CBR2.318H-F Drift- VecTor2 223
B.19 CBR3.318H-M Drift - VecTor2 223
B.20 CBR1.ACI-S Drift- VecTor2 224
B.21 MCBR1.ACI vs. MCBR2.318H - VecTor2 225
B.22 CBR1.ACI vs. CBR2.318H - VecTor2 225
B.23 MCBR1.ACI vs. MCBR2.318H-F - VecTor2 226
B.24 CBR1.ACI vs. CBR2.318H-F - VecTor2 226
B.25 MCBR1.ACI vs. MCBR3.318H-M - VecTor2 227
B.26 CBR1.ACI vs. CBR3.318H-M - VecTor2 227

LIST OF TABLES

Table Number		Page
2.1	Conventionally Reinforced Coupling Beam Properties - Building Inventory	6
2.2	Diagonally Reinforced Coupling Beam Properties - Building Inventory	7
2.3	Conventionally Reinforced Coupling Beam Properties	14
2.4	Conventionally Reinforced Coupling Beam Reinforcement	15
2.5	Diagonally Reinforced Coupling Beam Properties	16
2.6	Diagonally Reinforced Coupling Beam Reinforcement	17
2.7	Coupling Beam Performance	18
2.8	Coupling Beam Capacity	19
2.9	Coupling Beam Drift, Displacement & Ductility	20
3.1	Coupling Beam Behavior Modes	26
4.1	Constitutive Models used in Coupling Beam Simulations	45
4.2	Analysis Parameters used in Coupling Beam Simulations	46
4.3	Experimental Coupling Beam Strength Predictions	52
4.4	Experimental Coupling Beam Stiffness Predictions	53
4.5	Experimental Coupling Beam Displacement and Drift Predictions	54
5.1	Coupling Beam Confinement Variations	96
5.2	Coupling Beam Material Properties	97
5.3	Coupling Beam Stiffness Results	104
5.4	Coupling Beam Strength Results	107
5.5	Coupling Beam Strength vs. Reinforcement Ratio	108
5.6	Coupling Beam Drift Results	109
6.1	Coupling beam forces and diagonal reinforcement	126
6.2	Calculation of factored axial forces and moments on wall piers	127
6.3	Plastic mechanism calculations - External Work	129
6.4	Plastic mechanism calculations - Internal Work	130

6.5 Coupled Wall Reinforcement Ratios 134
6.6 VecTor2 Constitutive Models and Analysis Parameters 135
6.7 Coupled Wall Displaced Shapes 140
6.8 Coupled Wall Model List 142
6.9 Coupled Wall Base Reactions at Maximum Displacement 157
6.10 Coupled Wall Degree of Coupling 160
6.11 Coupled Wall Roof Drift 161
6.12 Coupled Wall Inter-story Drift 164
6.13 Coupling Beam Drift 165

GLOSSARY

A_d: total area of diagonal reinforcement for one set of diagonal bars.

A_{dt}: area of confinement ties around the diagonal bar group within distance s_t.

A_g: gross cross section area of coupling beam.

A_{sh}: confinement reinforcement requirement per ACI 318-05 §21.4.4.1(b).

A_s: total area of longitudinal reinforcement.

A_v: area of shear reinforcement within a distance s.

b_w: width of coupling beam or thickness of wall pier.

b_c: width of confined concrete core, measured out-to-out of confining reinforcement.

DCR: : is the demand capacity ratio, defined as the maximum shear force, V_u, divided by the design strength, V_n.

DOC: degree of coupling is a measure of the percentage of the overturning moment due to the base moment in the wall piers versus the percentage due to the wall axial load, which results from the shear forces in the coupling beams, defined as
$DOC = \frac{TL}{M_w}$ where,
T = axial load in walls due to shears in coupling beams;
L = distance between the centroids of the wall piers; and,
M_w = total overturning moment in the base of the wall.

d: overall depth of coupling beam.

d_b: nominal diameter of reinforcing bar.

d_c: depth of confined concrete core, measured out-to-out of confining reinforcement.

E_c: modulus of elasticity of concrete.

E_s: modulus of elasticity of reinforcement.

E_{sh}: strain hardening modulus of elasticity of reinforcement.

EI: measure of component stiffness, modulus of elasticity * moment of inertia.

$f_c^{'}$: specified compressive strength of concrete.

f_y: specified yield strength of reinforcement.

f_t: specified tensile strength of concrete.

f_u: specified ultimate strength of reinforcement.

K_i: initial secant stiffness of coupling beam from Vector2 simulations.

K_y: yield stiffness of coupling beam from Vector2 simulations, taken as the secant stiffness at the point of first reinforcment yield.

K_{ye}: observed yield stiffness of coupling beam from experimental tests, taken as the secant stiffness at the observed yeild point.

K_u: ultimate stiffness of coupling beam from Vector2 simulations, taken as the secant stiffness at V_u.

K_{ue}: ultimate stiffness of coupling beam from experimental tests, taken as the secant stiffness at V_{ue}.

$K_{1.5}$: secant stiffness of coupling beam at 1.5% drift in coupling beam.

$K_{1.5e}$: secant stiffness of coupling beam at 1.5% drift in coupling beam from experimental tests.

K_6: secant stiffness of coupling beam at 6.0% drift in coupling beam.

K_{6e}: secant stiffness of coupling beam at 6.0% drift in coupling beam from experimental tests.

l_n: clear span length of coupling beam.

M_n: calculated moment strength of coupling beam per ACI 318-05.

M_{pr}: plastic moment strength of coupling beam using expected material strengths.

M_u: moment demand in ACI design procedures.

s: horizontal spacing of shear reinforcement.

s_t: spacing of confinement ties on a diagonal bar group.

SSD: shear stress demand, calculated as $V_n/A_g f_c^{'}$.

V_{pr}: plastic shear demand, $= 2M_{pr}/L$.

V_{nACI}: shear strength of beam per ACI 318.

V_y: shear strength of coupling beam at yield point.

V_{ye}: measured shear strength at yield point of coupling beam from experimental tests.

V_u: ultimate strength of coupling beam. Also represents the shear demand in ACI design procedures.

V_{ue}: measured ultimate strength of coupling beam from experimental tests.

$V_{0.85u}$: shear strength of coupling beam at $0.85 * V_u$.

$V_{1.5}$: shear strength of coupling beam at 1.5% drift, taken from reported load-displacement plots.

$V_{6.0}$: shear strength of coupling beam at 6.0% drift, taken from reported load-displacement plots.

Δ_i: is the inter-story drift ratio for a single story of the wall with the effects of rigid body rotation removed.

Δ_{roof}: is the roof displacement over the height of the wall.

Δ_y: drift of coupling beam at displacement corresponding to yield point, δ_y/L.

Δ_{ye}: drift of coupling beam at displacement corresponding to reported yield point of experimental tests, δ_{ye}/L.

Δ_u: drift of coupling beam at displacement corresponding to ultimate strength point, δ_u/L.

Δ_{ue}: drift of coupling beam at displacement corresponding to reported ultimate strength point of experimental tests, δ_u/L.

$\Delta_{0.85u}$: drift of coupling beam at displacement corresponding to 0.85 of reported ultimate strength point, $\delta_{0.85u}/L$.

δ_i: is the horizontal displacement of each floor level, taken as the average of all the nodal the displacements at each of the levels.

δ_y: displacement of coupling beam at yield point.

δ_{ye}: displacement of coupling beam at reported yield point of experimental tests.

δ_u: displacement of coupling beam at ultimate strength point.

δ_{ue}: displacement of coupling beam at reported ultimate strength point of experimental tests.

$\delta_{0.85u}$: displacement of coupling beam at 0.85 of reported ultimate strength point.

$\delta_{1.5}$: displacement of coupling beam at 1.5% drift.

$\delta_{6.0}$: displacement of coupling beam at 6.0% drift.

ϵ_0: peak compressive strain of concrete prior to strength degradation.

ϵ_{sh}: reinforcement strain at initiation of strain hardening.

μ_u: displacement ductility of coupling beam at ultimate strength point, δ_u/δ_y.

$\mu_{0.85u}$: displacement ductility of coupling beam at point where strength has decreased to 0.85 ultimate strength, $\delta_{0.85u}/\delta_y$.

ϕ: ACI strength reduction factor, varies per behavior type (i.e. shear, flexure, axial compression).

ρ_b: reinforcement ratio of primary longitudinal steel in boundary element of wall pier.

ρ_d: diagonal reinforcement ratio, A_d/db.

ρ_{dv}: reinforcement ratio of ties around coupling beam diagonal bar group, $A_{dt}/d_c s_t$).

ρ_{dt}: reinforcement ratio of out-of-plane reinforcement around coupling beam diagonal bar group, $A_{dt}/b_c s_t$.

ρ_h: reinforcement ratio of horizontal shear reinforcement of wall pier, A_h/sb.

ρ_l: longitudinal reinforcement ratio, A_s/db.

ρ_t: out-of-plane reinforcement ratio for coupling beam or wall pier, A_t/ds.

ρ_v: vertical reinforcement ratio, A_v/sb.

θ_{CB}: coupling beam end rotation.

ACKNOWLEDGMENTS

The author would like to acknowledge the contributions of Professor Emeritus Neil Hawkins, Ron Klemencic and John Hooper of Magnusson Klemencic Associates, Seattle and Andrew Taylor and Andres LePage of KPFF Engineers, Seattle in designing the proposed test program, Assistant Professor Daniel Kuchma, Assistant Professor Jian Zhang, and Graduate Researcher Jun Ji from the University of Illinois at Urbana-Champagne in the experimental program. The research presented here was funded by the National Science Foundation through the Network for Earthquake Engineering Simulation Research Program, grant CMS–0421577.

The author wishes to thank Professors Laura Lowes and Dawn Lehman for their direction and assistance and to the Civil and Environmental Engineering department at the University of Washington for providing the opportunity and scholarships.

Most importantly, the author wishes to express sincere appreciation and gratitude to his wife Nadège, for her patience, love and support through the duration of this project.

Chapter 1

INTRODUCTION

Reinforced concrete shear walls are commonly used in tall buildings to resist lateral loads. Due to the presence of regular door and window openings these walls are often divided into smaller wall piers that are coupled by beams over the openings. The behavior of a coupled shear wall is determined by the combined flexure and shear response of both the wall piers and the coupling beams. Capacity based design methods are typically used to ensure that coupling beams and wall pierss exhibit flexural yielding and have sufficient shear strength to preclude brittle shear failure.

During earthquake loading, if the coupling beams are very strong, energy dissipation will typically occur through inelastic flexural action at the base of the wall piers, including yielding of longitudinal reinforcing steel and crushing/cracking of concrete. Since the wall piers also carry gravity loads, significant damage to them could compromise the safety of the building and thus is not a desirable mode of behavior. Alternatively, if the coupling beams are very weak, energy dissipation will be limited to that yielding associated with the coupling beams. While this mode of behavior will not compromise the vertical load carrying capacity of the building, it may not provide an adequate amount of lateral resistance to meet the lateral design requirements.

Current performance-based design methods attempt to optimize the behavior of coupled shear walls by maximizing the energy dissipation in both the coupling beams and the wall piers. However, these methods assume coupled wall behavior that, while desirable, may not actually occur. This study uses nonlinear finite element analysis to investigate the behavior of coupled shear walls and thereby provide an improved understanding of current

performance-based design methods.

1.1 Objectives

The primary objectives of this study were to improve understanding of the performance of coupled walls designed in accordance with current codes (2006 IBC, ACI 318-05), and to investigate the impact of coupling beam design on coupled wall performance. Research activities included:

1. Review previous research investigating coupled wall, planar wall, and coupling beam behavior.

2. Improve understanding of the capabilities of VecTor2 (Vecchio and Wong 2006), a nonlinear finite element analysis program that utilizes two-dimensional continuum elements considering shear and flexural effects based on the modified compression field theory (MCFT). An extensive evaluation study was done comparing simulated and observed data for coupling beams.

3. Design a one-third scale prototype coupled wall test specimen as part of an ongoing NSF-sponsored NEESR project.

4. Predict the performance of coupling beams with confinement reinforcement similar to, but not consistent with current code requirements.

5. Simulate the response of the prototype wall and variations of the prototype wall incorporating non-code-compliant coupling beams.

1.2 Outline of Thesis

The above research objectives are presented in this thesis as follows:

Chapter 2 discusses the data set of previous coupling beam experiments, previous analytical studies of shear walls, and the inventory of representative coupled shear wall buildings.

Chapter 3 studies the damage patterns, failure modes, performance correlations, and explores damage prediction parameters of the experimental coupling beam data set.

Chapter 4 presents a comparison of experimental coupling beam tests with nonlinear finite element simulations using VecTor2 to determine the capabilities and limitations of the program.

Chapter 5 discusses the current design methods for coupled shear walls and coupling beams and presents the performance-based design of the one-third scale coupled shear wall specimen.

Chapter 6 explores the effect of confinement reinforcement on the coupling beam response. Five confinement variations on the coupling beam designed for the coupled shear wall specimen are simulated using VecTor2.

Chapter 7 uses VecTor2 to simulate the response of the one-third scale coupled shear wall specimen and to predict the potential damage patterns.

Chapter 8 summarizes the thesis, presents the best practices for nonlinear continuum modeling using VecTor2, draws conclusions from the presented data in regard to the expected nonlinear behavior of coupled shear walls, discusses current coupled shear wall design methods, and makes recommendations for future performance based design and detailing of coupled shear walls and coupling beams.

Chapter 2
BACKGROUND RESEARCH

2.1 Building Inventory

A goal of this study is to design coupled wall test specimens that are representative of current construction. In 2004, a questionnaire requesting information on current practices and examples of current building designs was sent to 30 engineering firms. Five companies responded to this request with structural drawings of ten buildings. The buildings were designed for construction on the West Coast in Washington and California primarily using the 1991 to 1997 Uniform Building Code (UBC). From this set of buildings, four were found to contain coupled shear walls. An inventory of the individual coupling beams from these four buildings was compiled. The coupling beam properties are shown in Tables 2.1 and 2.2. The buildings are:

- MFC: 23-story office building designed per the 1997 UBC for construction in Seattle.
- EH: 30-story hotel designed per the 1991 UBC for construction in San Francisco.
- BTT: 20-story office building designed per the 1991 UBC for construction in Bellevue.
- FS: 25-story office building designed per the 1998 California Building Code (CBC) for construction in San Francisco.

2.2 Coupling Beams

A review of previous research suggests that coupling beams can be divided into three categories based on their reinforcement configuration: Conventional, Double Diagonal or Rhombic, and Diagonal. These different layouts are shown in Figure 2.1 and described below.

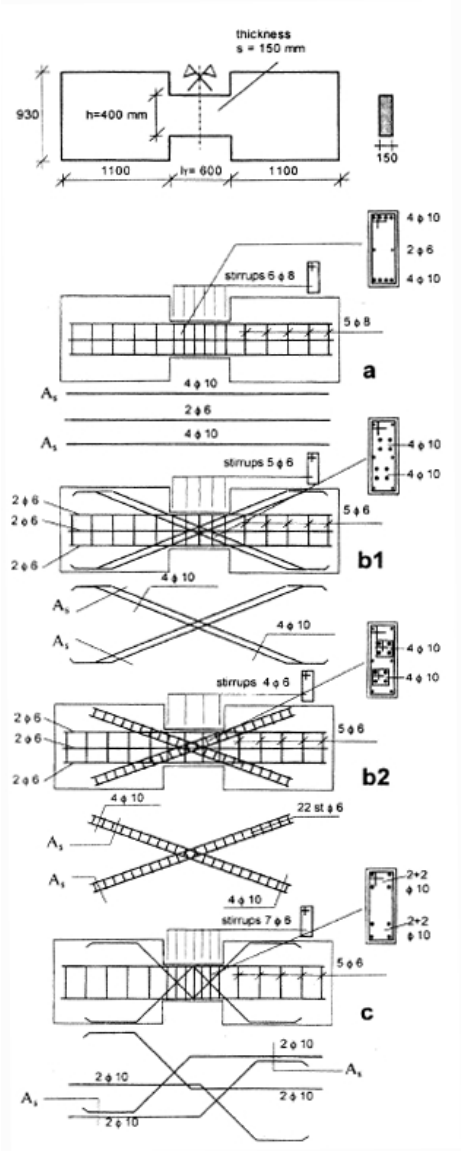

Figure 2.1: Coupling Beam Reinforcement Layouts (Galano and Vignoli 2000)

Table 2.1: Conventionally Reinforced Coupling Beam Properties - Building Inventory

	Dimensions				**Long. Reinf.**		**Shear Reinf.**		
Building	b	d	L	L/d	A_s	ρ_l	s_t	A_v	ρ_v
	(mm)	(mm)	(mm)		(mm^2)	(A_t/db)	(mm)	(mm^2)	(A_v/bs)
Conventional Longitudinal Reinforcement									
MFC	762	914	2947	3.2	4026	0.58%	102	600	0.78%
MFC	762	914	2947	3.2	5032	0.72%	102	600	0.78%
EH	610	711	2438	3.4	2581	0.60%	76	800	1.72%
EH	610	711	2438	3.4	5032	1.16%	102	800	1.29%
EH	457	710	2438	3.4	3019	0.93%	102	600	1.29%
EH	610	914	2438	2.7	2581	0.46%	102	600	0.97%
Average	635	813	2608	3.2	3712	0.74%	97	667	1.14%
Mean	610	813	2608	3.2	3712	0.74%	97	667	1.14%
Std. Dev	115	111	263	0.3	1151	0.26%	10	103	0.37%

Conventional Reinforcement

Conventional coupling beams typically have a reinforcement pattern that includes concentrated top and bottom longitudinal bars to resist flexural demands and closed vertical ties or stirrups distributed along the length of the beam to provide shear resistance and confinement of the cross section. Conventional coupling beams may have additional longitudinal reinforcement distributed over the depth of the section to provide additional resistance to sliding shear. Coupling beams with conventional reinforcement are allowed by the ACI 318 code if the shear stress demand is less than $4\sqrt{f_c'}b_w d$ and $l_n/d > 2$, where

$f_c^{'}$: specified compressive strength of concrete,

b_w : width of coupling beam or thickness of wall pier

d : overall depth of coupling beam, mm, and

l_n : clear span length of coupling beam.

Table 2.2: Diagonally Reinforced Coupling Beam Properties - Building Inventory

	Dimensions				**Long. Reinf.**		**Shear Reinf.**			**Diag. Reinf.**		**Diag. Ties**	
Building	b	d	L	L/d	A_s	ρ_l	s_t	A_v	ρ_v	A_d	ρ_d	*Bar#*	s_t
	(mm)	(mm)	(mm)		(mm^2)	(A_t/db)	(mm)	(mm^2)	(A_v/bs)	(mm^2)	(A_d/db)		(mm)
Diagonal Reinforcement													
BTT	610	1524	2438	1.6	4026	0.43%	102	400	0.65%	6039	0.65%	3	102
BTT	610	1219	1676	1.4	4026	0.54%	102	400	0.65%	6039	0.81%	3	102
BTT	610	1524	2438	1.6	4026	0.43%	102	400	0.65%	6039	0.65%	3	102
FS	610	610	1219	2.0	8052	2.17%	102	258	0.42%	8052	2.17%	5	89
FS	610	610	1929	3.2	8052	2.17%	102	258	0.42%	8052	2.17%	5	89
FS	610	610	1524	2.5	6555	1.76%	102	258	0.42%	6555	1.76%	5	89
MFC	762	914	1829	2.0	568	0.08%	152	400	0.34%	8052	1.16%	4	102
MFC	762	914	1320	1.4	568	0.08%	152	400	0.34%	6039	0.87%	4	102
MFC	762	914	1015	1.1	568	0.08%	152	400	0.34%	6555	0.94%	4	102
MFC	762	914	1320	1.4	568	0.08%	152	400	0.34%	10064	1.44%	4	102
EH	610	711	1015	1.4	1290	0.30%	203	258	0.21%	2581	0.60%	4	102
EH	457	711	1015	1.4	1019	0.31%	203	258	0.28%	2039	0.63%	4	102
EH	457	914	1015	1.1	568	0.14%	203	258	0.28%	1135	0.27%	4	102
Average	633	930	1520	1.7	3068	0.66%	141	334	0.41%	5941	1.09%	4	99
Mean	610	914	1320	1.4	1290	0.31%	152	400	0.34%	6039	0.87%	4	102
Std. Dev	105	315	514	0.6	2933	0.80%	42	74	0.15%	2594	0.62%	1	6

Double Diagonal Reinforcement

Double Diagonal or Rhombic, depending on the researcher's naming convention, coupling beams have a two sets of diagonal bars that cross twice near each end of the coupling beam. These diagonal bars are in addition to the longitudinal and vertical bars found in conventional coupling beams. The addition of the diagonal bars in intended to improve the seismic resistance and prevent a brittle failure. Double Diagonal coupling beams are included in many of the experimental test programs; however, they are not present in the building inventory and are not referenced in the ACI 318 code, for this reason they were not included in the analytical modeling of this study.

Diagonal Reinforcement

Diagonally reinforced coupling beams have two sets of diagonal bars extending through the entire coupling beam. The diagonal bars are the primary reinforcement of the coupling beam and provide both flexural and shear resistance. ACI 318-05 requires that nominal horizontal and vertical reinforcement be included to restrain the width of cracks in the coupling beam. The horizontal reinforcement is typically added as top and bottom reinforcement and possibly additional longitudinal bars distributed over the height of the beam. The vertical reinforcement is typically added as closed vertical ties distributed over the length of the beam, similar to a conventionally reinforced coupling beam. ACI 318-05 requires that the diagonal reinforcement be confined by closed ties place around the diagonal bars groups. However, in experimental studies, these ties are not always included, as shown in reinforcement pattern b1 of Figure 2.1. Coupling beams with diagonal reinforcement are allowed by the ACI 318 code if $l_n/d < 4$ and are required for $l_n/d < 2$ and a shear stress demand greater than $4\sqrt{f'_c}b_w d$.

2.3 Previous Experimental Coupling Beam Studies

Three criteria were used to select the coupling beam test specimens for inclusion in the current study. First, only coupling beams typical of modern construction with design pa-

rameters within the range seen in the building inventory were included. Second, only specimens subjected to pseudo-static cyclic or monotonic loading were included. Third, only tests for which data characteristics, geometry, material properties, and performance were available in published papers and research reports. Lack of sufficient data and age of the test specimen eliminated some test from inclusion in the current study. Specimens from Bristowe, Paulay, Shiu, and Santhakumar were not included. Following is a brief summary of the experimental programs and specimens that were included in this study. The load-displacement and load-rotation plots for the experimental specimens include in this study are included in Appendix A

2.3.1 Galano & Vignoli

Galano and Vignoli (2000) investigated the seismic performance of reinforced concrete coupling beams. The primary variables of the test were the reinforcment layout and the loading history of the specimens. Fifteen specimens with four different reinforcment layouts were tested; conventional, diagonal without confining ties, diagonal with confining ties, and rhombic. The loading setup consisted of series of steel rollers on the boundary blocks to provide restraint but allow rotation and two hydraulic jacks at the ends of the coupling beam specimen. A shearing deformation and rotation were applied to the coupling beam by pushing down with one jack while pulling up with the other. Figure 2.2 shows details of the experimental setup. The specimens were loaded both monotonically and cyclically to failure. Their test results showed that the beams with diagonal and rhomibic reinforcement layouts provide a higher rotational ductility than the beams with conventional reinforcement.

2.3.2 Kwan & Zhao

Kwan and Zhao (2002a) conducted two experimental programs to investigate the performance of reinforced concrete coupling beams. The first program was constrained to monotonic loading and the second program employed cyclic loading. Ten coupling beams of varying aspect ratio with similar longitudinal and transverse reinforcement ratios were tested.

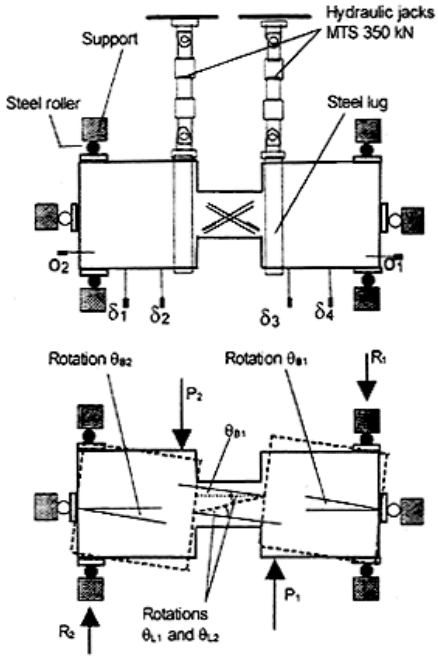

Figure 2.2: Galano & Vignoli Experimental Test Setup

A primary focus of the test program was to ensure equal end rotations of the coupling beam and to account for the local deformation at the beam-wall joint. To provide the required restraint, a fairly elaborate test set-up was used, see Figure 2.3. The researchers found that in short coupling beams the deformation due to joint rotation (i.e. rotation due to opening of a crack at the beam-anchor block interface) could represent more than 50% of the total deflection. They also noted that the diagonally reinforced coupling beams had much better energy dissipation capacity; however, their displacement ductility was very similar to the conventional coupling beams.

2.3.3 Tassios, Maretti, and Bezas

Tassios, Maretti, and Bezas (1996) investigated the seismic performance of ten reinforced concrete coupling beams subject to cyclic loading. The specimens were of varying aspect

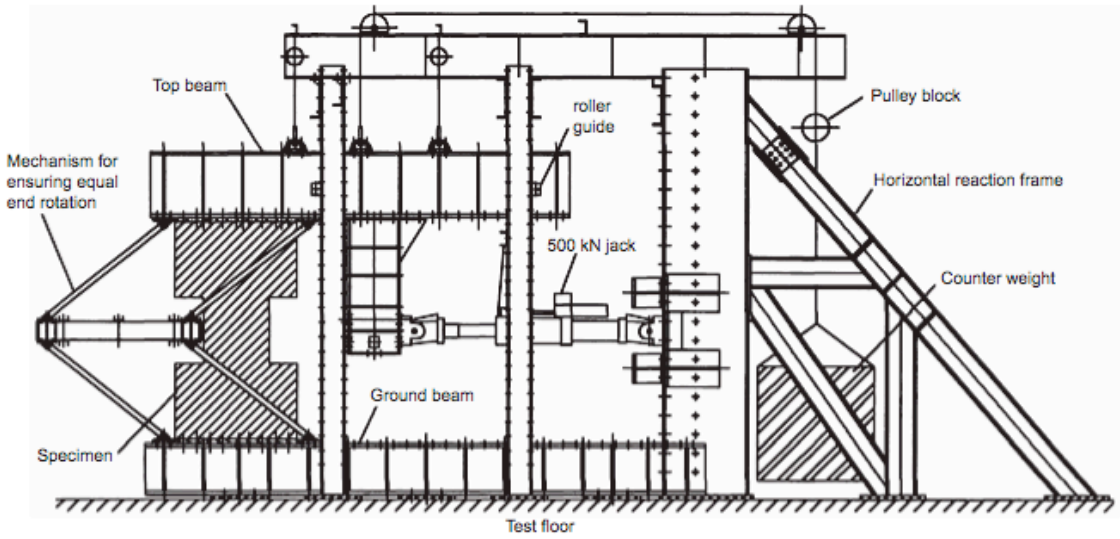

Figure 2.3: Kwan & Zhao Experimental Test Setup

ratios and reinforcement layouts of conventional, diagonal with ties, diagonal without ties, and double diagonal. The specimens were tested in a vertical position with the testing setup shown in Figure 2.4. The axis of the actuator coincided with the centerline of the specimen providing a point of zero moment at mid-span and a constant shear throughout the specimen. They noted that the diagonally reinforced specimens had a higher overall performance, (determined through comparisons of displacement ductility and normalized shear response), as compared with the other methods of reinforcement.

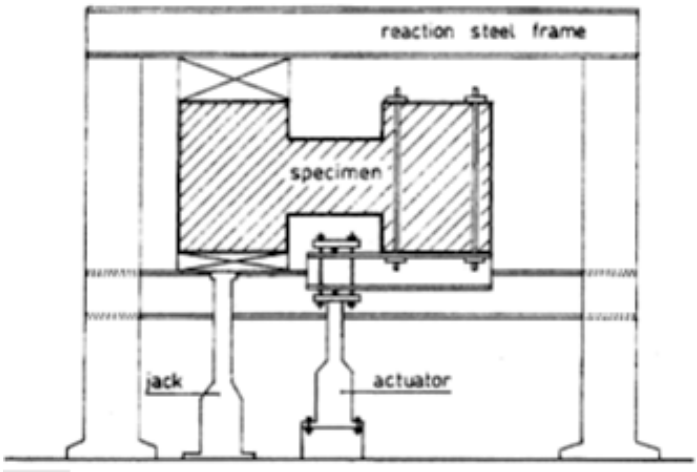

Figure 2.4: Tassios, Maretti, and Bezas Experimental Test Setup

2.3.4 Compiled Experiment Coupling Beam Data

Data from the experimental tests of coupling beams include in this study were compiled and evaluated to provide improved understanding of coupling beam performance. The tests are separated into conventionally and diagonally reinforced coupling beam lots. The geometry and material properties for each test specimen are summarized in Tables 2.3 and 2.5, reinforcement details in Tables 2.4 and 2.6, and experimental results in Tables 2.7, 2.8, and 2.9.

An evaluation of the impact of design parameters on the coupling beam performance is discussed in Chapter 3. A reduced set of the twenty-two tests was used to evaluate the finite element modeling capabilities of VecTor2; this is discussed in Chapter 4.

Table 2.3: Conventionally Reinforced Coupling Beam Properties

Conventional Coupling Beam Properties										
Specimen	*Scale*	*Load Type*	E_c (MPa)	$f_c^{'}$ (MPa)	f_y (MPa)	f_u (MPa)	b (mm)	d (mm)	L (mm)	L/d
Galano P01	0.49	M	24400	48.9	567	660	150	400	600	1.50
Galano P02	0.49	C	24400	44.5	567	660	150	400	600	1.50
Zhao CCB1	0.50	C	-	37.8	525	636	120	600	700	1.17
Zhao CCB2	0.50	C	-	37.8	525	636	120	500	700	1.40
Zhao CCB3	0.50	C	-	37.8	525	636	120	400	700	1.75
Zhao CCB4	0.50	C	-	37.8	525	636	120	350	700	2.00
Zhao CCB12	0.50	C	-	37.8	525	636	120	600	700	1.17
Zhao MCB1	0.50	M	24600	37.4	525	636	120	600	700	1.17
Zhao MCB2	0.50	M	23900	37.6	525	636	120	500	700	1.40
Zhao MCB3	0.50	M	23600	32.6	525	636	120	400	700	1.75
Zhao MCB4	0.50	M	24200	33.2	525	636	120	350	700	2.00
Tassios CB1A	0.50	C	-	32.8	484	771	130	500	500	1.00
Tassios CB1B	0.50	C	-	33.0	484	771	130	300	500	1.67
Tassios CB4A	0.50	C	-	29.8	484	771	130	500	500	1.00
Tassios CB4B	0.50	C	-	31.3	484	771	130	300	500	1.67

$Scale$: scale of specimen as defined by the experimental researchers.

$Load\,Type$: Method of load or displacement application, M - monotonic, C - cyclic.

E_c : modulus of elasticity of concrete if reported, otherwise shown as "-".

$f_c^{'}$: compressive strength of concrete based on cylinder or cube tests.

f_y : yield strength of longitudinal steel, based on rebar strength tests.

f_u : ultimate strength of longitudinal reinforcement, based on rebar strength tests.

b : width of coupling beam.

d : depth to longitudinal reinforcement.

L : clear span length of coupling beam.

L/d : aspect ratio of coupling beam.

Table 2.4: Conventionally Reinforced Coupling Beam Reinforcement

	Longitudinal Reinforcement							**Stirrups**		
Specimen	*#Long Bars*	d_b *Long* (mm)	A_s (mm^2)	ρ_l	*#Side Bars*	d_b *Side* (mm)	d_b *vert* (mm)	A_v (mm^2)	s (mm)	ρ_v
Galano P01	4	10	314.2	0.52%	2	6	6	56.5	80	0.84%
Galano P02	4	10	314.2	0.52%	2	6	6	56.5	80	0.84%
Zhao CCB1	3	12	334.8	0.49%	4	8	8	96.2	75	1.07%
Zhao CCB2	2, 1	12, 8	277.2	0.49%	4	8	8	96.2	75	1.07%
Zhao CCB3	2, 1	12, 8	277.2	0.50%	2	8	8	96.2	75	1.07%
Zhao CCB4	1, 2	12, 8	219.6	0.56%	2	8	8	96.2	75	1.07%
Zhao CCB12	3	12	335.0	0.49%	4	8	8	96.2	50	1.60%
Zhao MCB1	3	12	335.0	0.49%	4	8	8	96.2	75	1.07%
Zhao MCB2	2, 1	12, 8	277.2	0.49%	4	8	8	96.2	75	1.07%
Zhao MCB3	2	12	223.2	0.50%	2	8	8	96.2	75	1.07%
Zhao MCB4	1, 2	12, 8	219.2	0.56%	2	8	8	96.2	75	1.07%
Tassios CB1A	2	12	226.2	0.35%	4	6	8	100.5	75	1.03%
Tassios CB1B	2	12	226.2	0.58%	4	6	8	100.5	75	1.03%
Tassios CB4A	3	6	226.0	0.35%	4	20	8	100.5	75	1.03%
Tassios CB4B	3	6	226.0	0.58%	3	18	8	100.5	75	1.03%

$\#Long\ Bars$: number of longitudinal reinforcement bars per side (top or bottom).

$d_b\ Long$: diameter of longitudinal reinforcement.

A_s : total area of longitudinal reinforcement.

ρ_l : longitudinal reinforcement ration, defined as A_{st}/db.

$\#\ Side$: number of side or skin reinforcing bars.

$d_b\ Side$: diameter of side reinforcement.

$d_b\ vert$: diameter of vertical reinforcement or stirrups.

A_v : area of stirrups.

s : spacing of stirrups.

ρ_v : vertical reinforcement ratio, defined as A_v/sb.

Table 2.5: Diagonally Reinforced Coupling Beam Properties

Specimen	*Scale*	*Load Type*	E_c (MPa)	$f_c^{'}$ (MPa)	f_y (MPa)	f_u (MPa)	b (mm)	d (mm)	L (mm)	L/d
Galano P05	0.49	M	24400	39.9	567	660	150	400	600	1.50
Galano P07	0.49	C	24400	54.0	567	660	150	400	600	1.50
Galano P10	0.49	M	24400	46.8	567	660	150	400	600	1.50
Galano P12	0.49	C	24400	41.6	567	660	150	400	600	1.50
Zhao CCB11	0.50	C	-	37.8	525	636	120	600	700	1.17
Tassios CB2A	0.50	C	-	28.5	504	771	130	500	500	1.00
Tassios CB2B	0.50	C	-	26.3	504	771	130	300	500	1.67

Scale : scale of specimen as defined by the experimental researchers.

Load Type : Method of load or displacement application, M - monotonic, C - cyclic.

E_c : modulus of elasticity of concrete if reported, otherwise shown as "-".

$f_c^{'}$: compressive strength of concrete based on cylinder or cube tests.

f_y : yield strength of longitudinal steel, based on rebar strength tests.

f_u : ultimate strength of longitudinal reinforcement, based on rebar strength tests.

b : width of coupling beam.

d : depth to longitudinal reinforcement.

L : clear span length of coupling beam.

L/d : aspect ratio of coupling beam.

Table 2.6: Diagonally Reinforced Coupling Beam Reinforcement

	Longitudinal Reinforcement							**Stirrups**		
Specimen	*#Long Bars*	d_b*Long* (mm)	A_s (mm^2)	ρ_l	*#Side Bars*	d_b*Side* (mm)	d_b*vert* (mm)	A_v (mm^2)	s (mm)	ρ_v
Galano P05	2	6	85.0	0.14%	2	6	6	56.5	100	0.38%
Galano P07	2	6	85.0	0.14%	2	6	6	56.5	100	0.38%
Galano P10	2	6	85.0	0.14%	2	6	6	56.5	133	0.28%
Galano P12	2	6	85.0	0.14%	2	6	6	56.5	133	0.28%
Zhao CCB11	2	8	108.0	0.15%	4	8	8	92.6	140	0.55%
Tassios CB2A	3	6	84.8	0.13%	2	6	6	56.5	120	0.36%
Tassios CB2B	3	6	84.8	0.22%	2	6	6	56.5	120	0.36%

Table 2.6: (continued)

	Diagonal Bars					
Specimen	*No. Bar/Diag*	d_b*diag* (mm)	A_d (mm^2)	ρ_d	d_b*ties* (mm)	s_{ties} (mm)
Galano P05	4	10	314.2	0.52%	None	-
Galano P07	4	10	314.2	0.52%	None	-
Galano P10	4	10	314.2	0.52%	6	80
Galano P12	4	10	314.2	0.52%	6	80
Zhao CCB11	6	8	301.6	0.45%	6	60
Tassios CB2A	4	10	314.2	0.48%	6	50
Tassios CB2B	4	10	314.2	0.81%	6	50

$\#Long\ Bars$: number of longitudinal reinforcement bars per side (top or bottom).

$d_b\ Long$: diameter of longitudinal reinforcement.

A_s : total area of longitudinal reinforcement.

ρ_l : longitudinal reinforcement ration, defined as A_{st}/db.

$\#\ Side\ Bars$: number of side or skin reinforcing bars.

$d_b\ Side$: diameter of side reinforcement.

$d_b\ vert$: diameter of vertical reinforcement or stirrups.

A_v : area of stirrups.

s : spacing of stirrups.

ρ_v : vertical reinforcement ratio, defined as A_v/sb.

$No\ Bar/Diag$: number of diagonal reinforcement bars in each direction.

$d_b\ diag$: diameter of diagonal reinforcement.

A_d : total area of diagonal reinforcement.

ρ_d : diagonal reinforcement ratio, defined as A_d/db.

$d_b ties$: diameter of ties around diagonal bar group.

s_{ties} : spacing of ties around diagonal bar group.

Table 2.7: Coupling Beam Performance

	Shear Strength					Stiffness	
Specimen	V_y (KN)	V_u (KN)	$V_{0.85V_u}$ (KN)	$V_{1.5}$ (KN)	$V_{6.0}$ (KN)	K_y (KN/mm)	K_u (KN/mm)
Conventional Longitudinal Reinforcement							
Galano P01	223.9	223.9	190.3	225.0	150	44.3	9.3
Galano P02	210	230	195.5	225.0	120	41.2	13.7
Zhao CCB1	260	327	278.0	260.0	260	26.0	16.4
Zhao CCB2	190	227	193.0	220.0	-	31.7	18.9
Zhao CCB3	135	165	140.3	165.0	-	27.0	16.5
Zhao CCB4	110	123	104.6	123.0	75	18.3	10.3
Zhao CCB12	240	317	269.5	290.0	-	34.3	22.6
Zhao MCB1	262	344	292.4	265.0	344	25.0	7.6
Zhao MCB2	198	260	221.0	240.0	260	33.2	5.5
Zhao MCB3	126	159	135.2	150.0	159	31.5	3.8
Zhao MCB4	100	140	119.0	125.0	135	24.0	2.5
Tassios CB1A	179	212	180.2	180.0	-	22.9	12.5
Tassios CB1B	100	124	105.4	110.0	-	15.6	9.5
Tassios CB4A	282	282	239.7	-	-	26.9	25.6
Tassios CB4B	162	162	137.7	-	-	15.0	-
Average	185.2	219.7	186.8	198.3	187.9	27.8	12.5
Mean	190.0	223.9	190.3	220.0	154.5	26.9	11.4
Std. Dev.	61.5	74.2	63.1	59.8	90.4	8.5	6.9
Diagonal Reinforcement							
Galano P05	220	239.3	203.4	230.0	220	43.5	7.4
Galano P07	215	240	204.0	230.0	140	42.6	16.0
Galano P10	220	241.1	204.9	230.0	210	47.3	7.4
Galano P12	210	245	208.3	240.0	-	45.2	18.6
Zhao CCB11	290	346	294.1	280.0	-	30.5	18.2
Tassios CB2A	214	283	240.6	215.0	-	28.9	-
Tassios CB2B	115	170	144.5	110.0	-	13.5	6.8
Average	212.0	252.1	214.2	219.3	190.0	35.9	12.4
Mean	215.0	241.1	204.9	230.0	210.0	42.6	11.7
Std. Dev.	51.1	53.2	45.2	52.3	43.6	12.2	5.8

V_y : yield strength of coupling beam as specified by researcher.

V_u : ultimate strength of coupling beam as specified by researcher.

$V_{0.85V_u}$: 85% of V_u.

$V_{1.5}$: shear strength at 1.5% drift of coupling beam.

$V_{6.0}$: shear strength at 6.0% drift of coupling beam.

K_y : stiffness of coupling beam at the yield point, defined as V_y/δ_y.

K_u : stiffness of coupling beam at the ultimate strength point, defined as V_{u/δ_u}.

Table 2.8: Coupling Beam Capacity

		Capacity		
Specimen	M_n $(KN-mm)$	V_p (KN)	V_{nACI} (KN)	SSD
Conventional Longitudinal Reinforcement				
Galano P01	60996	203.3	316.4	5.8
Galano P02	60996	203.3	313.6	6.1
Zhao CCB1	90283	258.0	425.5	7.0
Zhao CCB2	62292	178.0	354.6	5.8
Zhao CCB3	49833	142.4	283.7	5.8
Zhao CCB4	34544	98.7	248.2	4.6
Zhao CCB12	90336	258.1	603.9	7.0
Zhao MCB1	90336	258.1	425.2	7.0
Zhao MCB2	62292	178.0	354.4	5.8
Zhao MCB3	40126	114.6	280.6	5.0
Zhao MCB4	34481	98.5	245.8	4.9
Tassios CB1A	46861	187.4	343.5	6.0
Tassios CB1B	28117	112.5	206.2	6.0
Tassios CB4A	46820	187.3	340.9	6.3
Tassios CB4B	28092	112.4	205.3	6.2
Average	55094	172.7	329.9	5.9
Mean	49833	178.0	316.4	6.0
Std. Dev.	21692	57.8	101.5	0.7
Diagonal Reinforcement				
Galano P05	59708	199.0	195.5	6.3
Galano P07	59708	199.0	195.5	5.4
Galano P10	59708	199.0	195.5	5.8
Galano P12	59708	199.0	195.5	6.1
Zhao CCB11	72646	207.6	203.9	5.6
Tassios CB2A	56380	225.5	221.6	7.8
Tassios CB2B	41022	164.1	161.2	9.8
Average	58411	199.0	195.5	6.7
Mean	59708	199.0	195.5	6.1
Std. Dev.	9272	18.2	17.9	1.6

M_n : moment strength of coupling beam calculated per ACI 318-05.

V_p : shear demand, calculated as $2M_{p/L}$.

V_{nACI} : shear strength of coupling beam calculated per ACI 318-05.

SSD shear stress demand, calculated as $V_p/A_g\sqrt{(f'_c)}$

Table 2.9: Coupling Beam Drift, Displacement & Ductility

	Drift			Displacement					Ductility	
Specimen	Δ_y	Δ_u	$\Delta_{0.85V_u}$	δ_y (mm)	δ_u (mm)	$\delta_{0.85u}$ (mm)	$\delta_{1.5}$ (mm)	$\delta_{6.0}$ (mm)	μ_u	$\mu_{0.85u}$
Conventional Longitudinal Reinforcement										
Galano P01	0.84%	4.00%	5.09%	5.1	24.0	30.5	4.7	18.8	4.8	6.0
Galano P02	0.85%	2.80%	4.60%	5.1	16.8	27.6	4.7	18.8	3.3	5.4
Zhao CCB1	1.43%	2.86%	5.71%	10.0	20.0	40.0	5.0	20.1	2.0	4.0
Zhao CCB2	0.86%	1.71%	4.29%	6.0	12.0	30.0	4.2	16.6	2.0	5.0
Zhao CCB3	0.71%	1.43%	3.57%	5.0	10.0	25.0	4.2	16.6	2.0	5.0
Zhao CCB4	0.86%	1.71%	5.14%	6.0	12.0	36.0	3.3	13.2	2.0	6.0
Zhao CCB12	1.00%	2.00%	4.29%	7.0	14.0	30.0	5.0	20.1	2.0	4.3
Zhao MCB1	1.50%	6.43%	8.57%	10.5	45.0	60.0	5.0	20.1	4.3	5.7
Zhao MCB2	0.85%	6.71%	9.86%	6.0	47.0	69.0	4.2	16.6	7.9	11.6
Zhao MCB3	0.57%	6.00%	7.00%	4.0	42.0	49.0	3.3	13.4	10.5	12.3
Zhao MCB4	0.59%	8.14%	10.00%	4.2	57.0	70.0	3.3	13.2	13.7	16.8
Tassios CB1A	1.56%	3.40%	4.84%	7.8	17.0	24.2	3.4	13.6	2.2	3.1
Tassios CB1B	1.28%	2.60%	3.71%	6.4	13.0	18.6	3.4	13.6	2.0	2.9
Tassios CB4A	2.10%	2.20%	9.66%	10.5	11.0	48.3	3.4	13.6	1.0	4.6
Tassios CB4B	2.16%	-	5.83%	10.8	-	29.2	3.4	13.6	-	2.7
Average	1.14%	3.71%	6.14%	7.0	24.3	39.2	4.0	16.1	4.3	6.4
Mean	0.86%	2.83%	5.14%	6.0	16.9	30.5	4.2	16.6	2.1	5.0
Std. Dev.	0.51%	2.20%	2.29%	2.4	16.1	16.5	0.7	2.9	3.8	4.0
Diagonal Reinforcement										
Galano P05	0.84%	5.40%	6.54%	5.1	32.4	39.2	1.3	5.1	6.4	7.8
Galano P07	0.84%	2.50%	5.20%	5.1	15.0	31.2	1.3	5.1	3.0	6.2
Galano P10	0.78%	5.40%	6.20%	4.7	32.4	37.2	1.3	5.1	7.0	8.0
Galano P12	0.78%	2.20%	3.90%	4.7	13.2	23.4	1.3	5.1	2.8	5.0
Zhao CCB11	1.36%	2.71%	5.43%	9.5	19.0	38.0	1.6	6.5	2.0	4.0
Tassios CB2A	1.48%	-	8.29%	7.4	-	41.4	1.3	5.1	-	5.6
Tassios CB2B	1.70%	5.00%	8.84%	8.5	25.0	44.2	1.3	5.1	2.9	5.2
Average	1.11%	3.87%	6.34%	6.4	22.8	36.4	1.3	5.3	4.0	6.0
Mean	0.84%	3.86%	6.20%	5.1	22.0	38.0	1.3	5.1	3.0	5.6
Std. Dev.	0.39%	1.55%	1.74%	2.0	8.4	7.0	0.1	0.5	2.1	1.5

δ_y : displacement at yield taken from load-displacment plots.

δ_u : displacement at ultimate shear force take from load displacement plots.

$\delta_{0.85V_u}$: displacement when shear force had dropped to 85% of V_u.

$\delta_{1.5}$: displacement at 1.5% coupling beam drift.

$\delta_{6.0}$: displacement at 6.0% coupling beam drift.

Δ_y : coupling beam drift at yield, δ_y/L.

Δ_u : coupling bean drift at ultimate shear force, δ_u/L.

μ_u : ultimate displacement ductility, δ_u/δ_y.

$\mu_{0.85V_u}$: displacement ductility when shear force had dropped to 85% of V_u, $\delta_{0.85V_u}/\delta_y$.

2.4 Previous Analyses

2.4.1 Oyen

Oyen (2006) investigated the nonlinear modeling of planar shear walls and compared the results from three types of analysis; lumped plasticity analysis using OpenSEES, section analysis using Response-2000, and nonlinear continuum analysis using VecTor2. His investigations support the following conclusions:

- Accurate prediction of the peak strength requires the modeling of effects of shear.
- Accurate simulation of the displacement response requires the modeling of shear deformation.
- Inclusion of a bar-slip model can improve the simulation of the displacement response.

2.4.2 Brown

Brown (2006) assembled a large database of previous experimental tests of planar walls. He developed fragility functions to define the probability that a specific method of repair will be required to restore a damaged planar wall to pre-earthquake condition. He also developed effective stiffness versus drift relationships for the experimental tests. The effective stiffness data was then used to calibrate models predicting the decay of flexural stiffness. Refer to Peter Brown's thesis for information about effective stiffness of shear walls.

2.4.3 Zhao et. al.

Zhao et al. (2004) investigated the behavior of deep coupling beams using a nonlinear finite element method they recently developed. Since the method has been presented in detail elsewhere, only a summary is presented herein.

The concrete and steel are modeled together by a four-noded isoparametric quadrilateral plane stress element with two extra non-conforming bending modes intended to remove

shear locking. The constitutive model of the element consists of two parts, one for the concrete and one for the steel. The concrete takes into consideration the biaxial behavior of the material, assuming isotropic behavior before cracking and orthotropic after cracking. Tension softening and compression softening are allowed for in the stress-strain relationships. A smeared crack model is utilized. The steel model assumes that the reinforcing bars are perfectly bonded to the concrete and uniformly smeared throughout the element. A trilinear stress-strain behavior is assumed. Stress transfer across cracks due to bond and dowel action is accounted for. This method is very similar to the Modified Compression Field Theory, however it is not referred to as such by the author.

The above method was used to analyze four monotonically loaded, conventionally reinforced coupling beams. The analytical models include the test specimen and the entire loading frame. The author was able to predict the ultimate strength with an average overestimation of only 6.2%. The analytical models were able to reach deflections that corresponded very well with the measured deflection at maximum load. However, the appearance of the load deflection curves does not agree very well with the experimental measured curves. The analytical specimens have a much higher stiffness prior to yield and reach the maximum load very early in the loading, whereas the experimental results gradually approach the maximum load near the end of the displacement history.

The author noted two main reasons for the discrepancies in the load-deflection curves of the analytical vs. experimental specimens.

1. The increased initial stiffness is due to the perfect bond model between the reinforcing bars and the concrete. In the experimental specimens flexural cracks gradually opened up and bond-slip of the main reinforcing bars occurred. The opening of the flexural cracks and slip of the reinforcing bars made a significant contribution to the lateral deflections of the coupling beam specimens, and thus reduced the initial stiffness.

2. In a real structure, tension strains are concentrated at the cracks and the concrete between cracks continues to contribute to the resistance of the structure through

tension stiffening. Use of the smeared crack model does not allow for proper modeling of the strain localization and tension stiffening that occurs in-between adjacent cracks formed in a real structure. This discrepancy caused the analytical models to loose strength rapidly after reaching the peak load and caused an underestimation of the post-yield effective stiffness.

Chapter 3

COUPLING BEAM PERFORMANCE AND DAMAGE PATTERNS

The behavior modes of coupling beams can vary widely from one configuration to another. The twenty two experimental coupling beams were compared to examine the influence of coupling beam parameters and performance measures on the observed behavior mode. In order to do this the behavior modes had to be defined and then assigned to each specimen. The following sections present the definition of the behavior modes, photographs of the specimens at failure, and plots comparing the behavior mode to various parameters.

3.1 Behavior Mode Definition

The coupling beams exhibited a wide variety of behavior and failure modes. In order to identify the failure mode of each specimen a clearly defined set of behavior criteria had to be developed. FEMA 306 provides a "Component Damage Classification Guide" for various reinforced concrete elements, however the specified behavior modes for coupling beams do not cover all of those observed. Six behavior modes were identified, the CB1 behavior modes are primarily seen in conventionally reinforced coupling beams while the CB2 modes are primarily seen in diagonally reinforced coupling beams. The behavior modes adapted from FEMA 306 and the additional ones defined are as follows:

CB1A Ductile Flexure: Spalling or vertical cracking occurs at toe regions in plastic hinge zone, typically limited to cover concrete. No buckled or fractured reinforcement.

CB1B Preemptive Diagonal Tension: For low levels of damage, appearance is similar to CB1A. At heavy damage levels behavior is characterized by wide diagonal cracks,

$\frac{1}{8}''$ to $\frac{3}{8}''$, extending from one corner of the beam to the other. Shear cracking is typically concentrated in a single crack.

CB1C Flexure/Diagonal Tension: For low levels of damage appearance is similar to CB1A. At heavy damage levels diagonal shear cracks become more prominent. Shear crack widths may exceed $\frac{1}{8}''$ but do not exceed $\frac{3}{8}''$. Higher width cracking is concentrated to one or more cracks.

CB1D Flexure/Sliding Shear: Development of a major vertical flexural crack along the entire beam depth, with some degradation of concrete along the crack, indicating that sliding has occurred. Possible small lateral offset at crack.

CB2G Diagonal Compression: Spalling of concrete at the center of the coupling beam where the two diagonal bar groups intersect. Flexural cracking occurs and ends of beam with wide diagonal shear cracks parallel to the diagonal reinforcement. Bucking of diagonal reinforcement may occur at the center of the coupling beam, within area of spalling.

CB2F Flexure Compression: Spalling and flexural cracking occurs at the toe regions in the plastic hinge zone. Diagonal shear cracks occur throughout the beam, typically following the direction of the diagonal reinforcement. Bucking of diagonal reinforcement may occur at the ends of the coupling beam.

3.2 Experimental Behavior Modes

The coupling beam behavior modes were determined based on photographs of the specimens found in the published reports and observations of the behavior by the experimental researchers. Table 3.1 shows the behavior modes for all the experimental coupling beams along with the parameters studied in section 3.3. Photographs of the coupling beams at failure are presented and grouped by behavior mode.

Table 3.1: Coupling Beam Behavior Modes

Specimen	*AR*	*Behavior Mode*	*SSD*	*Bond Demand*	Δ_u	ρ_v	ρ_d	μ_u
Conventional Longitudinal Reinforcement								
Galano P01	1.5	CB1B	5.8	60.0	4.00%	0.52%	0.84%	4.8
Galano P02	1.5	CB1A	6.1	60.0	2.80%	0.52%	0.84%	3.3
Tassios CB1A	1.0	CB1C	6.0	41.7	3.40%	0.35%	1.03%	2.2
Tassios CB1B	1.7	CB1B	6.0	41.7	2.60%	0.58%	1.03%	2.0
Tassios CB4A	1.0	CB1C	6.3	83.3	2.20%	0.35%	1.03%	1.0
Tassios CB4B	1.7	CB1C	6.2	83.3	-	0.58%	1.03%	-
Zhao CCB1	1.2	CB1C	7.0	58.3	2.86%	0.49%	1.07%	2.0
Zhao CCB2	1.4	CB1B	5.8	58.3	1.71%	0.49%	1.07%	2.0
Zhao CCB3	1.8	CB1D	5.8	58.3	1.43%	0.50%	1.07%	2.0
Zhao CCB4	2.0	CB1C	4.6	58.3	1.71%	0.56%	1.07%	2.0
Zhao CCB12	1.2	CB1D	7.0	58.3	2.00%	0.49%	1.60%	2.0
Zhao MCB1	1.2	CB1B	7.0	58.3	6.43%	0.49%	1.07%	4.3
Zhao MCB2	1.4	CB1C	5.8	58.3	6.71%	0.49%	1.07%	7.9
Zhao MCB3	1.8	CB1A	5.0	58.3	6.00%	0.50%	1.07%	10.5
Zhao MCB4	2.0	CB1A	4.9	58.3	8.14%	0.56%	1.07%	13.7
Average	1.4	-	6.0	68.2	3.45%	0.49%	1.12%	3.7
Median	1.4	-	6.0	58.3	2.20%	0.49%	1.07%	2.0
Std. Dev	0.3	-	0.8	10.5	2.24%	0.06%	0.17%	3.3
Diagonal Reinforcement								
Galano P05	1.5	-	6.3	72.1	5.40%	0.39%	0.52%	6.4
Galano P07	1.5	CB2G	5.4	72.1	2.50%	0.39%	0.52%	3.0
Galano P10	1.5	-	5.8	72.1	5.40%	0.31%	0.52%	7.0
Galano P12	1.5	CB2G	6.1	72.1	2.20%	0.31%	0.52%	2.8
Tassios CB2A	1.0	CB2F	7.8	70.7	-	0.36%	0.48%	-
Tassios CB2B	1.7	CB2F	9.8	58.3	5.00%	0.36%	0.81%	2.9
Zhao CCB11	1.2	CB2G	5.6	115.2	2.71%	0.57%	0.45%	2.0
Average	1.4	-	6.7	68.2	3.87%	0.38%	0.55%	4.0
Median	1.5	-	6.1	72.1	3.86%	0.36%	0.52%	3.0
Std. Dev	0.2	-	1.6	18.0	1.55%	0.09%	0.12%	2.1

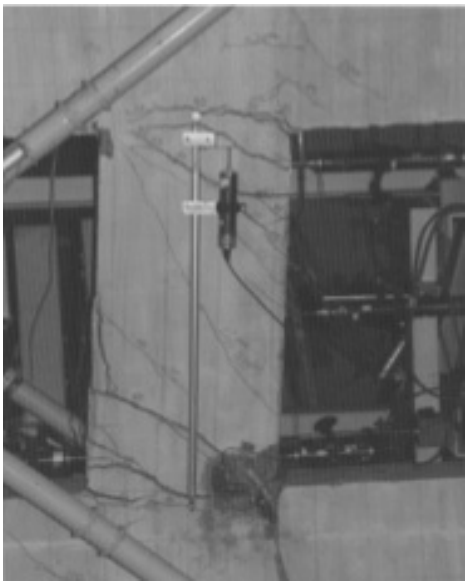

Zhao MCB4

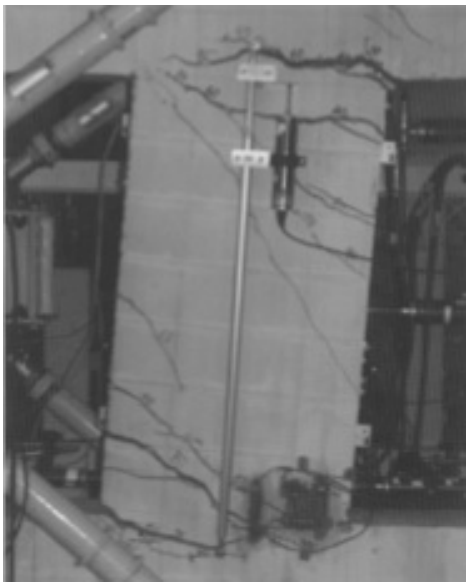

Zhao MCB3

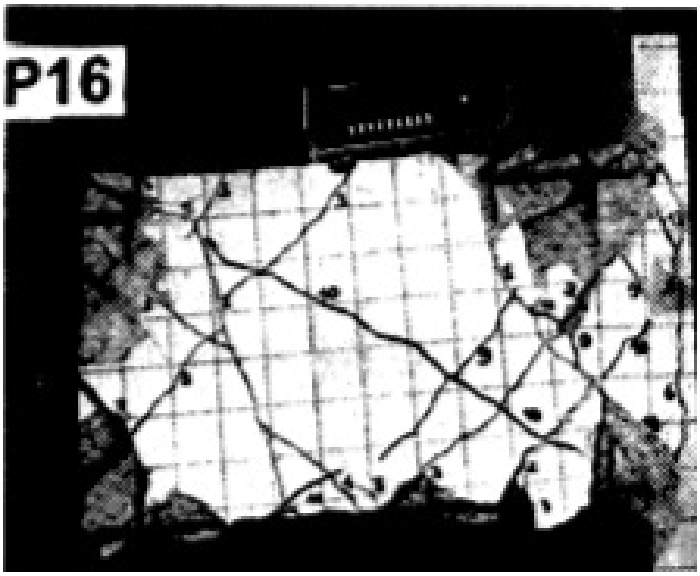

Galano P16

Figure 3.1: CB1A - Ductile Flexure

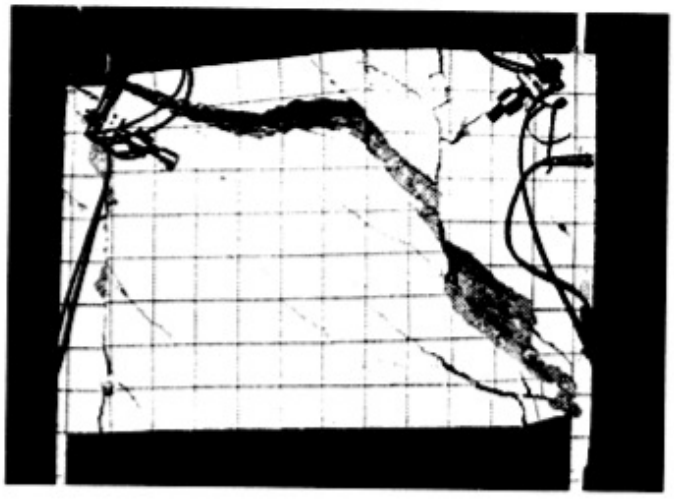

Galano P01

Zhao MCB1

Figure 3.2: CB1B - Preemptive Diagonal Tension

Tassios CB1B

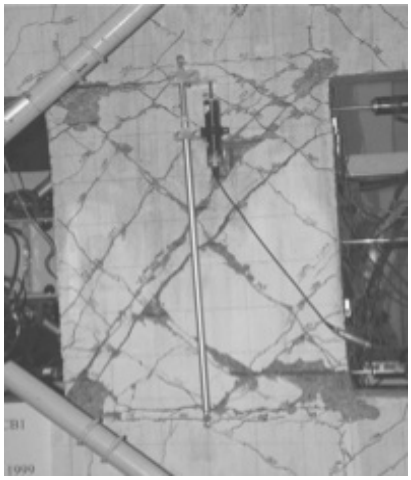

Zhao CCB1

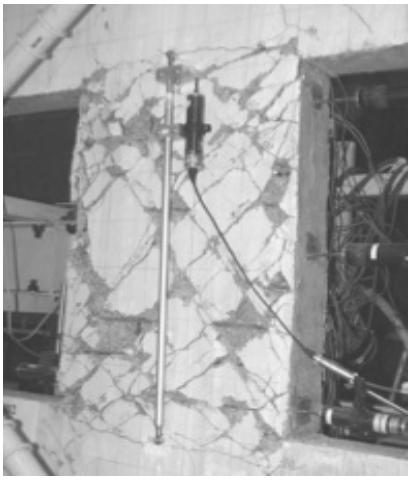

Zhao CCB2

Zhao CCB4

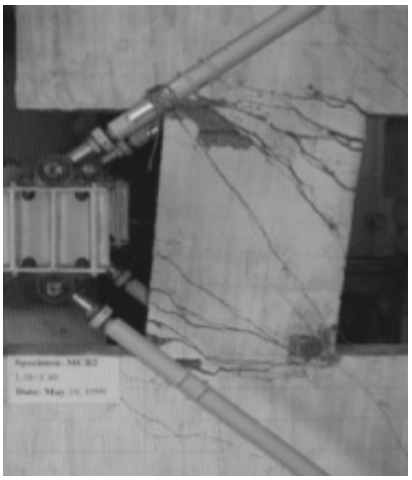

Zhao MCB2

Figure 3.3: CB1C - Flexure/Diagonal Tension

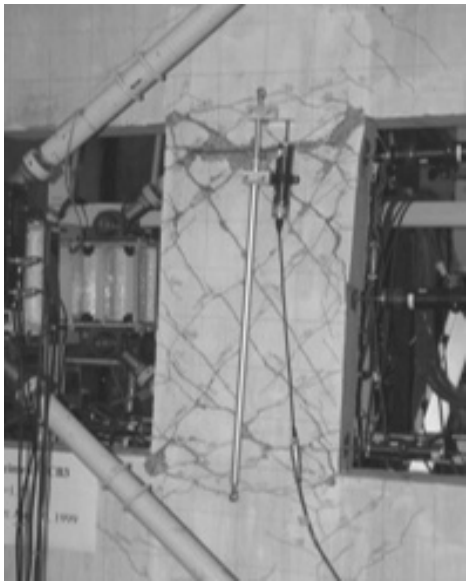

Zhao CCB3

Zhao CCB12

Figure 3.4: CB1D - Flexure/Sliding Shear

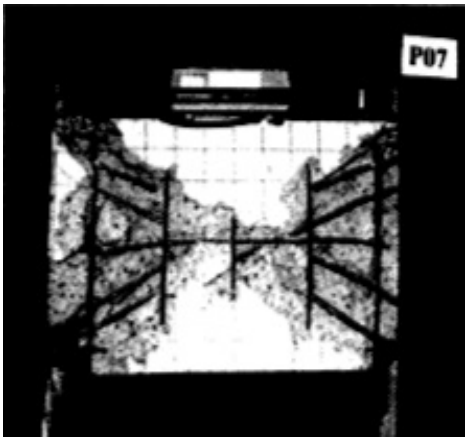

Galano P07

Galano P10

Tassios CB2A

Figure 3.5: CB2F - Flexure Compression

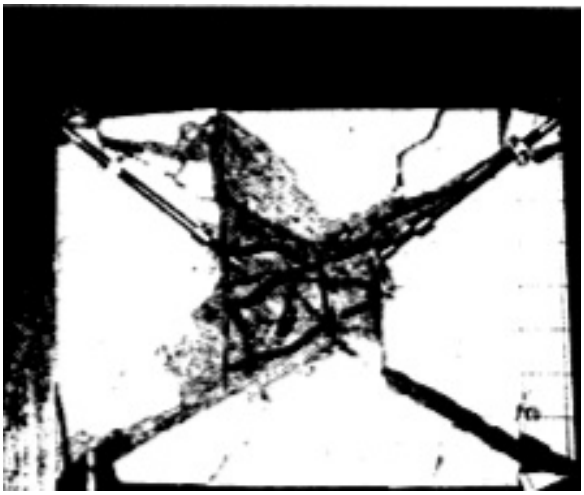

Galano P12

Zhao CCB11

Figure 3.6: CB2G - Diagonal Compression

3.3 Comparison Plots

For the conventionally reinforced coupling beams the aspect ratio, ρ_l, ρ_v, SSD, and bond demand were plotted against μ_u and Δ_u. For the diagonally reinforced coupling beams the aspect ratio, ρ_d, ρ_v, SSD, and bond demand were plotted against μ_u and Δ_u. For each comparison a plot was created with the data sorted by the behavior mode.

There were no discernible trends found between the behavior mode and the various parameters studied, this could be due to the wide variations in the coupling beam configurations that are included in this data set.

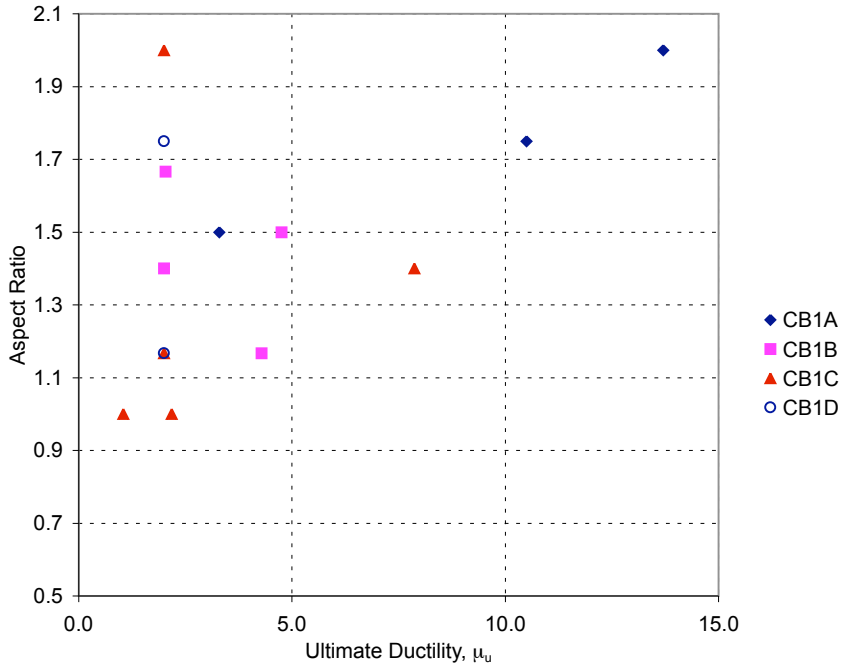

Figure 3.7: Conv. Reinf. Coupling Beams - Displacement Ductility vs. Aspect Ratio

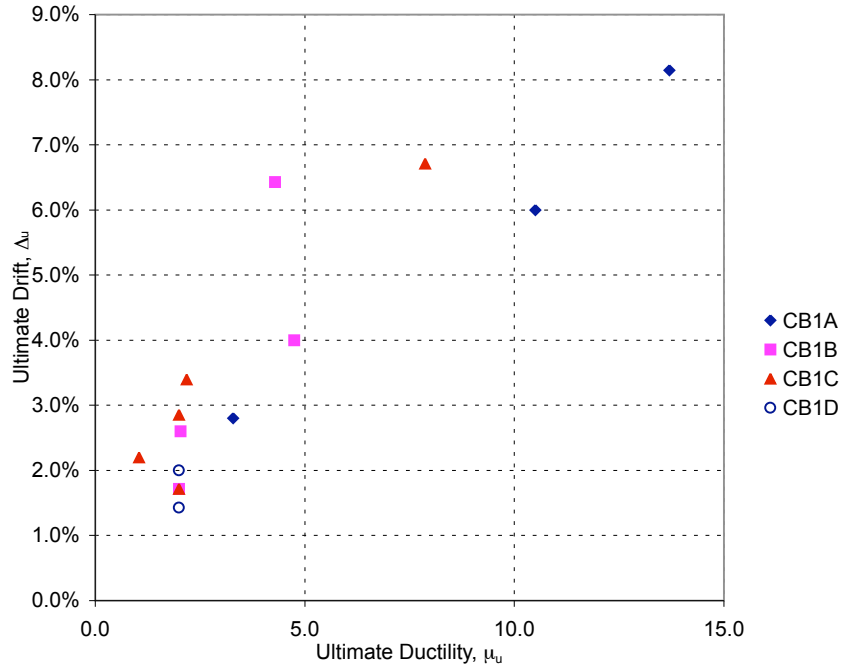

Figure 3.8: Conv. Reinf. Coupling Beams - Displacement Ductility vs. Ultimate Displacement

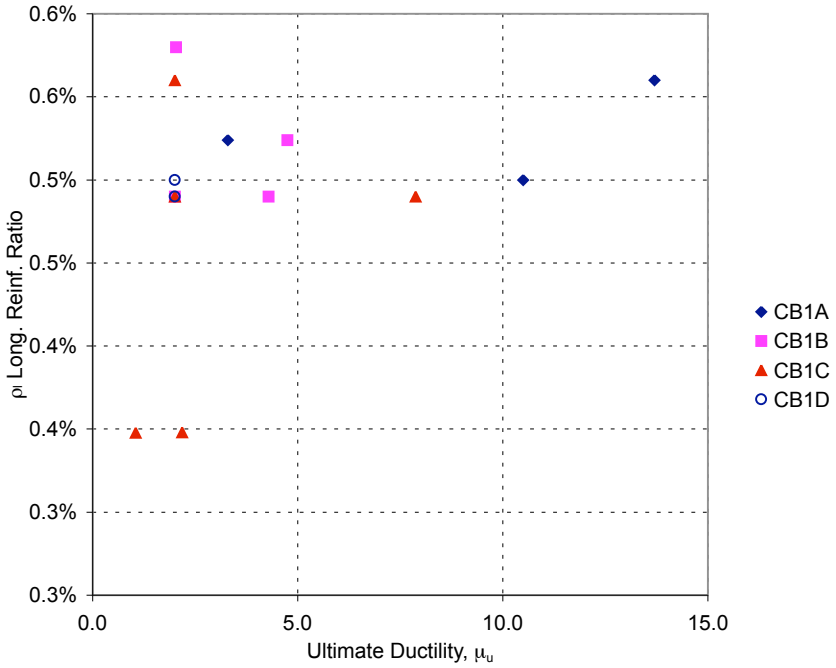

Figure 3.9: Conv. Reinf. Coupling Beams - Displacement Ductility vs. Longitudinal Reinforcement Ratio

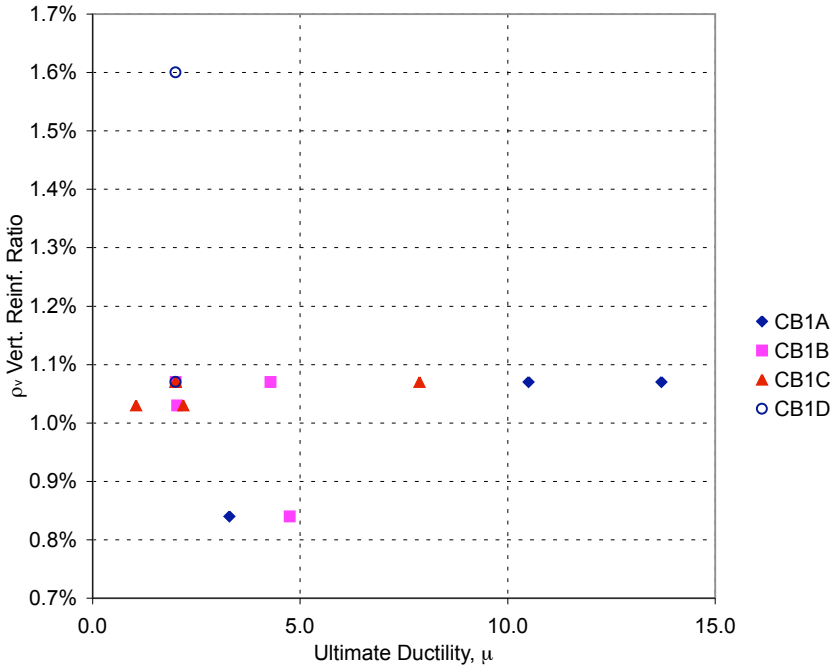

Figure 3.10: Conv. Reinf. Coupling Beams - Displacement Ductility vs. Vertical Reinforcement Ratio

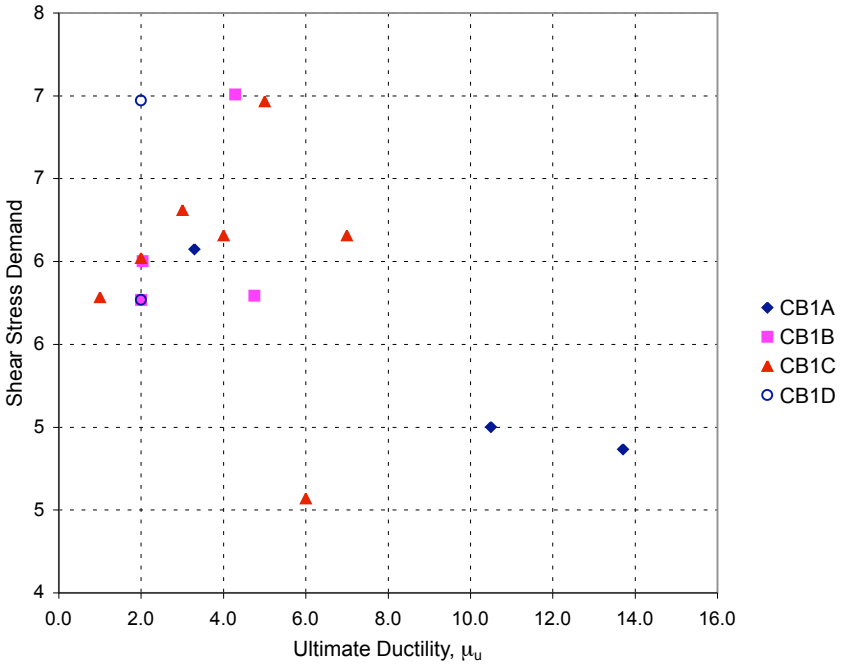

Figure 3.11: Conv. Reinf. Coupling Beams - Displacement Ductility vs. Shear Stress Demand

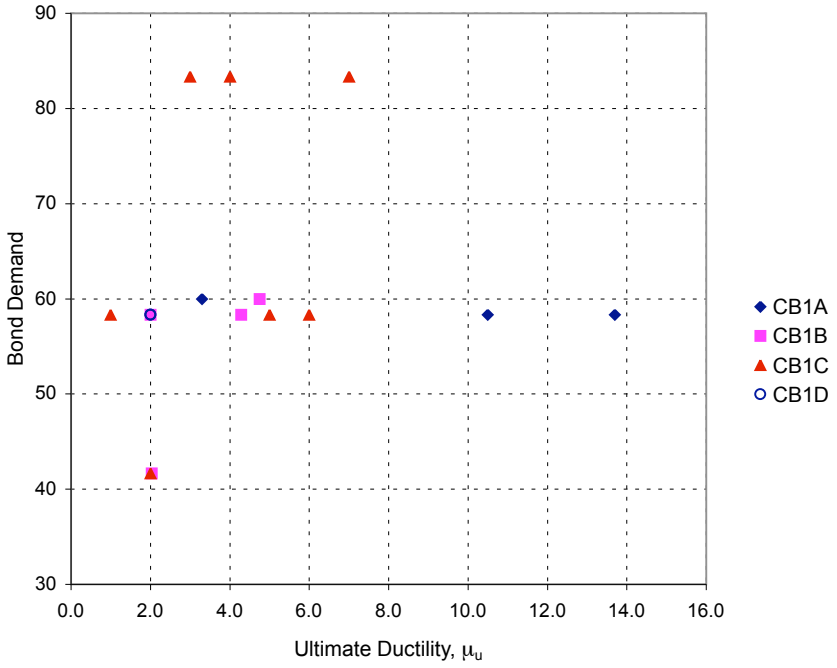

Figure 3.12: Conv. Reinf. Coupling Beams - Displacement Ductility vs. Bond Stress Demand

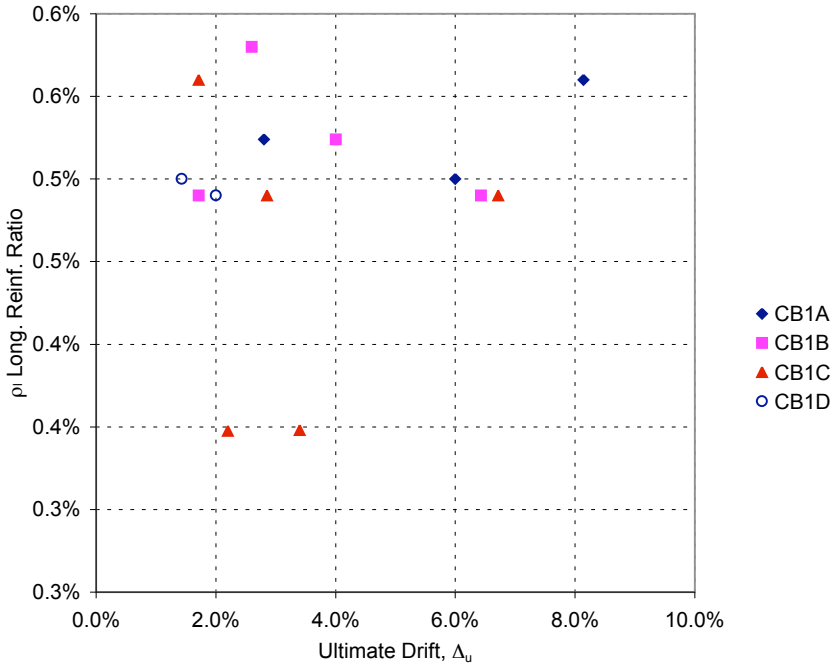

Figure 3.13: Conv. Reinf. Coupling Beams - Ultimate Displacement vs. Longitudinal Reinforcement Ratio

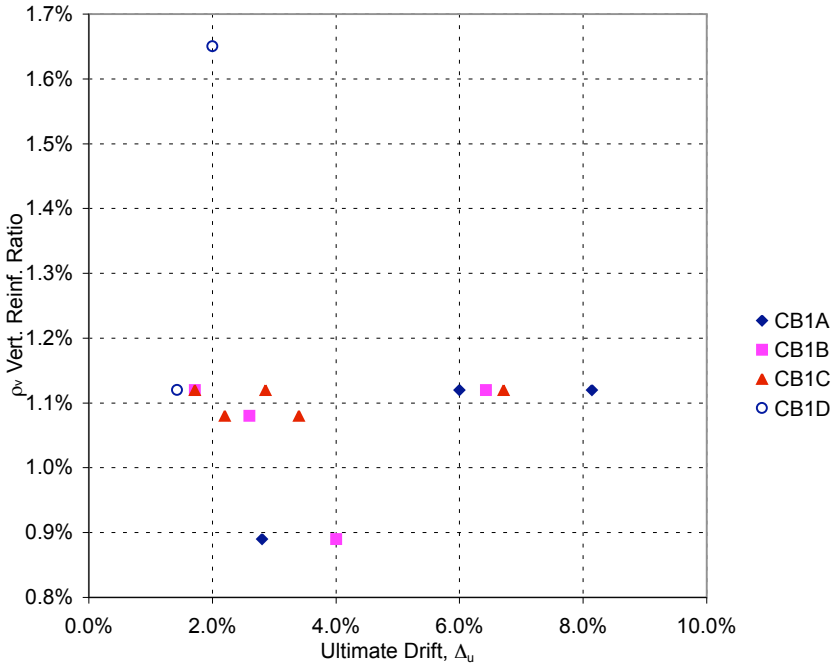

Figure 3.14: Conv. Reinf. Coupling Beams - Ultimate Displacement vs. Vertical Reinforcement Ratio

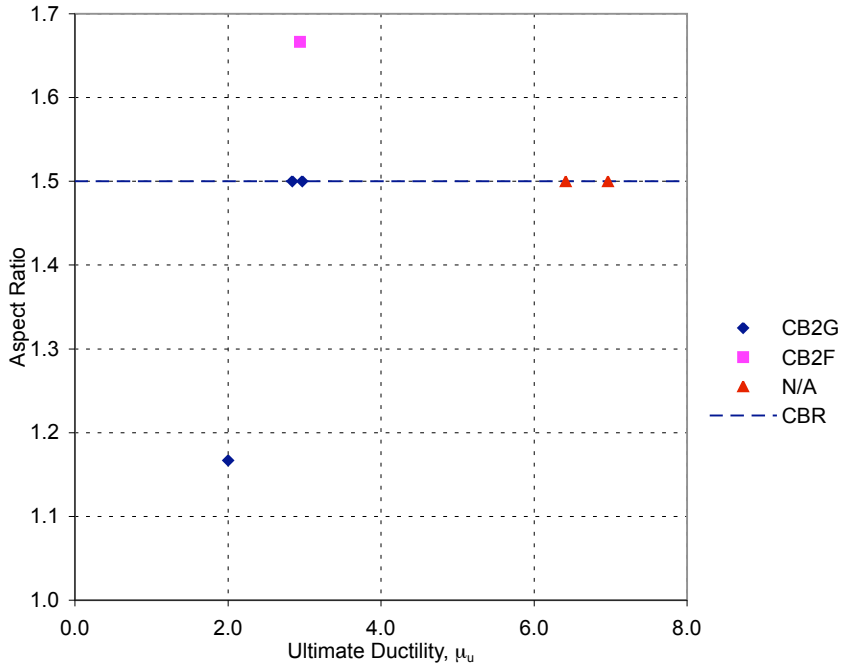

Figure 3.15: Diag. Reinf. Coupling Beams - Displacement Ductility vs. Aspect Ratio

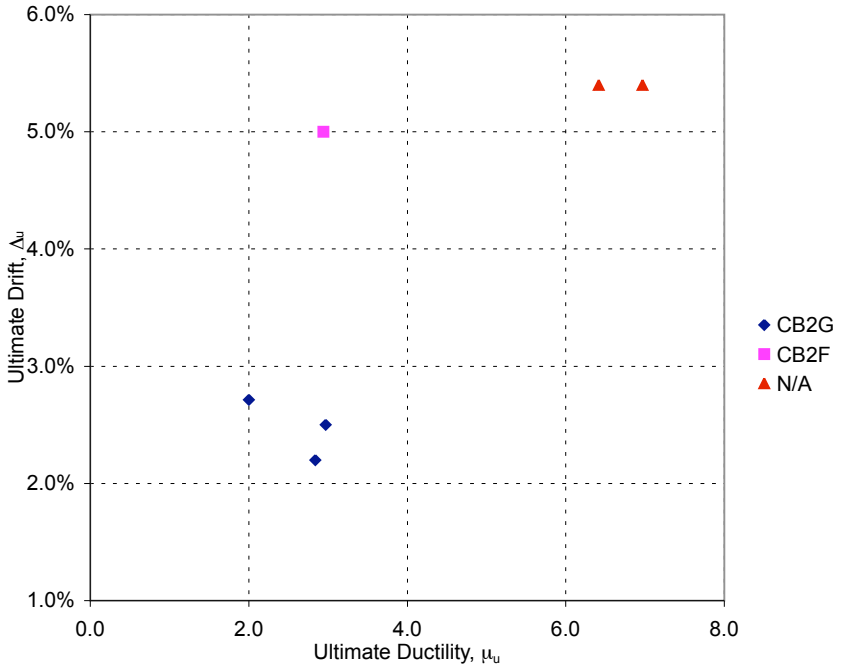

Figure 3.16: Diag. Reinf. Coupling Beams - Displacement Ductility vs. Ultimate Displacement

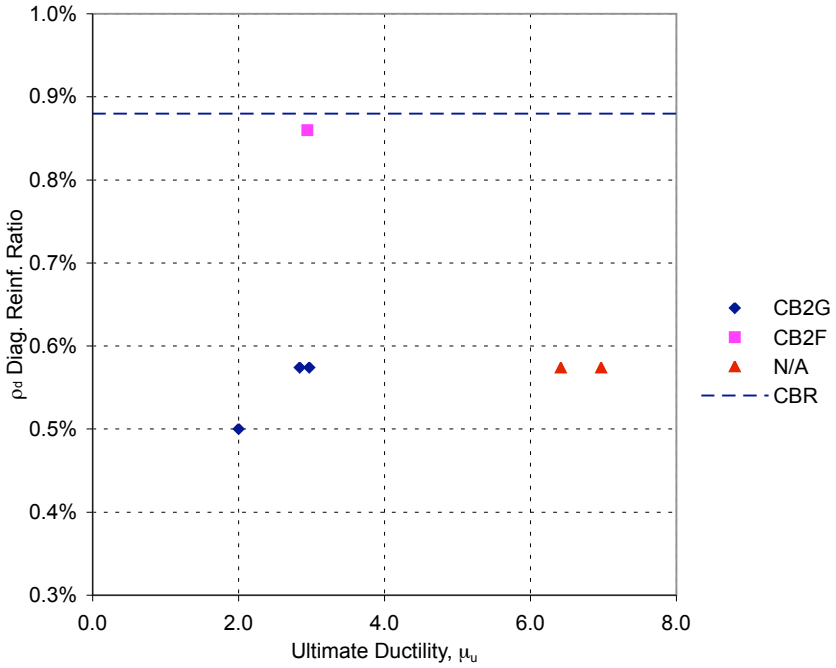

Figure 3.17: Diag. Reinf. Coupling Beams - Displacement Ductility vs. Diagonal Reinforcement Ratio

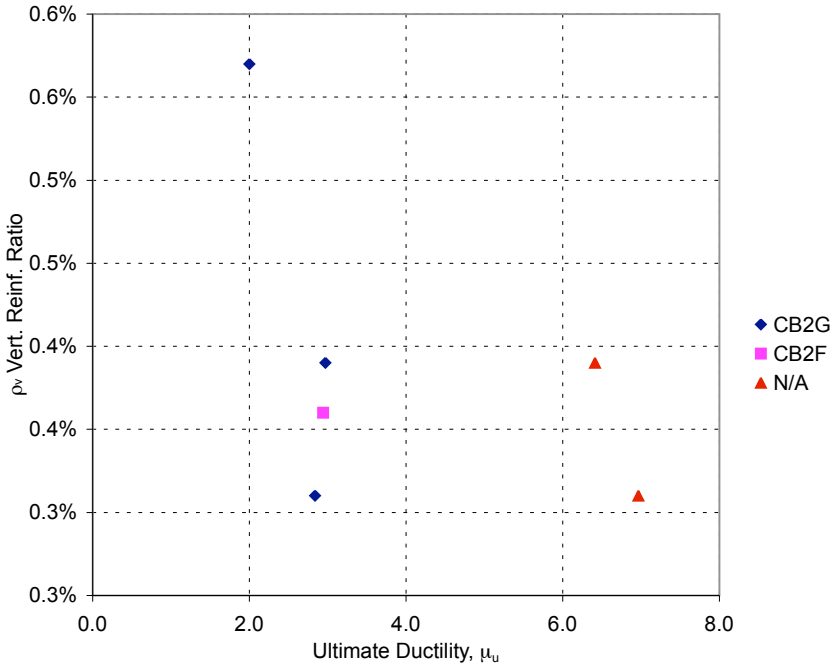

Figure 3.18: Diag. Reinf. Coupling Beams - Displacement Ductility vs. Vertical Reinforcement Ratio

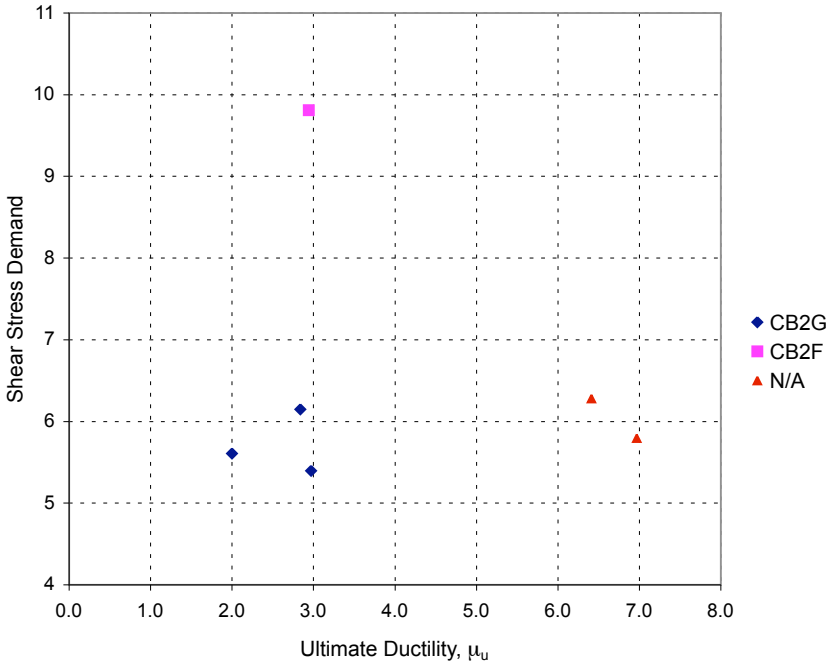

Figure 3.19: Diag. Reinf. Coupling Beams - Displacement Ductility vs. Shear Stress Demand

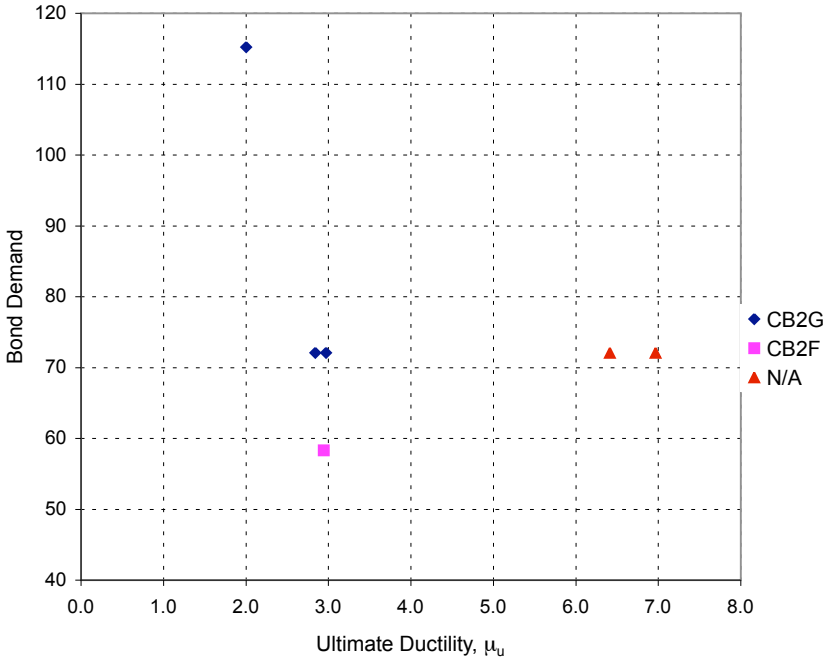

Figure 3.20: Diag. Reinf. Coupling Beams - Displacement Ductility vs. Bond Stress Demand

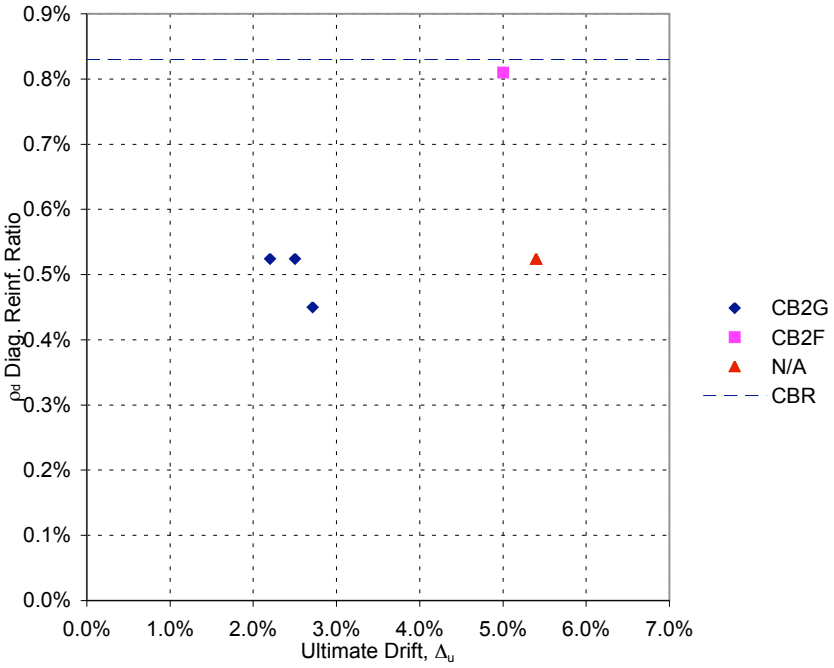

Figure 3.21: Diag. Reinf. Coupling Beams - Ultimate Displacement vs. Diagonal Reinforcement Ratio

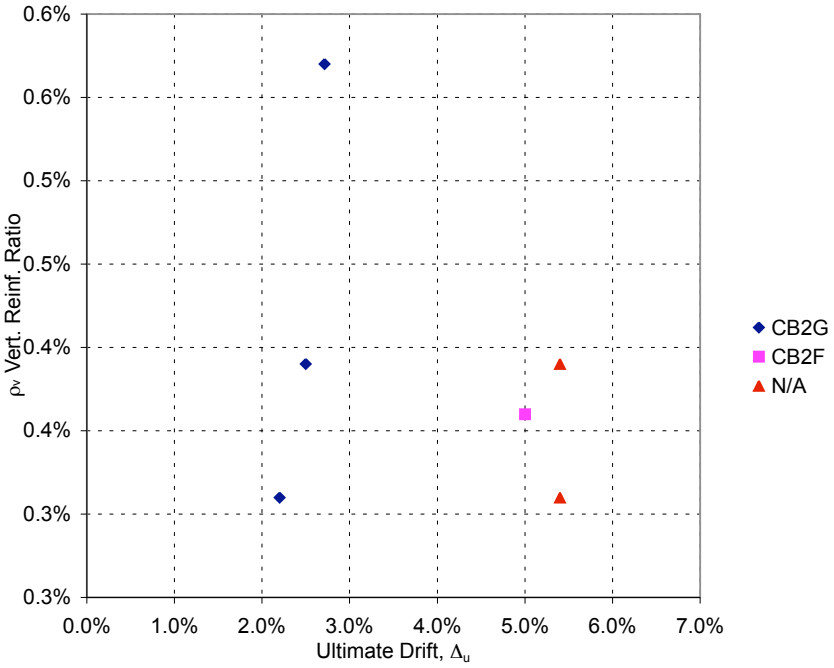

Figure 3.22: Diag. Reinf. Coupling Beams - Ultimate Displacement vs. Vertical Reinforcement Ratio

Chapter 4

NONLINEAR FINITE ELEMENT ANALYSIS OF COUPLING BEAM EXPERIMENTS

In this chapter, nonlinear finite element analysis of the experimental coupling beam data set introduced in Chapter 2 is presented, the results are compared to the observed response, and the capabilities of the analysis software are discussed. Analyses were completed using VecTor2 © (Vecchio and Wong 2006), a nonlinear finite element analysis program that utilizes two-dimensional continuum elements. The following sections describe the modeling parameters, constitutive models and modeling decisions for all of the simulations and present in detail the analytical results of three representative coupling beams. Full results for all of the coupling beams are presented in Appendix A.

4.1 VecTor2

VecTor2 is a computer program for the analysis of two-dimensional reinforced concrete structures. This program has been in ongoing development at the University of Toronto since 1990. The development of the program has been combined with experimental tests to support the abilities of VecTor2 to predict the load-deformation response of reinforced concrete structures. The program is based on the Modified Compression Field Theory (Vecchio and Collins 1986) and the Disturbed Stress Field Model (Vecchio 2000), both are analytical models for predicting the response of reinforced concrete elements subjected to in-plane normal and shear stresses. Cracked concrete is modeled as an orthotropic material with smeared cracks that are allowed to rotate. The program uses an incremental total load and iterative secant stiffness algorithm to solve for the nonlinear solution.

VecTor2 incorporates a number of constitutive models for second-order effects including compression softening, tension stiffening, tension softening, and tension splitting. It allows

the modeling of concrete confinement and expansion, crack shear slip deformations, dowel action of reinforcement, bar buckling, bond slip, hysteretic behavior, and loading history.

Finite element models are intended to include a fine mesh of elements that should be sufficient to capture the reinforcement patterns, local deformations and crack patterns. It's element library includes a four-node plane stress rectangular element, a four-node plane stress quadrilateral element, and a three-node constant strain triangle for modeling concrete with smeared reinforcement; a two-node truss-bar element for modeling discrete reinforcement; and a two-node link and four-node contact element for modeling bond-slip.

VecTor2 provides a graphical preprocessor program, FormWorks © , to facilitate model building and visual confirmation of the data. It provides tools for automatic mesh generation and model optimization to minimize computational demands. The companion software program Augustus © provides a graphical environment for post-processing the analytical results of VecTor2.

4.2 Modeling Decisions

Specification of a model in VecTor2 requires the definition of material properties, constitutive models, element mesh, reinforcement, boundary conditions, and a load or displacement history. Each of these items are presented and discussed in the following sections.

4.2.1 Material Properties

Reported material properties, where available, were used for all specimens. Details of the material properties are presented in Tables 2.3 and 2.5 from Chapter 2.

4.2.2 Constitutive Models

VecTor2 provides a large number of constitutive models for concrete and reinforcement. With the exception of the following, concrete compression pre and post-peak response, and concrete compression softening response, the default material properties were used.

The default constitutive model for the compressive pre-peak response is the *Hognestad (Parabola)* model and the default for compression post-peak response is the *Modified Park-Kent* model. Preliminary parameter studies found that the default concrete models caused a rapid loss of strength after the peak compressive strain was reached. This rapid loss of strength lead to a decrease in the displacement ductility of the specimen and an undesirable load-displacement response. The combination of the *Popovics Normal Strength Concrete* pre-peak response and the *Popovics/Mander* post-peak response provided a slower strength loss and thus allowed for larger displacement ductilities to be reached. The *Popovics (NSC)* and *Popovics/Mander* concrete constitutive models were used in all of the coupling beam simulations.

Compression softening occurs in cracked concrete and is the reduction of compressive strength and stiffness, in relation to the uniaxial compressive strength, due to the effects of transverse cracking and tensile straining. In VecTor2, compression softening is effected by the softening parameter β_d, which is calculated by the compression softening model. The models are based on statistical analysis of the stress-strain states of selected panel elements tested at the University of Tornono (Vecchio and Collins, 1992). The compression softening models are divided into two types; strength-and-strain softening and strength-only softening models.

Strength-and-strain softening models use the β_d factor to reduce both the compressive strength, $f_c^{'}$, and the corresponding strain, ϵ_0, to determine the peak compressive strength and peak compressive strain. Strength-only softening models use the β_d factor to reduce only the compressive strength, $f_c^{'}$, to determine the peak compressive stress, while the corresponding strain, ϵ_0, remains unmodified. The default constitutive model for compression softening is the *Vecchio 1992-A (e1/e2-Form)*, a strength-and-strain softening model. Preliminary parameter studies suggest that the *Vecchio 1992-B (e1/e0-Form)*, a strength-only compression softening model, provided a better approximation of the strength approximation at large displacements than the default model. The *Vecchio 1992-B (e1/e0-Form)* compression softening model was used in all of the coupling beam simulations.

Table 4.1: Constitutive Models used in Coupling Beam Simulations

Constitutive Behavior	Model
Compression Base Curve	Popovics (NSC)
Compression Post-Peak	Popovics / Mander
Compression Softening	Vecchio 1992-B (e1/e0-Form)
Tension Stiffening	Modified Bentz 2003
Tension Softening	Bilinear
Tension Splitting	Not Considered
Confinement Strength	Kupfer / Richart Model
Concrete Dilation	Variable - Kupfer
Cracking Criterion	Mohr-Coulomb (stress)
Crack Slip Check	Vecchio-Collins 1986
Crack Width Check	Agg/5 Max Crack Width
Slip Distortions	Vecchio-Lai
Concrete Hysteresis	Nonlinear w/ Plastic Offsets
Steel Hysteresis	Elastic-Plastic w/ Hardening
Rebar Dowel Action	Tassios (Crack Slip)

The default models were used for tension stiffening, tension softening, confinement, lateral expansion, crack slip, crack width, concrete hysteresis response, dowel action, and reinforcement hysteresis response. A complete list of the constitutive models used in shown in Table 4.1, and the analysis parameters used are shown in Table 4.2. The default constitutive models available in VecTor2 are documented in detail in the user manual (Vecchio and Wong 2006), and can be found online at (www.civ.utoronto.ca/vector).

4.2.3 Element Mesh

The FormWorks program provides automatic mesh generation capabilities based on user input parameters of element type, maximum element size, and maximum aspect ratio. These parameters can be changed for different regions to allow for varying levels of mesh

Table 4.2: Analysis Parameters used in Coupling Beam Simulations

Analysis Parameter	Model
Convergence Criteria	Displacements - Weighted
Strain History	Previous Loading Considered
Strain Rate Effects	Not Considered
Structural Damping	Not Considered
Geometric Nonlinearity	Considered
Crack Allocation Process	Uniform

refinement and element type within the model.

Element Type

The element type can be of three types, rectangular, quadrilateral, and/or triangular. VecTor2 allows for the mixing of all three element types within in model. For the conventionally reinforced coupling beams the mesh was composed solely of rectangular elements. This was possible because of the completely orthogonal geometry of the model. For the diagonally reinforced coupling beams the mesh was a combination of all three element types. The details of the mesh layout are handled by the FormWorks program and its automatic mesh generation capabilities.

Element Size

A preliminary parameter study was completed to determine the effect of element size on the performance of a coupling beam model. A conventionally reinforced coupling beam, taken from the experimental data-set, was modeled with three different levels of mesh refinement and compared to the reported load-displacement curve, the results are shown in Figure 4.1.

The d/7.5 mesh size is too coarse, causing a false stiffening of the coupling beam and resulting in larger yield and ultimate capacities than the reported values. The d/15 mesh size does not cause as much of an over-prediction of the yield force and provides a close

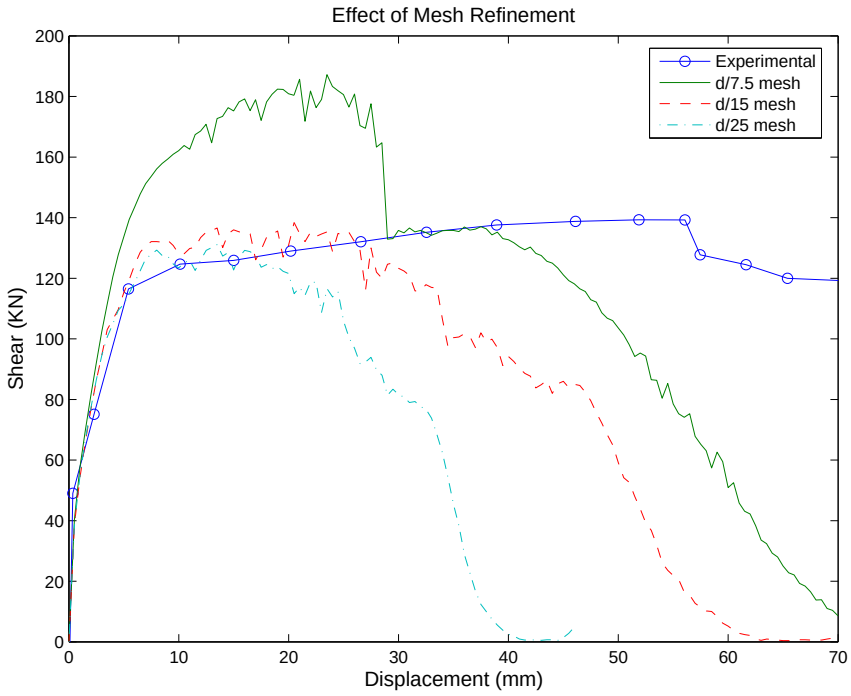

Figure 4.1: Effect of Mesh Refinement

agreement with the reported load-displacement curve through the initial portion of the load-displacement curve. The d/24 mesh size showed a small improvement over the d/15 mesh in regard to matching the experimental yield strength, however it also began to loose strength at an earlier displacement level.

These results suggest that the quality of the finite element simulation shows a mesh size dependency. Given the incremental gross over-prediction of the d/7.5 mesh the unfavorable early strength loss of the d/24 mesh, a maximum mesh size of d/15 for the coupling beams was chosen. This ratio was used as a guideline for all subsequent coupling beam models.

Aspect Ratio

VecTor2 allows the maximum aspect ratio for elements to be specified. During the automatic meshing process this limit will be followed and the element size adjusted to the largest

possible dimension that will meet the maximum aspect ratio. For all the coupling beam models the default aspect ratio of 1.5 was used.

4.2.4 Types of Reinforcement

VecTor2 allows for the reinforcement to be modeled in two different manners. Reinforcement can be modeled as a distributed reinforcement using a specified ratio, commonly referred to as smeared reinforcement, or as discrete truss-bar elements. For all of the coupling beams, both methods of modeling the reinforcement were used and two versions of each model were carried through the entire study.

- Smeared Reinforcement: For these models, all of the reinforcement in the coupling beam and in the loading blocks was modeled using smeared reinforcement elements. Reinforcement ratios, taken from the experimental data-set (Tables 2.4 & 2.6), were specified for each of the three primary directions; longitudinal, vertical, and out of plane.

- Truss-Bar Reinforcement: For these models the primary reinforcement was modeled with truss-bar elements and all other reinforcement was modeled using smeared reinforcement elements. For conventionally reinforced coupling beams the primary reinforcement is defined as the top and bottom longitudinal bars. For diagonally reinforced coupling beams, the primary reinforcement is defined as the diagonal reinforcing bars. The truss-bar elements were extended into the loading blocks a minimum of the bar development length. The reinforcement ratios for the vertical and out-of-plane reinforcement remain the same as the smeared reinforcement models. The longitudinal reinforcement ratio was taken as the area of the nominal longitudinal bars over the cross section area of the coupling beam.

4.2.5 Boundary Conditions

There were three types experimental test set-ups found in in the experimental coupling beam data-set. The different test set-ups are presented and described in detail in Chapter 2. Despite the differences in the experimental test configurations, they all seek to impose the same set of forces and displacements on the coupling beam specimen; imposing a constant shear force and shear deformation on the coupling beam without restraining axial deformations.

A single set of boundary conditions were used for all of the coupling beam models. To represent the loading conditions in the laboratory, the top and bottom edges of the left loading block were restrained against motion in the vertical direction, and the right edge of he right loading block was restrained against motion in the horizontal direction. These boundary conditions allowed for the ends of the coupling beam loading blocks to remain parallel without causing any axial restraint on the specimen.

4.2.6 Loading Parameters

A vertical displacement was applied to all of the nodes along the right edge of the right load block. For monotonically loaded specimens the displacement was applied incrementally up to the reported maximum displacement or until the model became numerically unstable. For cyclically loaded specimens the reported displacement history from the experimental test was replicated. When the experimental loading history was not available, the specimens were cycled three times at the yield displacement and then cycled three times at increasing multiples of the yield displacement, δ_y, $2\delta_y$,$4\delta_y$, and then pushed monotonically until failure.

4.3 Description of Evaluation Method

The quality of the predicted results are compared to the reported experimental response to determine the quality of the VecTor2 simulations. The performance parameters used in this study include:

l/d**:** coupling beam aspect ratio.

δ_y**:** is the displacement in the simulation at the point when the reported yield shear strength was reached.

δ_u**:** is the displacement in the simulation at the predicted maximum shear force was reached.

Δ_y**:** is the drift in the coupling beam simulation at the point when the reported yield shear strength was reached.

Δ_u**:** is the drift in the coupling beam simulation at the predicted maximum shear force.

$\Delta_{0.85V_u}$**:** is the drift in the coupling beam at the point where 85% of the maximum predicted shear, V_u, was reached.

DCR : is the demand capacity ratio defines as the maximum shear force, V_u, divided by the design strength, V_n.

K_y : is the secant stiffness at the reported point of first yield.

K_u**:** is the secant stiffness at the reported ultimate shear force.

$K_{1.5\%}$**:** is the secant stiffness corresponding to 1.5% drift in the coupling beam.

$K_{6.0\%}$**:** is the secant stiffness corresponding to 6.0% drift in the coupling beam.

V_y**:** is the shear in the coupling beam when first yielding is reported by the experimental researcher.

V_u**:** is the maximum shear observed in the coupling beam.

$V_{1.5\%}$**:** is the shear in the coupling beam at 1.5% drift, for the 10-Story reference wall this corresponds to 0.5% story drift and is the expected point of first yield.

$V_{6.0\%}$**:** is the shear in the coupling beam at 6.0% drift, for the 10-story reference wall this corresponds to 2.0% story drift and is the maximum design level drift.

SSD**:** shear stress demand, defined as $V_p/A_g f_c^{'}$

where

$V_p = 2M_n/l$,

M_n = flexural strength of coupling beam based on the longitudinal or diagonal reinforcement depending on the configuration,

l = coupling beam clear span length,

A_g = coupling beam cross section area, and

$f_c^{'}$ = compressive strength of concrete.

These simulation results and comparisons to the observed data are shown in Table 4.3 through 4.5.

Table 4.3: Experimental Coupling Beam Strength Predictions

Specimen	V_y	V_y/V_{ye}	V_u	V_u/V_{ue}	$V_{1.5\%}$	$V_{6.0\%}$
GalanoP01_DT	200.6	0.90	239.9	1.07	238.0	27.9
GalanoP02_DT	196.6	0.94	234.4	1.00	230.5	0.0
GalanoP05_DT	166.6	0.76	221.7	0.93	221.7	-5.8
GalanoP07_T	236.9	1.10	244.2	1.02	244.2	0.0
GalanoP10_DT	226.3	1.03	239.0	0.99	238.0	10.8
GalanoP12_DT	223.0	1.06	234.6	0.96	234.6	0.0
TassiosCB1A_DT	203.2	1.14	214.3	1.01	214.2	0.0
TassiosCB1B_DT	149.9	1.50	149.9	1.21	141.5	0.0
TassiosCB2A_DT	202.0	0.94	210.1	0.74	179.9	0.0
TassiosCB2B_DT	135.9	1.18	158.7	0.93	156.0	0.0
ZhaoCCB11_T	324.6	1.12	348.9	1.01	298.3	0.0
ZhaoCCB2_DT	220.7	1.16	229.1	1.01	198.6	0.0
ZhaoCCB4_DT	94.8	0.86	129.4	1.05	118.0	0.0
ZhaoMCB1_DT	291.7	1.11	295.0	0.86	266.7	0.8
ZhaoMCB2_DT	226.7	1.14	244.8	0.94	221.7	0.8
ZhaoMCB3_DT	132.9	1.05	161.3	1.01	151.1	0.7
ZhaoMCB4_DT	88.7	0.89	126.1	0.90	116.8	0.0
Average	195.4	1.05	216.6	0.98	204.1	5.9
$Median$	202.0	1.06	229.1	1.00	221.7	0.8
Std.Dev.	62.8	0.17	58.0	0.10	52.3	12.0
Max	324.6	1.50	348.9	1.21	298.3	27.9
Min	88.7	0.76	126.1	0.74	116.8	-5.8

Strength (V) in KN

$*$ *0 values indicate data not available*

Table 4.4: Experimental Coupling Beam Stiffness Predictions

Specimen	K_y	K_y/K_{ye}	K_u	K_u/K_{ue}	$K_{1.5}$	$K_{1.5}/K_{1.5e}$	K_6	K_6/K_{6e}
GalanoP01_DT	36.6	0.83	26.7	2.9	28.1	1.12	0.8	0.18
GalanoP02_DT	32.9	0.80	22.4	1.8	25.7	1.03	0.0	0.00
GalanoP05_DT	41.7	0.97	26.1	3.5	26.1	1.02	-0.2	-0.03
GalanoP07_T	31.1	0.74	26.7	1.7	26.7	1.04	0.0	0.00
GalanoP10_DT	34.9	0.75	29.9	4.0	28.0	1.10	0.3	0.05
GalanoP12_DT	31.7	0.71	27.8	1.5	27.8	1.04	0.0	0.00
TassiosCB1A_DT	41.2	1.79	31.1	2.5	27.2	1.13	0.0	0.00
TassiosCB1B_DT	25.1	1.60	25.1	2.6	20.3	1.38	0.0	0.00
TassiosCB2A_DT	41.3	1.43	30.8	1.6	23.5	0.82	0.0	0.00
TassiosCB2B_DT	34.1	2.52	6.6	1.0	22.4	1.52	0.0	0.00
ZhaoCCB11_T	59.5	1.95	39.0	2.1	30.0	1.12	0.0	0.00
ZhaoCCB2_DT	40.2	1.27	38.3	2.0	18.9	0.90	0.0	0.00
ZhaoCCB4_DT	35.1	1.92	21.6	2.1	10.9	0.93	0.0	0.00
ZhaoMCB1_DT	41.8	1.68	39.5	5.2	26.7	1.06	0.0	0.00
ZhaoMCB2_DT	41.3	1.25	35.1	6.3	22.2	0.97	0.0	0.00
ZhaoMCB3_DT	33.3	1.06	17.0	4.5	15.1	1.06	0.0	0.00
ZhaoMCB4_DT	35.5	1.49	15.8	6.4	11.7	0.98	0.0	0.00
Average	37.5	1.34	27.0	3.0	23.0	1.07	0.1	0.01
Median	35.5	1.27	26.7	2.5	25.7	1.04	0.0	0.00
Std.Dev.	7.4	0.52	8.8	1.7	5.8	0.17	0.2	0.05
Max	59.5	2.52	39.5	6.4	30.0	1.52	0.8	0.18
Min	25.1	0.71	6.6	1.0	10.9	0.82	-0.2	-0.03

Stiffness (K) in KN-mm

$*$ *0 values indicate data not available*

Table 4.5: Experimental Coupling Beam Displacement and Drift Predictions

Specimen	δ_y	δ_y/δ_{ye}	δ_u	δ_u/δ_{ue}	Δ_y	Δ_y/Δ_{ye}	Δ_u	Δ_u/Δ_{ue}	$\Delta_{0.85V_u}$
GalanoP01_DT	5.5	1.07	9.0	0.37	0.91%	1.07	1.50%	0.38	5.37%
GalanoP02_DT	6.0	1.17	10.5	0.62	1.00%	1.18	1.75%	0.63	3.47%
GalanoP05_DT	4.0	0.78	8.5	0.26	0.67%	0.79	1.41%	0.26	2.13%
GalanoP07_T	7.6	1.49	9.2	0.61	1.27%	1.49	1.52%	0.61	2.95%
GalanoP10_DT	6.5	1.38	8.0	0.25	1.08%	1.38	1.33%	0.25	2.30%
GalanoP12_DT	7.0	1.50	8.5	0.64	1.17%	1.49	1.41%	0.64	2.36%
TassiosCB1A_DT	4.9	0.63	6.9	0.41	0.99%	0.63	1.38%	0.41	2.56%
TassiosCB1B_DT	6.0	0.93	6.0	0.46	1.20%	0.94	1.20%	0.46	-
TassiosCB2A_DT	4.9	0.66	6.8	0.45	0.98%	0.66	1.36%	0.45	3.50%
TassiosCB2B_DT	4.0	0.47	24.0	0.92	0.80%	0.47	4.80%	0.92	-
ZhaoCCB11_T	5.5	0.57	8.9	0.47	0.78%	0.57	1.28%	0.47	2.56%
ZhaoCCB2_DT	5.5	0.92	6.0	0.50	0.78%	0.91	0.86%	0.50	2.81%
ZhaoCCB4_DT	2.7	0.45	6.0	0.50	0.39%	0.46	0.86%	0.50	2.60%
ZhaoMCB1_DT	7.0	0.66	7.5	0.17	1.00%	0.67	1.07%	0.17	2.81%
ZhaoMCB2_DT	5.5	0.92	7.0	0.15	0.78%	0.91	1.00%	0.15	3.35%
ZhaoMCB3_DT	4.0	1.00	9.5	0.23	0.57%	1.00	1.36%	0.23	3.21%
ZhaoMCB4_DT	2.5	0.60	8.0	0.14	0.36%	0.60	1.14%	0.14	4.00%
Average	5.2	0.89	8.8	0.42	0.87%	0.90	1.48%	0.42	3.07%
Median	5.5	0.92	8.0	0.45	0.91%	0.91	1.36%	0.45	2.81%
Std.Dev.	1.5	0.34	4.1	0.21	0.26%	0.34	0.89%	0.21	0.82%
Max	7.6	1.50	24.0	0.92	1.27%	1.49	4.80%	0.92	5.37%
Min	2.5	0.45	6.0	0.14	0.36%	0.46	0.86%	0.14	2.13%

Displacement (δ) *in mm*

4.4 Reduced Data Set for Illustration of VecTor2 Capabilities

Selected coupling beams were chosen to illustrate the capabilities of VecTor2. The selected coupling beams represent the two methods of loading, monotonic vs. cyclic, and the two reinforcement patterns, conventional vs. diagonal reinforcement.

The three test specimens are:

- Galano P01 - monotonically loaded with conventional reinforcement,
- Galano P02 - cyclically loaded with conventional reinforcement (same reinforcement as Galano P01), and
- Tassios CB2B - cyclically loaded with diagonal reinforcement.

4.5 Description of Results

4.5.1 Galano P01

Figures 4.2 and 4.3 show the simulated load-displacement response and the experimental response history. Figures 4.4 - 4.6 show crack patterns at reported yield strength, predicted ultimate strength and 80% of the predicted ultimate strength. Initial yielding of the primary longitudinal reinforcement is predicted at a drift of 0.42%, corresponding to a 142.9-KN applied load. The reported drift at yield was 0.85%, with a 223.9-KN applied load. However, the reported yield strength and drift corresponds to the point where the stiffness changes abruptly and the load-displacement response begins to level out, whereas the initial yield in the VecTor2 simulation is taken as the first point where the yield stress was reached in the longitudinal reinforcment. Comparing the predicted strength at the reported yield drift results in a much closer comparison; a predicted strength of 200.6-KN, an under-prediction of 10% (Figure 4.2).

The model continues to gain strength up to the maximum value of 239.9-KN at a drift of 1.50%. The maximum strength is over-predicted by 10%, however the drift at maximum

strength is greatly under-predicted with ratio of predicted-to-observed of 0.38. The displacement and cracking at the predicted maximum strength are shown in Figure 4.5. This figure shows that wide cracks are beginning to form in the web elements at the left end of the beam. The web elements have a smaller horizontal reinforcement ratio than the two elements at the top and bottom of the beam representing the longitudinal reinforcement, and can be expected to provide less resistance to tensile cracking. The majority of the elements in the coupling beam have diagonally oriented crack directions following a diagonal compression strut from one end of the beam to the other, indicating that the beam is primarily behaving in a shear mode. At the predicted maximum strength, all of the primary longitudinal steel has yielded and entered into the strain hardening region.

As displacement is increased beyond the point of maximum strength, the predicted strength drops abruptly due to crushing in the extreme compression elements. The compressive stress is redistributed around the crushed elements and the strength then levels out to a value near the experimental peak strength. As the compressive elements crush the vertical strain is increased and the shear reinforcement begins to yield near the ends of the coupling beam.

The model begins to loose strength at 4.7% drift, which is very close to the initiation of strength loss in the experiment. Wide flexural cracks have opened up at both ends of the beam and continue through approximately half of the beam depth an then transition to shear cracks in the compression zone. Skewed elements and diagonal cracking in the compression zone indicate a concentration of shear stress and strain distortion. At this load step, yielding of the shear reinforcement has occurred and is spread over the first four elements at each end of the coupling beam, or 1/6 of the length. Rapid strength loss continues at drifts greater than 4.7%. Figure 4.6 shows wide shear cracks concentrated at the left interface of the coupling beam and the loading block in conjunction with significantly skewed elements, indicating a large concentration of shear strain and stress at this location. The predicted failure mode is similar to a sliding-shear failure, however the experimental specimen failed due to fracture of the stirrups at one end of the beam and resulted in the opening of a single

large diagonal crack extending from one corner of the beam to the other, (Figure 4.7).

4.5.2 Galano P02

Figures 4.8 and 4.9 show the simulated load-displacement response and the experimental response history. Figures 4.10 - 4.12 show crack patterns at reported yield strength, predicted ultimate strength and 80% of the predicted ultimate strength. Initial yielding of the primary longitudinal reinforcement is predicted in the third displacement cycle at a drift of 0.42% and a shear force of 140.7-KN. The force at the experimental reported yield drift was 196.6-KN, compared to the reported yield force of 211-KN. The predicted ultimate force or 234-KN was the same as reported from the experiment, however it did occur at lower drift level, 1.75% vs. 2.78%, only 63% of the reported value. In the negative displacement direction, the peak strength was 208.4-KN, which is again very close to the reported strength of 213-KN. The displacement and cracking at the predicted ultimate strength are shown in Figure 4.11. At this load step, wide cracks are beginning to form in the web elements of the coupling beam. Flexural cracks are still present in the extreme tensile zones at each end of the coupling beam, but quickly transition into diagonal cracks toward the center of the beam.

In the displacement cycle following the peak strength, the specimen was only able to reach 200-KN in the positive direction, and 194.5-KN in the negative direction. The predicted shear strengths at yield, ultimate and the cycles following the ultimate strength are very close to the reported values, all with an under-prediction of less than 10%.

The behavior of the simulation and the experiment began to diverge after the peak strength was reached. The simulation began to loose strength at an earlier drift level and at a faster rate. The simulation began to loose substantial strength (more than 20%) at 3.3% drift compared to approximately 5.0% in the experiment. Additionally, when the strength loss in the simulation dropped all the way to zero, where the experiment retained approximately 20% of the peak.

The strength loss of the simulation was due to a sliding-failure. All of the longitudi-

nal reinforcement had yielded and gone through strain hardening, at the load step where strength loss occurred, the steel fractured and lost all of its load carrying capacity. The failure in the longitudinal steel allowed the concrete to expand axially and undergo large shear deformations without any additional force, and resulted in the sudden shear slip at the ends of the coupling beam. Figure 4.12 shows the displaced shape and crack pattern at 80% of V_u, the concentration of shear deformation can be seen at both ends of the beam.

While VecTor2 was able to provide a good prediction of the strength and deformation response, the failure mode was not correct. In the experiment the coupling beam experienced heavy spalling over the middle half of the beam and into the corners, however the ends remained relatively intact as seen in Figure 4.13.

4.5.3 Tasssios CB2B

Figures 4.14 and 4.15 show the simulated load-displacement response and the experimental response history. Figures 4.16 - 4.18 show crack patterns at reported yield strength, predicted ultimate strength and the predicted maximum displacement.

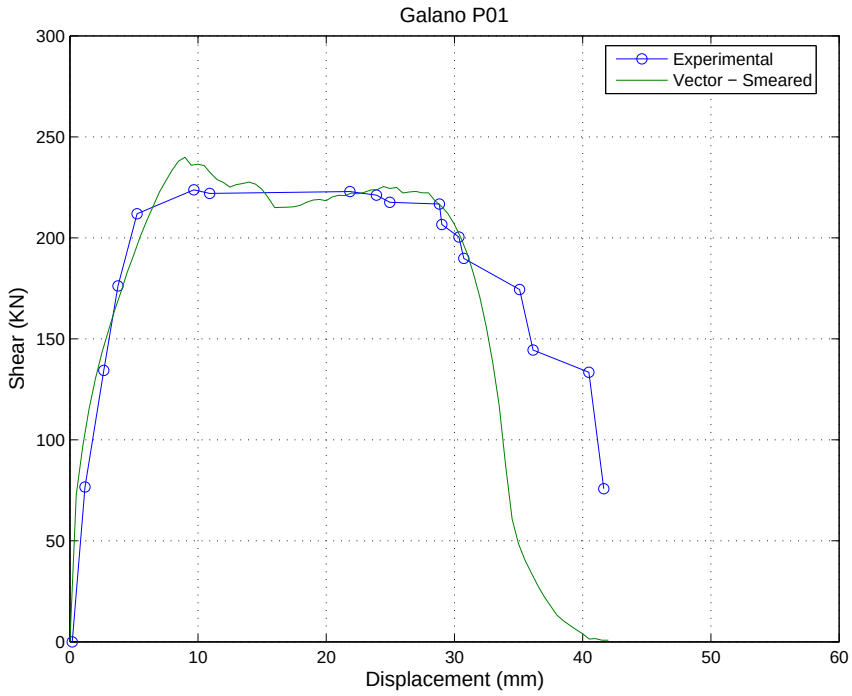

Figure 4.2: VecTor2 Predicted Response of Galano P01

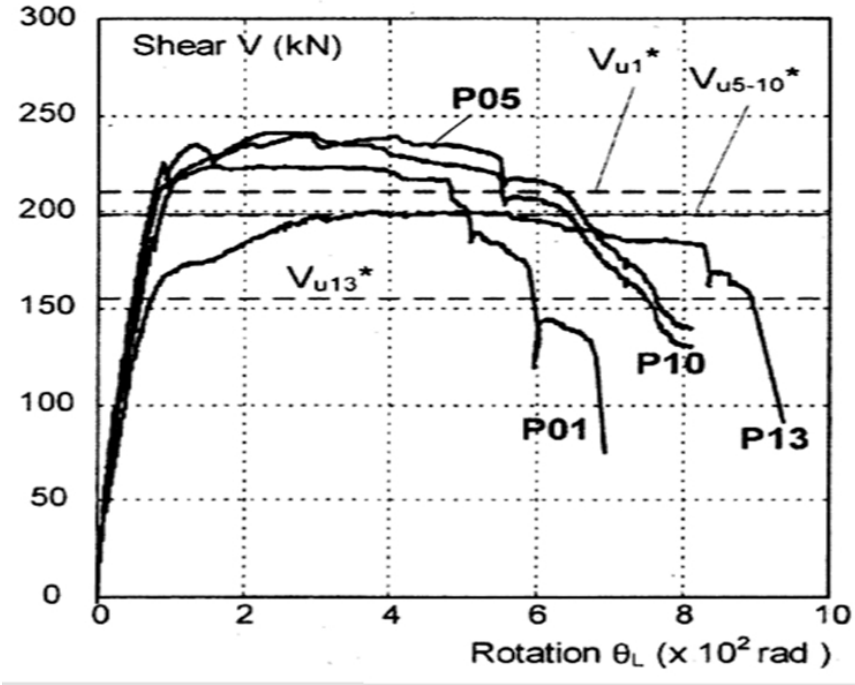

Figure 4.3: Experimental Response of Galano Specimens

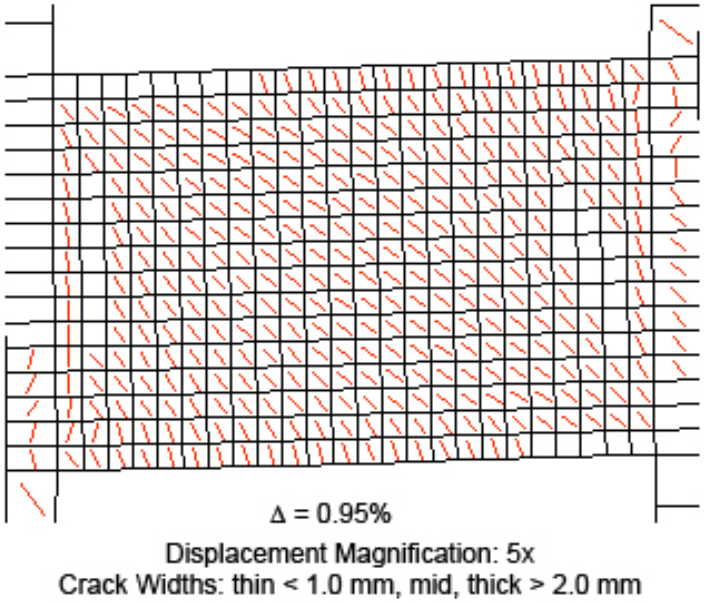

Figure 4.4: Displaced Shape and Crack Pattern at V_y of Galano P01

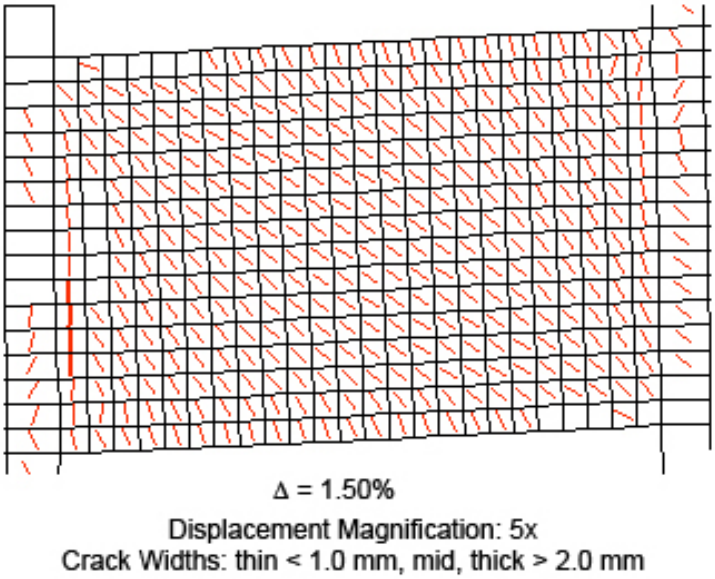

Figure 4.5: Displaced Shape and Crack Pattern at V_u of Galano P01

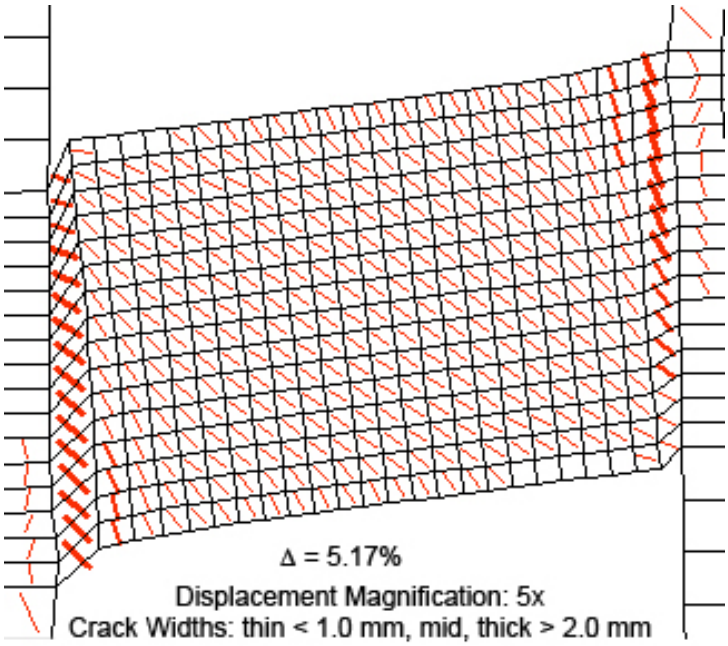

Figure 4.6: Displaced Shape and Crack Pattern at $0.8V_u$ of Galano P01

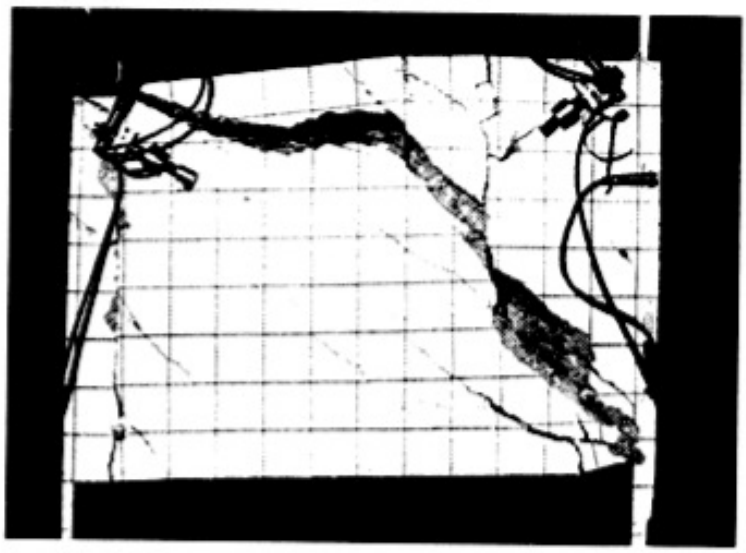

Figure 4.7: Experimental Failure of Galano P01

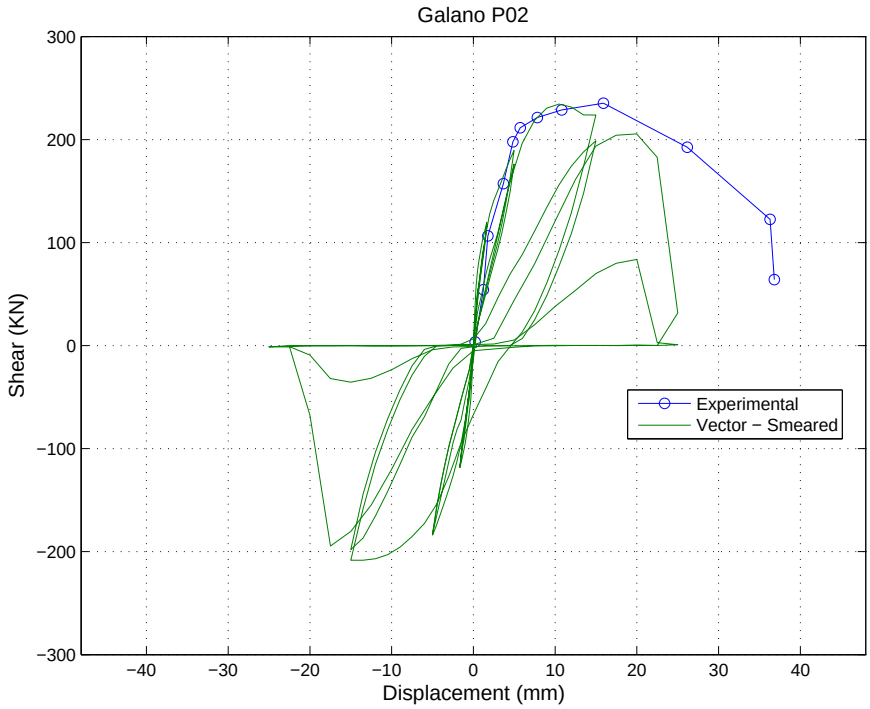

Figure 4.8: VecTor2 Predicted Response of Galano P02

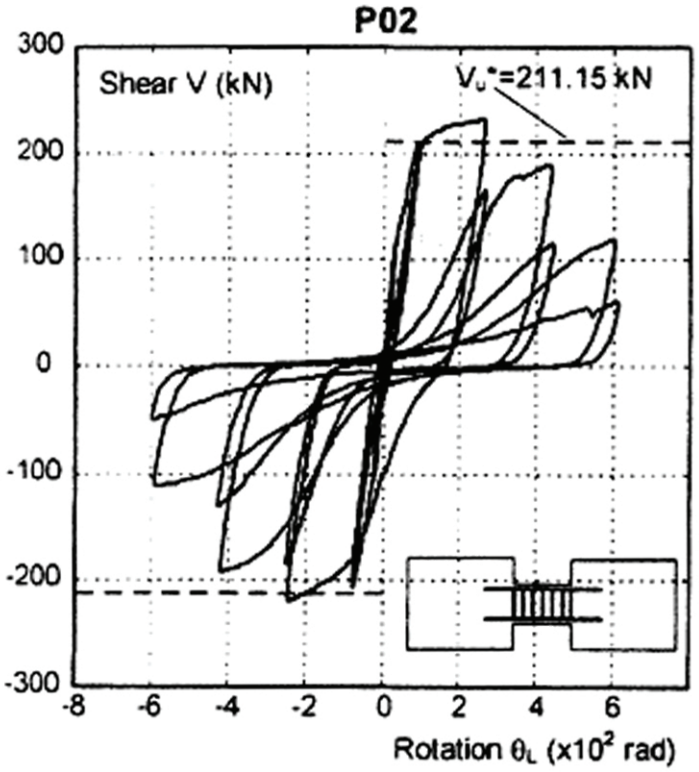

Figure 4.9: Experimental Response of Galano P02

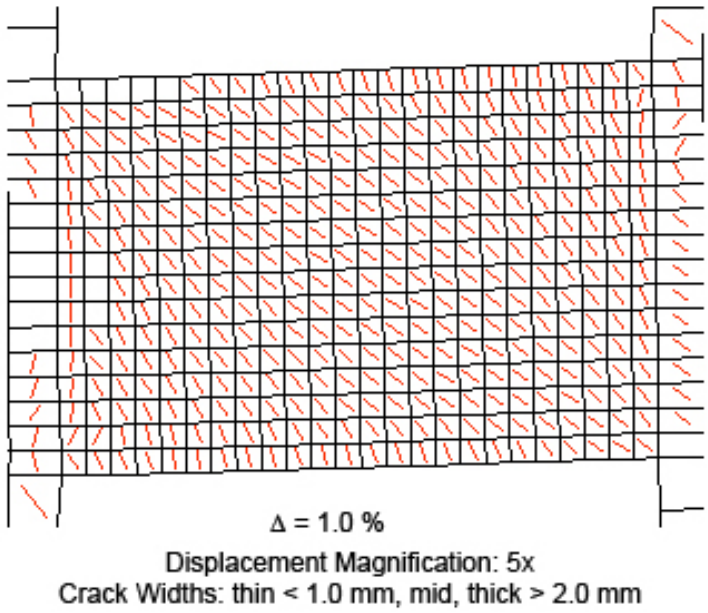

Figure 4.10: Displaced Shape and Crack Pattern at V_y of Galano P02

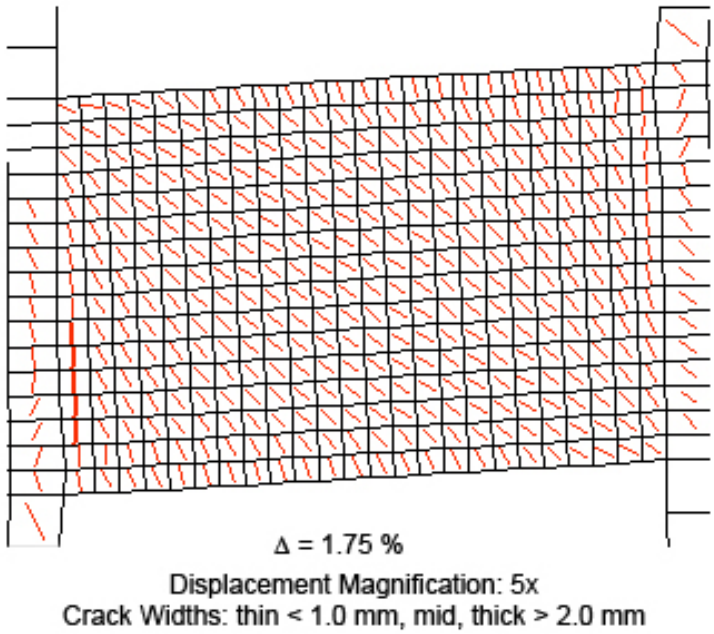

Figure 4.11: Displaced Shape and Crack Pattern at V_u of Galano P02

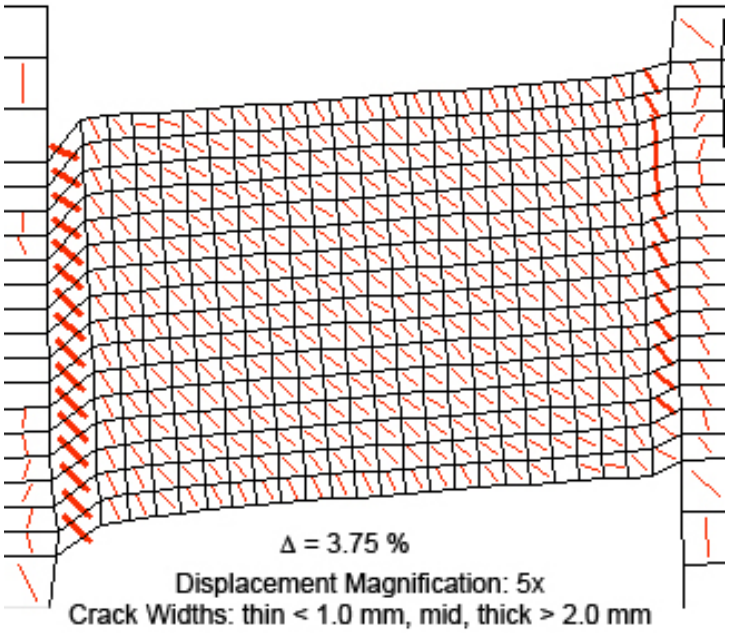

Figure 4.12: Displaced Shape and Crack Pattern at $0.8V_u$ of Galano P02

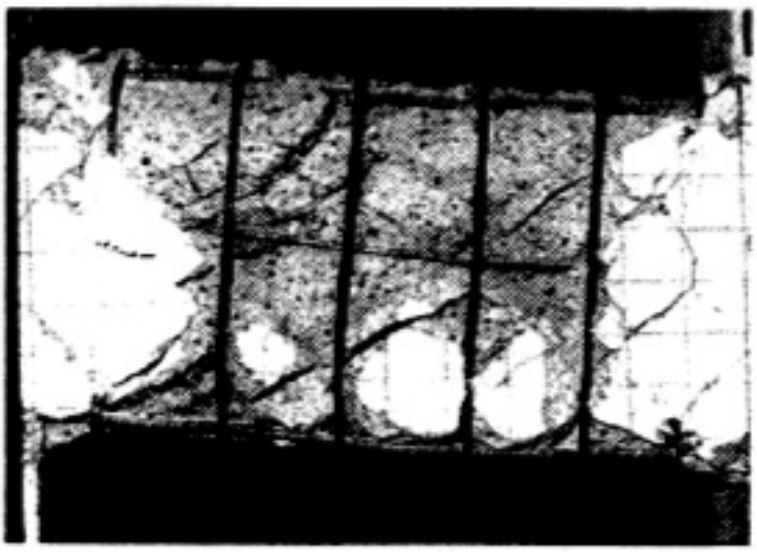

Figure 4.13: Experimental Failure of Galano P02

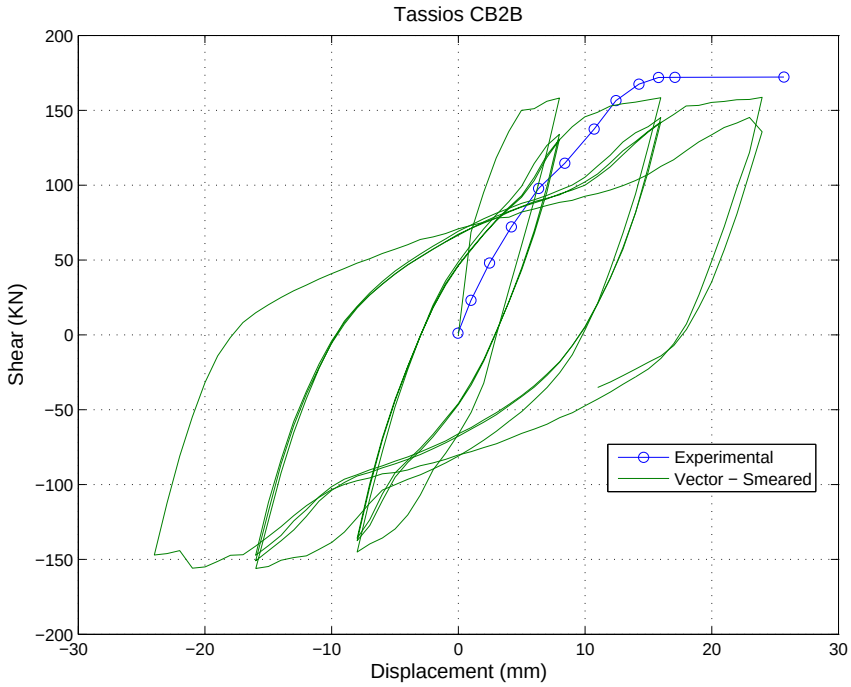

Figure 4.14: VecTor2 Predicted Response of Tassios CB2B

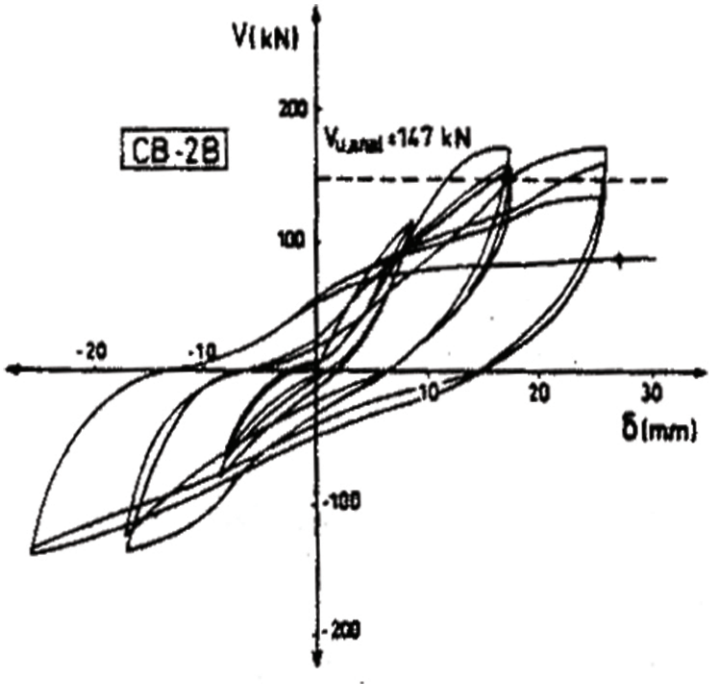

Figure 4.15: Experimental Response of Tassios CB2B

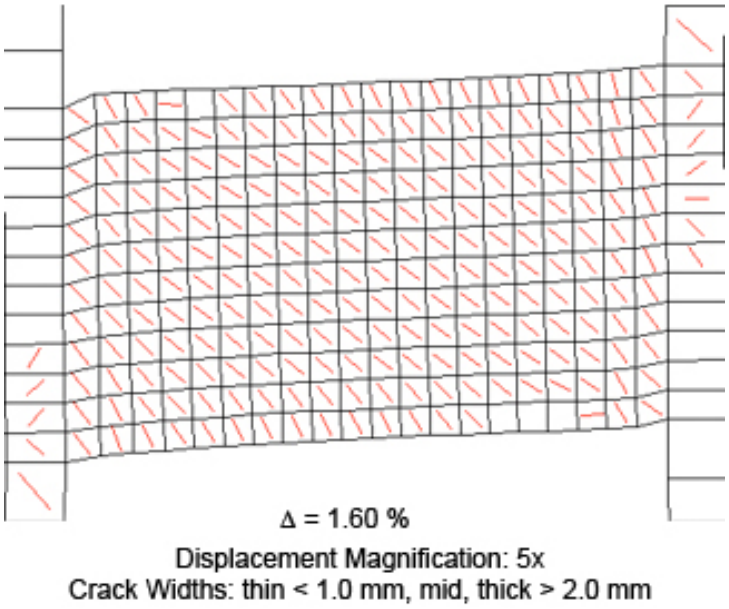

Figure 4.16: Displaced Shape and Crack Pattern at V_y of Tassios CB2B

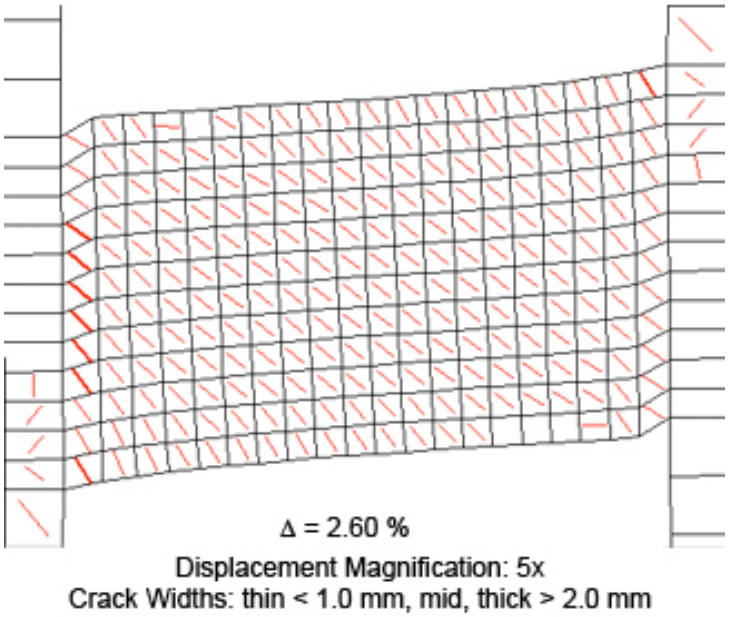

Figure 4.17: Displaced Shape and Crack Pattern at V_u of Tassios CB2B

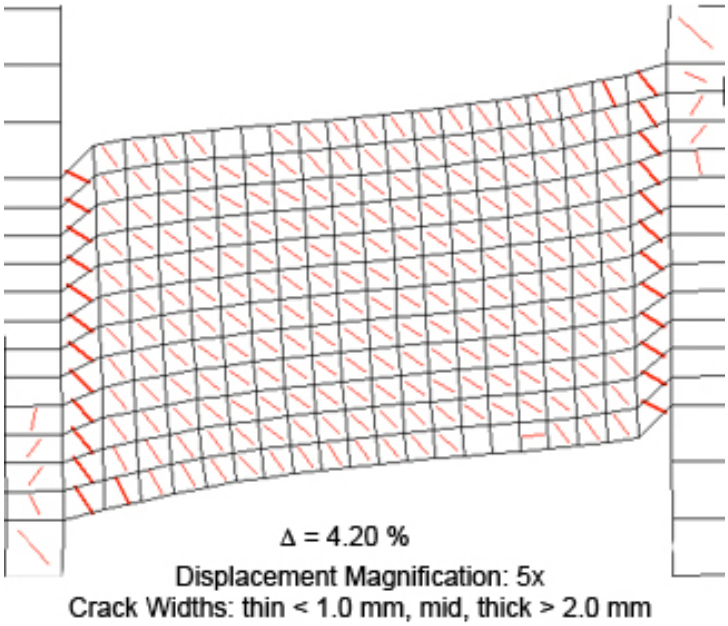

Figure 4.18: Displaced Shape and Crack Pattern at Δ_{max} of Tassios CB2B

Figure 4.19: Experimental Failure of Tassios CB2B

4.6 Data Analysis and Trends

The results of the Experimental Coupling Beam simulations were plotted versus various engineering demand parameters to investigate any patterns in the behavior. The model results were first separated by the loading method, monotonic or cyclical. The following results, V_y, V_u, δ_u, K_y, and K_u, were plotted against the aspect ratio, ρ_v, shear demand to capacity ratio, and the shear stress demand. The strength and displacement results were normalized against the experimental results.

No discernible trends were discovered in the studied response parameters. The plots have been included for informational purposes.

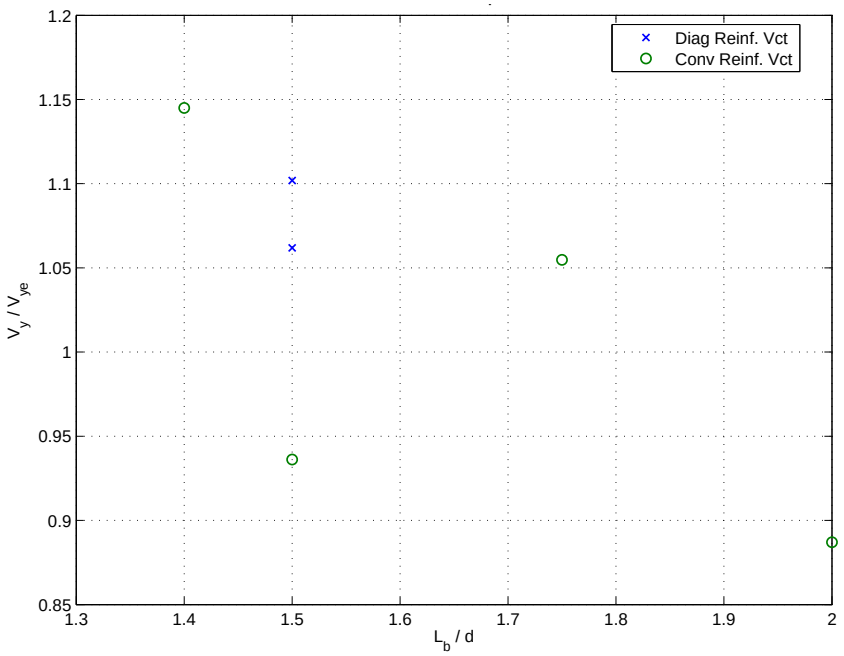

Figure 4.20: Mono. Coupling Beams - Yield Strength vs. Aspect Ratio

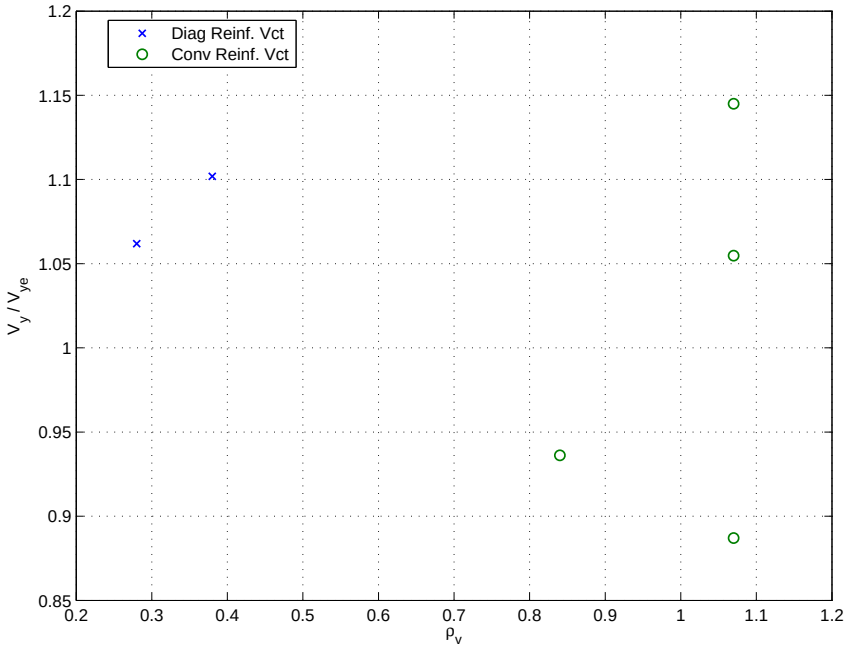

Figure 4.21: Mono. Coupling Beams - Yield Strength vs. Vertical Reinforcement Ratio

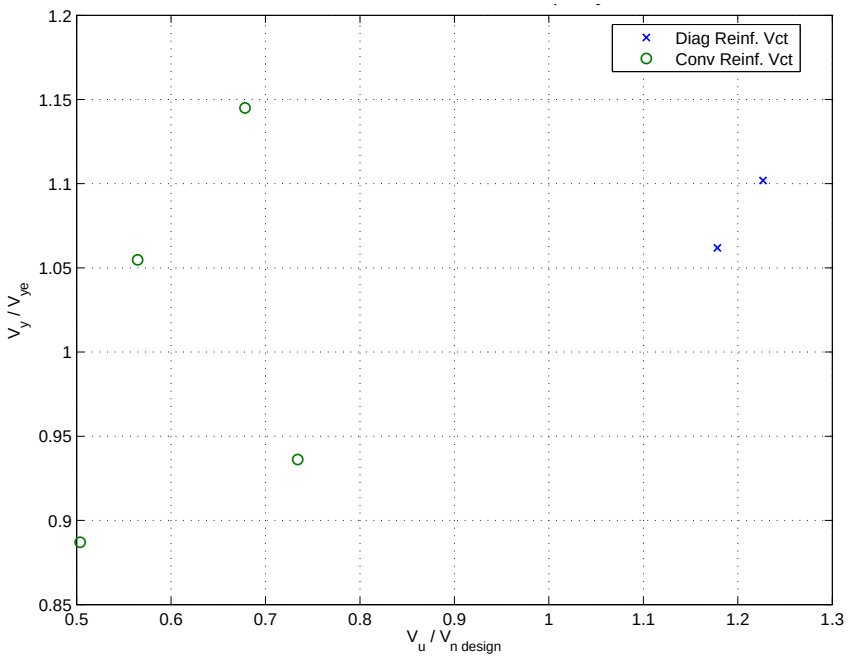

Figure 4.22: Mono. Coupling Beams - Yield Strength vs. Shear Demand Capacity Ratio

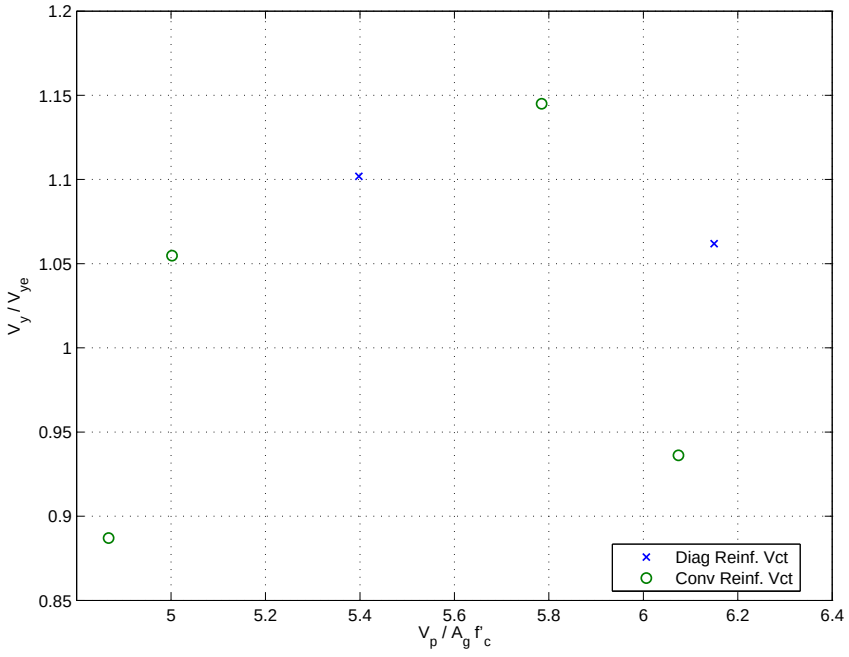

Figure 4.23: Mono. Coupling Beams - Yield Strength vs. Shear Stress Demand

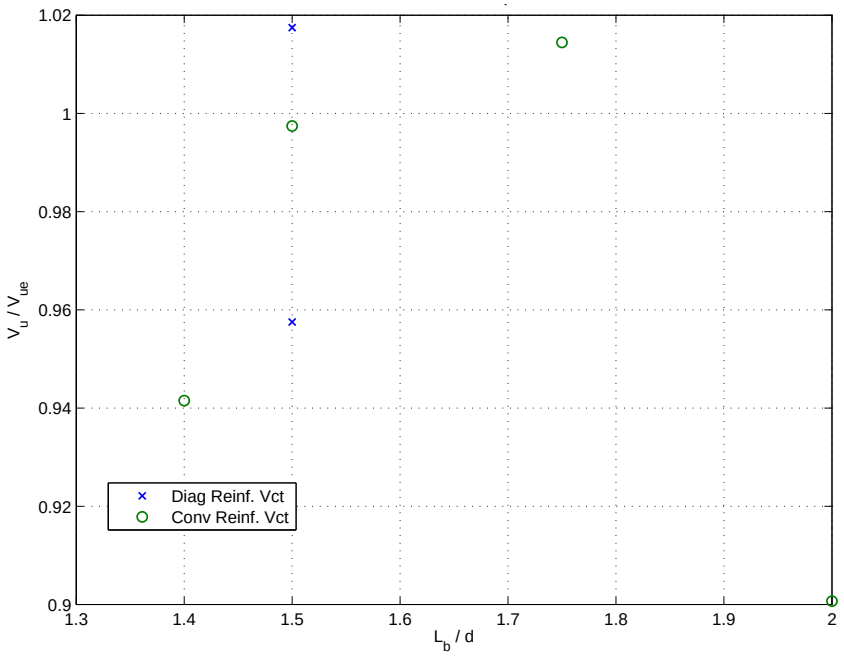

Figure 4.24: Mono. Coupling Beams - Ultimate Strength vs. Aspect Ratio

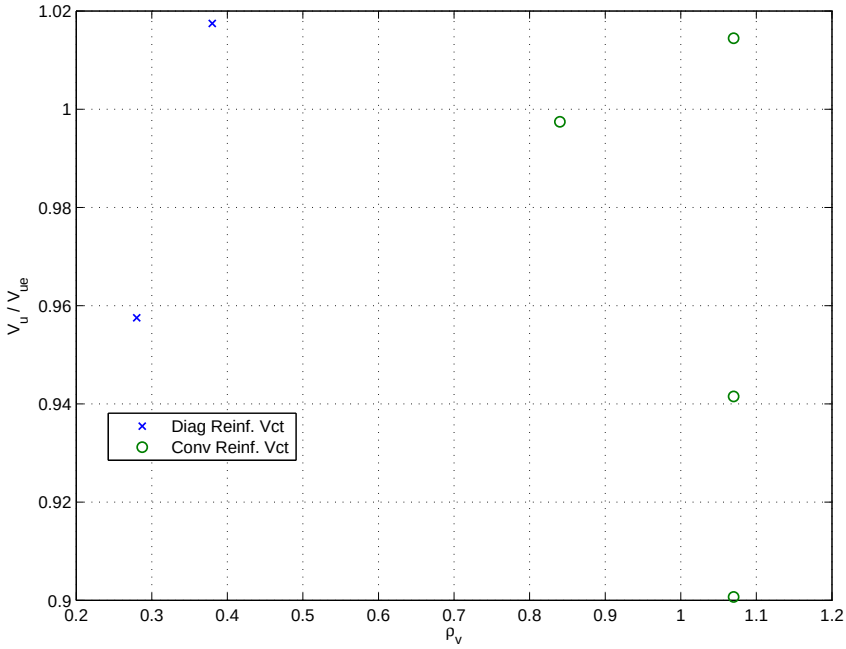

Figure 4.25: Mono. Coupling Beams - Ultimate Strength vs. Vertical Reinforcement Ratio

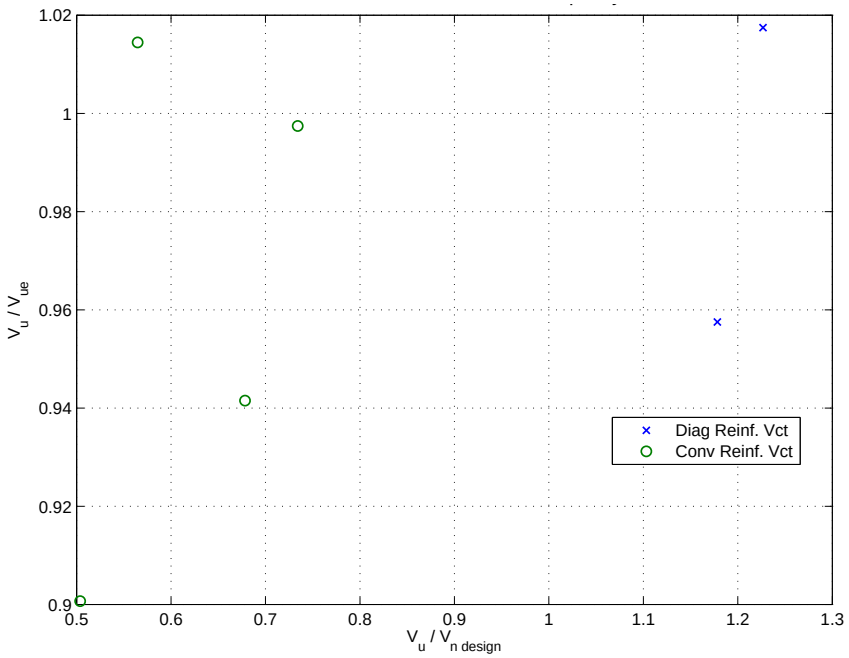

Figure 4.26: Mono. Coupling Beams - Ultimate Strength vs. Shear Demand Capacity Ratio

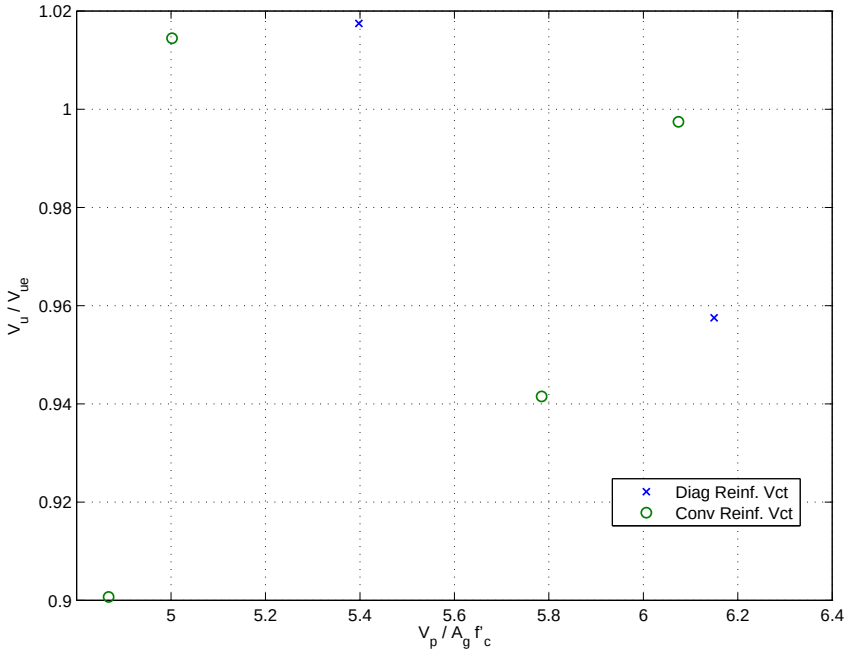

Figure 4.27: Mono. Coupling Beams - Ultimate Strength vs. Shear Stress Demand

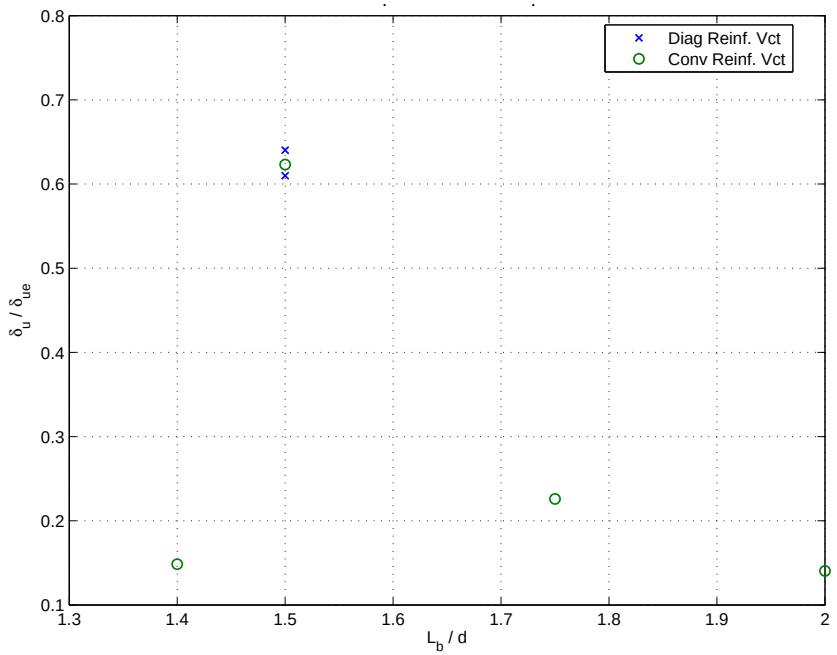

Figure 4.28: Mono. Coupling Beams - Ultimate Displacement vs. Aspect Ratio

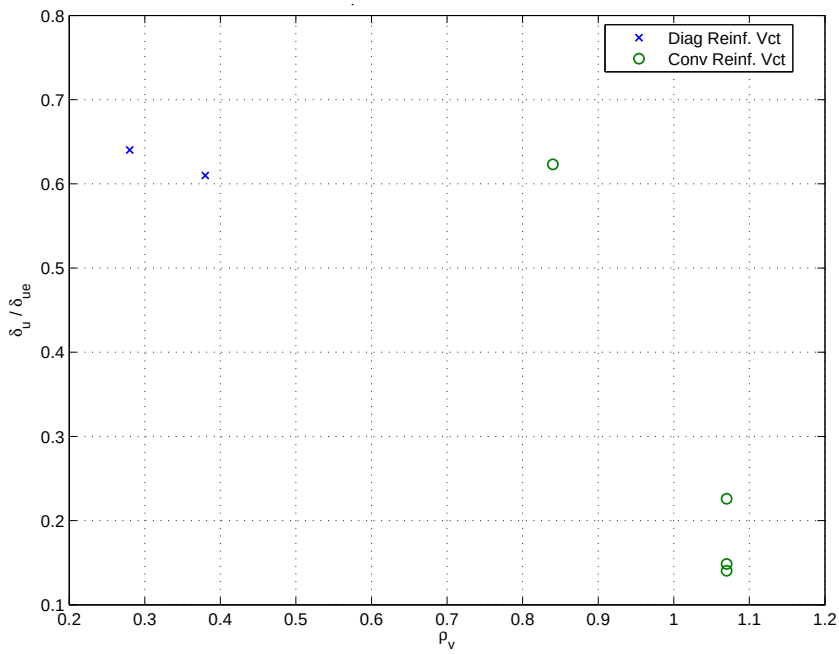

Figure 4.29: Mono. Coupling Beams - Ultimate Displacement vs. Vertical Reinforcement Ratio

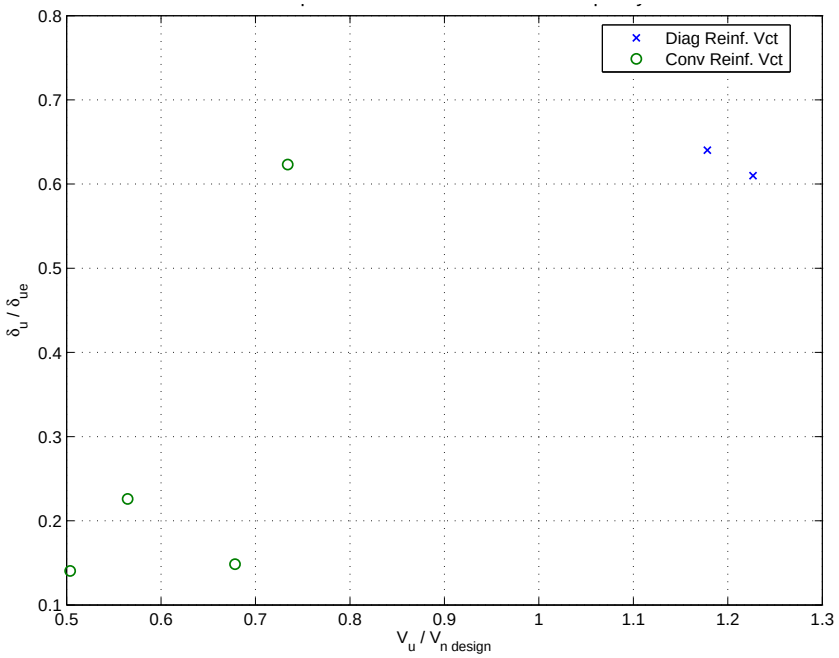

Figure 4.30: Mono. Coupling Beams - Ultimate Displacement vs. Shear Demand Capacity Ratio

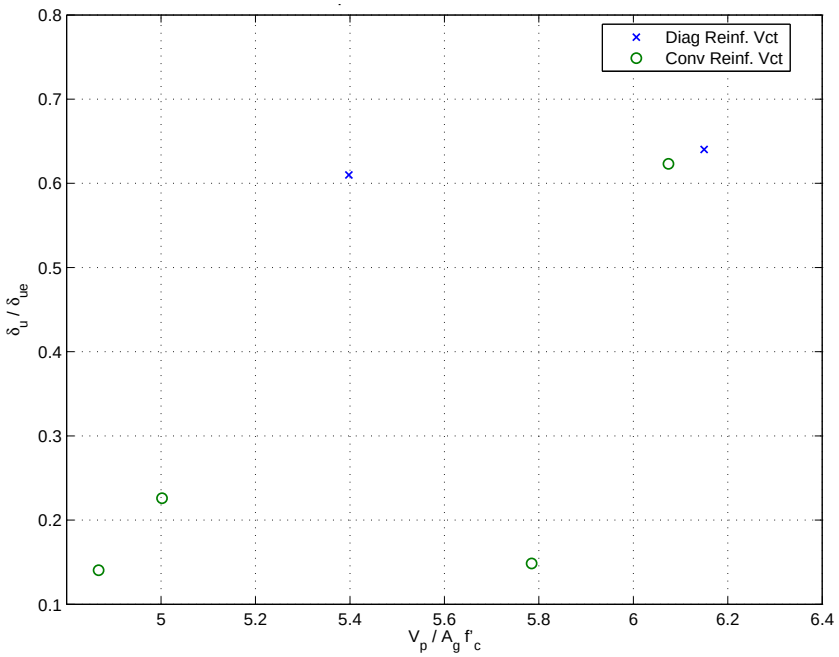

Figure 4.31: Mono. Coupling Beams - Ultimate Displacement vs. Shear Stress Demand

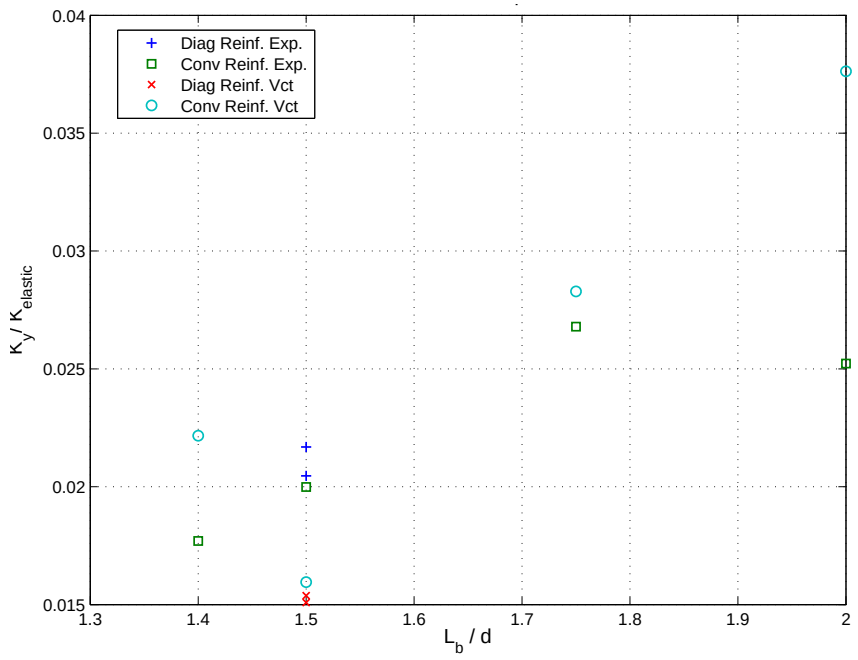

Figure 4.32: Mono. Coupling Beams - Yield Stiffness vs. Aspect Ratio

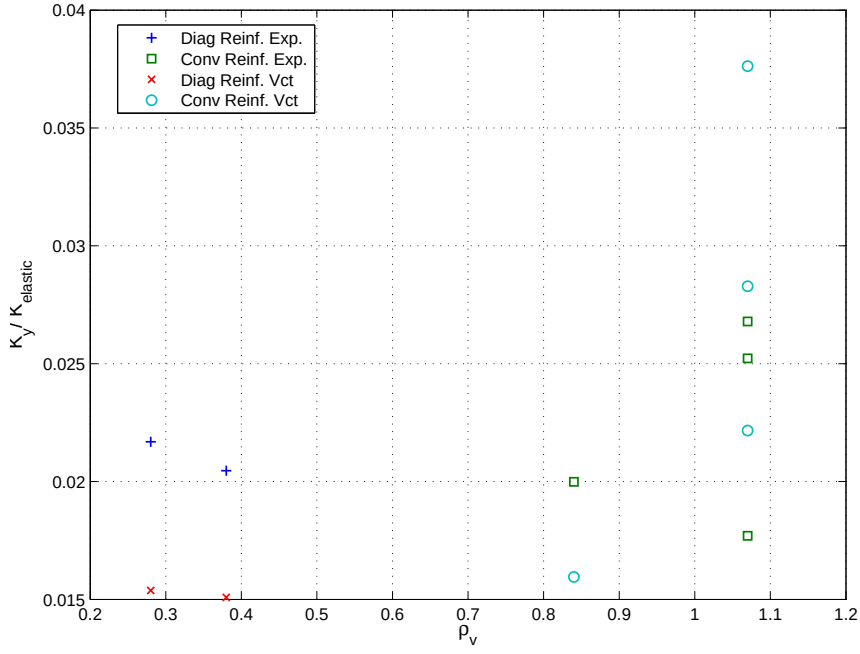

Figure 4.33: Mono. Coupling Beams - Yield Stiffness vs. Vertical Reinforcement Ratio

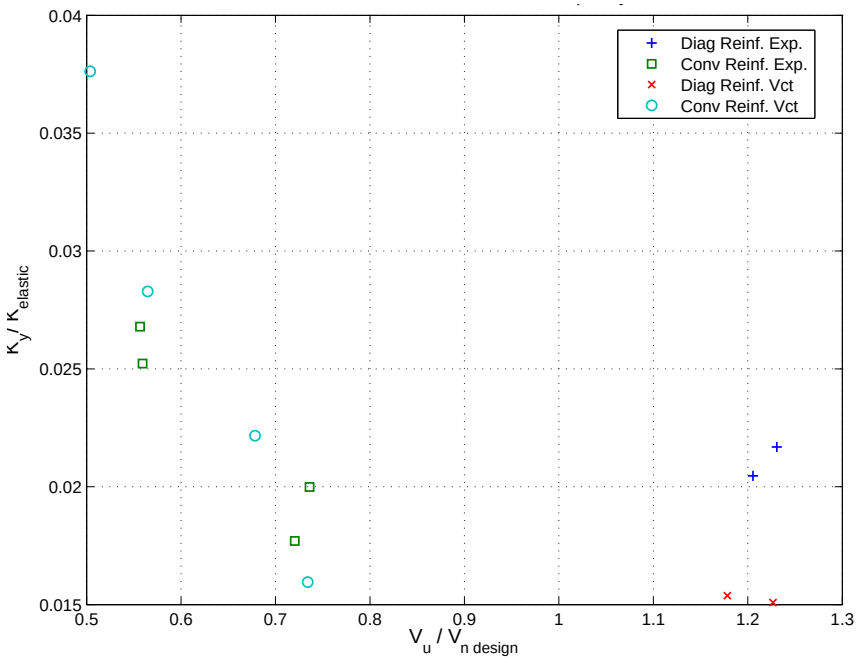

Figure 4.34: Mono. Coupling Beams - Yield Stiffness vs. Shear Demand Capacity Ratio

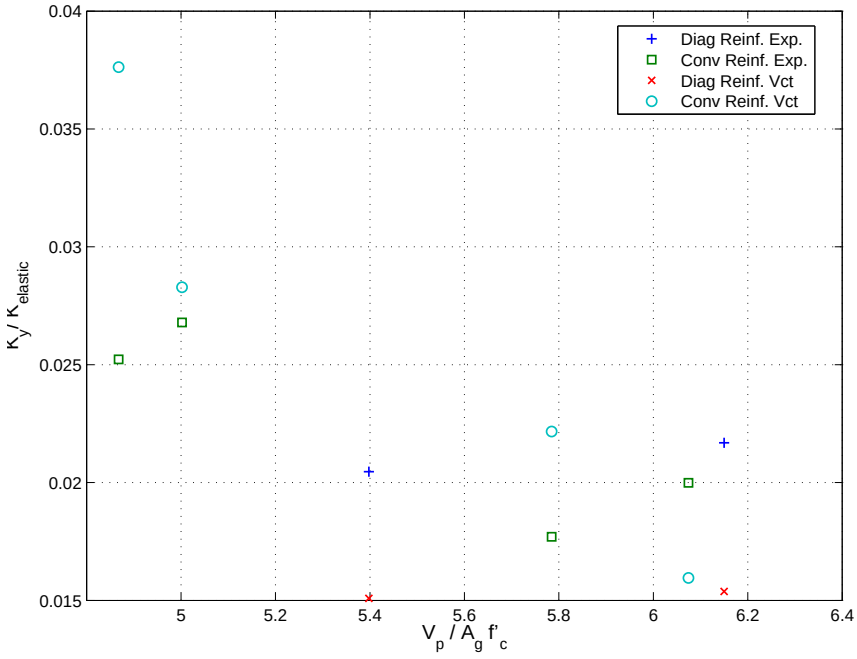

Figure 4.35: Mono. Coupling Beams - Yield Stiffness vs. Shear Stress Demand

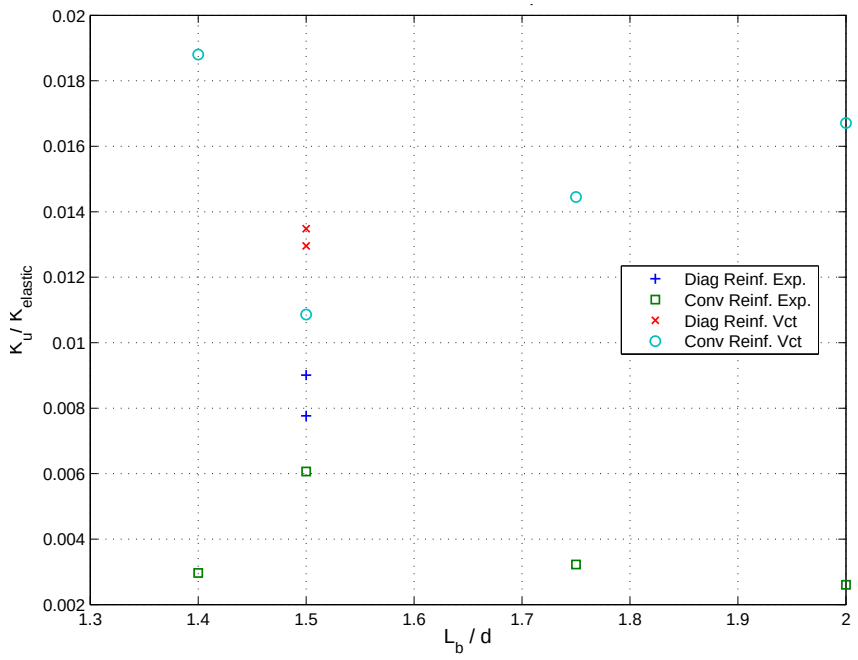

Figure 4.36: Mono. Coupling Beams - Ultimate Stiffness vs. Aspect Ratio

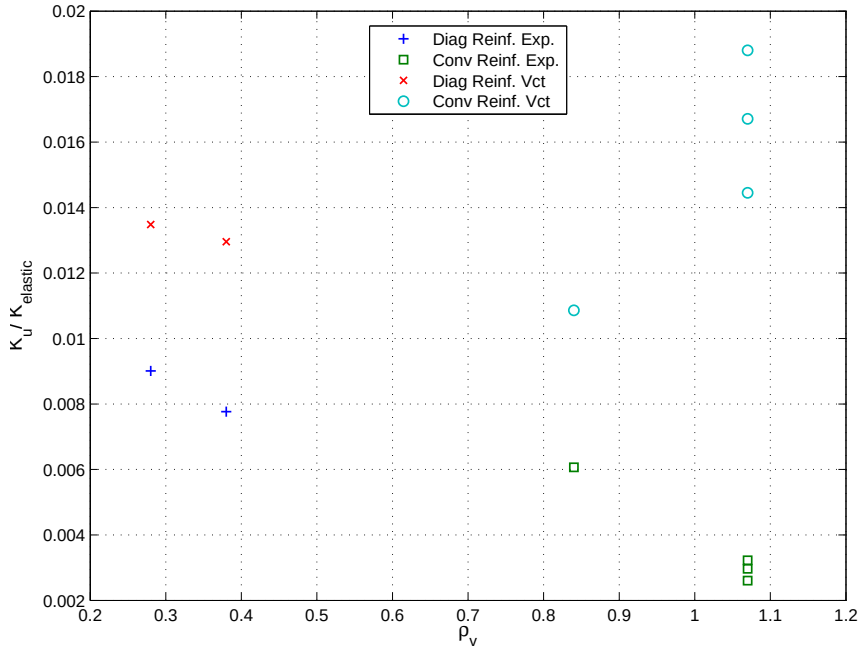

Figure 4.37: Mono. Coupling Beams - Ultimate Stiffness vs. Vertical Reinforcement Ratio

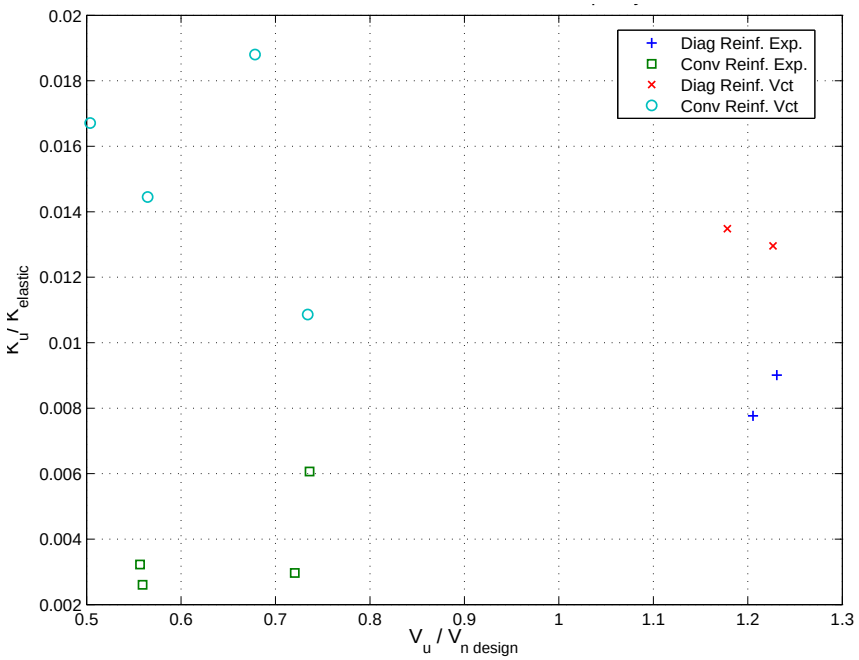

Figure 4.38: Mono. Coupling Beams - Ultimate Stiffness vs. Shear Demand Capacity Ratio

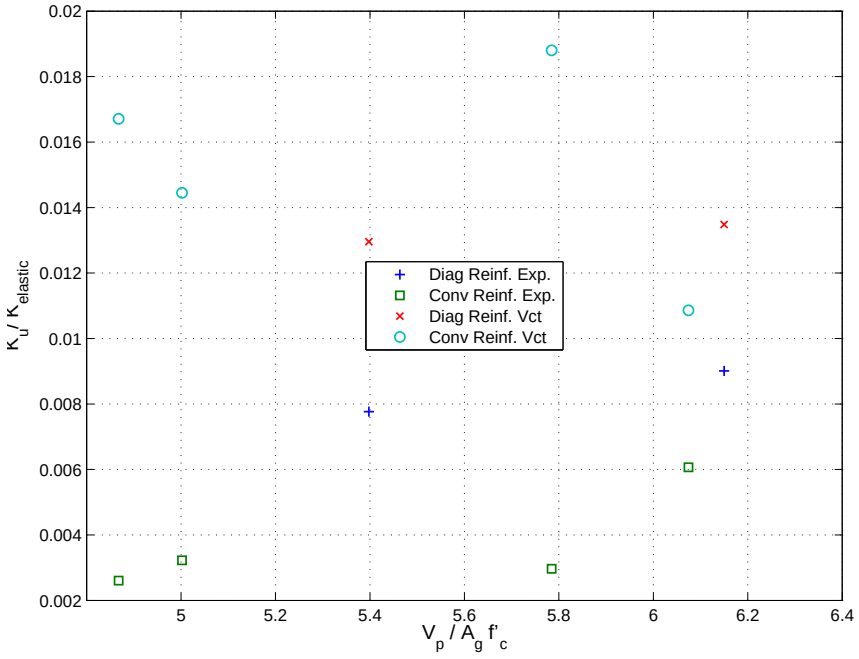

Figure 4.39: Mono. Coupling Beams - Ultimate Stiffness vs. Shear Stress Demand

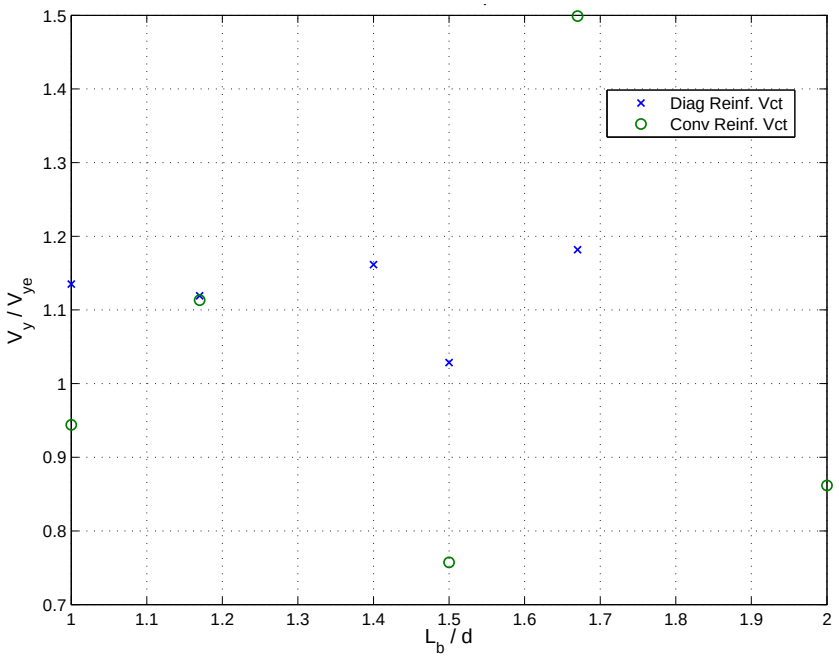

Figure 4.40: Cyclic Coupling Beams - Yield Strength vs. Aspect Ratio

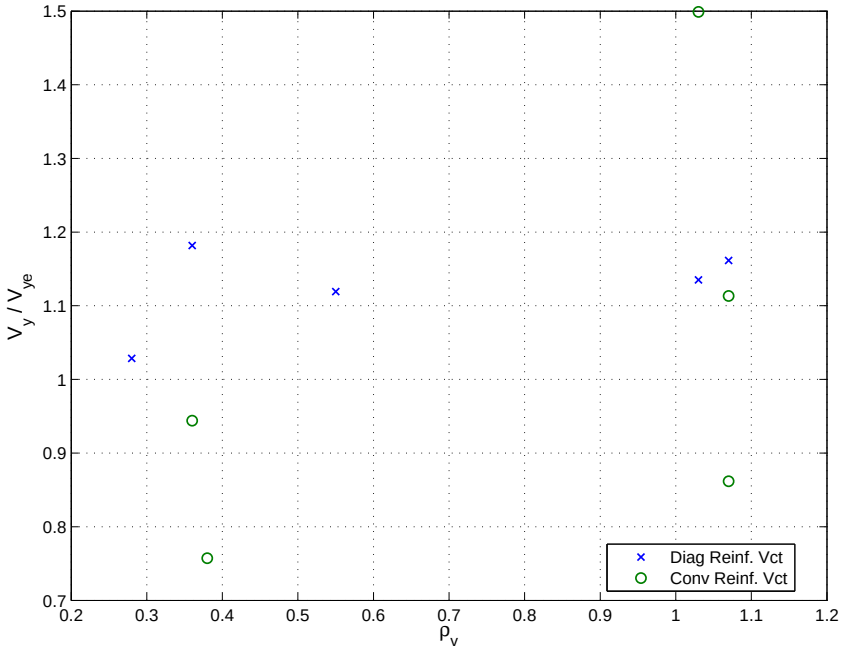

Figure 4.41: Cyclic Coupling Beams - Yield Strength vs. Vertical Reinforcement Ratio

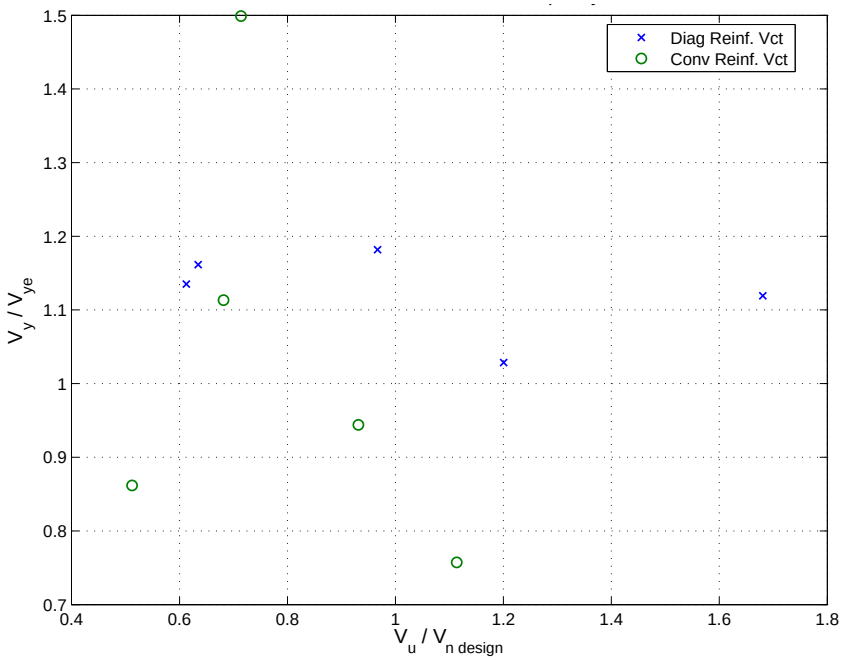

Figure 4.42: Cyclic Coupling Beams - Yield Strength vs. Shear Demand Capacity Ratio

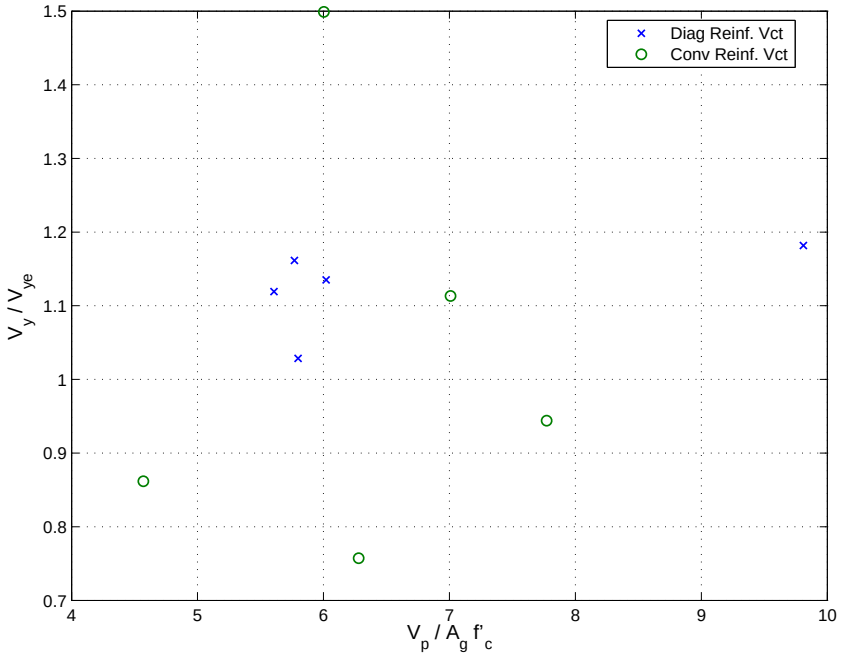

Figure 4.43: Cyclic Coupling Beams - Yield Strength vs. Shear Stress Demand

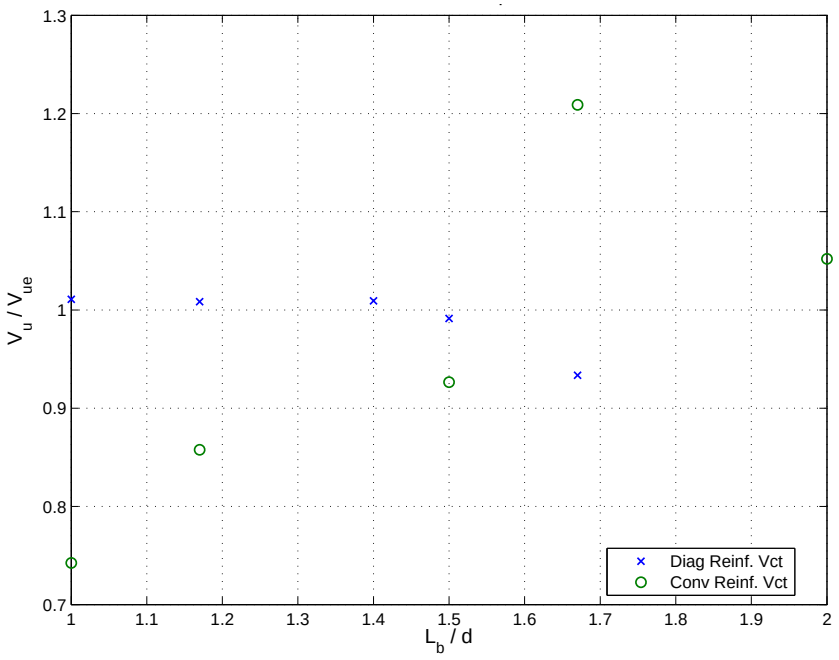

Figure 4.44: Cyclic Coupling Beams - Ultimate Strength vs. Aspect Ratio

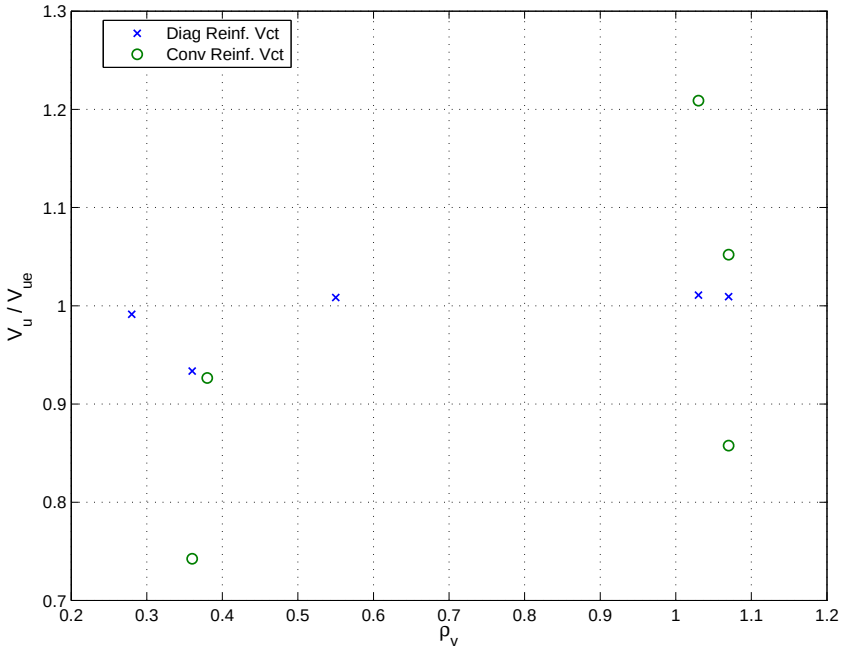

Figure 4.45: Cyclic Coupling Beams - Ultimate Strength vs. Vertical Reinforcement Ratio

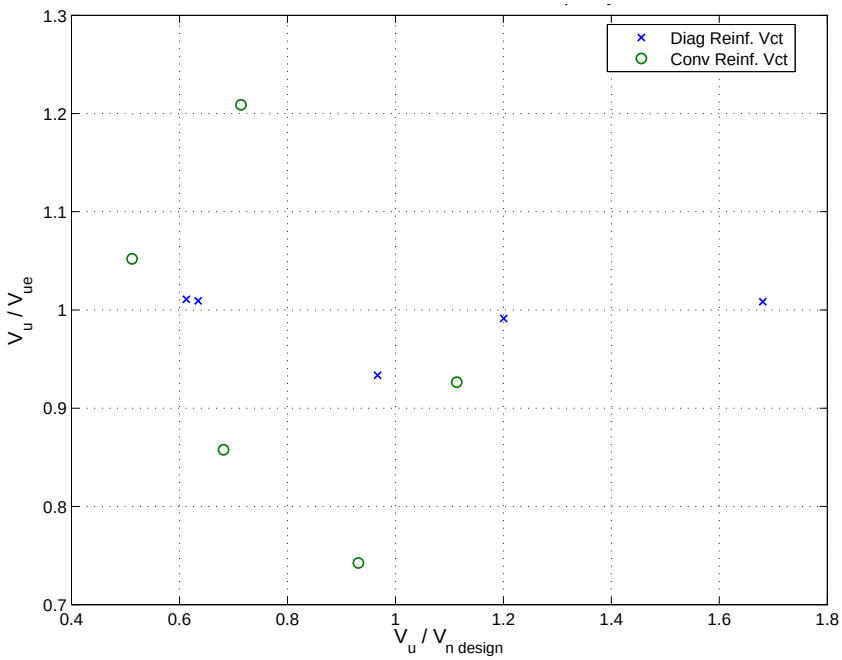

Figure 4.46: Cyclic Coupling Beams - Ultimate Strength vs. Shear Demand Capacity Ratio

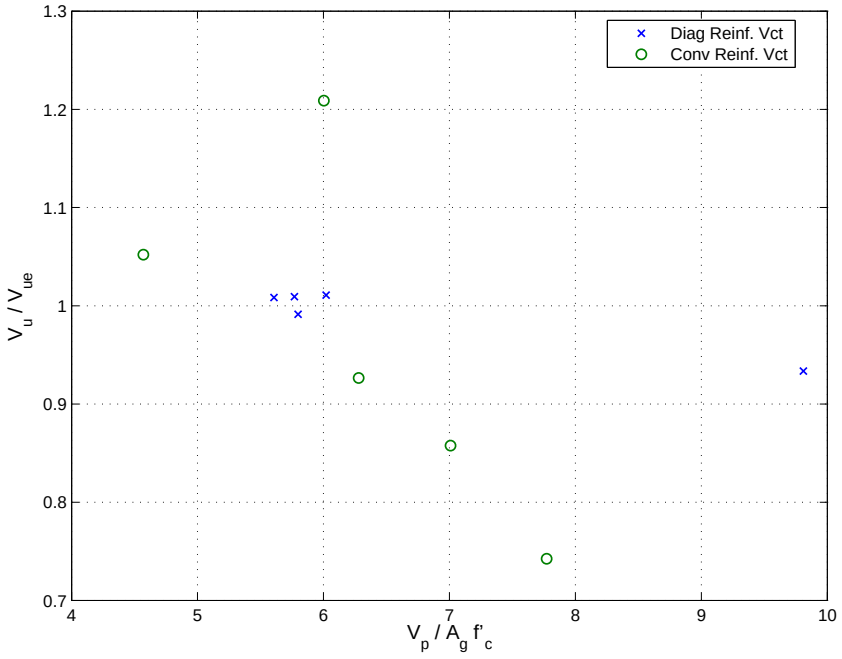

Figure 4.47: Cyclic Coupling Beams - Ultimate Strength vs. Shear Stress Demand

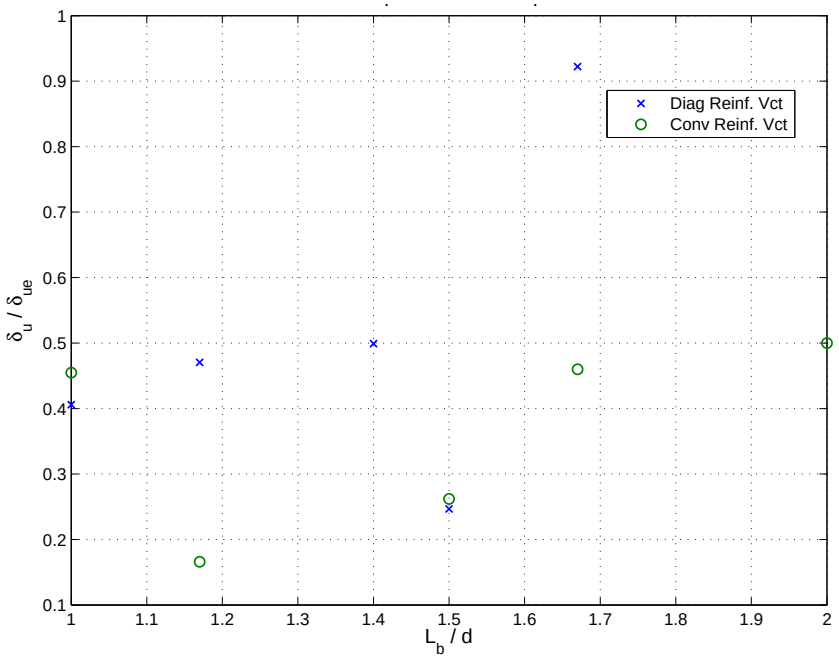

Figure 4.48: Cyclic Coupling Beams - Ultimate Displacement vs. Aspect Ratio

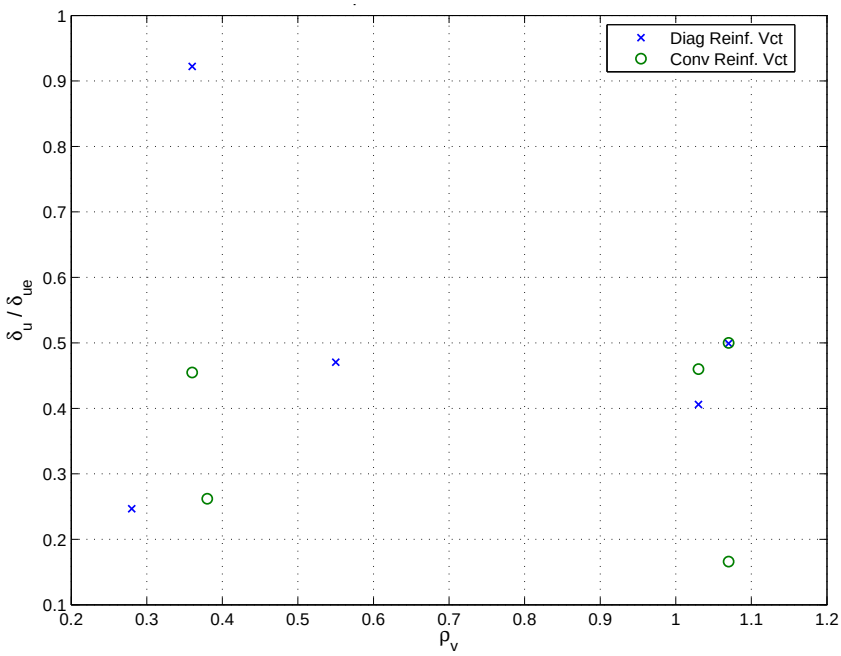

Figure 4.49: Cyclic Coupling Beams - Ultimate Displacement vs. Vertical Reinforcement Ratio

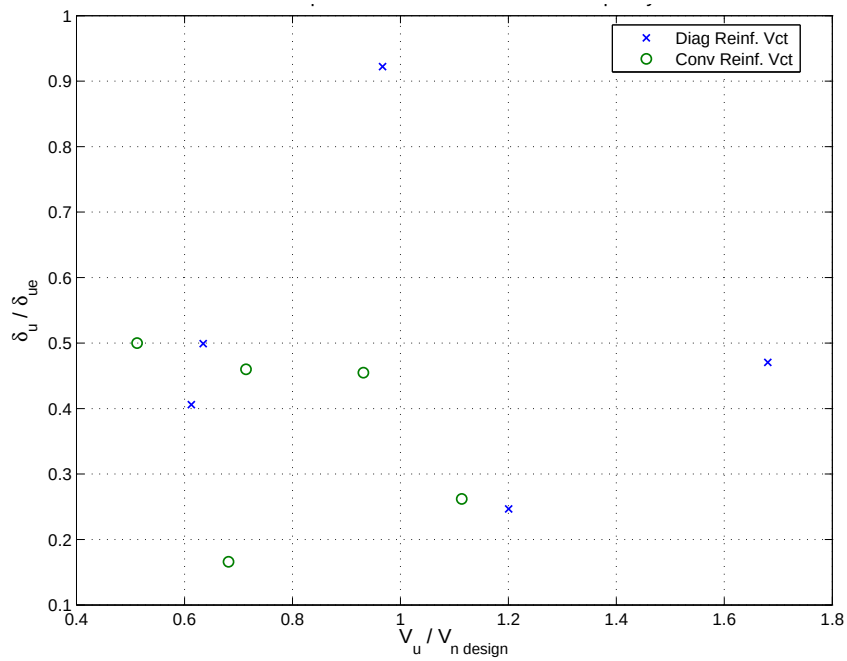

Figure 4.50: Cyclic Coupling Beams - Ultimate Displacement vs. Shear Demand Capacity Ratio

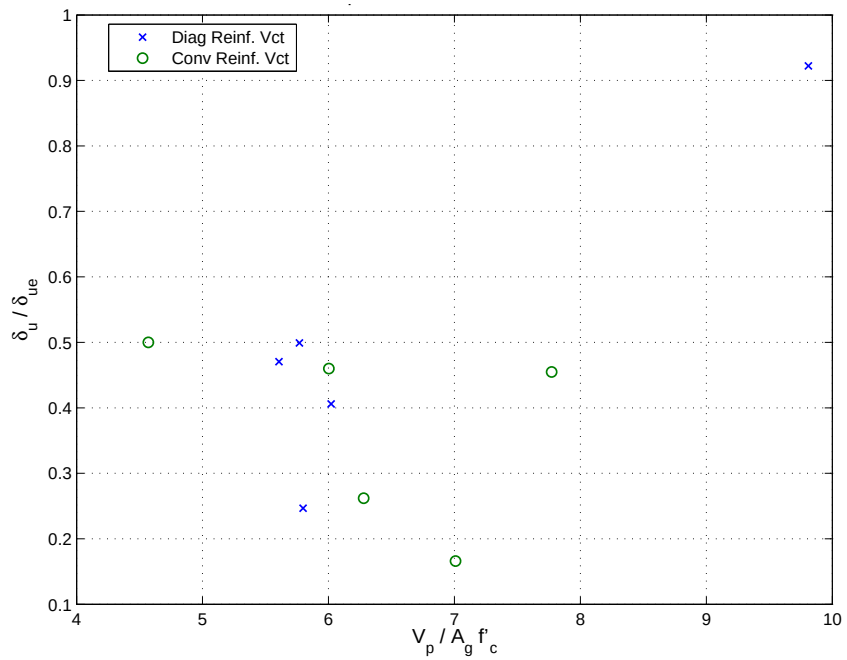

Figure 4.51: Cyclic Coupling Beams - Ultimate Displacement vs. Shear Stress Demand

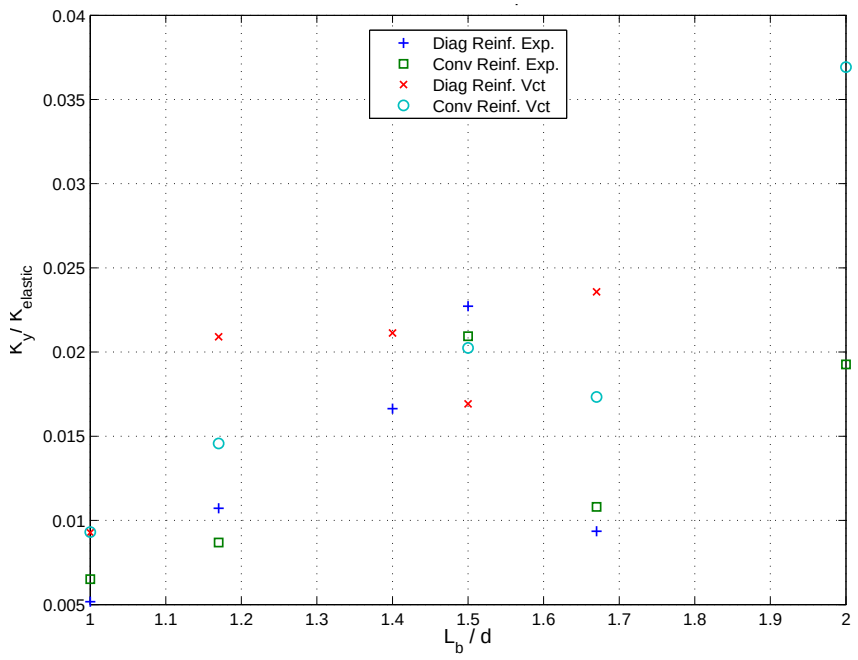

Figure 4.52: Cyclic Coupling Beams - Yield Stiffness vs. Aspect Ratio

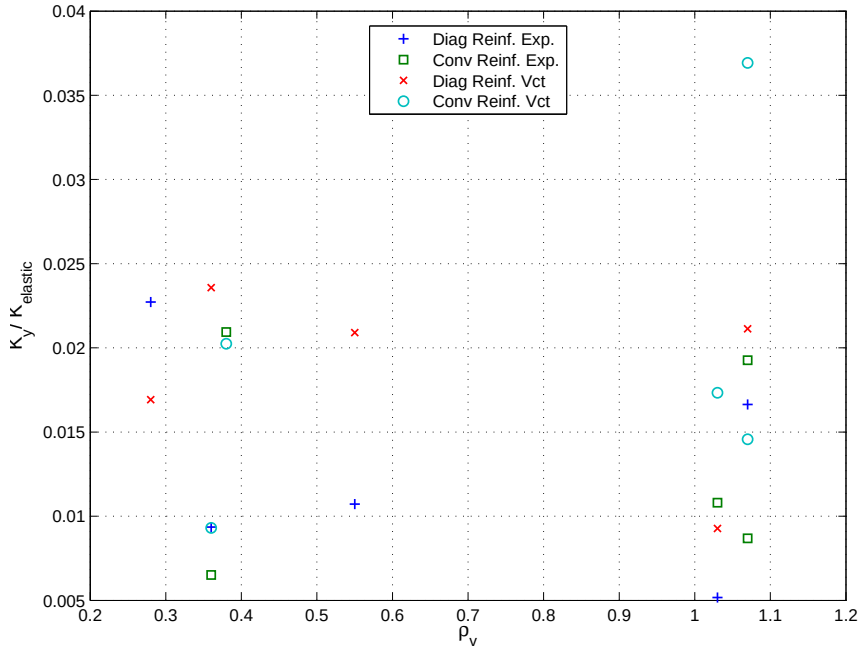

Figure 4.53: Cyclic Coupling Beams - Yield Stiffness vs. Vertical Reinforcement Ratio

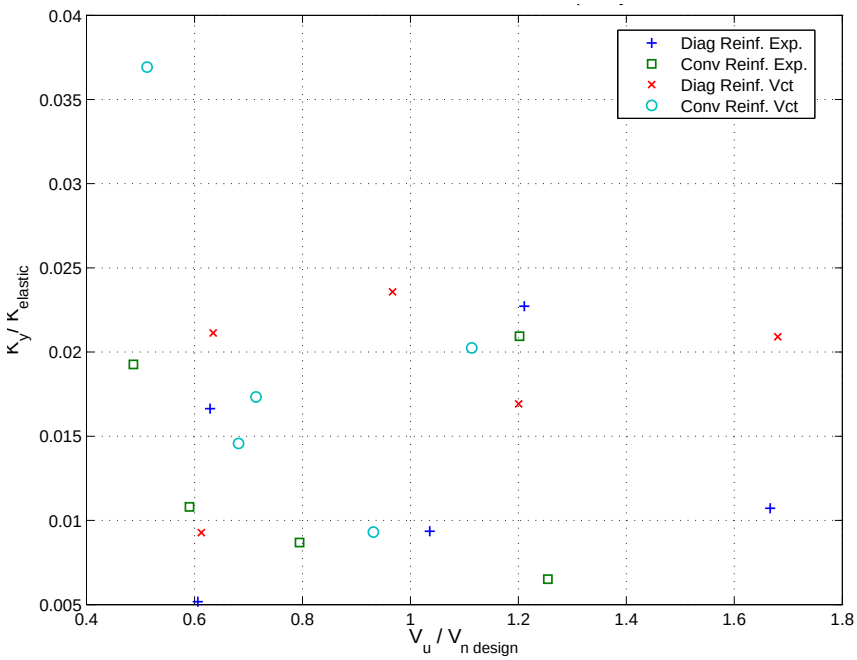

Figure 4.54: Cyclic Coupling Beams - Yield Stiffness vs. Shear Demand Capacity Ratio

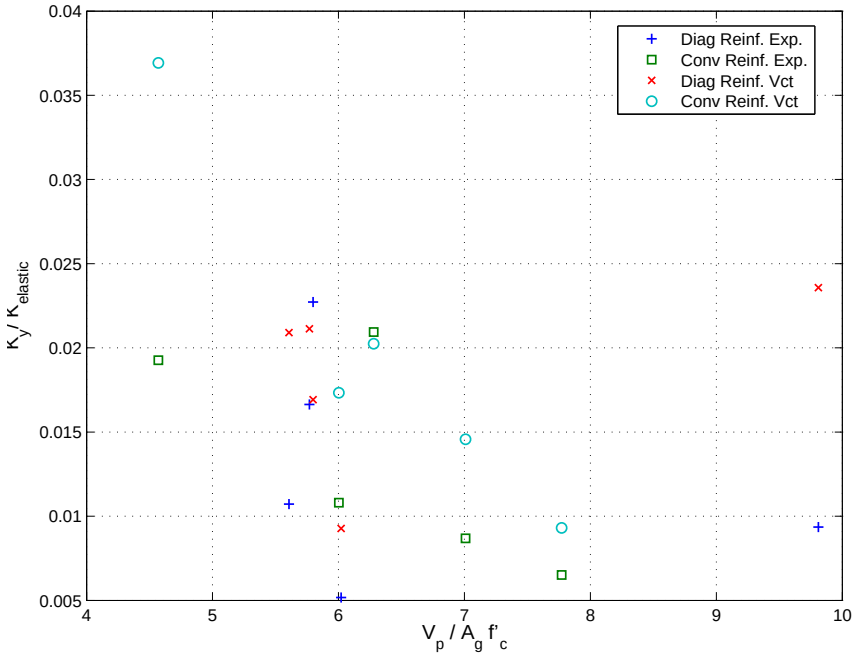

Figure 4.55: Cyclic Coupling Beams - Yield Stiffness vs. Shear Stress Demand

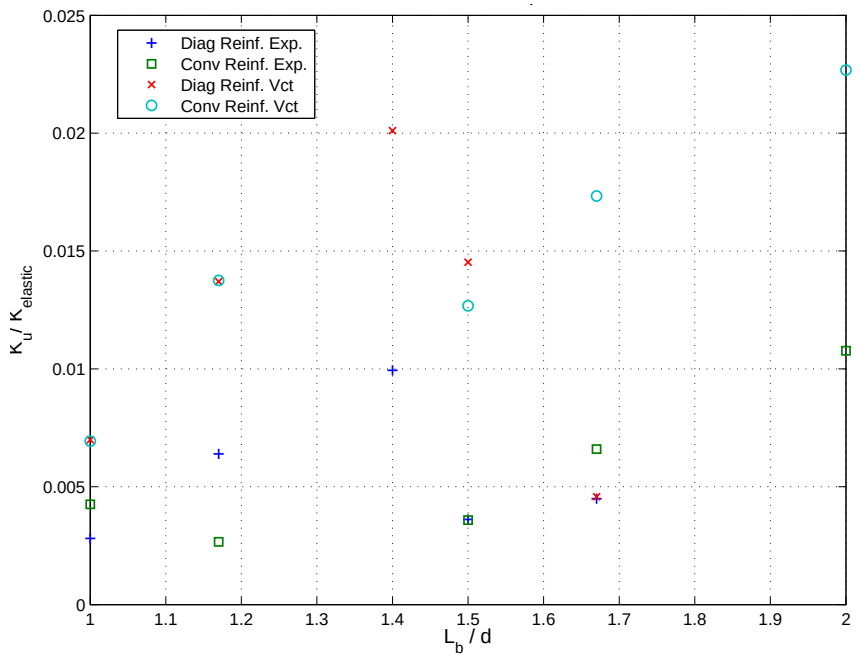

Figure 4.56: Cyclic Coupling Beams - Ultimate Stiffness vs. Aspect Ratio

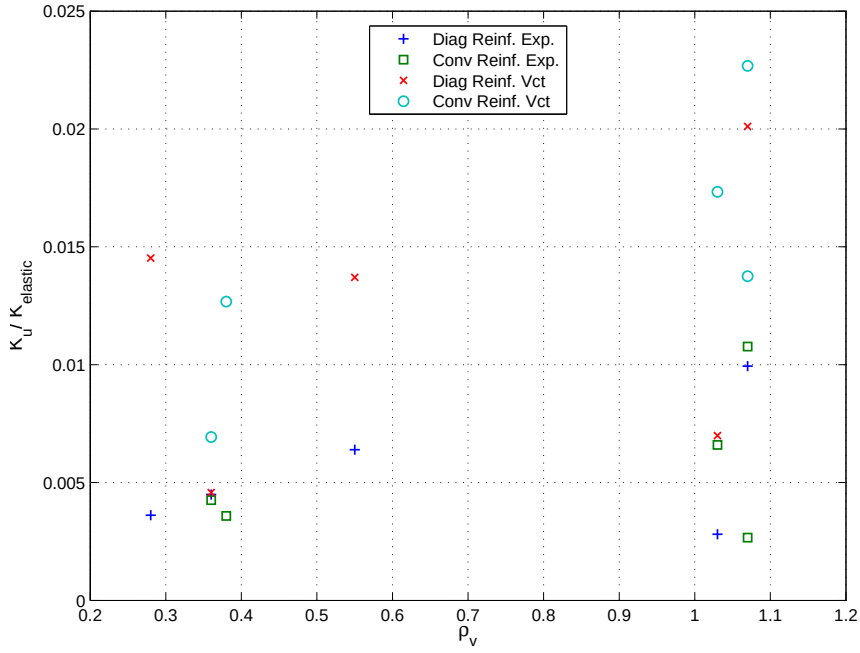

Figure 4.57: Cyclic Coupling Beams - Ultimate Stiffness vs. Vertical Reinforcement Ratio

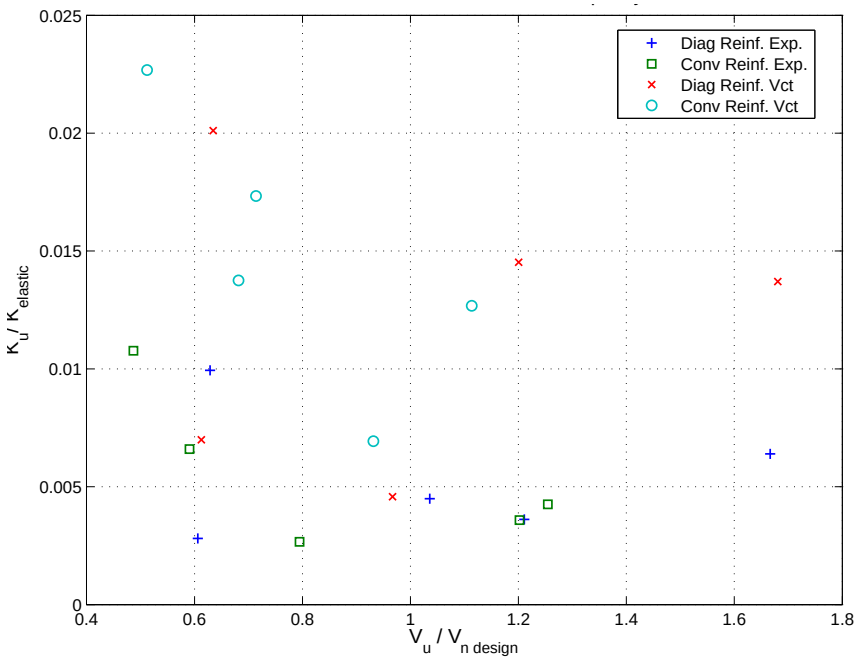

Figure 4.58: Cyclic Coupling Beams - Ultimate Stiffness vs. Shear Demand Capacity Ratio

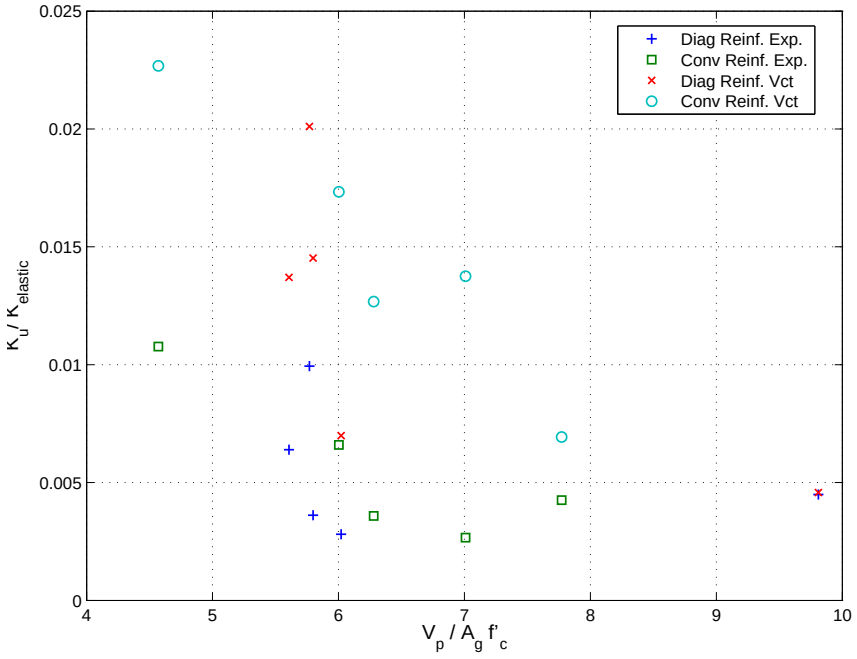

Figure 4.59: Cyclic Coupling Beams - Ultimate Stiffness vs. Shear Stress Demand

4.7 Discussion and Comparison of Results

Comparison of simulation and experimental data indicates that Vector2 can provide a good prediction of the behavior through the yield point and up to the ultimate strength; however, it generally underestimates the ultimate displacement of the specimens. The analytical models were able to predict the yield strength with an average error of 5% over strength and the ultimate strength with an average error of only 2% under strength. The analytical model provides a fairly good prediction of yield displacement, typically under predicting it by 11%. However, the model greatly under predicts ultimate displacement; the predicted values were, on average, 42% of the experimental values.

In general, the analytical specimens have a higher stiffness prior to yield and reach the maximum load early in the load sequence, whereas the experimental results tend to gradually approach the maximum load near the end of the displacement history. The increased stiffness of the model is due, in part, to the assumption of perfect bond between the reinforcing bars and the concrete. In the experimental specimens, flexural cracks would gradually open and bond-slip of the main reinforcing bars would occur. The opening of flexural cracks and the slip of the reinforcing bars provide a significant contribution to the lateral deflections of the coupling beam and thus reduce the effective stiffness. The premature failure of the model occurs when an extreme fiber crushes and the model cannot simulate the redistribution of the loads. The crushed element cannot support any load and forces a concentration of stress in the next element, causing a rapid progression of failure through the specimen.

With the modeling parameters and analysis capabilities of Vector2 understood, the predictive analysis of the NEESR coupling beams could be completed with an adequate level of confidence.

4.8 Model Parameter Study

4.8.1 Vecchio and Palermo Parameters

After the completion of the experimental coupling beam models a report detailing the use of VecTor2 to model the behavior of planar shear walls was published by Vecchio and Palermo (2007). This report utilized a slight variation on the set of constitutive models used, the author felt it would be prudent to see if the settings used by Vecchio and Palermo could improve the behavior of the coupling beam models. The Zhao MCB2 specimen was chosen for this study because it showed a post-elastic behavior that did not match the reported experimental data. In addition to these settings, the model was also rerun with a smaller convergence criteria and an increased number of iterations per displacement step.

The Vecchio settings differ in the following areas. The compression softening model used was Vecchio 1992-A (e1/e2-Form), this is a strength and strain softening model vs. the strength only softening model previously used. Tension Softening and Rebar Dowel Action were not considered.

Figure 4.60 shows a comparison between the base model and the Vecchio settings. The settings used by Vecchio provide the same performance up to the peak strength and a slight increase in displacement ductility after the peak was reached. The improvement in post-peak performance was nominal and did not provide a large enough improvement to warrant a re-modeling of all the experimental coupling beam specimens.

Figure 4.61 shows a comparison of between the base model and the with an increased iteration allowance. The two results are essentially identical, showing that the maximum of 100 iterations per displacement step is sufficient to provide convergence.

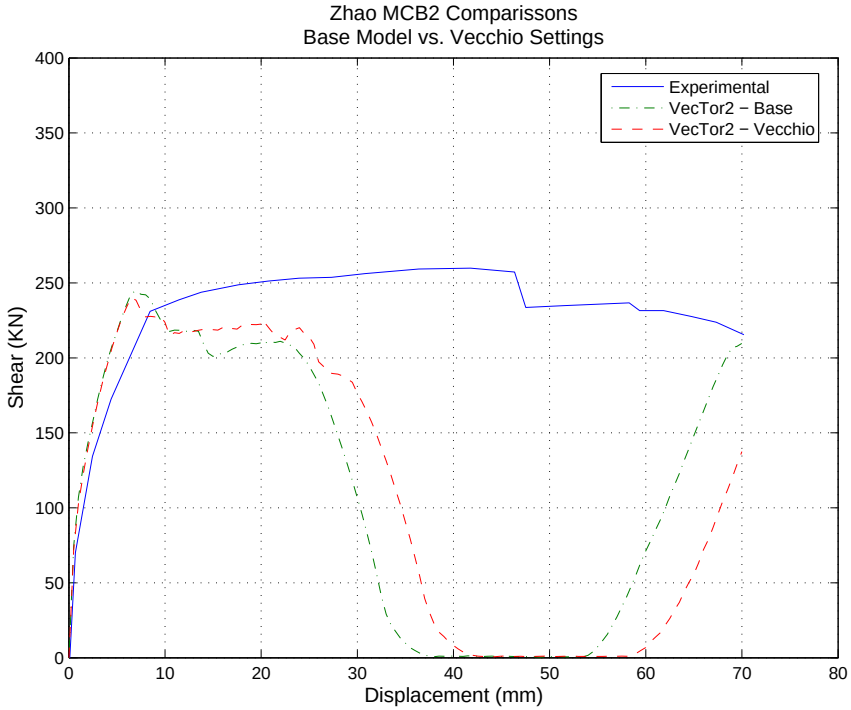

Figure 4.60: Zhao MCB2 Model Comparisons

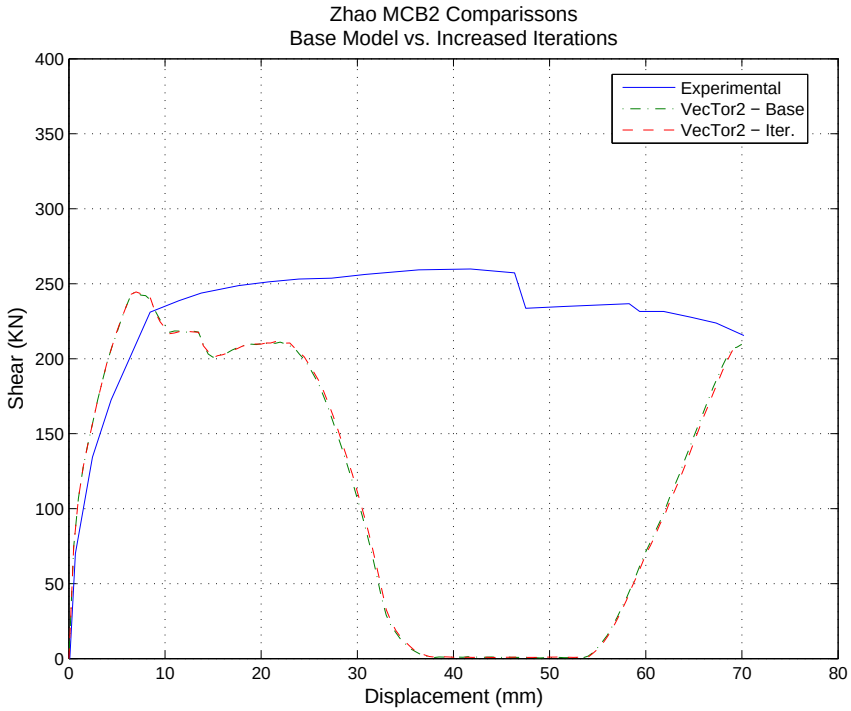

Figure 4.61: Zhao MCB2 Model Comparisons

Chapter 5

EVALUATION OF TRANSVERSE REINFORCEMENT OF COUPLING BEAMS

5.1 Introduction

The primary objective of this section was to determine the effect of transverse reinforcement, or confinement, on the performance of diagonally reinforced coupling beams. The performance of a coupling beam with code compliant transverse reinforcement was compared to three different transverse confinement configurations. Additionally, the effects of the adjacent slab reinforcement on the coupling beam were investigated.

Discussions with an external advisory board (Hooper, Hawkins, etc. 2006) indicate that current code requirements often result in diagonally reinforced coupling beams that have highly congested transverse reinforcement resulting in difficult and expensive construction. A revision to the current code confinement methods has been proposed by ACI committee 318H; the proposal will allow for greater transverse reinforcement spacing and introduce an alternative design procedure that will allow for a less congested transverse reinforcement configuration.

5.1.1 Approach

Nonlinear finite element analysis using VecTor2 were completed to simulate the performance of the coupling beam variations when subjected to in-plane displacements. The design of the coupling beam from the coupled wall model discussed in Chapter 6 was used as the reference design (in terms of dimensions, materials, and diagonal reinforcement). The analysis assumptions determined in Chapter 4 were used for each of the coupling beam models explored.

5.1.2 Organization of Chapter

The following provides a brief outline of this chapter.

Section 5.2 describes the current and proposed design requirements.

Section 5.3 describes the different coupling beam models and their confinement variations.

Section 5.4 discusses the finite element modeling techniques.

Section 5.5 discusses how the analysis results were compared to the reference model.

Section 5.6 discusses the simulation results from the VecTor2 finite element analysis.

Section 5.7 compares the overall performance of the confinement variations.

5.2 Design Requirements

5.2.1 ACI 318-05 Current Code

The current ACI 318 code specifies that diagonal reinforcement must be used in coupling beams with aspect ratio, l_n/d, that is less than two or with factored shear force V_u exceeding $4\sqrt{f_c'}b_w d$. Additional confinement is required on the diagonal reinforcement per §21.7.7.4. The confinement requirement adopts §21.4.4, transverse reinforcement for columns in Special Moment Resistant Frames, including the following limits

- §21.4.4.1 Area of transverse reinforcement shall not be less than:
  $A_{sh} = 0.3(sb_c f_c^{'}/f_{yt})(A_g/A_{ch} - 1)$ Equation (21-3)
  $A_{sh} = 0.09sb_c f_c^{'}/f_t$ Equation (21-4)

- §21.4.4.2 Spacing of transverse reinforcement shall not exceed the smallest of (a), (b), and (c):
  (a) one-quarter of the minimum member dimension;

(b) six times the diameter of the longitudinal reinforcement; and

(c) $s_o = 4 + \frac{14 - h_x}{3}$

For diagonally reinforced coupling beams, the "member" is defined as cross section of the diagonal bar cage (out to out) plus the nominal cover dimension.

5.2.2 ACI 318H-CH047d Proposal

ACI Committee 318H has submitted proposal CH047 which seeks to modify the transverse reinforcement requirements for diagonally reinforced coupling beams. It is likely that this proposal will be incorporated into the next revision of ACI 318, set to be published in 2008. The proposal is separated into two sections; a revision to the current spacing limits and an alternative confinement method. The first section changes the spacing requirements of the transverse reinforcement by removing the "one-quarter of the minimum member dimension" requirement. The second section introduces an alternative design method that will allow the entire coupling beam to be enclosed in transverse reinforcement satisfying the requirements of §21.4.4.1(b) and (c), and §21.4.4.2, except for Equation (21-3) and the spacing of cross-ties or legs in the plane of the cross section of the coupling beam shall not exceed 8 inches. Equation (21-3) defines the required area of transverse reinforcement based on a ratio of the confined core to the gross area of the member; it is specifically applicable to column sections and need not apply to diagonal bar groups. In summary, the alternative design method will allow the entire coupling beam to be confined rather than just the diagonal bar groups provided the transverse reinforcement meet the same requirements as currently specified in the ACI 318-05 code less with the additional spacing limit on cross tie spacing.

5.3 Description of Models

Five different coupling beam confinement options were explored; the first model was designed to meet the current ACI code, the second model was intended to represent the effect of additional top steel from the adjacent slab and/or collector elements, the third and fourth

models are based on the ACI 318H-CH047 proposal, the fifth model introduces a modified ACI 318H-CH047 proposal with one half the confinement reinforcement.

The coupling beam confinement was designed at full scale and the resulting reinforcement ratios applied to the one-third scale models, allowing the models to better reflect full scale applications. The reinforcement ratios of the coupling beam models are shown in Table 5.1, tie spacing and ties sizes are approximate based on the one-third scale model. Each of the coupling beam variations is described in detail in the following sections.

5.3.1 CBR-ACI: ACI318-05 Reference Model

This model was designed to meet the current ACI 318-05 code. Confinement was provided around each diagonal bar group by #2 ties @ 1" o.c. Additional nominal reinforcement consists of 2 #2 bars top and bottom plus 1 #2 on each face. Nominal #2 stirrups at 6" o.c. are provided around the entire beam. The tie spacing around the diagonal bar groups was controlled by the one quarter of the member dimension limit in §21.4.4.2(a).

5.3.2 CBR-ACI-S: Reference model with additional slab steel

This model contains the same reinforcement as the CBR-ACI base model, except for additional top steel to simulate the contribution of the slab reinforcement and/or collector steel as is often seen in typical building construction.

5.3.3 CBR-318H: Confinement to meet the ACI 318H proposal

This model was designed to meet the reduced spacing proposal. The spacing of the ties around each diagonal bar group can be increased to 1 1/2" due to the removal of the one quarter of the member dimension spacing limit. Tie spacing was controlled by the area of steel required, A_{sh}. Additional reinforcement and nominal ties remain the same as the reference model.

Table 5.1: Coupling Beam Confinement Variations

Model	ρ_l (A_s/db)	ρ_v (A_v/sb)	ρ_t (A_t/ds)	A_d (mm^2)	ρ_{dv} $(A_{dt}/d_c s_t)$	ρ_{dt} $(A_{dt}/b_c s_t)$
CBR-ACI	0.31%	0.27%	0.10%	516.1	1.63%	3.27%
CBR-ACI-S	0.31%*	0.27%	0.10%	516.1	1.63%	3.27%
CBR-318H	0.31%	0.27%	0.10%	516.1	1.09%	2.18%
CBR-318H-F	0.42%	0.74%	0.74%	516.1	-	-
CBR-318H-M	0.28%	0.56%	0.35%	516.1	-	-

* plus additional top steel of 194.8 mm^2

5.3.4 CBR-318H-F: Confinement of the entire section to meet ACI 318H proposal

This model was designed to meet the proposed alternative detailing methods. The entire beam was confined by stirrups with both vertical and horizontal cross ties. Tie spacing was controlled by the one quarter of the member dimension requirement, while the area and number of cross ties was controlled by the A_{sh} requirement and the maximum spacing between cross ties.

5.3.5 CBR-318H-M: Confinement of the entire section with reduced trans. reinf.

The confinement of this model is based on a reduced A_{sh} requirement. A_{sh} was reduced by half to $0.045 s b_c f_c^{'}/f_y$. The tie spacing limits as proposed in ACI 318H-CH047 are used.

5.4 Finite Element Modeling

The finite element model for the coupling beams uses the same constitutive models and analysis parameters as previously discussed in Chapter 4. The diagonal reinforcement in all models and the slab steel in CBR-ACI-S were modeled with discrete truss-bar elements. The material properties are shown in Table 5.2.

The coupling beams were simulated both monotonically and cyclically. The monotonic simulations were continued until significant strength loss occurred or the model became numerically unstable. The cyclic simulations had three repetitions per cycle with increasing

Table 5.2: Coupling Beam Material Properties

Concrete			Reinforcement		
$f_c^{'}$	5.0	ksi	f_y	60	ksi
f_t	0.50	ksi	f_u	90	ksi
E_c	4030	ksi	E_s	29000	ksi
ϵ_0	0.003		E_{sh}	170	ksi
			ϵ_{sh}	0.010	

magnitude per cycle, to the approximate yield displacement (δ_y), $2\delta_y$, $4\delta_y$, $6\delta_y$. If the models had not failed at $6\delta_y$, they were then pushed monotonically to failure. Monotonic model names are preceded with an "M", i.e. MCBR-ACI is the monotonically loaded version of CBR-ACI.

5.5 Description of Evaluation Method

The analysis results from each of the coupling beam simulation was evaluated to determine the predicted mechanisms of deformation, initial reinforcement yielding, ultimate strength, loss of stiffness, and loss of strength. The studied response parameters include:

V_y**:** shear observed in the coupling beam at first yield of diagonal bars.

V_u**:** maximum shear observed in the coupling beam.

$V_{1.5\%}$**:** shear in the coupling beam at 1.5% drift.

$V_{6.0\%}$**:** shear in the coupling beam at 6.0% drift.

K_y**:** secant stiffness at the first yield of the diagonal bars.

K_u**:** secant stiffness at the ultimate shear strength.

$K_{1.5\%}$: secant stiffness corresponding to 1.5% drift in the coupling beam.

$K_{6.0\%}$**:** secant stiffness corresponding to 6.0% drift in the coupling beam.

δ_y**:** displacement at the first yield of the diagonal bars.

δ_u**:** displacement at the maximum predicted shear.

Δ_y**:** drift in the coupling beam at the first yield of the diagonal bars, δ_y/L.

Δ_u**:** drift in the coupling beam at the maximum predicted shear, δ_u/L.

$\Delta_{0.85V_u}$**:** drift in the coupling beam when 85% of the predicted maximum strength, V_u, was reached.

μ_u**:** displacement ductility at the maximum predicted shear, δ_u/δ_y.

5.6 Simulation Results

The VecTor2 simulation results and load-drift response plots are discussed in the following sections.

5.6.1 Load Drift Plots

Load-drift plots for all models are shown in Figures 5.1 to 5.10. The load-drift plots have been annotated to show the locations of initial yield and ultimate shear strength. The design shear strength, $V_n = 50kips$, calculated using the ACI 318 code method, is shown on the load-drift plots with a dotted line.

Some of the cyclic simulations show results that are "jagged" at the higher displacement cycles. The jaggedness of the load-drift results are due to incomplete convergence within VecTor2. The convergence criteria was limited to one hundred iterations, and thus did not allow the model to completely converge at every displacement step. The "jagged" portions of the curve can be assumed to fluctuate around the correct solution, however, the lack of convergence is an indication that some elements may be highly stressed or distorted.

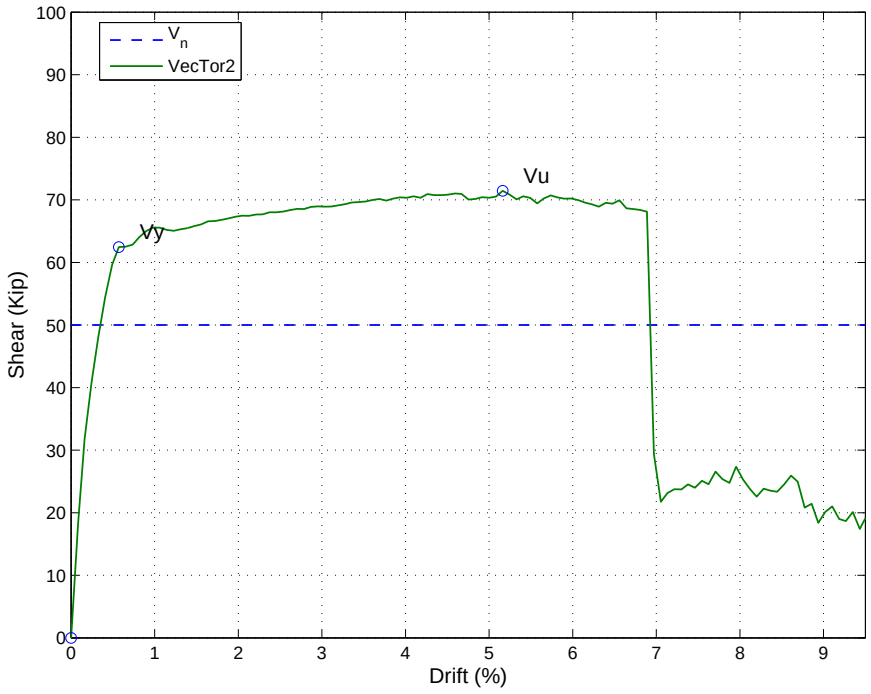

Figure 5.1: MCBR-ACI Load-Drift Response

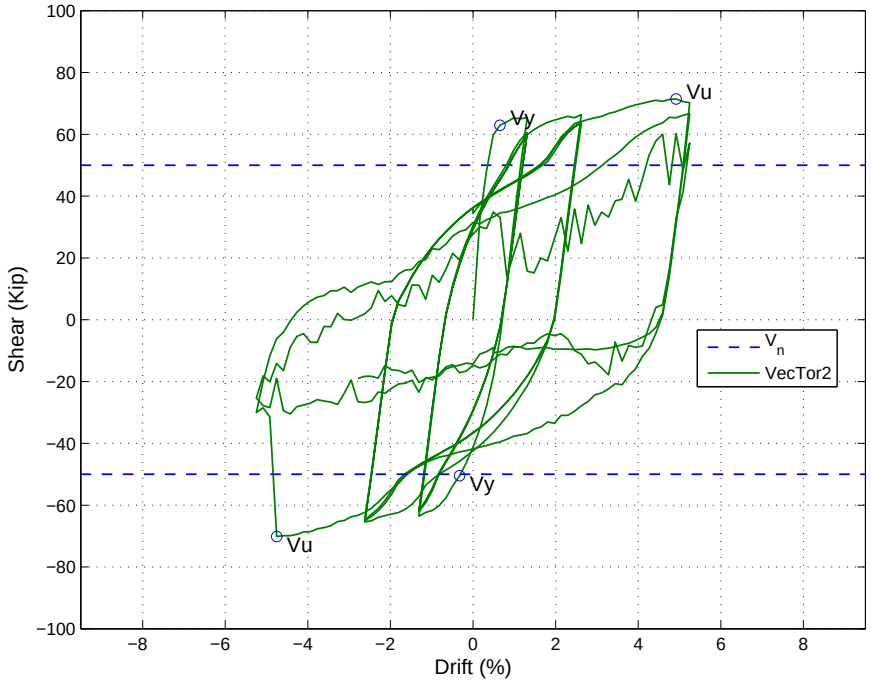

Figure 5.2: CBR-ACI Load-Drift Response

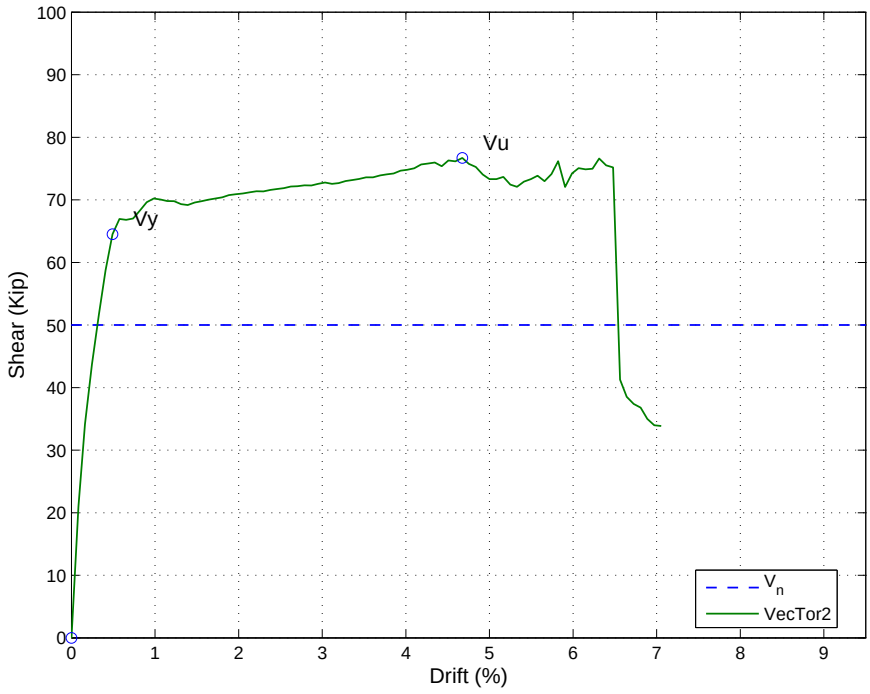

Figure 5.3: MCBR-ACI-S Load-Drift Response

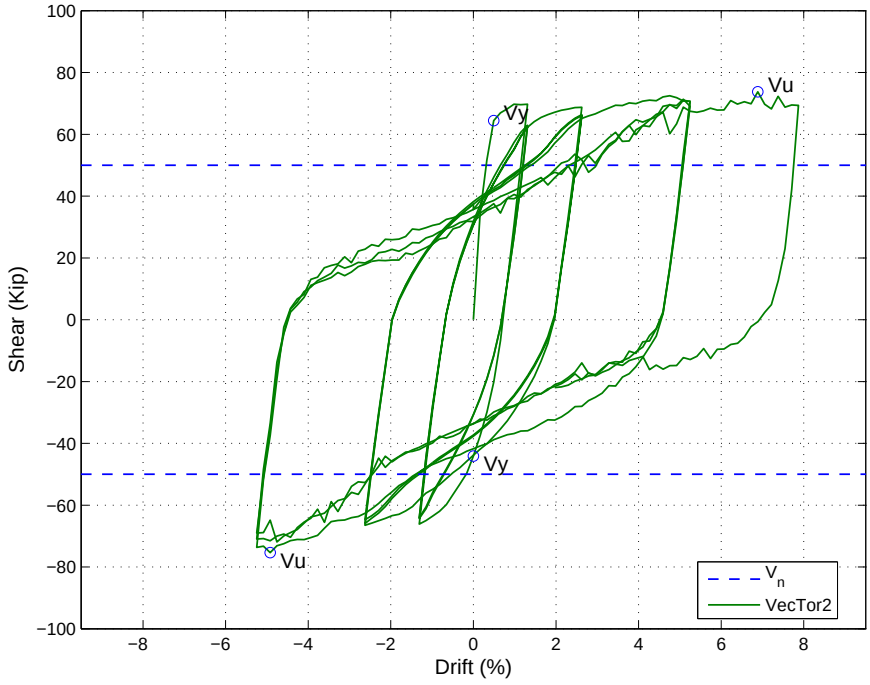

Figure 5.4: CBR-ACI-S Load-Drift Response

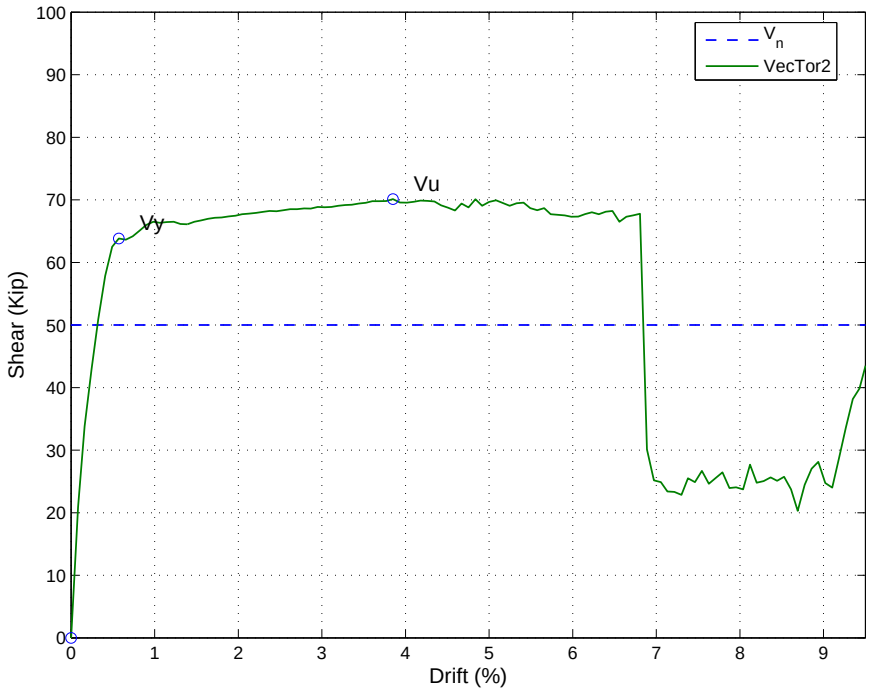

Figure 5.5: MCBR-318H Load-Drift Response

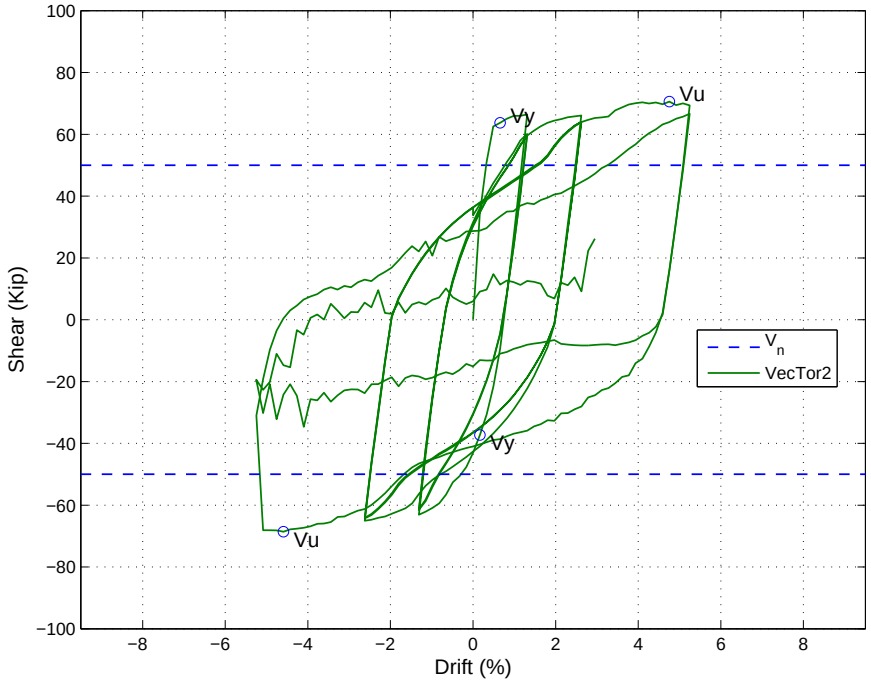

Figure 5.6: CBR-318H Load-Drift Response

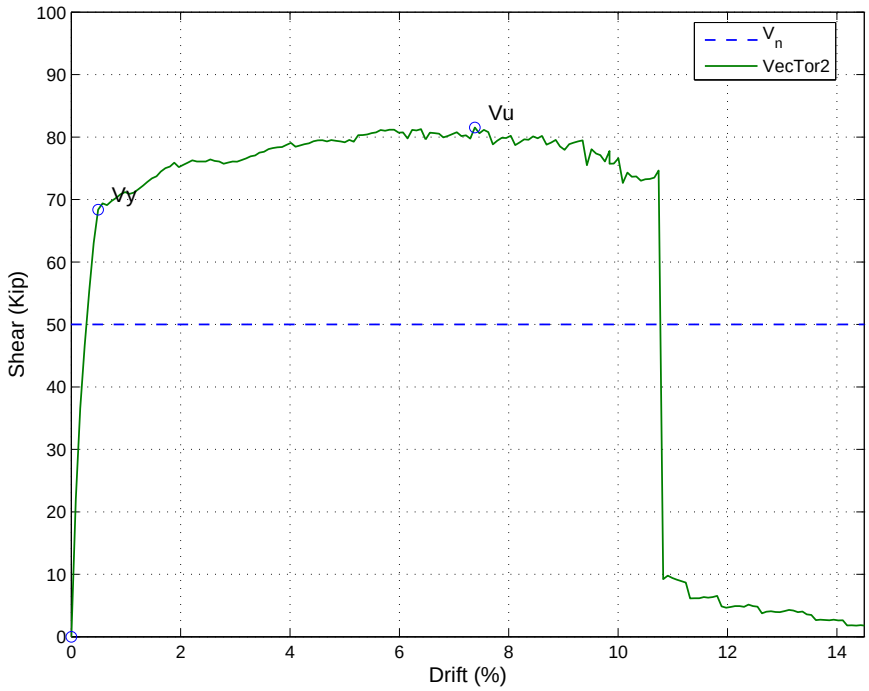

Figure 5.7: MCBR-318H-F Load-Drift Response

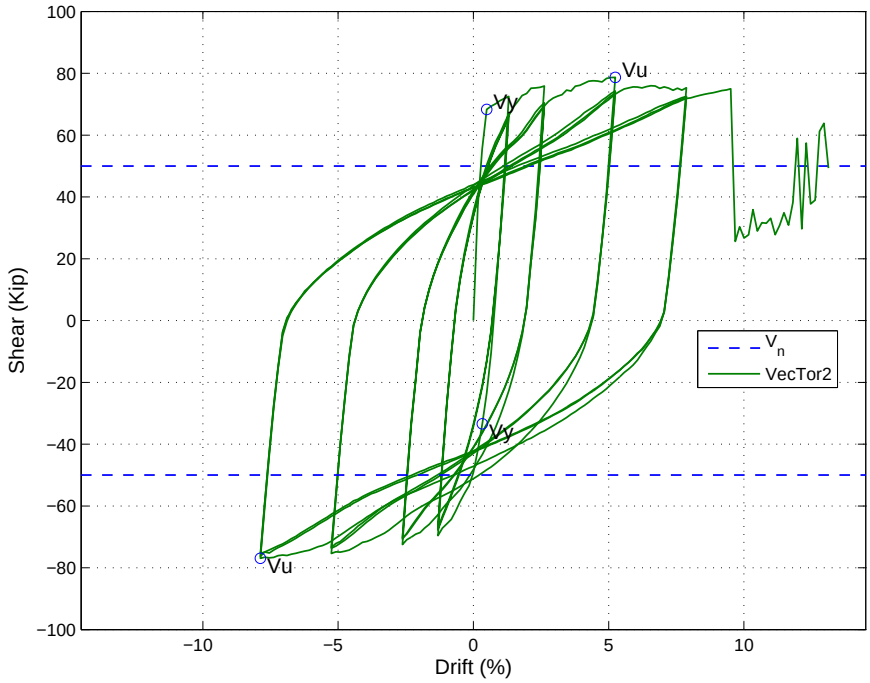

Figure 5.8: CBR-318H-F Load-Drift Response

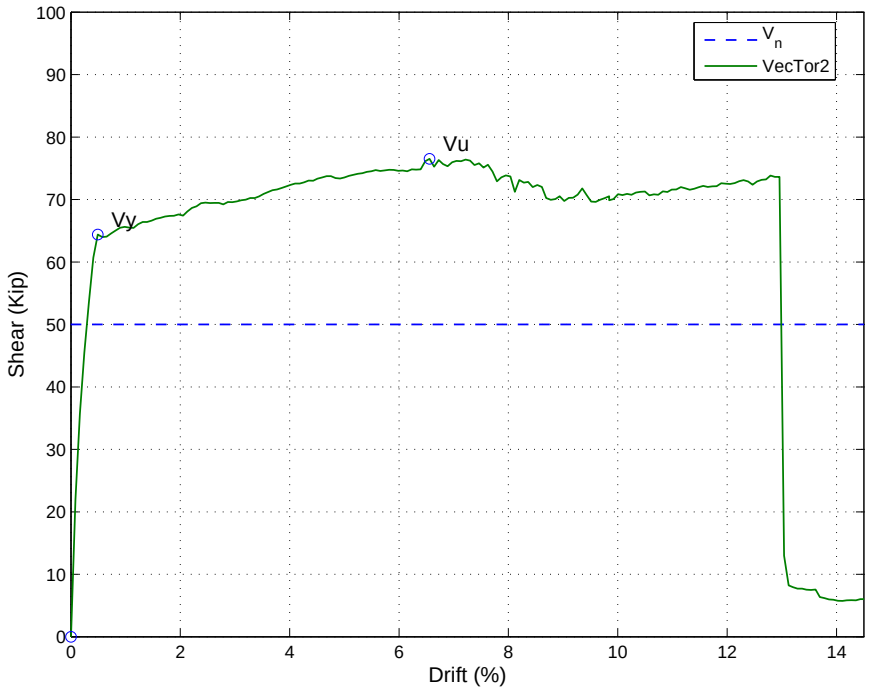

Figure 5.9: MCBR-318H-M Load-Drift Response

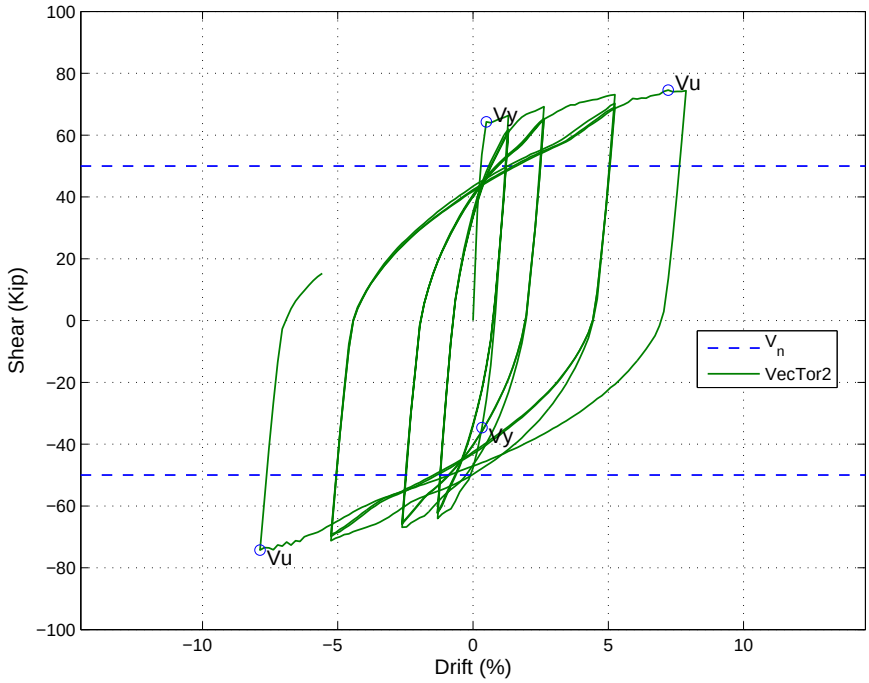

Figure 5.10: CBR-318H-M Load-Drift Response

Table 5.3: Coupling Beam Stiffness Results

Model	K_y	Δ_{Ref}	K_u	Δ_{Ref}	$K_{1.5\%}$	Δ_{Ref}	$K_{6.0\%}$	Δ_{Ref}
MCBR-ACI	455.9	0.00%	57.7	0.00%	185.9	0.00%	48.1	0.00%
MCBR-ACIS	546.6	19.91%	68.4	18.56%	196.6	5.74%	51.6	7.28%
MCBR-318H	465.9	2.20%	75.9	31.62%	187.9	1.06%	46.2	-3.77%
MCBR-318H-F	579.4	27.09%	46.0	-20.17%	207.3	11.51%	55.5	15.42%
MCBR-318H-M	545.6	19.70%	48.6	-15.71%	188.2	1.23%	51.3	6.68%
Average	518.7	13.78%	59.3	2.86%	193.1	3.91%	50.5	5.12%
CBR-ACI	401.3	0.00%	60.5	0.00%	173.9	0.00%	-	-
CBR-ACIS	546.6	36.22%	44.6	-26.26%	181.0	4.09%	46.6	-
CBR-318H	406.1	1.20%	61.9	2.21%	172.9	-0.57%	-	-
CBR-318H-F	580.0	44.54%	62.5	3.26%	195.1	12.23%	51.9	-
CBR-318H-M	545.9	36.02%	43.1	-28.84%	177.3	1.98%	49.2	-
Average	496.0	23.60%	54.5	-9.93%	180.0	3.55%	49.2	-

Stiffness (K) in K-in

Δ_{Ref} : *percentage change relative to reference model*

5.6.2 Stiffness

The secant stiffness of the coupling beams was calculated at yield, ultimate shear, 1.5% drift, and 6.0% drift and is summarized in Table 5.3. The average yield stiffness and ultimate stiffness are 507.3 and 56.9 K-in respectively. However, separating the couplings beams with ACI confinement (CBR-ACI, CBR-318H and CBR-ACI-S) from those with the proposed full confinement (CBR-318H-F and CBR-318H-M) shows that the ACI coupling beams have a lower average yield stiffness of 432.3 k-in and a higher average ultimate stiffness of 64.0 k-in, while the full confinement beams have a higher average yield stiffness of 562.7 k-in and a lower average ultimate stiffness of 50.0 k-in. The full confinement method results in a 23% higher yield stiffness and a 28% lower ultimate stiffness than the ACI confinement method.

It is useful to compare the predicted stiffness of the coupling beams at the expected performance level to the elastic stiffness. This comparison is referred to as the effective stiffness and is commonly used in preliminary analysis models to represent the cracked stiffness of an element in order to provide a more accurate distribution of forces throughout the structure. The elastic stiffness, K_{el}, was determined using a SAP2000 finite element model with nominal material properties and gross section dimensions. K_{el} is based on the concrete properties and dimensions and is independent of the reinforcement layouts, thus, it is the same for all variations of the coupling beam; $K_{el} = 1470.6K/in.$

For the ACI confined coupling beams, the average effective stiffness is 29% at yield and 4% at ultimate strength. For the full confinement coupling beams, the average effective stiffness is 38% at yield and 3% at ultimate strength. By comparison, following the recommended reduced member stiffness formulas from the Canadian and New Zealand design codes results in an effective stiffness of 17% and 14% respectively. The VecTor2 simulations suggest that the code recommendations are appropriate for representing the post-yield effective stiffness of the diagonally reinforced coupling beams.

5.6.3 Shear Force

The shear strengths were recorded at the first yield of diagonal reinforcement, ultimate shear, 1.5% drift, and 6.0% drift are summarized in Table 5.4.

The simulated strength of all the coupling beams at yield, V_y, is higher than the calculated design strength, V_n, per ACI 318-05. The average yield strength was 64.7 kips, compared to the design strength of 50 kips. The design strength in ACI is based on the observations of Paulay and Binney (1974) and is calculated with the following formula:

$$V_n = 2A_{vd}f_y sin\alpha \leq 10\sqrt{f'_c}b_w d$$

where:

A_{vd}**:** is the total area of reinforcement in each group of diagonal bars,

f_y**:** is the yield strength of the diagonal reinforcement,

α**:** is the angle between the diagonally placed bars and the longitudinal axis of the coupling beam,

$f_c^{'}$**:** is the compressive strength of the concrete,

b_w**:** is the width of the beam, and

d**:** is the distance from the extreme compression fiber to the centroid of the longitudinal tension reinforcement.

Paulay and Binney's research suggested a method for calculating the ultimate capacity of a diagonally reinforced coupling beam based on the assumption that after first yielding and load reversal the diagonal reinforcement will resist all the forces. Following this assumption, the shear resistance is the sum of the vertical force components of the diagonal bar in tension and in compression. At the ultimate strength it is assumed that the bars will be fully stressed in tension and compression, thus leading to the above formula for strength. The ACI code has assumed that the reinforcement does not gain any strength after yield; an elastic-perfectly-plastic steel model. This assumption allows the ultimate shear strength calculation of Paulay and Binney to apply at the yield point, and to be used as the design strength.

The following illustration of internal forces and moments are taken from the simulation of model CRB-ACI, however the resulting trend is similar for all the models. The VecTor2 simulations show that, at yield, the internal forces are not the same as the internal force mechanisms Paulay and Binney proposed for the ultimate state. At the yield point, the diagonal bars in tension have yielded, however the diagonal bars in compression are at approximately 95% of yield. At subsequent load cycles, the stress level in the compression bars continue to lag behind the tension bars by an average of 3 to 5%. At the displacement step where the tension bar reaches the yield stress, the tensile stress ends up being slightly

Table 5.4: Coupling Beam Strength Results

Model	V_y	Δ_{Ref}	V_u	Δ_{Ref}	$V_{1.5\%}$	Δ_{Ref}	$V_{6.0\%}$	Δ_{Ref}
MCBR-ACI	62.5	0.00%	71.4	0.00%	65.8	0.00%	70.0	0.00%
MCBR-ACIS	64.5	3.28%	76.7	7.36%	69.6	5.74%	75.1	7.29%
MCBR-318H	63.8	2.19%	70.1	-1.85%	66.5	1.06%	67.3	-3.76%
MCBR-318H-F	68.4	9.46%	81.5	14.11%	73.4	11.52%	80.8	15.42%
MCBR-318H-M	64.4	3.11%	76.5	7.08%	66.6	1.23%	74.6	6.69%
Average	64.7	3.61%	75.3	5.34%	68.4	3.91%	73.5	5.13%
CBR-ACI	62.9	0.00%	71.4	0.00%	61.5	0.00%	-	-
CBR-ACIS	64.4	2.38%	73.8	3.26%	64.1	4.20%	67.9	-
CBR-318H	63.7	1.24%	70.6	-1.20%	61.2	-0.55%	-	-
CBR-318H-F	68.3	8.53%	78.7	10.16%	69.1	12.31%	75.6	-
CBR-318H-M	64.3	2.18%	74.6	4.40%	62.8	2.08%	71.7	-
Average	64.7	2.87%	73.8	3.32%	63.7	3.61%	71.7	-

Strength (V) in Kips

Δ_{Ref} : *percentage change relative to reference model*

higher than 60 ksi while the stress in the compression bar is slightly lower than 60 ksi. As a result, the combined shear strength of the two diagonal bars matches the theoretical value calculated using the Paulay and Binney method. However, the strength of the diagonal bars only accounts for approximately 75% of the overall shear capacity of the coupling beam. Additional shear demand is developed by the flexural response of the beam through tensile yielding of the longitudinal reinforcement and compressive stress in the concrete. The moment developed by this couple has to be balanced by shear forces in the vertical reinforcement and shear stress in the concrete; this additional shear force accounts for the remaining 25% of the shear strength of the coupling beam. The coupling beams never reach the theoretical point where all of the resistance is provided by the diagonal reinforcement, there is always a contribution from the vertical reinforcement.

Table 5.5: Coupling Beam Strength vs. Reinforcement Ratio

Model	V_y	V_u	ρ_l	ρ_v
MCBR-ACI	62.5	71.4	0.31	0.27
CBR-ACI	62.9	71.4	0.31	0.27
CBR-318H	63.7	70.6	0.31	0.27
MCBR-318H	63.8	70.1	0.31	0.27
CBR-318H-M	64.3	74.6	0.28	0.56
MCBR-318H-M	64.4	76.5	0.28	0.56
CBR-318H-F	68.3	78.7	0.42	0.74
MCBR-318H-F	68.4	81.5	0.42	0.74

Strength (V) in Kips

The yield and ultimate shear strength, appear to be related to the amount of vertical and horizontal reinforcement. Sorting the coupling beams by their yield strengths reveals a positive correlation to the vertical reinforcement ratio as indicated in Table 5.5. A larger vertical reinforcement ratio resulted in a higher yield force. There is a similar relationship between the horizontal reinforcement ratio, with exception of the 318H-M model. However the difference in the longitudinal reinforcement ratio and the shear strength between models ACI, 318H and 318H-M is so small, only 3%, that the relationship is not clearly discernible. Due to the effects of the additional top steel, model CBR-ACI-S has been excluded from this comparison, as it is considered significantly different from the rest of the coupling beams.

5.6.4 Displacement and Drift

The vertical displacements and coupling beam drifts were noted at the first yield of diagonal reinforcement and at the ultimate strength. The displacements, drifts, and displacement ductility are summarized in Table 5.6. The yield drift was very consistent across all of the coupling beams. The average yield drift was 0.5%, with a small standard deviation of 0.07%. However at the drift at the ultimate strength point showed a clear separation between

Table 5.6: Coupling Beam Drift Results

Model	Δ_y	Δ_{Ref}	Δ_u	Δ_{Ref}	μ_u	Δ_{Ref}	$\Delta_{0.85V_u}$
MCBR-ACI	0.57%	1.0	5.16%	1.0	8.9	1.0	6.90%
MCBR-ACIS	0.49%	0.9	4.68%	0.9	9.3	1.1	9.00%
MCBR-318H	0.57%	1.0	3.85%	0.7	6.6	0.7	7.40%
MCBR-318H-F	0.49%	0.9	7.38%	1.4	14.8	1.7	10.75%
MCBR-318H-M	0.49%	1.0	6.56%	1.0	13.1	1.0	12.97%
Average	0.52%	0.9	5.53%	1.0	10.5	1.1	9.40%
CBR-ACI	0.65%	1.3	4.92%	0.8	7.4	0.6	5.21%
CBR-ACIS	0.49%	1.0	6.89%	1.1	13.8	1.1	-
CBR-318H	0.65%	1.3	4.75%	0.7	7.1	0.5	5.18%
CBR-318H-F	0.49%	1.0	5.25%	0.8	10.5	0.8	9.49%
CBR-318H-M	0.49%	1.0	7.22%	1.1	14.4	1.1	-
Average	0.55%	1.1	5.81%	0.9	10.6	0.8	6.63%

Δ_{Ref} : *percentage change relative to reference model*

the ACI confinement and the full confinement methods. The coupling beams with ACI confinement had an average ultimate drift of 4.7% while the average for the full confinement coupling beams was 6.6%. These ultimate displacements result in an average displacement ductility of 7.5 for the ACI confinement and and 13.2 for the full confinement method. These results suggest that the full confinement method can provide better confinement of the coupling beam and allow it to behave in a more ductile manner in the post-yield region.

5.7 Comparison of Confinement Variations

5.7.1 CBR-ACI vs. CBR-318H

Figure 5.11 shows a comparison between the monotonic load-drift response of the reference model , (MCBR-ACI), and the reduced tie spacing model, (MCBR-318H). Figure 5.12 shows a similar comparison between the cyclic simulations. The ACI 318H-CH047 reduced spacing proposal, model ACI-318H, shows only a slight reduction in displacement ductility and provides essentially the same ultimate strength capacity. These results suggest that the reduced spacing requirements can provide equivalent confinement of the diagonal reinforcement to that of the current ACI specifications with only a minimal reduction in displacement ductility capacity at the point when the shear force drops below 85% of V_u in the monotonic simulations. The cyclic simulations do not show any significant reduction in displacement or shear force capacity.

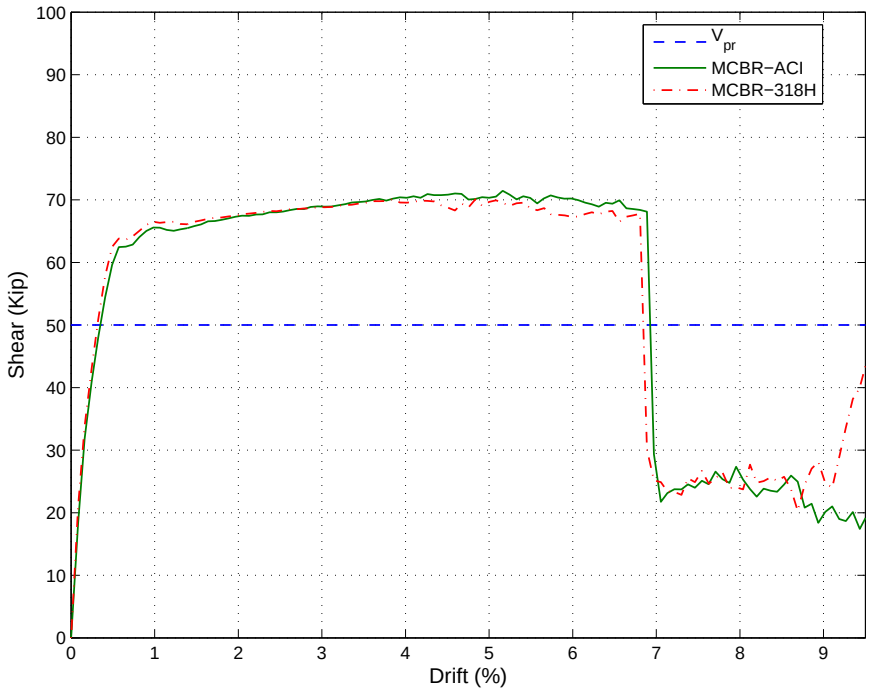

Figure 5.11: MCBR-ACI vs. MCBR-318H Load-Drift Response

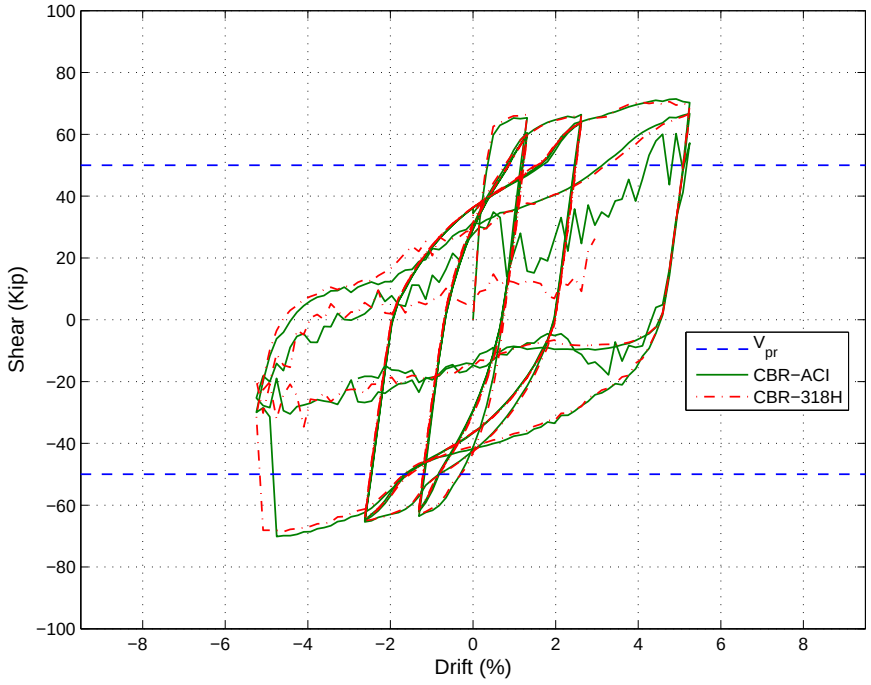

Figure 5.12: CBR-ACI vs. CBR-318H Load-Drift Response

5.7.2 CBR-ACI vs CBR-318H-F

Figure 5.13 shows a comparison between the monotonic load-drift response of the reference model , (MCBR-ACI), and the full confinement model, (MCBR-318H-F). Figure 5.14 shows a similar comparison between the cyclic simulations.

The ACI 318H-CH047 full confinement proposal, model ACI-318H-F, shows a significant increase in yield strength, ultimate strength, and displacement ductility when compared to the base ACI design. In addition to the increased displacement ductility, the VecTor2 output was much smoother at larger deformations than that of the ACI design. The increase in displacement ductility and stability of the model can be attributed increased area of fully confined concrete. Confining the whole section results in a larger spread of the tensile strains and increased crack distribution over the entire coupling beam, as shown in the comparison of the crack patterns at 5.25% drift (the ultimate drift capacity of M+CBR-ACI) of both models in Figures 5.15 and 5.16.

The increase in yield and ultimate strength can be attributed to the increase in both vertical and horizontal reinforcement ratios, as discussed in Section 5.6.3. While this may seem a welcome improvement, use of full confinement on coupling beams in performance-based designs should be used cautiously until a reliable method for predicting the actual strength can be developed.

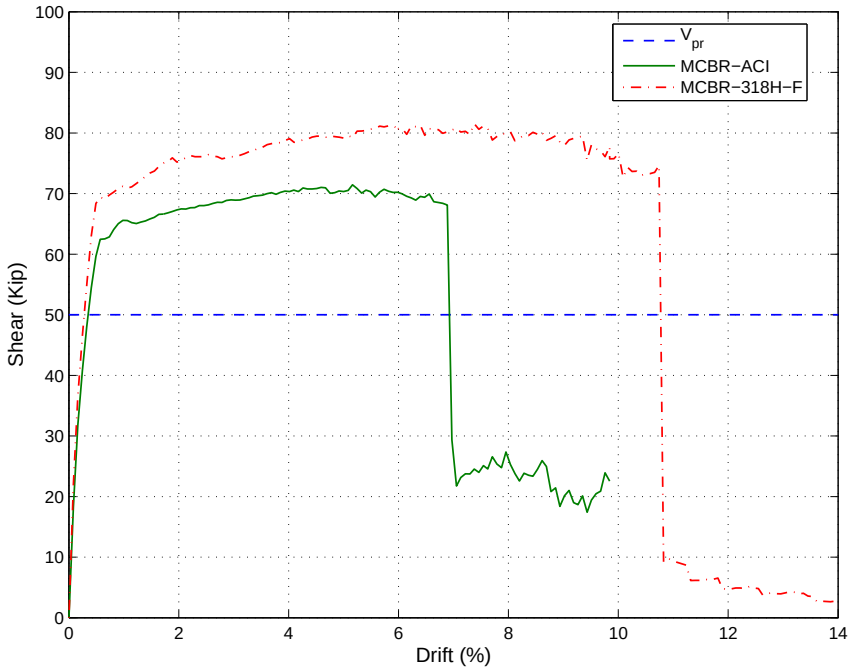

Figure 5.13: MCBR-ACI vs. MCBR-318H-F Load-Drift Response

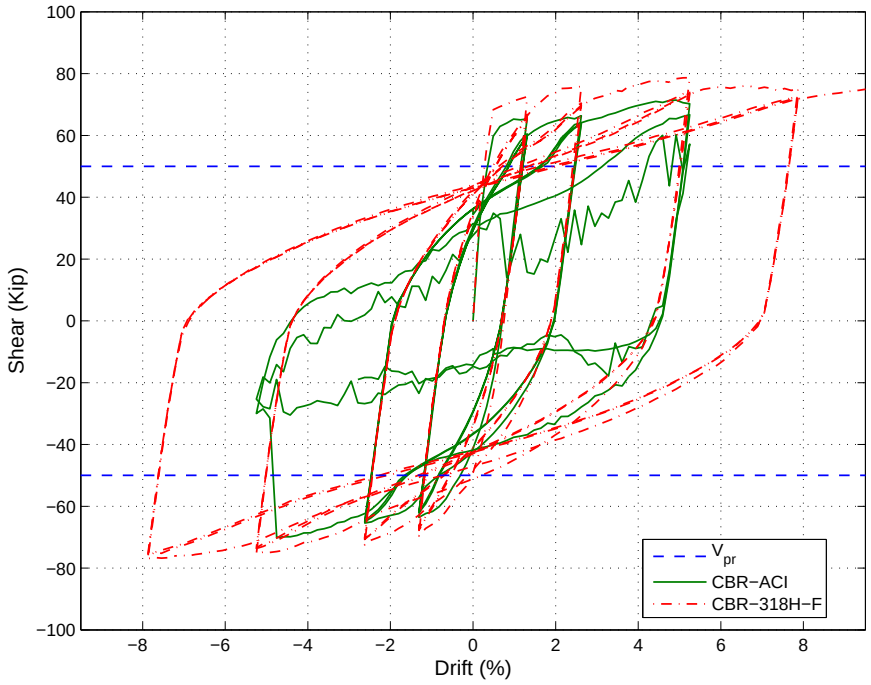

Figure 5.14: CBR-ACI vs. CBR-318H-F Load-Drift Response

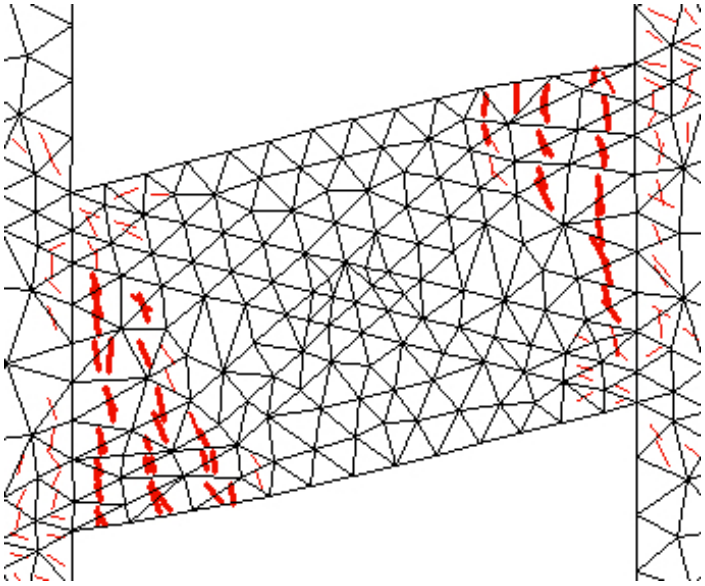

Figure 5.15: CBR-ACI Crack Distribution at 5.25 % drift

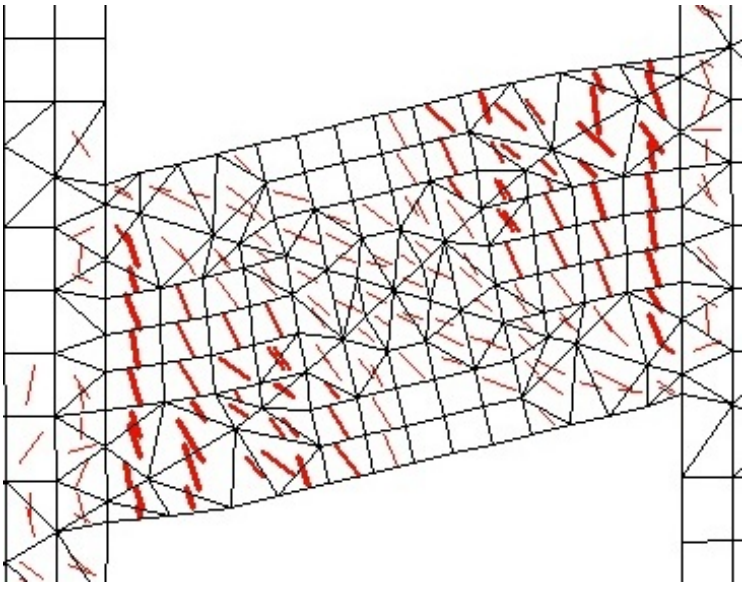

Figure 5.16: CBR-318H-F Crack Distribution at 5.25 % drift

5.7.3 CBR-ACI and CBR-318H-M

Figure 5.17 shows a comparison between the monotonic load-drift response of the reference model, (MCBR-ACI), and the modified full confinement model, (MCBR-318H-M). Figure 5.18 shows a similar comparison between the cyclic simulations. The strength of model MCBR-318H-M begins to degrade at approximately 7.3% drift due to crushing of the concrete at the ends of the coupling beam. The shear stress capacity is reduced and the model begins to loose shear force, then at 8.33% drift the shear force begins to increase again as the tensile stress in the diagonal reinforcement continues to strain harden.

The two models have nearly the same response up to the yield point and both yield at a very similar force (62.5 and 64.4 kips), however the full confined model (MCBR-318H-M) continues to gain strength and is able to undergo nearly twice the deformation. Both models have the same diagonal reinforcement and have very similar longitudinal reinforcement ratios (0.31% vs. 0.28%), thus resulting in their similar yield strength. The full confinement of model MCBR-318H-M allows the model to undergo larger displacements than the reference specimen which allows the diagonal reinforcement to reach higher strains and results in a larger ultimate shear force. The increase in the vertical reinforcement also allows for the cracking to be well distributed throughout the model, as discussed in the previous section.

5.8 Conclusions

VecTor2 simulations of the coupling beam confinement variations supports the following conclusions.

- The VecTor2 simulations suggest that an effective stiffness between approximately 5% and 30% would be appropriate to use in an elastic model to represent the post-yield stiffness of diagonally reinforced coupling beams. A decision to use a lower effective stiffness should be used with the understanding that it represents a higher level of expected damage to the coupling beam.

- The ACI 318H-CH047 proposed revision to the spacing requirements on the closed

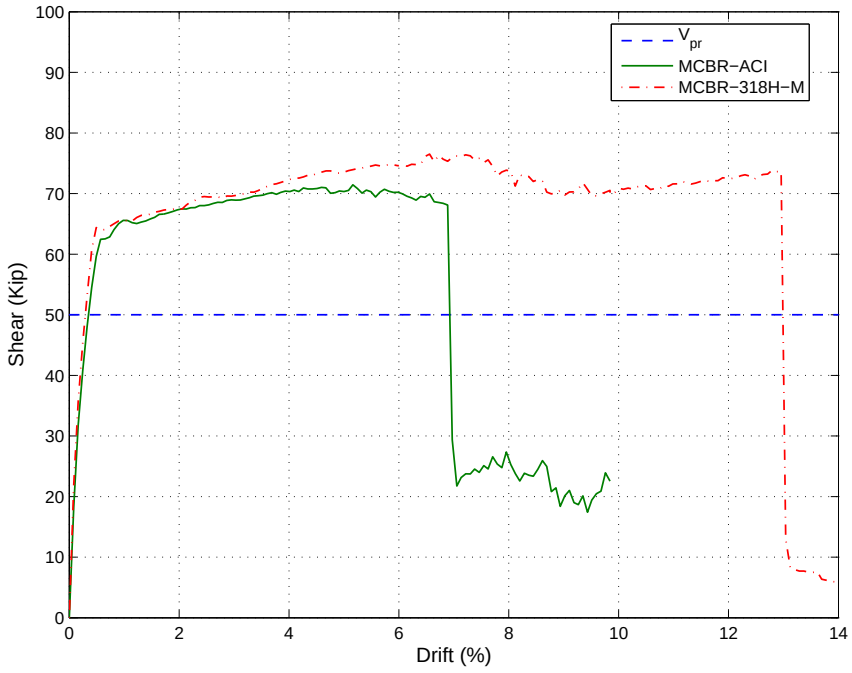

Figure 5.17: MCBR-ACI vs. MCBR-318H-M Load-Drift Response

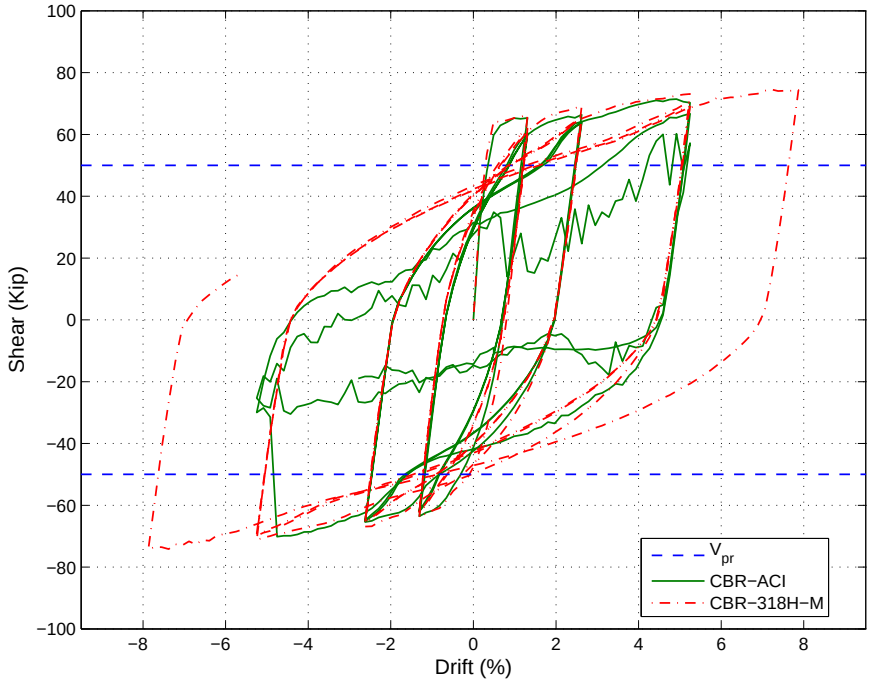

Figure 5.18: CBR-ACI vs. CBR-318H-M Load-Drift Response

ties around the diagonally placed reinforcement will have a negligible effect on the performance of the coupling beam. It is capable of providing an adequate level of confinement so as to allow the coupling beam to reach essentially the same displacement ductility and shear strength as the current ACI 318-05 specifications.

- The ACI 318H-047 full confinement proposal results in a 9% average increase in the shear strength at yield and a 12% average increase in the ultimate strength. It increases the average drift from 4.67% to 6.60% resulting in an increase in 76% increase in the displacement ductility from 7.5 to 13.2. VecTor2 simulations of coupling beams designed to meet the ACI 318H-CH047 proposal suggests that the performance of diagonally reinforced coupling beams can be improved by providing full confinement of the entire section.

- The ACI method for calculating the shear strength of a diagonally reinforced coupling beams tends to be less than that predicted using VecTor2 finite element simulations. The ACI method notes that the "diagonally placed bars shall be considered to contribute to M_n of the coupling beam", indicating that the flexural strength of the coupling beam is affected by both the longitudinal and diagonal reinforcement. However, only the diagonal reinforcement is allowed to be used in calculating the shear strength of the coupling beam, resulting in an under-estimation of the true strength of the beam. The intent of these specifications is to ensure that the diagonally reinforced coupling beams will be flexural controlled, however it is not specified that the shear strength be checked against the plastic shear demand of $V_p = 2M_p/L$.

- The ACI 318H-CH047 full confinement proposal will result in coupling beams with higher longitudinal and vertical reinforcement ratios in order to meet the confinement and spacing requirements. While this additional steel will provide confinement of the entire section, it will also increase the flexural and shear strength of the coupling beam. Before this proposal is improved the method for calculating the shear strength

needs to be revised to reflect the shear strength due to the additional reinforcement.

Chapter 6

COUPLED WALL DESIGN AND ANALYSIS

6.1 Objective

Performance based design methods are intended to produce a coupled wall that will behave in a ductile manner and allow for the maximum distribution of energy dissipation during lateral loading. By assuming a plastic mechanism in the wall, the maximum plastic shear demand at the base of the wall can be determined and adequate reinforcement provided to meet the demand. However, the validity of this design method is dependent upon the assumption that the assumed plastic mechanism will occur in the wall.

Through nonlinear continuum analysis, the plastic mechanism in the wall can be simulated and compared to the design assumptions. Additionally, the effects of vertical load distribution and coupling beam strength can easily be explored. For this study, the VecTor2 software was used to simulate the response of the ten-story coupled wall specimen. Modeling decisions, results, parameter studies, and comparisons between simulated response and assumed design parameters are presented.

6.2 Current Design Methods Background

6.2.1 Code Design

The coupled wall design in this study follows the requirements of the current building code, International Building Code 2006 (IBC), which is based on the general building code requirements of ASCE 7-05. For structural concrete design, ASCE 7-05 references the American Concrete Institute Building Code (ACI 318-05). ACI 318-05 contains the detailed requirements and limitations upon any design.

The basic code design for a coupled shear wall is a multi-step process that follows the

following steps:

1. Determine initial geometry of wall and estimate of element thicknesses.

2. Determine global demand for vertical and lateral forces based on the International Building Code (IBC) requirements.

3. Equivalent elastic analysis using effective stiffness values for each component to determine the force demands within the wall. Typically shear walls are modeled using finite element analysis software such as SAP2000 or Etabs. ACI and IBC do not give any recommendations for the effective stiffness values, engineers typically rely on experience and judgement, however, the New Zealand (NZS 3101-2006) and the Canadian (CSA A23.3 - 2004) do provide recommendations for effective stiffness values of coupled shear wall components.

4. Complete a strength based design to meet the ACI 318-05 requirements.

5. Provide ACI 318 code compliant reinforcement details.

While this design process will meet the requirements of the code and provide the minimum safety and stability standards, it is based on the elastic response and empirical design expressions and therefore does not address the post-elastic behavior or provide an understanding of, or design for, the expected performance when subjected to seismic forces.

6.2.2 2006 IBC Structural/Seismic Design Recommendations

The International Code Council (ICC) recently published the 2006 IBC Structural/Seismic Design Manual. This document provides design examples for reinforced concrete walls that follow the ACI 318 code requirements and it provides a recommended plastic analysis and design method. A plastic analysis is not required, but can be useful in establishing the shear demand corresponding to the flexural strength of the wall and coupling beams, and to identify potential plastic hinge regions.

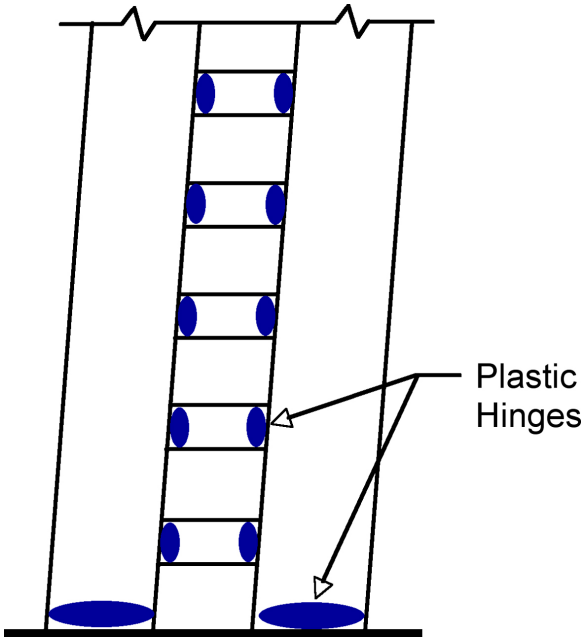

Figure 6.1: Assumed Coupled Wall Plastic Mechanism

A plastic analysis can be conducted after the initial design of the wall for elastic forces has been completed. The plastic analysis method involves determining the probable moment strength, choosing a plastic mechanism, evaluating the shear strength of the plastic mechanism. These steps are detailed below:

1. Determine the plastic mechanism. A wall could have more than one plastic mechanism depending on the relative strengths of the components and the distribution of loads within the wall. The effect of different mechanisms should be determined and the one the results in the highest plastic demand should be chosen. For a coupled wall, the IBC states that the preferred plastic mechanism includes plastic hinges at the base of the wall piers and at the end of each coupling beam, shown in Figure 6.1. This mechanism allows for flexural yielding, maximum energy dissipation, and the avoidance of brittle shear failures.

2. Determine the probable moment strength, M_{pr}, of the coupled wall components. The probable moment strength is the maximum design strength of a reinforced concrete element detailed for seismic design. M_{pr}, as defined by ACI 318 §21.0, is calculated assuming a tensile stress in the longitudinal reinforcement of $1.25f_y$, and a strength reduction factor, ϕ, of 1.0. This strength is required for each plastic hinge location.

3. Determine the plastic shear demand at the base of the wall. A plastic shear demand is created at the base of the wall as a result of the flexural strengths at each of the plastic hinge locations. The magnitude can be determine by equating the sum of the external work to the sum of the internal work. The external work calculated as the sum of the story forces, f_{xi}, times the story displacements, Δ_i. The story forces and displacements are taken from the elastic analysis completed for the initial design. The internal work is calculated as the sum of the M_{pr} times the θ for the coupling beams and the base wall piers.

4. Design for the plastic shear demand. Once the plastic analysis has been completed the shear reinforcement at the base of the wall must be designed to ensure that the wall piers have sufficient shear strength to enable the plastic hinges throughout the wall to form.

6.3 Design of Coupled Wall Specimen

To design a coupled shear wall that is representative of current design practices, an external advisory board of practicing engineers was consulted and construction drawings of recent reinforced concrete shear wall buildings were reviewed. The building inventory, introduced in Chapter 2, consisted of thirteen coupled walls from four buildings designed using UBC 1991 to 1997 for construction on the West Coast. Based upon the discussions with the external advisors and the existing building review, the following initial assumptions and specifications were made for the coupled wall specimen:

- One-third scale wall geometry as shown in Figure 6.2

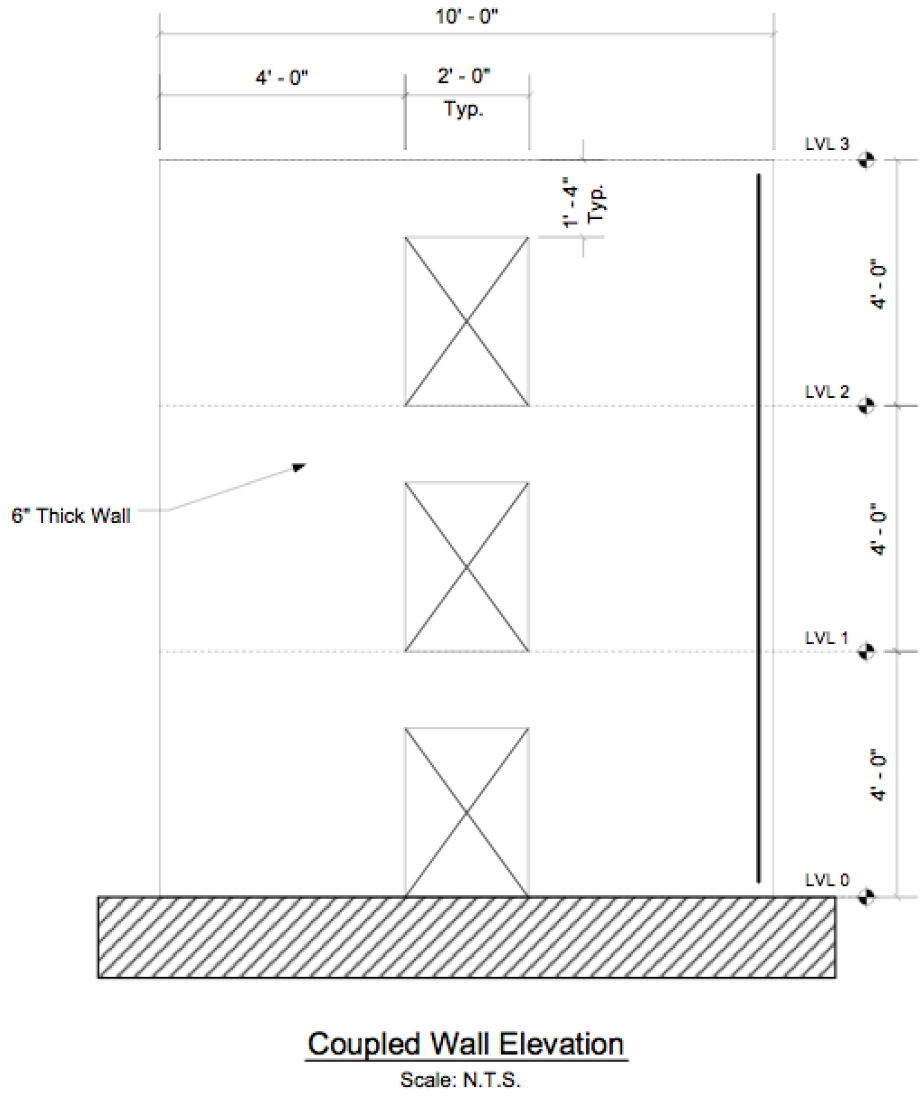

Figure 6.2: Coupled Wall Dimensions

- Coupling beam aspect ratio of 1.5
- Concrete specified compressive strength of $5000psi$
- Reinforcement specified yield strength of $60ksi$
- Wall axial load equal to $0.1A_g f_c$
- Coupling beam diagonal reinforcement ratio approx. $= 0.87\%$

Given these initial assumptions, the following process was used to complete the design of the coupled wall specimen: The coupled wall specimen was designed to meet the current code and to follow the 2006 IBC Seismic Design Manual. The experimental coupled wall specimen will represent only the lower three stories of the wall. The steps involved and resulting design are presented in the following sections.

6.4 Strength Design

The following steps were taken to design the coupled shear wall specimen for the elastic force demand.

1. Determine the nominal shear strength of the wall corresponding to the minimum allowable shear reinforcement, V_n, per ACI 318-05.

$$V_n = A_{cv}(2\sqrt{f'_c} + \rho f_y)$$

$$V_n = 167.9K, \rho_h = 0.27\%$$

2. Determine the shear demand, V_u given the ACI 318-05 requirement of $\phi V_n > V_u$ with $\phi = 0.60$. This shear demand takes the place of the seismic base shear in a typical design process.

$$V_u = 100.7K$$

3. Create an elastic 2D shell element model using SAP2000. The effective EI for the coupling beams was taken as $0.10EI_{gross}$ and the EI for the walls was taken as $0.70EI_{gross}$, both within the ranges recommended by the New Zealand and Canadian building codes.

4. Determine the flexural and shear demands at the base of the wall and ends of the coupling beams using an inverted triangular vertical distribution of the lateral load per ASCE 7-05.

5. Design the reinforcement for the coupling beams. The code requires that diagonal reinforcement be provided in coupling beams where the shear demand exceeds $4\sqrt{f'_c}A_{cw}$. As shown in Table 6.1 $V_u/b_w h\sqrt{f'_c}$ is greater than 4 in seven of the ten coupling beams. To focus on the behavior of diagonally reinforced coupling beams, diagonal reinforcing was used in all of the coupling beams. The capacity of the coupling beams was checked per ACI 318-05 to achieve $\phi V_n > V_u$, per ACI 318-05 §9.3.4, where:

   V_u = maximum shear force in coupling beam from SAP2000 analysis

   $\phi V_n = 2\phi f_y sin\alpha A_d$

   $\phi = 0.85$

   α = angle of diagonal reinforcement with longitudinal axis of coupling beam, as shown in Figure 5

   A_d = total area of one group of diagonal bars

6. Design the wall piers for flexure per ACI 318-05 to achieve $\phi M_n > M_u$, where:

   M_u = maximum moment demand from the SAP2000 elastic analysis

   M_n = flexural strength of wall piers determine using flexural design theory.

   $\phi = 0.9$

   Table 6.2 shows the pier forces from the elastic analysis and the design strengths.

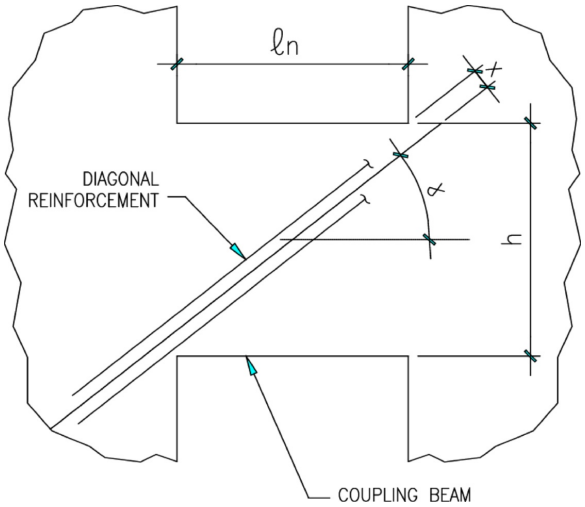

Figure 6.3: Geometry of coupling beam diagonal bars (ICC 2007)

Table 6.1: Coupling beam forces and diagonal reinforcement

Level	V_u $(kips)$	$V_u/A_g\sqrt{f'_c}$ (in)	*Diagonal Bars*	A_d (in^2)	ρ_d	θ $(degrees)$	ϕV_n $(kips)$	$V_u/\phi V_n$
10th	19.3	2.8	4-#4	0.8	0.83%	31.4	42	0.45
9th	24.1	3.6	4-#4	0.8	0.83%	31.4	42	0.57
8th	28.4	4.2	4-#4	0.8	0.83%	31.4	42	0.67
7th	32.9	4.8	4-#4	0.8	0.83%	31.4	42	0.77
6th	36.8	5.4	4-#4	0.8	0.83%	31.4	42	0.87
5th	39.6	5.8	4-#4	0.8	0.83%	31.4	42	0.93
4th	40.5	6.0	4-#4	0.8	0.83%	31.4	42	0.95
3rd	38.5	5.7	4-#4	0.8	0.83%	31.4	42	0.91
2nd	32.3	4.8	4-#4	0.8	0.83%	31.4	42	0.76
1st	19.6	2.9	4-#4	0.8	0.83%	31.4	42	0.46

Table 6.2: Calculation of factored axial forces and moments on wall piers

Level	*Pier*	A_g (in^2)	P_D* (k)	P_E (k)	P_{umin} (k)	P_{umax} (k)	M_u $(k-ft)$	ϕM_n $(kips)$	$M_u/\phi M_n$
1st	A	288	144	-311.9	-206.3	-115.1	501.0	163	3.07
1st	B	288	144	311.9	417.5	508.7	501.0	904	0.55
						Sum	1002.0	1067	0.94**

*(Assumed $0.1A_g f_c^{'}$)

**Total $\phi M_n > M_u$, moment redistribution assumed

6.5 Recommended Plastic Design

As previously mentioned, the the 2006 IBC Seismic Design Manual recommends that a plastic analysis be completed. The following steps detail the recommended plastic analysis process and subsequent redesign of the wall piers.

1. Assume a behavior mechanism with plastic hinging at the base of the wall piers and at each end of all the coupling beams as shown in Figure 6.1.

2. Determine the probable flexural strength, M_{pr}, of the coupling beams and piers. The IBC example ignores the effect of axial loads on the wall piers due to seismic forces; making the assumption that the increase in moment strength of the compression pier and the decrease in moment strength of the tension pier will offset one another. While in some cases this may be true, it is not always correct. In the plastic analysis of the coupled wall for this study, the effect of axial loads due to seismic forces was significant and was therefore included in the determination of M_{pr}. For the wall piers M_{pr} was determined based on a moment curvature analysis of the pier section using $1.25f_y$ and included the axial force due to gravity and seismic loads. For the coupling beams M_{pr} was calculated as $1.25V_n l_n/2$, assuming $1.25f_y$ and only accounting for the contribution from the diagonal reinforcement. This method ignores the effect of

additional longitudinal reinforcement that may be present in the beam to support the stirrups and/or to provide skin reinforcement, however it is consistent with method used to initially design the coupling beam.

3. Evaluate the plastic mechanism using internal vs. external work to determine the plastic shear demand at the base of the wall.

   The external work is calculated as the sum of the story displacement, δ_i, times the story force, f_{xi} as shown in Table 6.3. Plastic story displacements increase linearly from the base to the top of the wall with he magnitude of δ_{roof} set to 2% at the roof. The magnitude of the story displacements is arbitrary and will not change the output. The story forces come from the code specified vertical distribution.

   The internal work is calculated as the sum of the probable moment strength, M_{pr}, times the plastic rotation angle, θ, for the coupling beams and the base wall piers as shown in Table 6.4. The plastic rotation angle of the wall piers equals the roof displacement divided by the roof height above the midpoint of the plastic hinge. The plastic hinge length of the piers is assumed to be the wall length over two, $l_p = l_{w/2}$, in this case $2ft$. The plastic rotation angle of the coupling beams is calculated as follows:

$$\theta_{cb} = \theta \frac{l_c}{l_n}$$

   where:

   l_n = the clear length of the coupling beams

   l_c = the distance between centroids of the wall piers

   Assuming M_{pr} of the coupling beams equals $1.25V_n l_n/2$, the internal work for each coupling beam (counting both ends), can be calculated as $\theta 1.25V_n l_c$.

   Equating the internal work with the external work provides the base shear, or the plastic shear demand. The calculations have are shown for the method of ignoring

Table 6.3: Plastic mechanism calculations - External Work

External Work						
Level	h_i (ft)	$h_i - l_p/2$ (ft)	δ_i (ft)	f_{xi} (k)	f_{xi}/V	$Work/V$ (ft)
10th	40	39	0.80	22.3	0.22	0.18
9th	36	35	0.72	15.5	0.16	0.11
8th	32	31	0.64	13.8	0.14	0.09
7th	28	27	0.55	12.1	0.12	0.07
6th	24	23	0.47	10.4	0.10	0.05
5th	20	19	0.39	8.6	0.09	0.03
4th	16	15	0.31	6.9	0.07	0.02
3rd	12	11	0.23	5.2	0.05	0.01
2nd	8	7	0.14	3.5	0.04	0.01
1st	4	3	0.06	1.7	0.02	0.00
Sum		210		100	1.00	0.57

earthquake axial and including it. In this case, including the earthquake axial forces resulted in a base shear of $191.0k$, approximately 5% less than if it had been ignored.

4. Compare the plastic shear demand with the nominal shear strength, ϕV_n, and adjust the shear reinforcement to ensure flexural behavior in the wall. In this case, the plastic shear demand was 190% of the initial shear demand used to design the wall. The horizontal reinforcement in the first floor piers had to be doubled to $\rho = 0.54\%$ in order to meet the increased shear demand.

The plastic analysis and design method resulted in an increase amount of shear reinforcement in the wall piers in he first level only, all other wall reinforcement remains per the strength design. The final reinforcement layout shown in Figure 6.4.

6.6 Coupling Beam Reinforcement Details

The coupling beam confinement reinforcing was designed using two different approaches, the current ACI 318 requirements and the proposed method from ACI Committee 318H-CH047.

Table 6.4: Plastic mechanism calculations - Internal Work

Internal Work, Coupling Beams

Level	$1.25V_n$ (k)	L_c (ft)	$Work$ $(k-ft)$
10th	62.4	6	7.7
9th	62.4	6	7.7
8th	62.4	6	7.7
7th	62.4	6	7.7
6th	62.4	6	7.7
5th	62.4	6	7.7
4th	62.4	6	7.7
3rd	62.4	6	7.7
2nd	62.4	6	7.7
1st	62.4	6	7.7
Sum	624.4		76.9

Internal Work, Wall Piers $\theta_w =$ 0.0205

			Work (k-ft)	
Pier	*Level*	$M_{pr}(k-ft)$	*No EQ*	*EQ*
A	Base	893.0	18.3	-
B	Base	893.0	18.3	-
A	Base	450.00	-	9.2
B	Base	1075.00	-	22.1
		Sum	36.6	31.3

Plastic Shear Demand

V_{pl} = *(Internal/External Work)*	200.5	(k)	*Ignoring EQ Axial*
V_{pl} = *(Internal/External Work)*	191.0	(k)	*Including EQ Axial*
V_u = *(From min. horiz. steel)*	109.2	(k)	
$V_{pl}/V_u =$	1.90		

The current ACI 318-05 code requires that each group of diagonally place bars be confined per §21.4.4.1 through §21.4.4.3. Following these sections results in #2 ties at 2" O.C. along the diagonal bars and #2 ties at 6" O.C. around the entire beam section.

The alternative design procedure of proposal 318H-CH047 allows for the entire coupling beam section to be confined instead of providing confinement around each diagonal bar group. Following this design method results in #2 ties at 1 1/2" O.C. around the entire beam section. Additional cross ties are required to meet the minimum cross sectional reinforcement area, A_{sh}, and to satisfy the 8 inch spacing limit for cross-ties.

The two confinement options are shown in Figure 6.5 for the third scale coupling beam.

6.7 Coupled Wall Model Variations

A finite element model of the full ten-story coupled shear wall was created in VecTor2 at one-third scale. Three variations of the wall were modeled, each with different coupling beam reinforcement. The wall was modeled with coupling beams CBR-ACI, CBR-318H-F, and CBR-318H-FR. A brief description of the coupling beams is presented here.

CBR-ACI This coupling beam is designed to meet the current ACI 318-05 code requirements. It contains diagonal reinforcing bars that are have confinement reinforcement around each group of diagonal bars.

CBR-318H-F This coupling beam was detailed per ACI 318H-CH047 which will be published in the 2008 version of the ACI code. It has the same diagonal reinforcing bars as CBR-ACI, and thus the same design strength. However, in this design, confining reinforcement is placed around the entire beam rather than just around he diagonal bar groups.

CBR-318H-FR This coupling beam is designed to have a flexure/shear strength that is 25% of CBR-318-HF. his coupling beam design was included because analysis of coupled wall CW-318HF with coupling beam CBR-318-HF indicated that the coupling

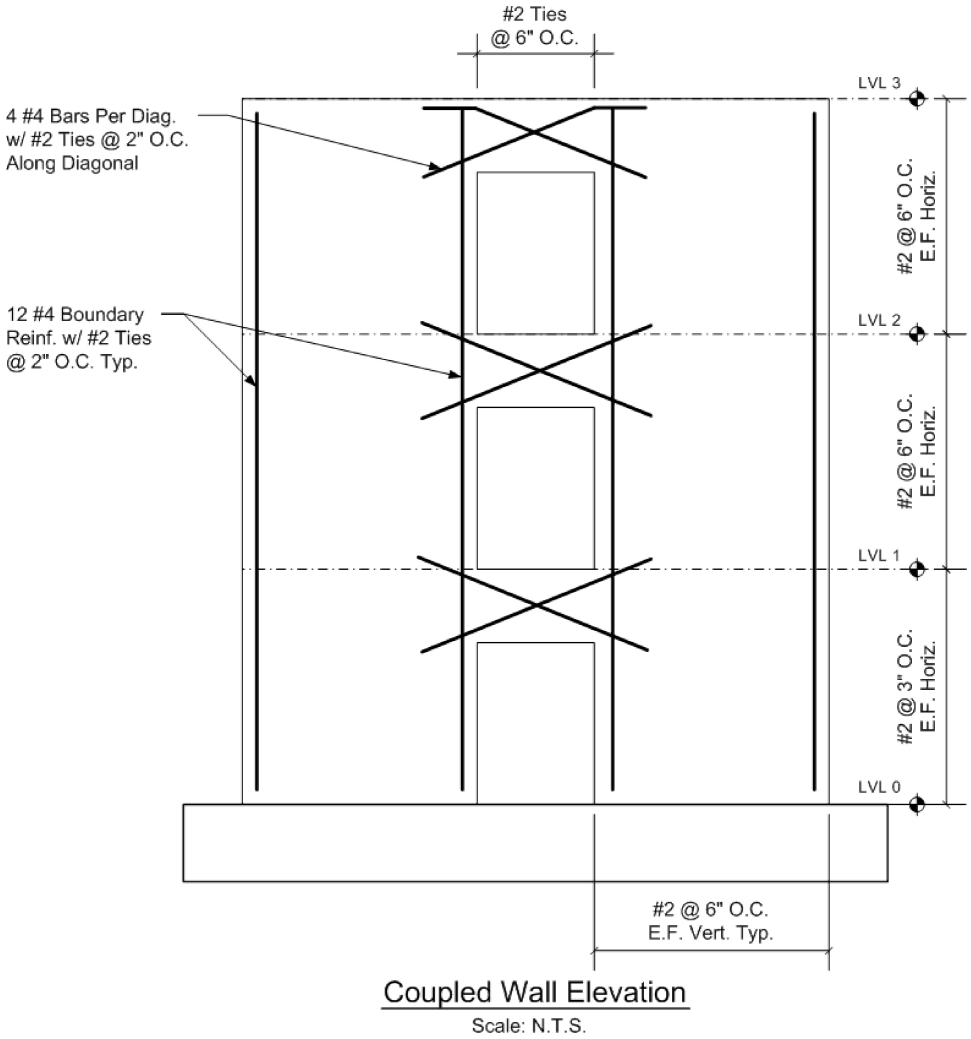

Figure 6.4: Coupled Wall Reinforcement from Plastic Design

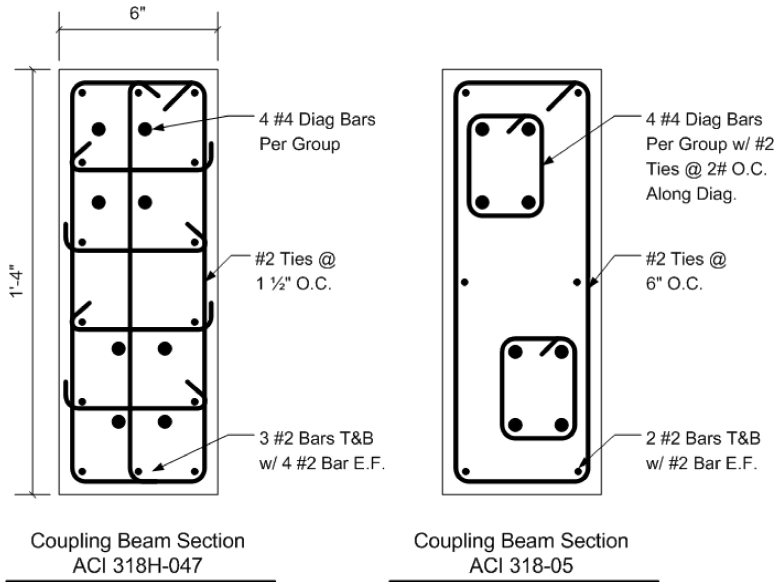

Figure 6.5: Coupling Beam Details

beams were not yielding and the assumed plastic mechanism was not being developed. The amount of diagonal reinforcement in CBR-318H-FR was reduced from that in CBR-318HF so that coupling beams would yield when the design level base shear, V_n, was applied. The 75% reduction in strength was done by determining the tensile stress demand in the diagonal bars of CW-318HF at the design level base shear and then reducing the area of steel so that resulting force would be the same but the bars would be at the yield stress level.

The three coupled wall models were identified as CW-ACI (includes coupling beam CBR-ACI), CW-318HF (includes coupling beam CBR-318H-F), CW-318HFR (includes coupling beam CBR-318H-FR). Details of the coupling beam designs and their expected performance is presented in Chapter 5. Table 6.5 shows a summary of the reinforcement ratios for the three coupled wall variations.

Table 6.5: Coupled Wall Reinforcement Ratios

Wall Pier Reinforcement

	Boundary Elements			Web		
	$\rho_b(\%)$	$\rho_h(\%)$	$\rho_t(\%)$	$\rho_v(\%)$	$\rho_h(\%)$	$\rho_t(\%)$
1st Flr	3.64	0.82	0.54	0.27	0.54	0
Upper Flrs	3.64	0.82	0.54	0.27	0.27	0

Coupling Beam Reinfocement Variations

	Ortagonal Bars			Diagonal Bars		
	$\rho_l(\%)$	$\rho_v(\%)$	$\rho_t(\%)$	$A_d(in^2)$	$\rho_{dt}(\%)$	$\rho_{dv}(\%)$
CBR-ACI	0.31%	0.27%	0.10%	0.80	1.63%	3.27%
CBR-318HF	0.42%	0.74%	0.74%	0.80	-	-
CBR-318HFR	0.11%	0.74%	0.74%	0.20	-	-

6.8 Modeling Decisions

The following sections discuss the modeling decisions made in creating the VecTor2 (ref) models of the walls.

6.8.1 Constitutive Models

The same constitutive models and analysis parameters we were used to model the coupling beam experiments were used for the coupled walls (Chapter 4). A summary of these is provided in Table 6.6.

6.8.2 Element Mesh

Due to the large size of the ten-story wall, the mesh generation was limited by the number of nodes and elements allowed in by VecTor2. The element discretization was prioritized

Table 6.6: VecTor2 Constitutive Models and Analysis Parameters

Constitutive Behavior	Model
Compression Base Curve	Popovics (NSC)
Compression Post-Peak	Popovics / Mander
Compression Softening	Vecchio 1992-B (e1/e0-Form)
Tension Stiffening	Modified Bentz 2003
Tension Softening	Bilinear
Tension Splitting	Not Considered
Confinement Strength	Kupfer / Richart Model
Concrete Dilation	Variable - Kupfer
Cracking Criterion	Mohr-Coulomb (stress)
Crack Slip Check	Vecchio-Collins 1986
Crack Width Check	Agg/5 Max Crack Width
Slip Distortions	Vecchio-Lai
Concrete Hysteresis	Nonlinear w/ Plastic Offsets
Steel Hysteresis	Elastic-Plastic w/ Hardening
Rebar Dowel Action	Tassios (Crack Slip)

Analysis Parameter	Model
Convergence Criteria	Displacements - Weighted
Strain History	Previous Loading Considered
Strain Rate Effects	Not Considered
Structural Damping	Not Considered
Geometric Nonlinearity	Considered
Crack Allocation Process	Uniform

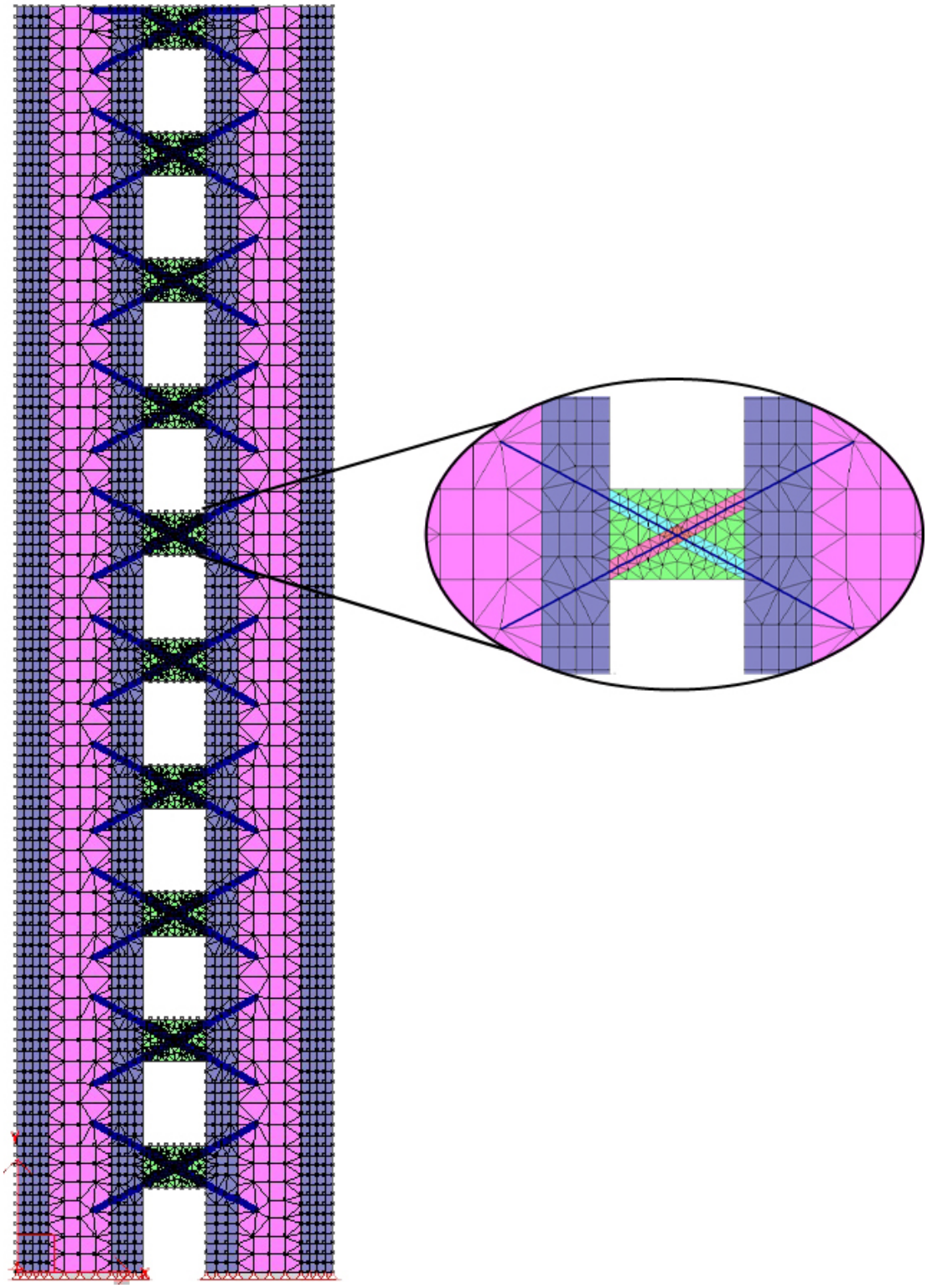

Figure 6.6: CW-ACI Coupled Wall Mesh

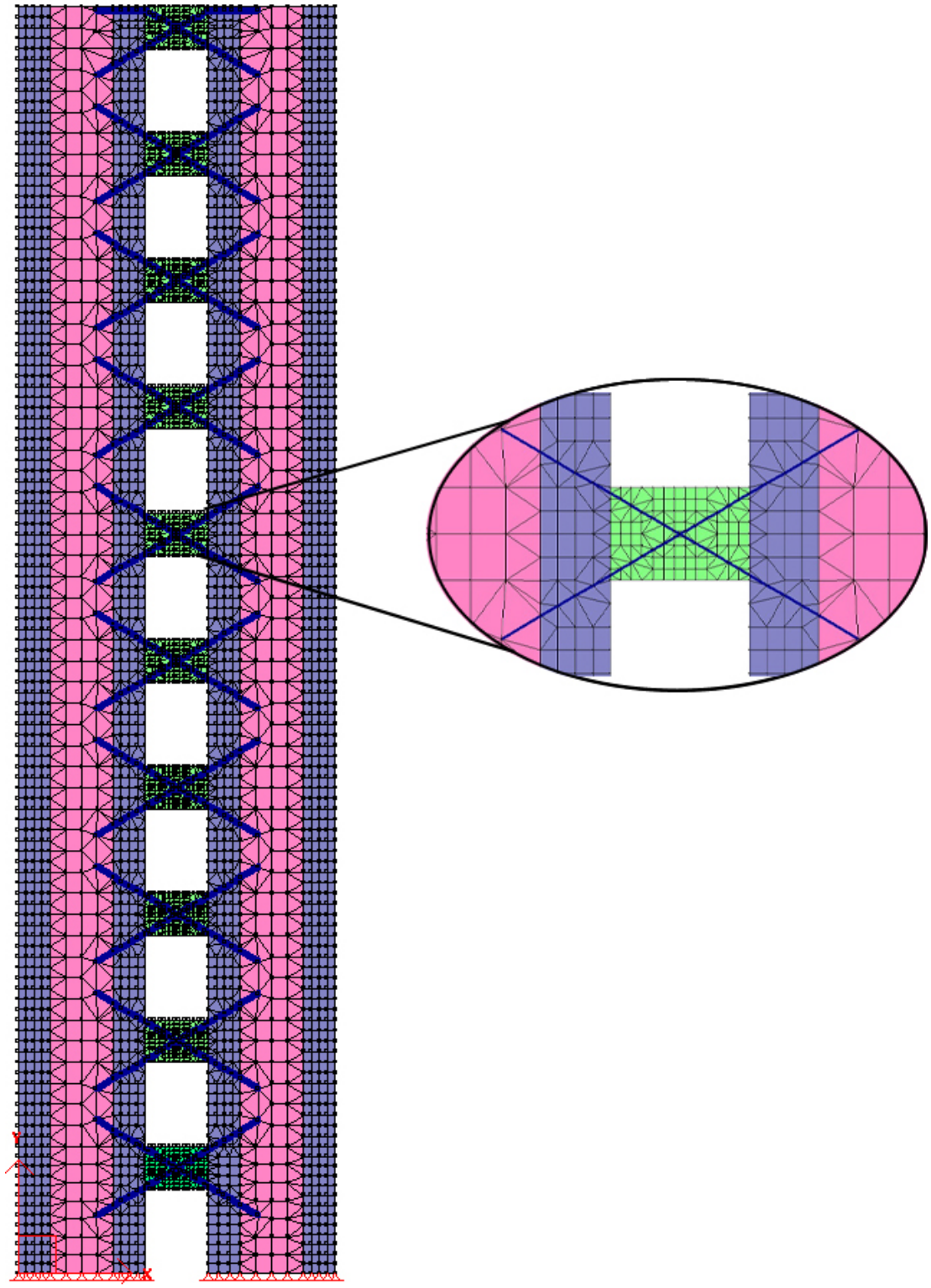

Figure 6.7: CW-318HF and CW-318HFR Coupled Wall Mesh

to allow for a finer mesh in the coupling beams and the boundary elements of the wall piers, where more deformation and damage are expected, and a larger mesh size in the web zone of the wall piers. The boundary zones and the web zone were each divided into four elements. The coupling beams were divided into nine elements vertically and thirteen elements longitudinally.

The mesh was generated using a grid of rectilinear elements and with the insertion of triangular elements at transition between zones and along the diagonal truss bar elements. Model CW-ACI is shown in its entirety with a detail of a single coupling beam in Figure 6.6. The mesh for CW-318HF and CW-318HFR are the same and is shown in Figure 6.7.

6.8.3 Reinforcement Model

The diagonal reinforcing bars of each coupling beam were grouped together and modeled with a discrete truss-bar element. The remaining reinforcement in the coupling beams (longitudinal, vertical, and out-of-plane) and all reinforcement in the wall piers was modeled with smeared reinforcement.

6.8.4 Boundary Conditions

The wall was designed assuming a fixed base, as is commonly done in engineering design offices. To model this in VecTor2, all nodes along the bottom of the wall were fixed against translation in both directions.

6.8.5 Loading Parameters

Two approaches were considered to control the analyses and apply lateral load to the wall. The coupled wall was first modeled using displacement control and the assumption of a linear deformed shape for the wall. However, this approach was abandoned when it was determined that the story force distribution due to the assumed deformed shapes did not match those expected due to earthquake loading. Details of the displacement control analysis and are presented in section 6.10. Ultimately, the coupled walls were modeled using load control with

three different lateral load distributions. Due to the limitations in the VecTor2 software, specifically the inability to maintain constant load pattern while increasing a second load pattern, gravity load was not applied to the walls. Details of the loading parameters are shown below.

Displacement Control

Two displaced shapes were considered; the displaced shape from the elastic SAP2000 model and the displaced shape resulting from the assumed plastic mechanism used in the wall design process. The elastic displaced shape was taken as an average of the displaced shapes resulting from the uniform load pattern and the inverted triangular load pattern. The resulting elastic displaced shape resembles that of a cantilevered beam with higher curvature near the base of the wall and a near linear shape above the third floor. The plastic displaced shape is purely a function of the assumed plastic hinges at the base of the wall and at the ends of all the coupling beams and results in a linearly increasing displacement up the height of the wall.

The two displaced shapes have been arbitrarily scaled to 10 at the top of the wall and are shown in Table 6.7 and Figure 6.8 along with the uniform and triangular shapes.

Load Control

Three different lateral load distributions were considered; inverted triangular, uniform, and uniform up to a height of $0.6H_{wall}$ to produce an effective height for the lateral load of $0.3H_{wall}$. These load distributions are discussed in detail below:

- The Inverted Triangular lateral load distribution was defined using ASCE7-05, which is the basis for the International Code Council 2007 design guidelines. Each story is assumed to have the same mass. A "-T" is appended to the model name to indicate this load distribution.

- Uniform lateral load distribution. Here the same load is applied to each story. A "-U"

Table 6.7: Coupled Wall Displaced Shapes

	Scaled Displacement Level			
Level	Plastic	Unif.	Tri.	Elastic
10	10.00	10.00	10.00	10.00
9	9.00	8.95	8.86	8.88
8	8.00	7.87	7.70	7.76
7	7.00	6.75	6.50	6.64
6	6.00	5.58	5.29	5.53
5	5.00	4.40	4.08	4.41
4	4.00	3.23	2.93	3.29
3	3.00	2.12	1.87	2.17
2	2.00	1.14	0.97	1.05
1	1.00	0.38	0.31	0.35
0	0.00	0.00	0.00	0.00

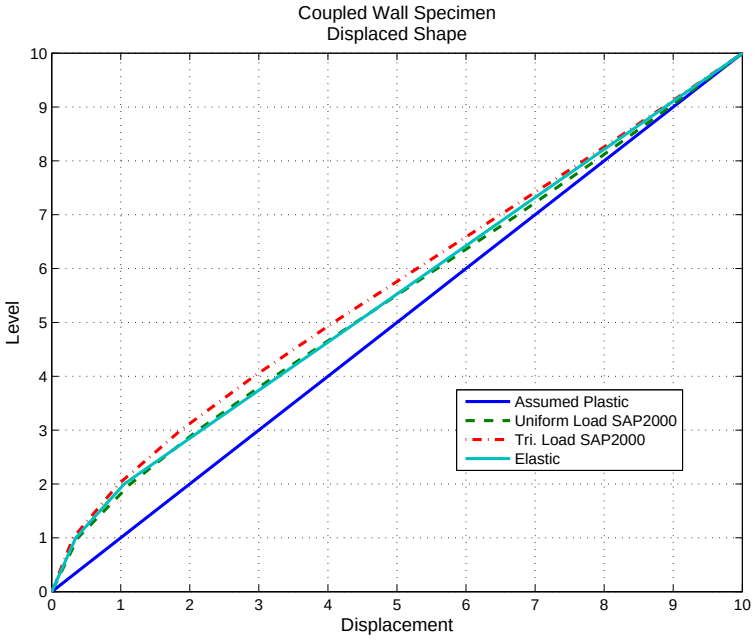

Figure 6.8: Coupled Wall Applied Displaced Shapes

is appended to the model name to indicate this load distribution.

- 0.3H Effective Height. This vertical distribution is designed to set the effective shear height to 0.3 times the height of the wall. The same load is applied to the bottom six floors of the wall. A "-3H" is appended to the model name to indicate this load distribution.

For all of the load distributions, the load at each floor level was applied as four point load distributed across the wall. The total load was increased monotonically until the model became numerically unstable. Because the load, rather than the lateral displacement, increased with each step in the analysis strength degradation of the wall could not be simulated.

6.8.6 Summary of Coupled Wall Model Variations

With the multiple coupled wall models, control methods, and lateral load variations a matrix of fifteen coupled wall models was necessary. The model name and a short summary of the model characteristics are shown in Table 6.8.

Table 6.8: Coupled Wall Model List

Model	Coupling Beam	Analysis Method	Load/Disp. Distribution
CW-ACI-T	CBR-ACI	Load Control	Inv. Triangular
CW-ACI-U	CBR-ACI	Load Control	Uniform
CW-ACI-3H	CBR-ACI	Load Control	0.3H Eff. Height
CW-318HF-T	CBR-318H-F	Load Control	Inv. Triangular
CW-318HF-U	CBR-318H-F	Load Control	Uniform
CW-318HF-3H	CBR-318H-F	Load Control	0.3H Eff. Height
CW-318HFR-T	CBR-318H-FR	Load Control	Inv. Triangular
CW-318HFR-U	CBR-318H-FR	Load Control	Uniform
CW-318HFR-3H	CBR-318H-FR	Load Control	0.3H Eff. Height
CW-ACI-PL	CBR-ACI	Disp. Control	Plastic
CW-ACI-EL	CBR-ACI	Disp. Control	Elastic
CW-318HF-PL	CBR-318H-F	Disp. Control	Plastic
CW-318HF-EL	CBR-318H-F	Disp. Control	Elastic
CW-318HFR-PL	CBR-318H-F	Disp. Control	Plastic
CW-318HFR-EL	CBR-318H-F	Disp. Control	Elastic

6.9 Description of Evaluation Method

The output from each of the VecTor2 simulations was evaluated to determine the predicted mechanisms of deformation, loss of stiffness, and loss of strength. Output data considered included the following:

- Base Reactions, including moment, M, shear, V, and axial, P forces.
- Story Displacement, δ_i, is the horizontal displacement of each floor level, taken as the average of all the nodal the displacements at each of the levels.
- Inter-story Drift, Δ_i, is the drift ratio for a single story of the wall, taken as the difference in story displacement from one level to the next over the story height. Rigid body rotations of the floor levels are removed from Δ_i.
- Roof Drift, Δ_{roof}, is the roof displacement over the height of the wall.
- Coupling Beam Rotation, θ_{CB}. This is defined by the following equation:

$$\theta_{CB} = \theta_{56} + \frac{\theta_{12} + \theta_{34}}{2}$$

where rotations are defined in Figure 6.9

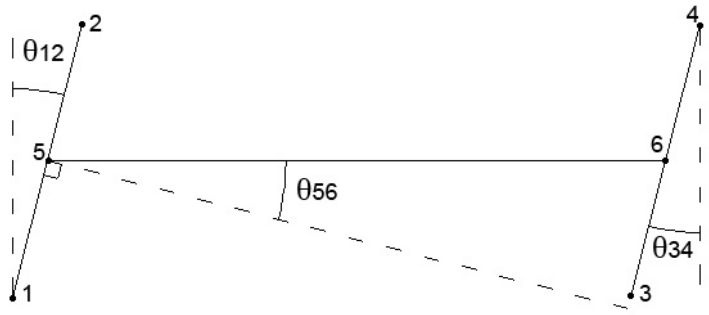

Figure 6.9: Coupling Beam Rotations

- Coupling Beam Displacement, δ, is calculated assuming small rotations and ignoring axial elongation of the beam as:

$$\delta = \theta L$$

  where θ_{CB} is defined in Eqn. 6.9 and L is the length of the coupling beam.

- Coupling Beam Drift, Δ, is the coupling beam displacement over the its length, according to Eqn. 6.9 $\Delta = \theta_{CB}$.

- Degree of Coupling, DOC, is a measure of the percentage of the overturning moment due to the base moment in the wall piers versus the percentage due to the wall axial load, which results from the shear forces in the coupling beams (Harries 2001), defined as:

$$DOC = \frac{TL}{M_w} \tag{6.1}$$

  where,
  T = axial load in walls due to shears in coupling beams;
  L = distance between the centroids of the wall piers; and,
  M_w = total overturning moment in the base of the wall.

Additionally, the displaced shape, predicted plastic mechanism, crack patterns and failure modes are discussed.

6.10 Displacement Control Results

The VecTor2 simulations were first attempted using an applied displacement approach. The applied displacement was intended to simulate the displaced shape assumed during the plastic design procedure. Due to the limitations of VecTor2, when using an applied displacement, only the magnitude of the displacements can be incremented. There is no capability to modify the displaced shape over the course of the simulation. This, of course,

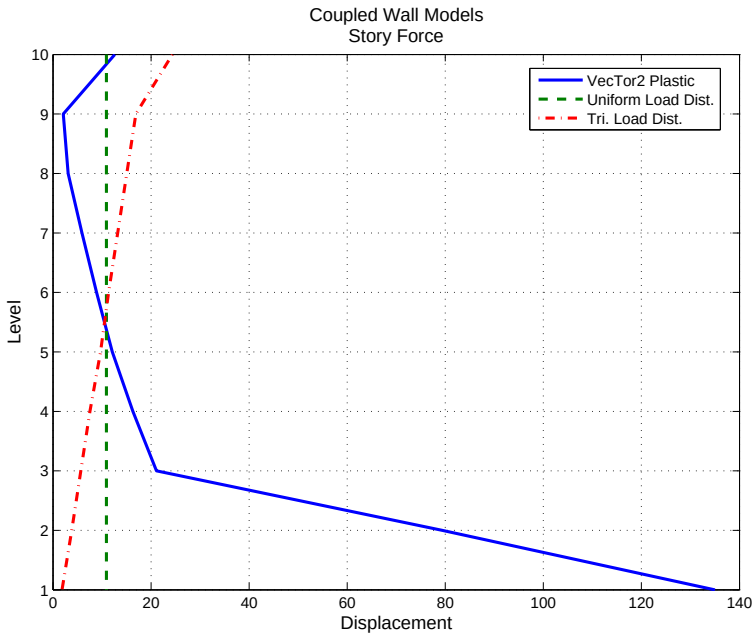

Figure 6.10: Coupled Wall Story Force

does not represent the true displacement history of a coupled wall. The displaced shape of the coupled wall will change with the magnitude and distribution of the applied load, with the level of yielding and plastic deformation within the wall. The displaced shape could approach the assumed plastic displaced shape if full plastic hinging is reached in the wall piers and coupling beams.

Figure 6.10 shows the distribution of story shears under the assumed plastic displaced shape compared to the story forces resulting from a uniform lateral force distribution and the inverted triangular load distribution that was used during the design. The plot shows that nearly all of the base shear in the plastic displaced shape model is developed over the first story, indicating that the coupled wall is not behaving as expected.

The approach of applying a displacement to the wall proved to be inappropriate for simulating the response of the coupled wall and was ultimately abandoned in favor of following the load control approach. To accurately simulate the behavior of a coupled wall during a

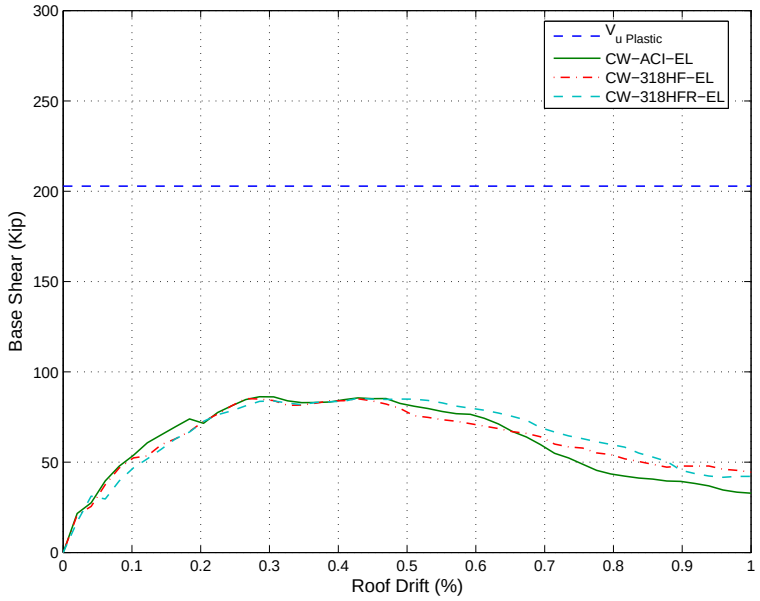

Figure 6.11: Coupled Wall Response with Applied Elastic Displacement

pushover analysis, the displaced shape cannot remain fixed, it must remain free to adapt to the changing behavior of the coupled wall. The base shear vs. roof drift histories are shown in Figures 6.11 and 6.12 for information only.

6.11 Load Control Results

6.11.1 Deformed Shape and Crack Patterns

The following section discusses the deformed shapes of the walls at the point of first yield and at the maximum predicted base shear. The roof displacement and drift are noted on each figure. The displacements have been magnified 20 times in order to make the curvature and displacement patterns more visible. The crack directions for each shell element are show with the red lines. A thin red line indicates a crack that is less than 0.04 in (1 mm) and a thick red line indicates a crack larger than .08 in (2 mm).

The deformed shape and crack patterns are shown for all the coupled wall models.

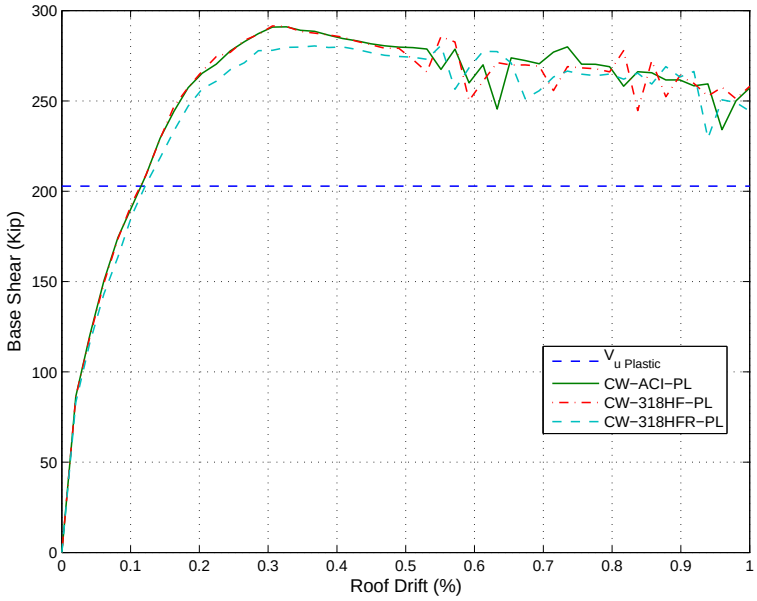

Figure 6.12: Coupled Wall Response with Applied Plastic Displacement

Figures 6.13, 6.14, and 6.15 are grouped by coupled wall model and show the effects of the lateral load distribution on at the maximum predicted base shear. Figures 6.16 to 6.21 are grouped by lateral load distribution and show the effects of the changes in the coupling beam reinforcement at the first yield point and at the maximum predicted base shear.

These figures show that there is a nominal difference in displaced shape and crack patterns between the reference model, CW-ACI, and the full confinement model, CW-318HF. Both models have the same concentration of plastic deformation and cracking at the base of the wall piers with little to no deformation in the coupling beams. On the other hand, the reduced coupling beam strength model, CW-318HFR, has a dramatically different displaced shape with plastic deformation and cracking distributed over the ends of all of the coupling beams and at the base of the wall piers.

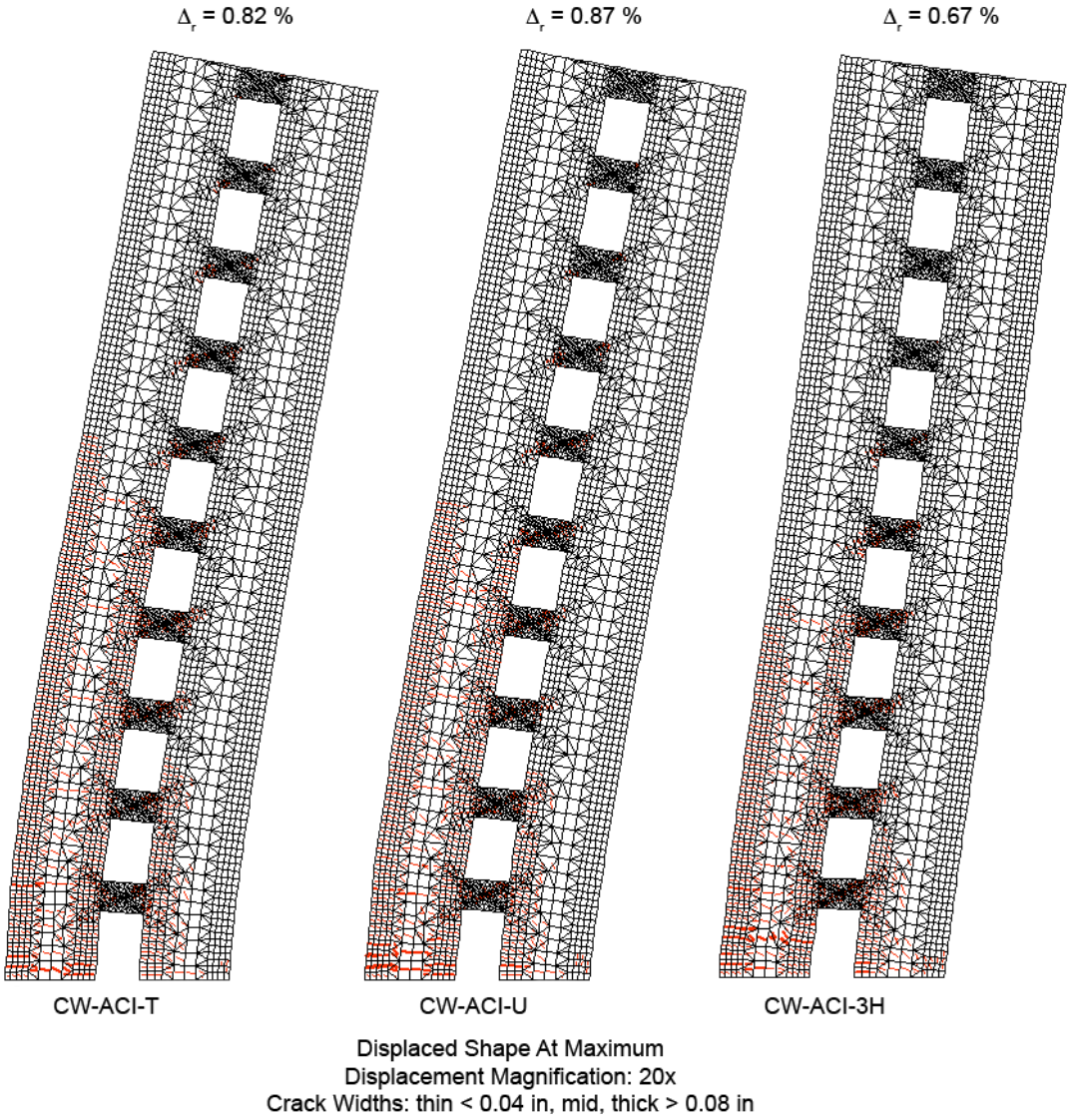

Figure 6.13: CW-ACI Displacement Comparisson

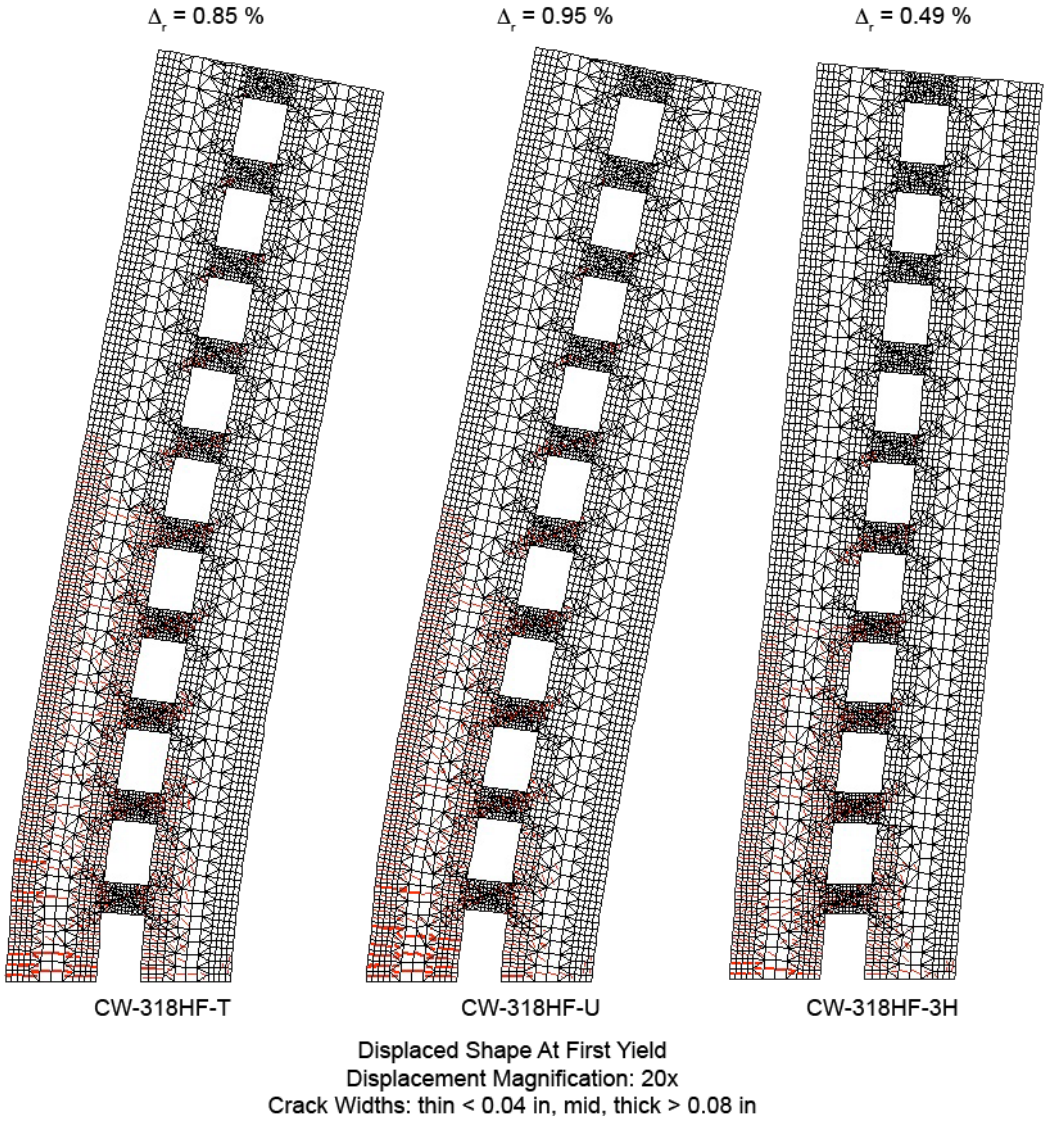

Figure 6.14: CW-318HF Displacement Comparisson

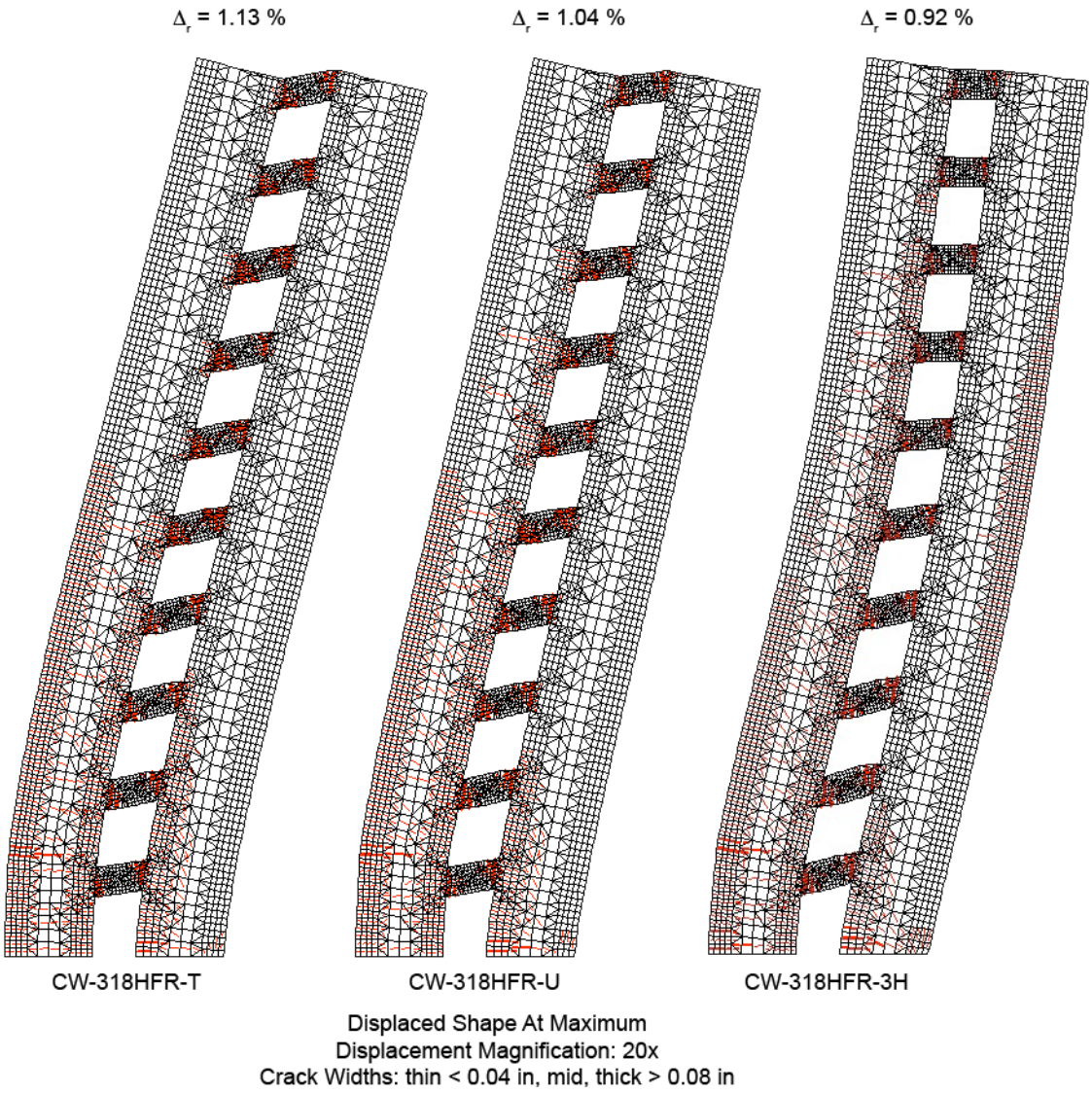

Figure 6.15: CW-318HFR Displacement Comparison

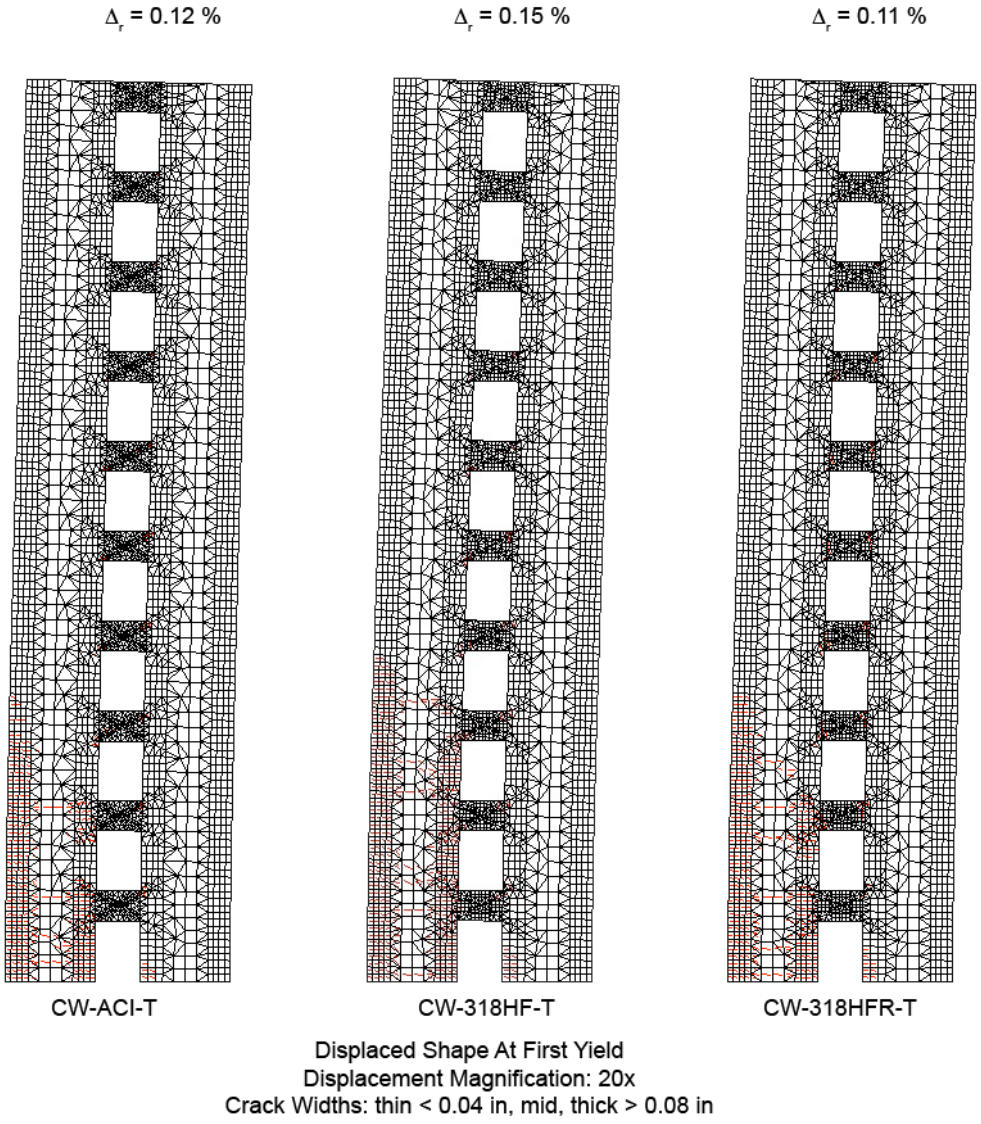

Figure 6.16: Displacement Comparison at First Yield - Inverted Triangular Load

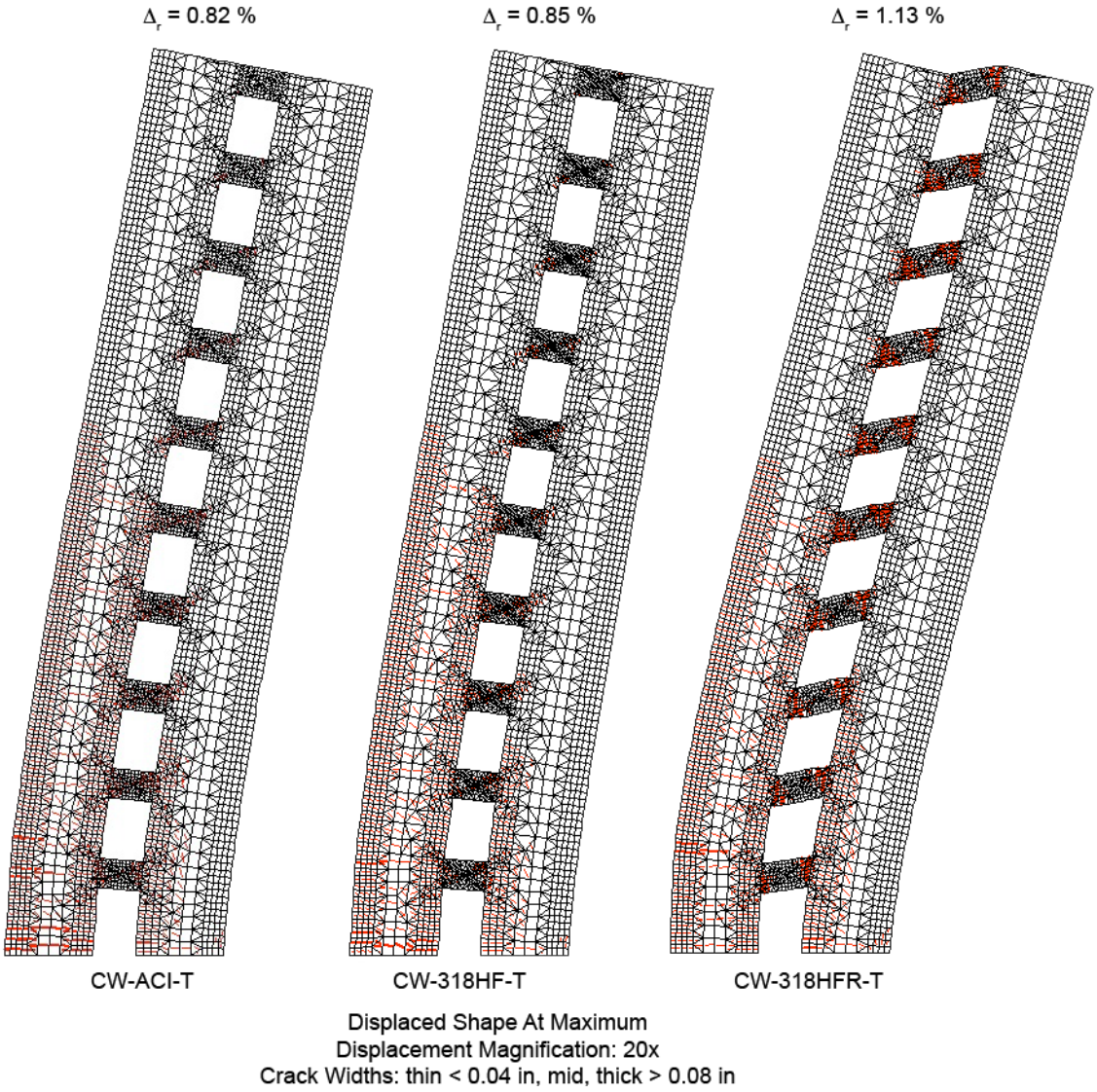

Figure 6.17: Displacement Comparison at Maximum Base Shear - Inverted Triangular Load

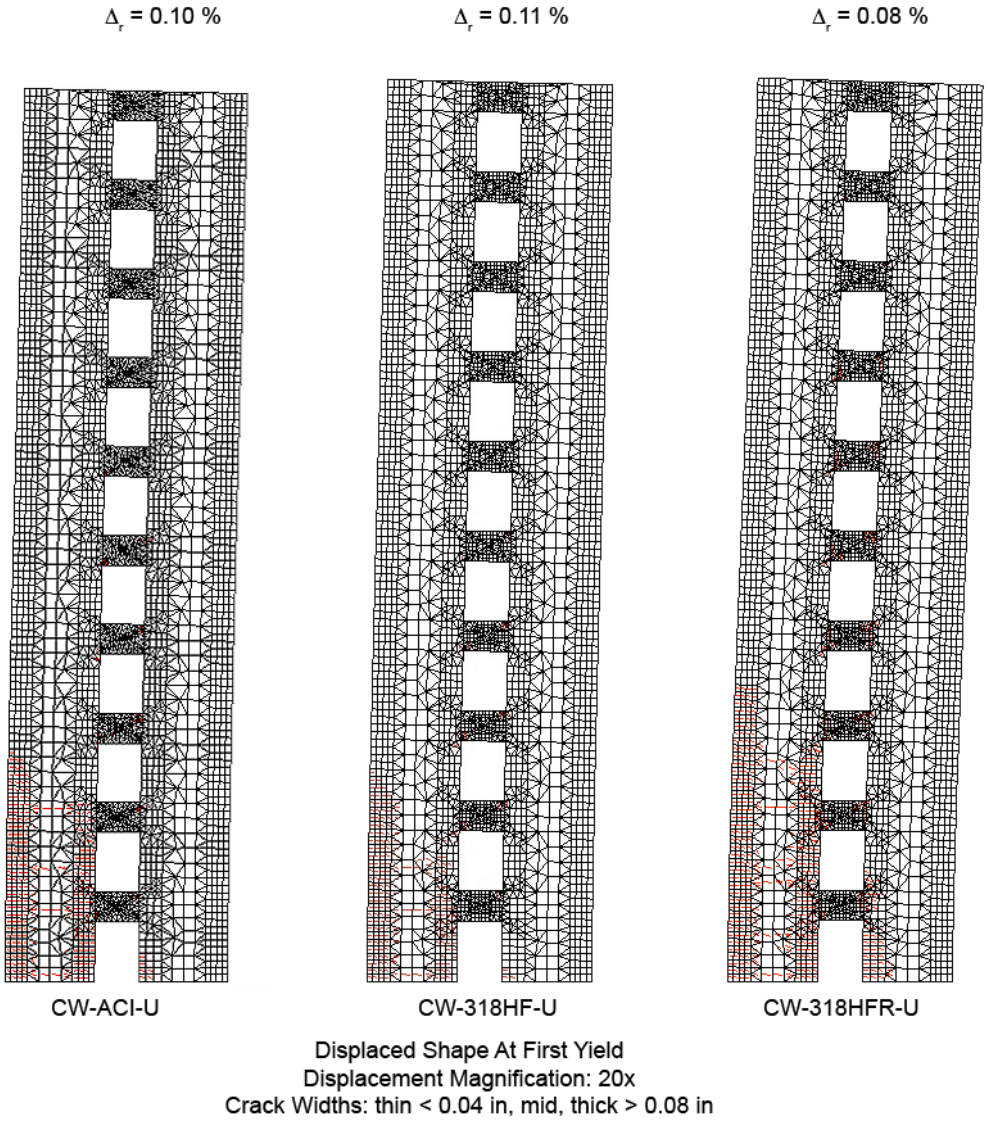

Figure 6.18: Displacement Comparison at First Yield - Uniform Load

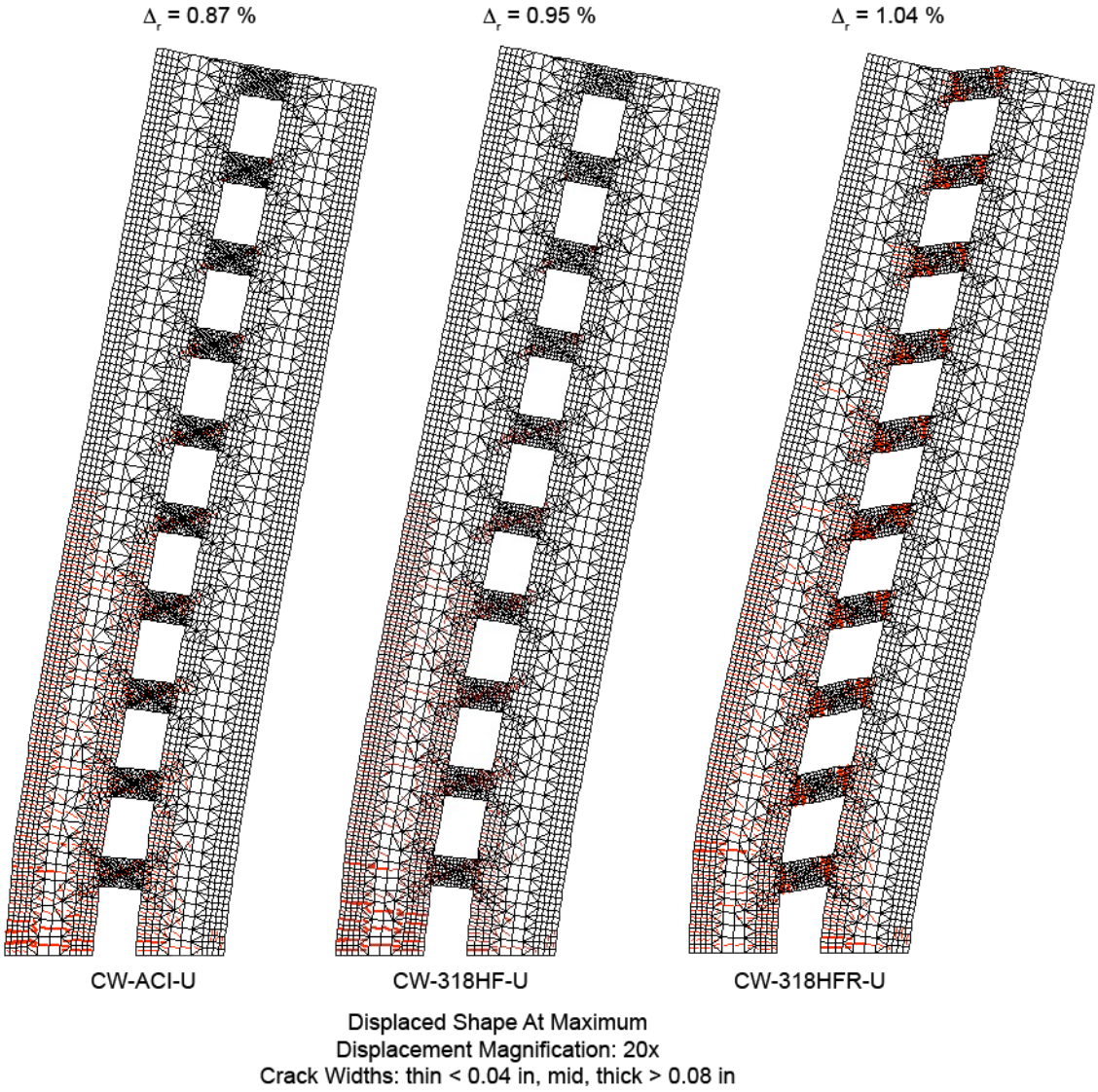

Figure 6.19: Displacement Comparison at Maximum Base Shear - Uniform Load

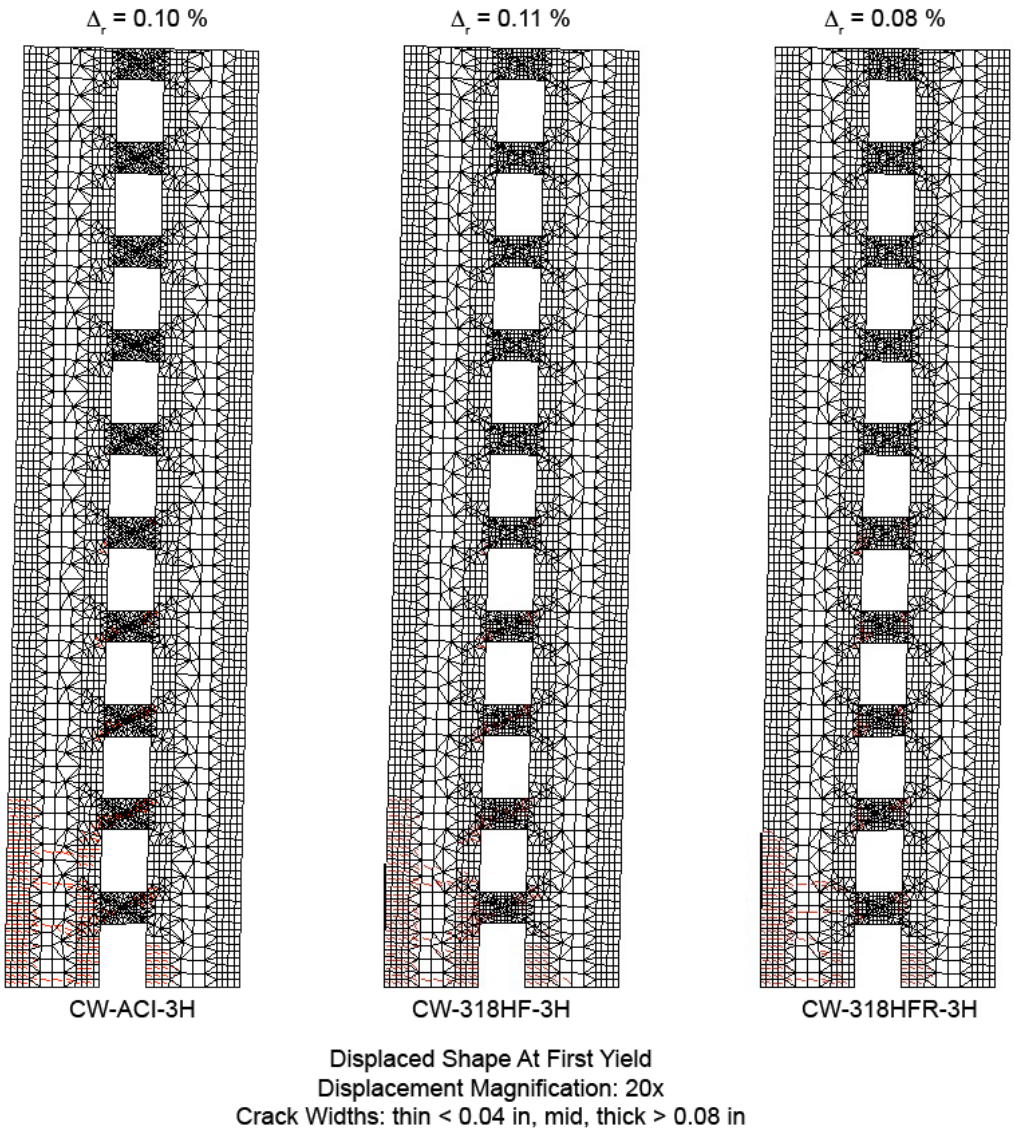

Figure 6.20: Displacement Comparison at First Yield - 0.3H Effective Height Load

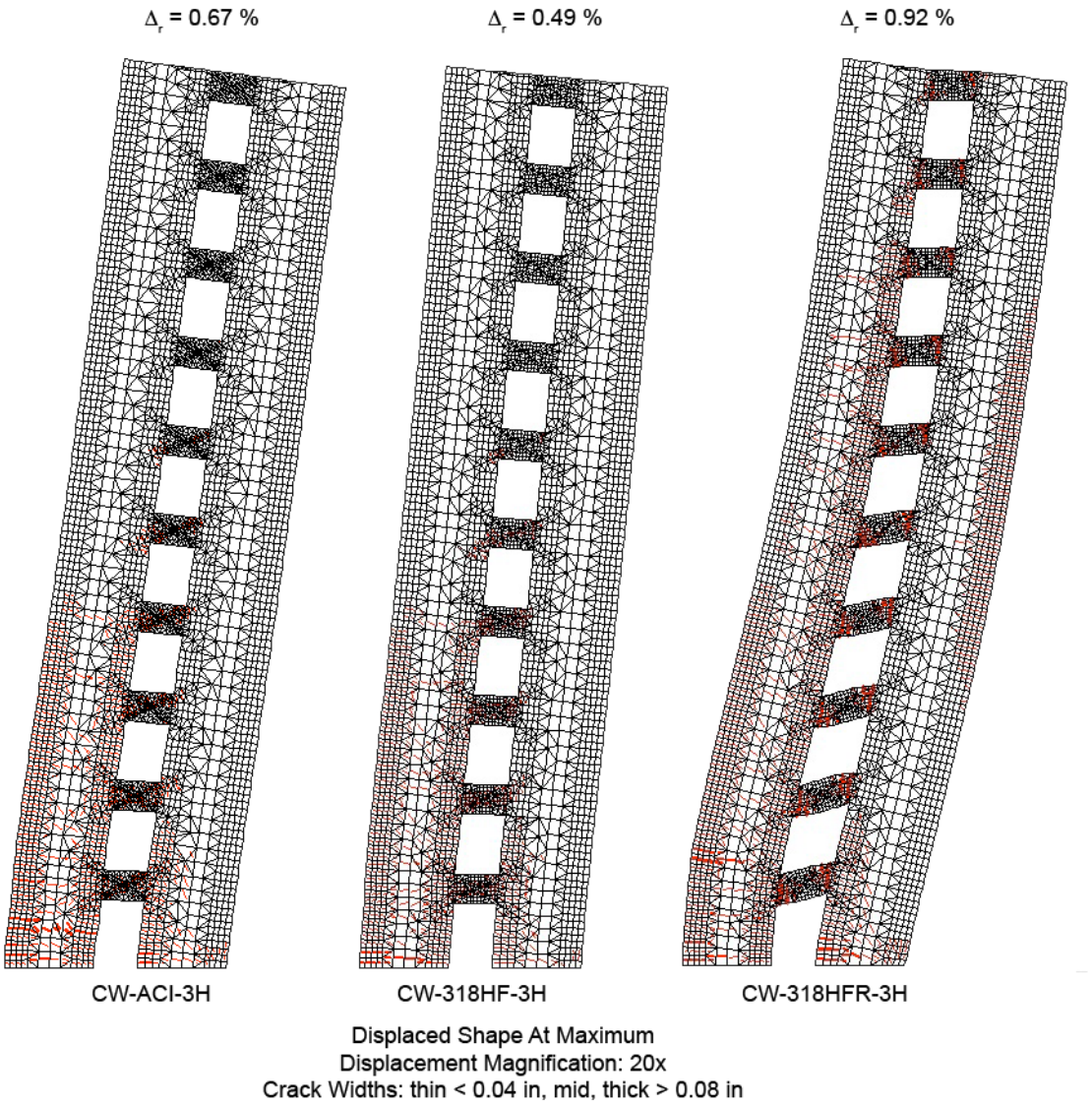

Figure 6.21: Displacement Comparison at Maximum Base Shear - 0.3H Effective Height Load

Table 6.9: Coupled Wall Base Reactions at Maximum Displacement

Model	Total Wall			Tension Pier			Compression Pier		
	M $(k-ft)$	V (kip)	P (kip)	M $(k-ft)$	V (kip)	P (kip)	M $(k-ft)$	V (kip)	P (kip)
CW-318HF-T	3203.5	112.5	0.2	6.7	9.3	350.5	1054.0	103.2	350.7
CW-318HF-U	3167.0	143.8	0.9	5.0	6.5	346.4	1057.2	137.3	347.3
CW-318HF-3H	3175.1	226.3	1.1	9.9	14.5	344.5	1034.8	211.8	345.7
CW-318HFR-T	2860.0	100.3	0.7	83.6	1.1	290.4	997.5	99.3	291.1
CW-318HFR-U	2970.9	134.6	0.8	65.6	2.0	305.1	1019.1	132.5	305.9
CW-318HFR-3H	2954.8	204.7	3.4	77.7	5.8	300.3	1022.0	199.0	296.9
CW-ACI-T	3201.6	108.8	0.9	-23.1	5.6	352.6	1055.9	103.2	351.7
CW-ACI-U	3272.9	158.5	7.3	-18.9	21.9	350.0	1070.1	136.5	357.3
CW-ACI-3H	3211.7	228.9	0.7	-23.1	11.8	346.1	1048.5	217.1	346.8

6.11.2 Base Reactions

The base reactions (moment, shear and axial) at the maximum predicted load by VecTor2 are summarized in Table 6.9. At the maximum predicted displacement the tension pier is subjected to large tensile loads and contributes almost no flexural or shear resistance. The compression pier carries between 82% and 96% of the total shear and between 33% and 38% of the total overturning moment. For each model, the maximum base moment and maximum axial reactions remain essentially the same, while the base shear changes with each of the three load distributions. This indicates that the behavior of the wall piers is controlled by flexural, as intended. Base hear may be computed as the flexural strength of the wall divided by the effective height of the applied lateral load. Thus, base shear is inversely proportional to the effective shear height of the applied load; a lower effective shear height results in a larger base shear. The smaller moment arm of the 0.3H effective shear height, as compared to the 0.67H effective shear height of the inverted triangular load, requires a larger shear force to reach the same overturning moment. Figures 6.22, 6.23, and 6.24 show that the effect of the lateral load distribution on the base shear vs. roof drift relationship is the same across all three models.

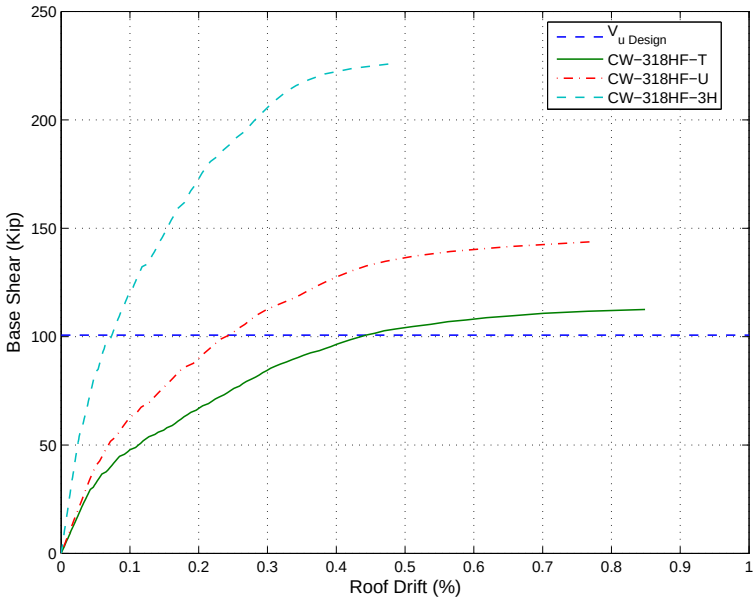

Figure 6.22: CW-318HF - Effect of Load Distribution

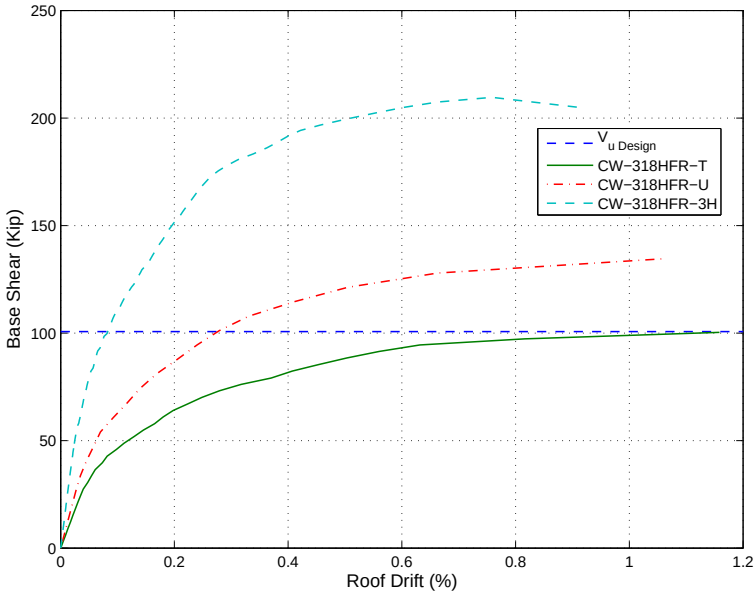

Figure 6.23: CW-318HFR - Effect of Load Distribution

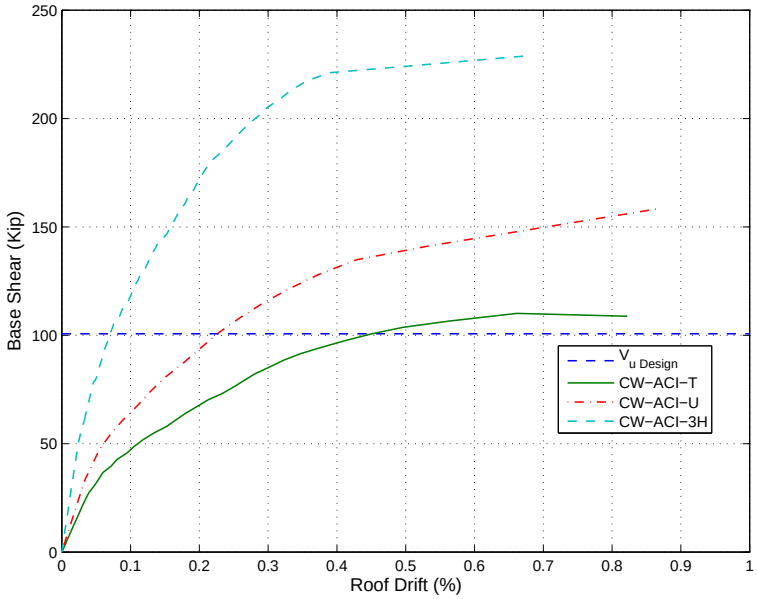

Figure 6.24: CW-ACI - Effect of Load Distribution

Table 6.10: Coupled Wall Degree of Coupling

Model	T (kip)	M_w $(k-ft)$	TL $(k-ft)$	DOC $VecTor2$	DOC $Theoretical$
CW-318HF-T	350.6	3203.5	2103.6	0.66	0.71
CW-318HF-U	346.9	3167.0	2081.1	0.66	0.71
CW-318HF-3H	345.1	3175.1	2070.6	0.65	0.71
CW-318HFR-T	290.8	2860.0	1744.5	0.61	0.38
CW-318HFR-U	305.5	2970.9	1833.0	0.62	0.38
CW-318HFR-3H	298.6	2954.8	1791.6	0.61	0.38
CW-ACI-T	352.2	3201.6	2112.9	0.66	0.71
CW-ACI-U	353.7	3272.9	2121.9	0.65	0.71
CW-ACI-3H	346.5	3211.7	2078.7	0.65	0.71

6.11.3 Degree of Coupling

The degree of coupling (DOC) calculated using the internal forces at the maximum predicted load is summarized in Table 6.10. The theoretical degree of coupling for walls CW-ACI and CW-318HF, based on the expected strengths (V_{pr}, M_{pr}), is 0.71. The lower value computed using results from the VecTor2 analysis shows the coupling beams are carrying less of the resistance than assumed during the design. This is due to the fact that only a few, rather than all, of the coupling beams actually yielded.

To obtain the desired behavior mode, with yielding at the base of the wall piers and at the ends of all of the coupling beams, Harries (2001) recommends that the degree of coupling should not exceed 0.50. This recommendation is based on a comprehensive analysis of approximately thirty coupled wall models completed by nine researchers over the last thirty years. His study found that a high degree of coupling will cause a coupled wall to behave

Table 6.11: Coupled Wall Roof Drift

Model	First Yield			Max Predicted Disp.		
	V_y (kip)	δ_y (in)	Δ_y (%)	V_u (kip)	δ_u (in)	Δ_u (%)
CW-318HF-T	56.9	0.72	0.15%	112.5	4.09	0.85%
CW-318HF-U	67.4	0.56	0.12%	143.8	4.54	0.95%
CW-318HF-3H	126.8	0.53	0.11%	226.3	2.36	0.49%
CW-318HFR-T	51.9	0.62	0.11%	100.3	5.44	1.13%
CW-318HFR-U	60.7	0.44	0.09%	134.6	5.01	1.04%
CW-318HFR-3H	99.8	0.39	0.08%	209.6	4.40	0.92%
CW-ACI-T	51.9	0.57	0.12%	108.8	3.94	0.82%
CW-ACI-U	74.1	0.62	0.13%	158.5	4.17	0.87%
CW-ACI-3H	118.7	0.48	0.10%	228.9	3.24	0.67%

similar to a planar wall where the energy dissipation and plastic deformation is concentrated at the base of the wall.

6.11.4 Displacement and Drift at Yield and Maximum

The roof drift and base shear at first yield of the wall piers and at the maximum predicted base shear are summarized in Table 6.11. Models CW-ACI and CW-318HF have very similar roof drift ratios at both points of reference. This similarity is expected given that the two coupled wall models have the same design strength for the piers and coupling beams. Model CW-318HFR, while reaching a lower base shear strength, has the highest roof drift ratios of all the models.

Brown (2006) reviewed experimental data for planar wall tests and found that the mean drift at first yield in the walls was 0.47% and the mean drift at the ultimate or failure point

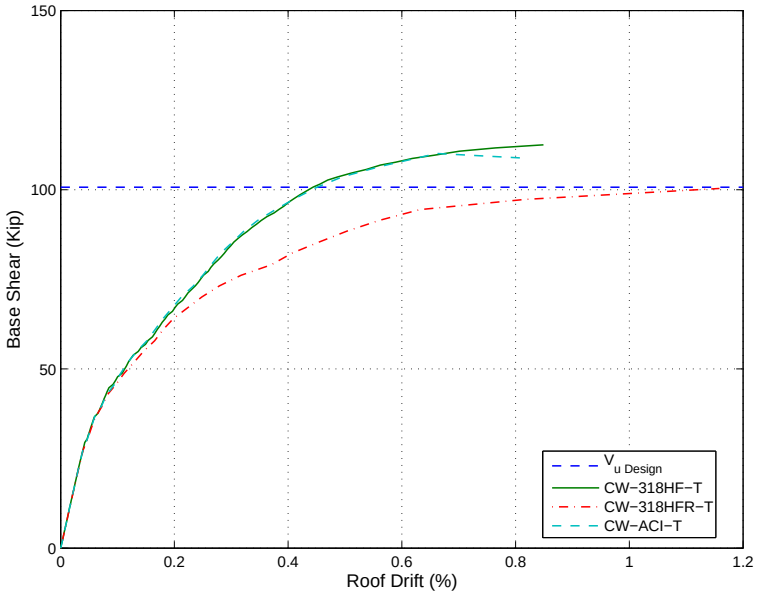

Figure 6.25: Base Shear vs. Roof Drift - Triangular Load

was 1.92%. The coupled wall drift values predicted by VecTor2 are lower than these averages, however this difference is likely due to the modeling limitations of the finite element analysis within VecTor2 and not the limitations of the wall. Recall that in the coupling validation study presented in Chapter 4, VecTor2 under-predicted the yield drift by an average of 11% and under-predicted the ultimate drift by an average of 42%. If these averages are be applied to the average coupled wall model drifts, the true yield drift would be approximately 13%. Correspondingly, the true ultimate drifts would be 1.34% for CW-ACI and CW-318HF and 1.78% for CW-318HFR.

6.11.5 Base Shear vs. Drift Comparisons

Figures 6.25, 6.26, and 6.27 illustrate the effect of the reduced strength coupling beams on the load-drift plots for coupled wall models under each of the three loading methods. Model CW-318HFR on average has reaches an ultimate shear capacity that is 10% less than the other two models, however maximum shear is reached at a drift that is 30% larger than for

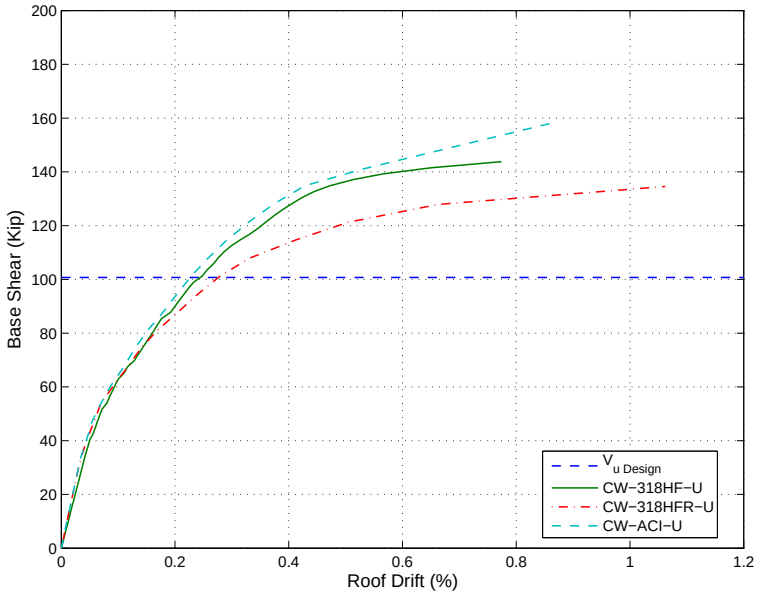

Figure 6.26: Base Shear vs. Roof Drift - Uniform Load

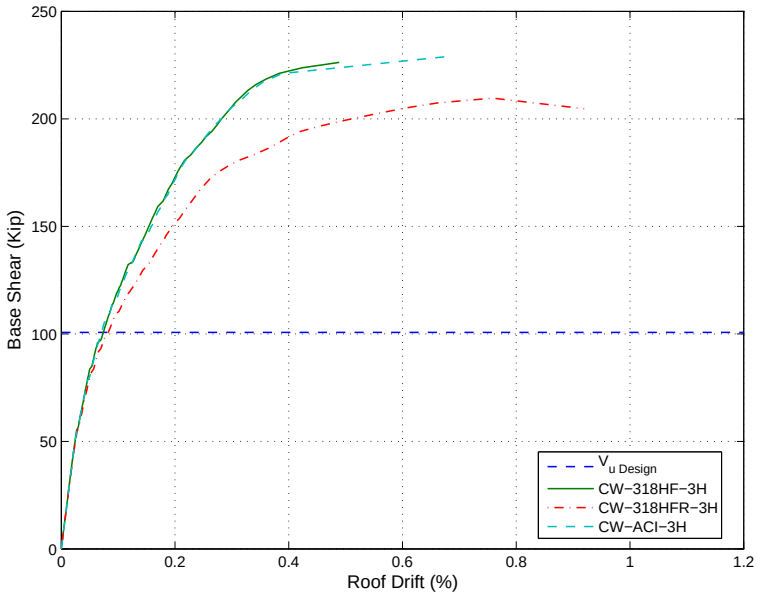

Figure 6.27: Base Shear vs. Roof Drift - 0.3H Effective Height Load

Table 6.12: Coupled Wall Inter-story Drift

Inter-story Drift, Δ_{fi} (%)

	CW-ACI			CW-318HF			CW-318HFR		
Level	T	U	3H	T	U	3H	T	U	3H
1	0.42	0.55	0.60	0.43	0.62	0.40	0.42	0.51	0.80
2	0.20	0.23	0.21	0.18	0.17	0.19	0.59	0.62	0.72
3	0.14	0.14	0.15	0.13	0.13	0.13	0.56	0.54	0.61
4	0.11	0.10	0.08	0.11	0.11	0.07	0.57	0.52	0.53
5	0.09	0.07	0.04	0.08	0.06	0.03	0.56	0.48	0.40
6	0.05	0.04	0.02	0.05	0.04	0.01	0.52	0.43	0.30
7	0.03	0.03	0.00	0.03	0.03	0.00	0.51	0.40	0.20
8	0.02	0.02	0.00	0.02	0.02	0.00	0.49	0.37	0.15
9	0.02	0.01	0.00	0.02	0.01	0.00	0.47	0.35	0.12
10	0.01	0.01	0.00	0.01	0.01	0.00	0.46	0.34	0.11
Average	0.11	0.12	0.11	0.11	0.12	0.08	0.52	0.46	0.39

the other models.

6.11.6 Inter-story Drift

The inter-story drift was calculated at the drift level corresponding to the maximum predicted base shear. The effect of rigid body rotation has been removed so that the values presented here represent the true inter-story drift ratio. Table 6.12 summarizes the inter-story drifts at each story level and for each lateral load distribution.

The inter-story drifts for the refernce model, CW-ACI, and the full confinement model, CW-318HF, show a high drift at the base level which rapidly decreases and approaches zero in the upper levels. This distribution of inter-story drift illustrates that these specimens have a concentration of deformation and plastic behavior at the base of the wall with little to no deformation over the height of the wall, as previously shown in the displaced shape plots in Section 6.11.1. The reduced strength model, CW-318HFR, shows a relatively uniform

Table 6.13: Coupling Beam Drift

Coupling Beam Drift, Δ_{CB} (%)

	CW-ACI			CW-318HF			CW-318HFR		
Level	T	U	3H	T	U	3H	T	U	3H
1	0.03	0.05	0.16	0.03	0.04	0.15	1.11	1.30	2.04
2	0.09	0.14	0.25	0.09	0.12	0.21	2.00	2.12	2.65
3	0.16	0.18	0.23	0.10	0.13	0.17	2.31	2.25	2.56
4	0.12	0.13	0.17	0.09	0.10	0.13	2.46	2.22	2.25
5	0.10	0.11	0.10	0.08	0.10	0.08	2.51	2.13	1.82
6	0.10	0.09	0.05	0.08	0.08	0.04	2.47	2.02	1.36
7	0.08	0.07	0.02	0.07	0.06	0.01	2.42	1.89	0.95
8	0.06	0.04	0.01	0.05	0.04	0.00	2.35	1.79	0.70
9	0.04	0.03	0.00	0.04	0.03	0.00	2.29	1.71	0.58
10	0.02	0.01	0.00	0.02	0.01	0.00	2.11	1.55	0.46
Average	0.08	0.08	0.10	0.07	0.07	0.08	2.20	1.90	1.54

distribution of inter-story drift over the hight of the wall, indicating a uniform distribution of deformation and plastic behavior.

6.11.7 Coupling Beam Rotation

The coupling beam drift can be compared to the drift predictions of the coupling beam simulations presented in chapter 5. The coupling beam simulations predicted a yield drift of 0.57% for CBR-ACI and CBR-318H-F. These are the same coupling beams as are present in the coupled wall models, CW-ACI and CW-318HF. The maximum coupling beam drift predicted in these two coupled walls was 0.25%, which is well below the drift demand at the predicted yield point of the coupling beams. This further illustrates that plastic hinges did not form at the ends of the coupling beams as assumed during the plastic analysis and design.

The reduced strength model, CW-318HFR, shows coupling beam drifts ranging from

0.46% to 2.65% over the height of the wall. These drifts indicate that coupling beams were subjected to sufficient drift demands to cause yielding and plastic hinging to occur in the coupling beam ends.

6.11.8 Reinforcement Yield

In this section the base shear versus roof drift plots for each of the coupled wall models are presented. The plots are annoted to show the locations of first yielding for the different components within the wall. The locations and type of reinforcement where yielding was observed include:

- first yield of longitudinal (vertical) reinforcement in the tension pier,
- first yield of of the horizontal reinforcement in a coupling beam,
- first yield of longitudinal (vertical) reinforcement in the compression pier,
- first yield of the diagonal reinforcement in a coupling beam,
- majority of coupling beam diagonal bars yielded, five or more coupling beams.

The results from the reference model, CW-ACI, and the full confinement model, CW-318HF, predicted an early yielding of the longitudinal reinforcement in the tension pier, followed by yielding of the horizontal reinforcement in the coupling beams and yielding of the longitudinal reinforcement in the compression pier. The diagonal reinforcement in the coupling beams did not yield when subjected to the uniform or the inverted triangular lateral load distributions, however under the 0.3H effective height distribution yielding of the diagonal reinforcement did occur near the maximum predicted base shear.

The results from the reduced strength model, CW-318HFR, predicted that yielding of the longintudinal reinforcement in the tension pier and the diagonal reinforcement of the coupling beams occured at similar drift levels. The majority of the coupling beams yielded within 0.05% roof drift of the point when the first diagonal bar yielded.

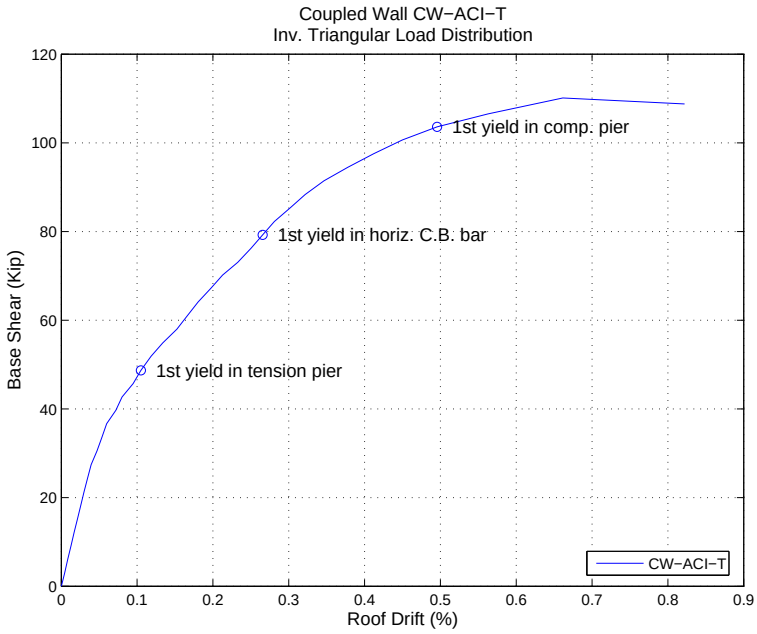

Figure 6.28: CW-ACI-T Roof Drift vs. Base Shear Response

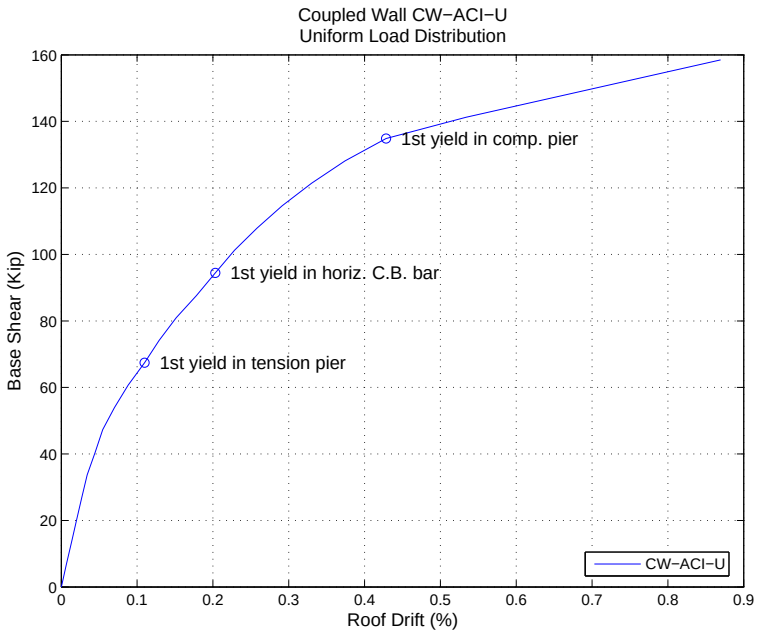

Figure 6.29: Coupled Wall ACI-U Roof Drift vs. Base Shear Response

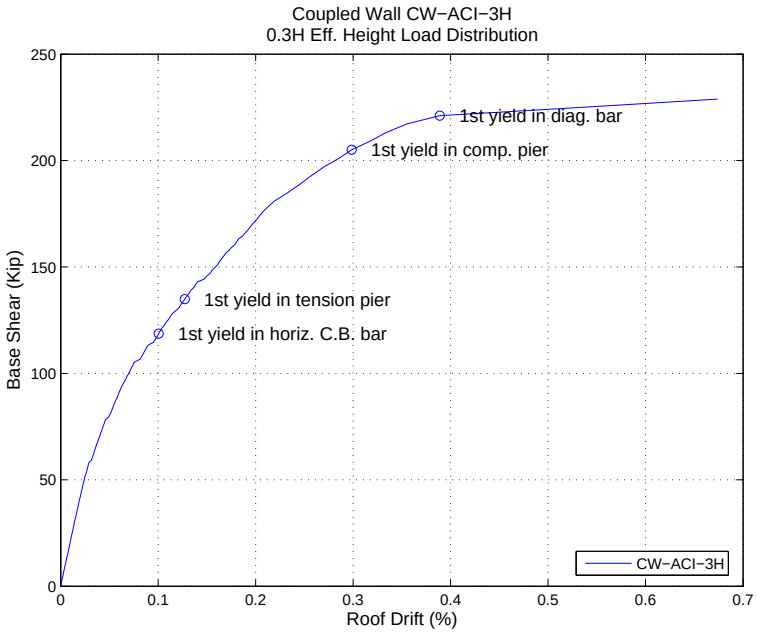

Figure 6.30: Coupled Wall ACI-3H Roof Drift vs. Base Shear Response

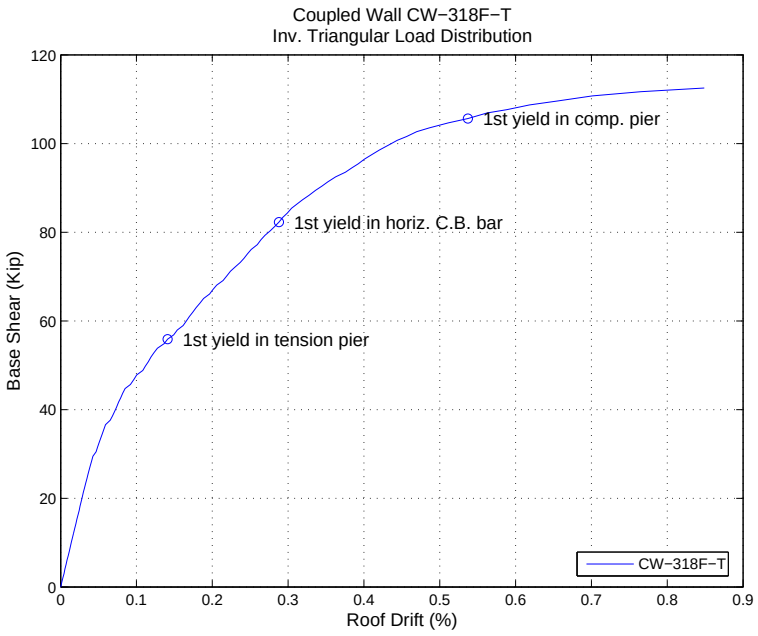

Figure 6.31: CW-318HF-T Roof Drift vs. Base Shear Response

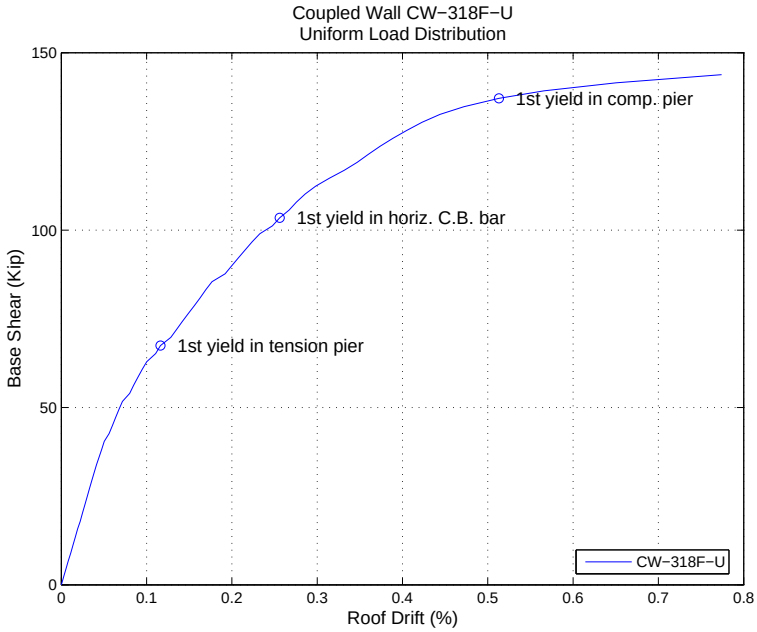

Figure 6.32: CW-318HF-U Roof Drift vs. Base Shear Response

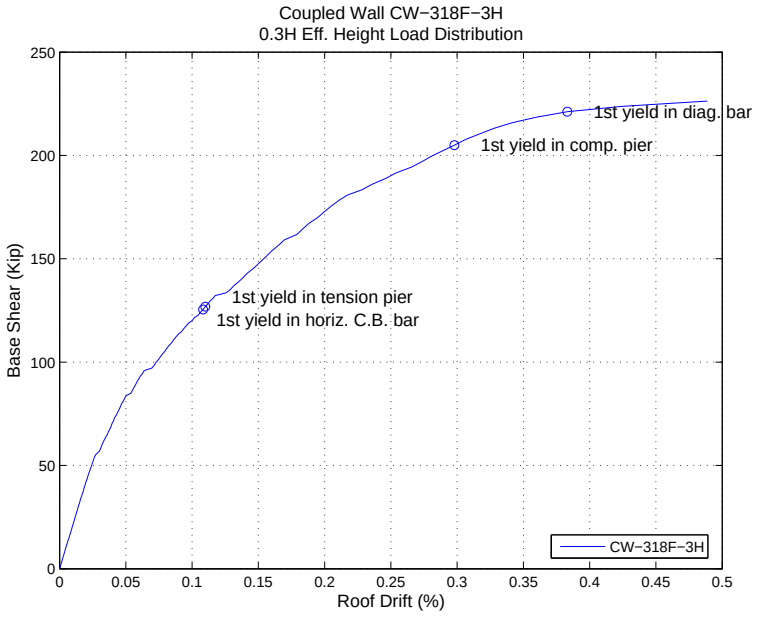

Figure 6.33: CW-318HF-3H Roof Drift vs. Base Shear Response

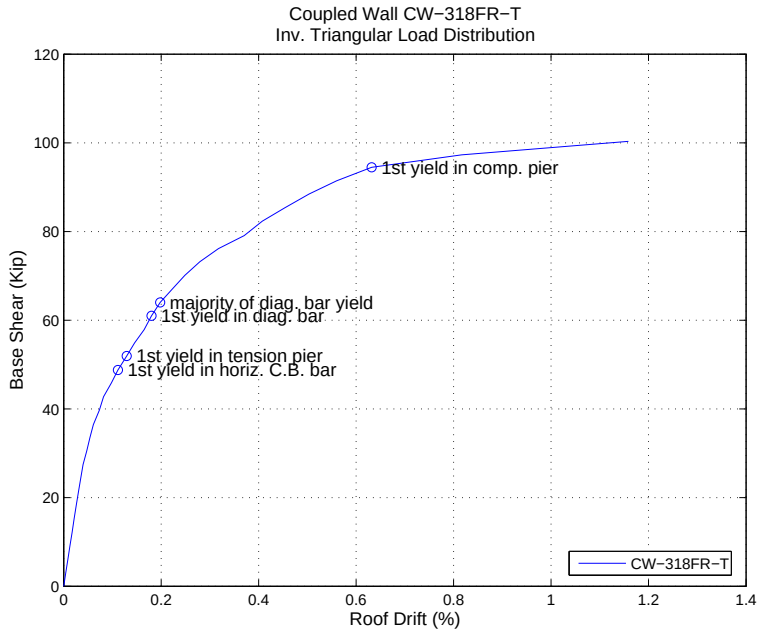

Figure 6.34: CW-318HFR-T Roof Drift vs. Base Shear Response

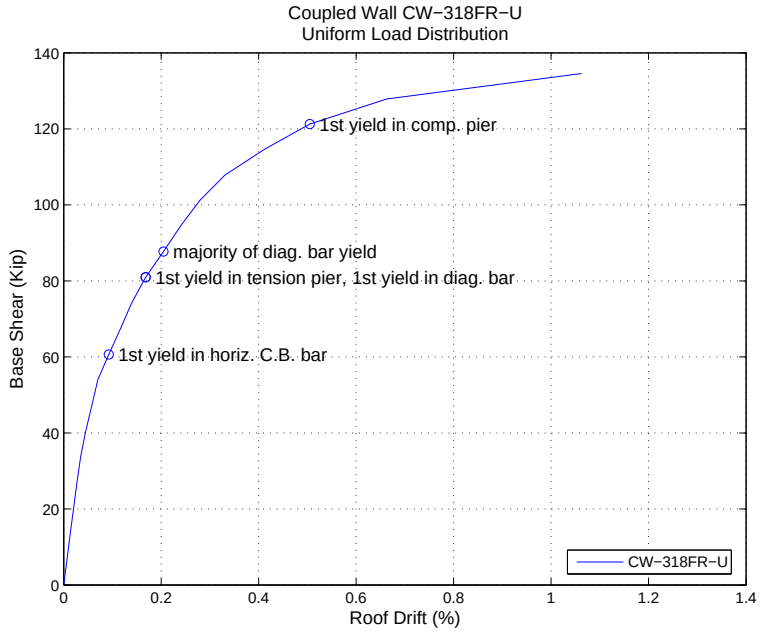

Figure 6.35: CW-318HFR-U Roof Drift vs. Base Shear Response

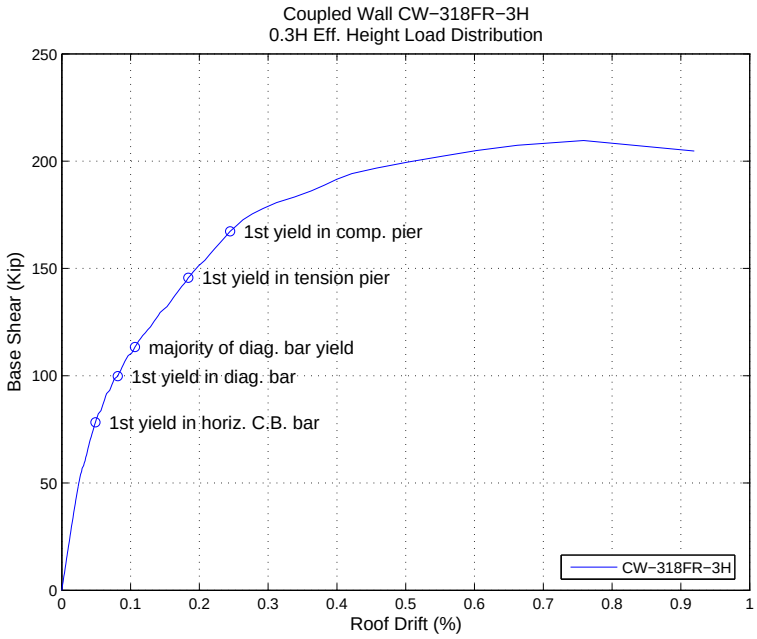

Figure 6.36: CW-318HFR-3H Roof Drift vs. Base Shear Response

6.12 Conclusions

Evaluation of the VecTor2 simulation of the coupled wall modes supports the following observations and conclusions:

- VecTor2 should not be used to complete a displacement based pushover analysis where the displaced shape of the model may change during the simulation.

- The effects of the lateral load distribution can be related to the effective shear height of the applied load. A higher effective shear height (i.e. inverted triangular distribution) will cause the coupled wall to develop a smaller base shear and will allow it to reach a higher roof drift. Conversely, a lower effective shear height (i.e. 0.3H effective shear height distribution) will cause the coupled wall to develop a higher base shear but will cause it to fail at a smaller roof drift. These results were expected and add support to the validity of the VecTor2 analysis software.

- The VecTor2 simulations shows that the "desired" plastic mechanism for a coupled wall, as recommended by the International Code Council (2007), is unlikely to occur in a coupled wall that is designed according to these recommendations. The coupling beams are too strong in comparison to the wall piers; yielding of the wall reinforcement and crushing failure at the toe of the wall occur before the coupling beams can be subjected to sufficient drift demands to cause yielding. The maximum coupling beam drift seen in the coupled wall models designed using the ICC recommendations was 0.21%, which is far below the 0.57% average yield drift predicted in Chapter 5.

- In order to achieve the desired plastic mechanism in the coupled wall, the shear and moment strength of the coupling beams was reduced to 25% of the design strength. This reduced strength was determined by balancing the area of steel in the diagonal reinforcement with the tensile stress demand in those bars at the design level base shear. The reduced strength of the coupling beams allowed the coupled wall to perform

as desired with plastic hinging at the base of the wall piers and at the ends of all the coupling beams. Despite the much lower shear and flexural strength of the coupling beams, the maximum base shear of the coupled wall was only reduced on average by 10%.

Chapter 7

SUMMARY AND CONCLUSIONS

7.1 Summary

A ten-story coupled shear wall specimen was designed using state of the art performance based design methods with the intent to provide a wall that will behave in a ductile manner under seismic loading. The coupled wall is designed to develop plastic hinges at the base of the wall piers and at the ends of all the coupling beams. Nonlinear finite element models were created and pushover simulations completed to predict the behavior of the wall. Multiple versions of the coupled wall with different coupling beam reinforcement were analyzed to investigate the effect of coupling beam confinement reinforcement and coupling beam strength on the behavior of the wall. The simulation results suggest that a coupled wall designed per current design recommendations will not behave as intended. The coupling beam strength must be greatly reduced in order to achieve the desired plastic mechanism and behavior mode.

The effects of coupling beam confinement on diagonally reinforced coupling beams were investigated. Coupling beams following the current code requirements, with confinement around the diagonal bar groups, were compared to proposed alternative design methods with full confinement of the entire beam section. Finite element simulations suggest that the proposed full confinement methods can meet or exceed the current detailing methods. Data from previous experimental studies of coupling beam behavior were used to validate the nonlinear analysis software and modeling assumptions.

7.2 Conclusions

The results of this study support the following observations and conclusions about coupling beam confinement effects and coupled shear wall behavior:

Coupling Beams

- The ACI 318H-CH047 proposed revision to increase the spacing requirements on the confinement ties around the diagonally placed reinforcement will have a negligible effect on the performance of the coupling beam, and is capable of meeting the design intent of the current ACI 318-05 specifications.

- VecTor2 simulations of coupling beams designed to meet the alternative design methods of the ACI 318H-CH047 proposal suggests that the shear strength and drift capacity of diagonally reinforced coupling beams can be increased by providing full confinement of the entire section.

Coupled Shear Walls

- The VecTor2 simulations shows that the "desired" plastic mechanism for a coupled wall, as recommended by the International Code Council (2007), is unlikely to occur in a coupled wall that is designed according to these recommendations. The coupling beams are too strong in comparison to the wall piers; yielding of the wall reinforcement and crushing failure at the toe of the wall occur before the coupling beams can be subjected to sufficient drift demands to cause yielding. The maximum coupling beam drift seen in the coupled wall models designed using the ICC recommendations was 0.21%, which is far below the 0.57% average yield drift predicted in Chapter 5.

- In order to achieve the desired plastic mechanism in the coupled wall, the shear and moment strength of the coupling beams was reduced to 25% of the design strength. The reduced strength of the coupling beams allowed the coupled wall to perform as

desired, with plastic hinging at the base of the wall piers and at the ends of the coupling beams. Despite the lower shear and flexural strength of the coupling beams, the maximum base shear of the coupled wall was only reduced on average by 10%.

7.3 Recommendations for Further Work

- Explore the effect of the coupling beam aspect ratio on the coupled wall performance. It is possible that the "desired" plastic mechanism may be easier to achieve if the coupling beam aspect ratio is larger.

- Find a way to model strength degradation portion of the coupled wall push-over curve. It would be useful to understand what the displacement capacity of the coupled wall system is after the maximum predicted base shear is reached.

- Complete the analysis of the coupled wall models under cyclic loading.

- Include the effects of gravity loads on the coupled wall model simulations.

- Develop a design methodology that can provide a coupled wall that will allow yielding in the wall piers and at the ends of all the coupling beams.

- Develop a method to account for the over-strenth in coupling beams that are confined with the full confinement method proposed in ACI 319H-CH047.

BIBLIOGRAPHY

ACI Committee 318 (2005). *Building Code Requirements for Structural Concrete and Commentary*. Farmington Hills, Mich.: American Concrete Institute. 430 pp.

Bristowe, S. (2000). *Seismic Response of Normal and High Strength Concrete Members*. Ph. D. thesis, McGill University, Montreal, Quebec, Canada. 244 pp.

Brown, P. (2006). Probabilistic earthquake damage prediction for reinforced concrete building components. Master's thesis, University of Washington, Seattle.

Canadian Standards Association (2004). *CSA A23.3-04: Design of Concrete Structures*. CSA International. 240 pp.

Galano, L. and A. Vignoli (2000, November). Seismic behavior of short coupling beams with different reinforcement layouts. *ACI Structural Journal 97*(6), 876–885.

Harries, K. A. (2001, August). Ductility and Deformability of Coupling Beams in Reinforced Concrete Coupled Walls. *Earthquake Spectra 17*(3), 457–478.

Harries, K. A., P. J. Fortney, B. M. Shahrooz, and P. J. Brienen (2005, November). Practical Design of Diagonally Reinforced Concrete Coupling Beams - Critical Review of ACI 318 Requirements. *ACI Structural Journal 102*(6), 876–882.

Harries, K. A., B. Gong, and B. M. Shahrooz (2000, November). Behavior and Design of Reinforced Concrete, Steel, and Steel-Concrete Coupling Beams. *Earthquake Spectra 16*(4), 775–799.

Harries, K. A., J. D. Moulton, and R. L. Clemson (2004, March). Parametric Study of Coupled Wall Behavior - Implications for the Design of Coupling Beams. *Journal of Structural Engineering 130*(3), 480–488.

International Code Council (January 2007). *2006 IBC Structural/Seismic Design Manual*, Volume 3. ICC.

Kwan, A. K. H. and Z. Z. Zhao (2002a, August). Cyclic behavior of deep reinforced concrete coupling beams. *Structures & Buildings 152*(3), 283–293.

Kwan, A. K. H. and Z. Z. Zhao (2002b, February). Testing of coupling beams with equal end rotations maintained and local joint deformations allowed. *Structures & Buildings 152*(1), 67–78.

MATLAB (2005). Version 7.1. The MathWorks. www.mathworks.com/.

New Zealand Standards Association (2006). *NZS 3101 Parts 1 and 2: 2006 Concrete Structures Standard*. New Zealand Standards Association. 646 pp.

Oyen, P. (2006). Evaluation of analytical tools for determining the seismic response of reinforced concrete shear walls. Master's thesis, University of Washington, Seattle.

Paulay, T. (1971). Coupling beams of reinforced concrete shear walls. *Journal of the Structural Division, ASCE 97*(ST3), 843–862.

Paulay, T. and J. R. Binney (1974). Diagonally Reinforced Coupling Beams of Shear Walls. *ACI Special Publication 42 - Shear in Reinforced Concrete*, 579–598.

Santhakumar, A. R. (1974). *Ductility of Coupled Shear Walls*. Ph. D. thesis, University of Canterbury, New Zealand.

SAP2000 (2006). Version 9.2. Computers and Structures, Inc. www.csiberkeley.com/.

Shiu, K. N., A. E. Fiorato, G. B. Barney, and W. G. Corley (1978). Reversing load tests of reinforced concrete coupling beams. *Central American Conference on Earthquake Engineering*, 239–249.

Structural Engineering Institute (2006). *Minimum Design Loads for Buildings And Other Structures: ASCE/SEI 7-05 (ASCE Standard No. 7-05)*. Reston, Virginia: American Society of Civil Engineers. 424 pp.

Tassios, T. P., M. Maretti, and A. Bezas (1996, November). On the behavior and ductility of reinforced concrete coupling beams of shear walls. *ACI Structural Journal 93*(6), 711–720.

Tegos, I. A. and G. G. Penelis (1988). Seismic resistance of short columns and coupling beams reinforced with inclined bars. *ACI Structural Journal 85*(1), 82–88.

Vecchio, F. J. (2000). Disturbed stress field model for reinforced concrete: Formulation. *Journal of Structural Engineering 126*(9), 1070–1077.

Vecchio, F. J. (2001). Disturbed stress field model for reinforced concrete: Implementation. *Journal of Structural Engineering 127*(1), 12–20.

Vecchio, F. J. and M. P. Collins (1986). The modified compression-field theory for reinforced concrete elements subject to shear. *Journal of the American Concrete Institute 83*(2), 258–268.

Vecchio, F. J. and P. S. Wong (2006). *VecTor2 & FormWorks User's Manual*. Vector Analysis Group, University of Toronto. 201 pp.

VecTor2 (2006). Version 2.3. Vector Analysis Group. www.civ.utoronto.ca/vector/.

Zhao, Z. Z., A. K. H. Kwan, and X. G. He (2004, January). Nonlinear finite element analysis of deep reinforced concrete coupling beams. *Engineering Structures 26*(1), 13–25.

Appendix A

EXPERIMENTAL COUPLING BEAM LOAD DISPLACEMENT PLOTS

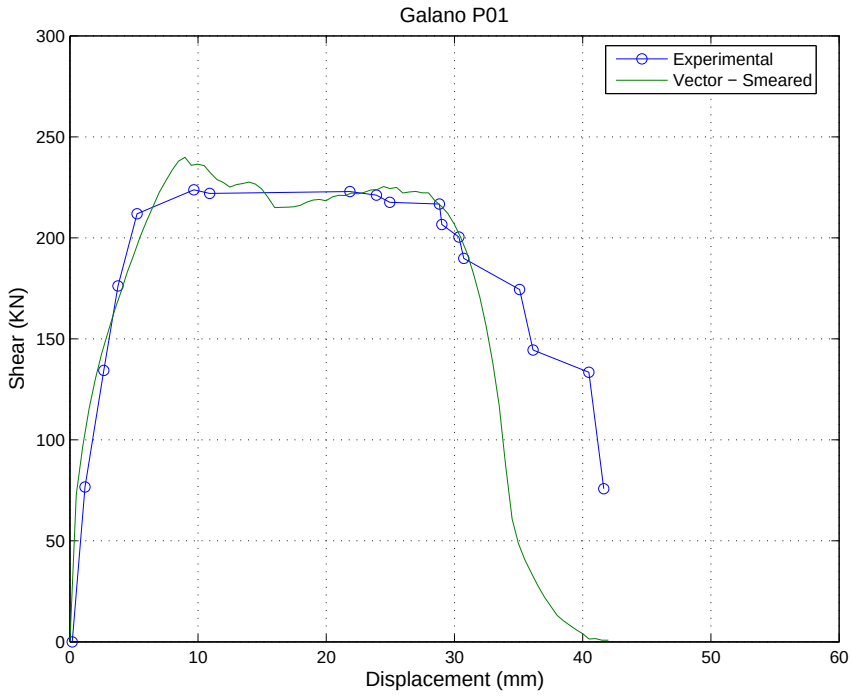

Figure A.1: Galano P01 - Vector2 Force-Disp. Smeared Reinf.

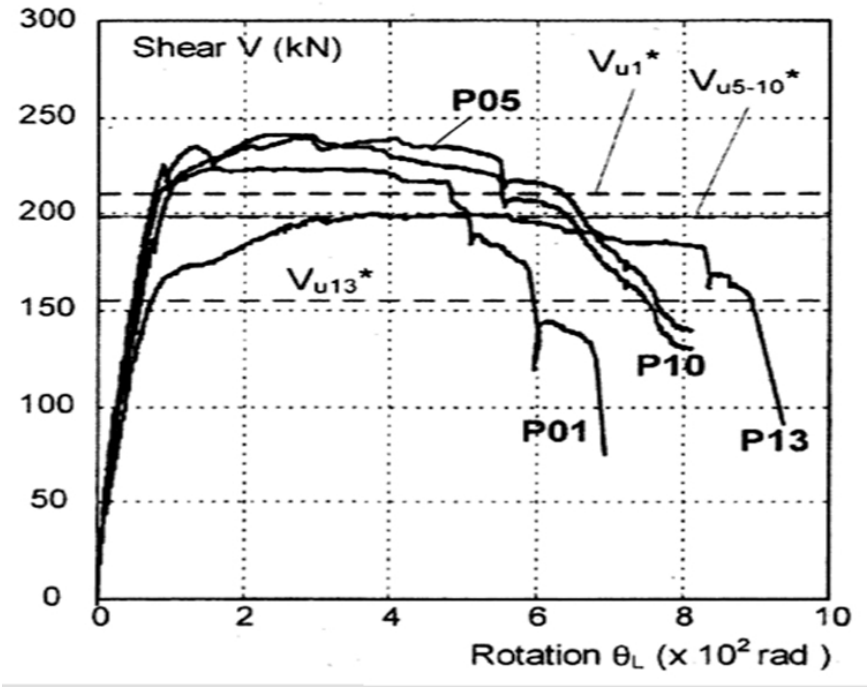

Figure A.2: Galano - Experimental Force-Disp. Plot

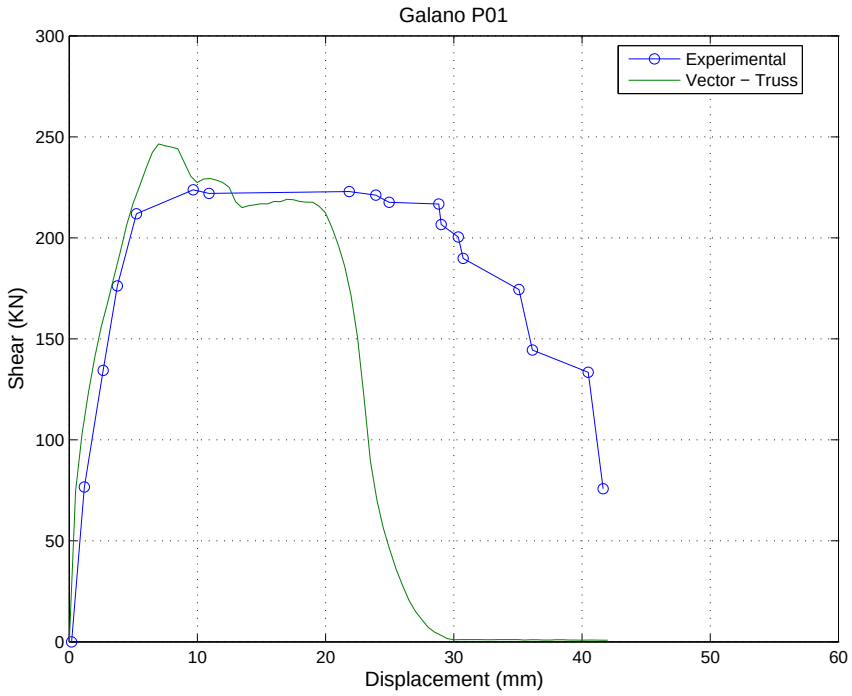

Figure A.3: Galano P01 - Vector2 Force-Disp. Truss Reinf.

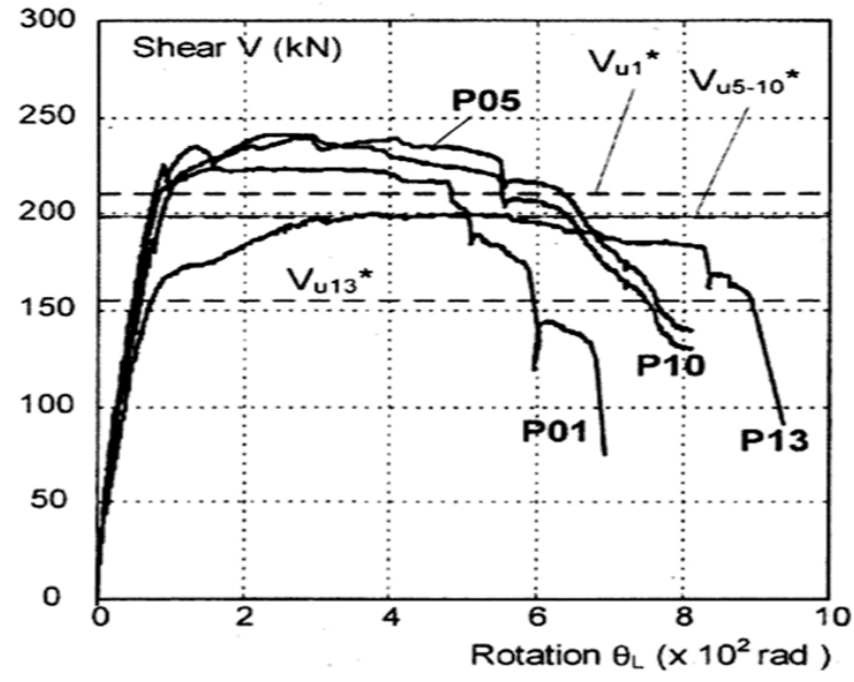

Figure A.4: Galano - Experimental Force-Disp. Plot

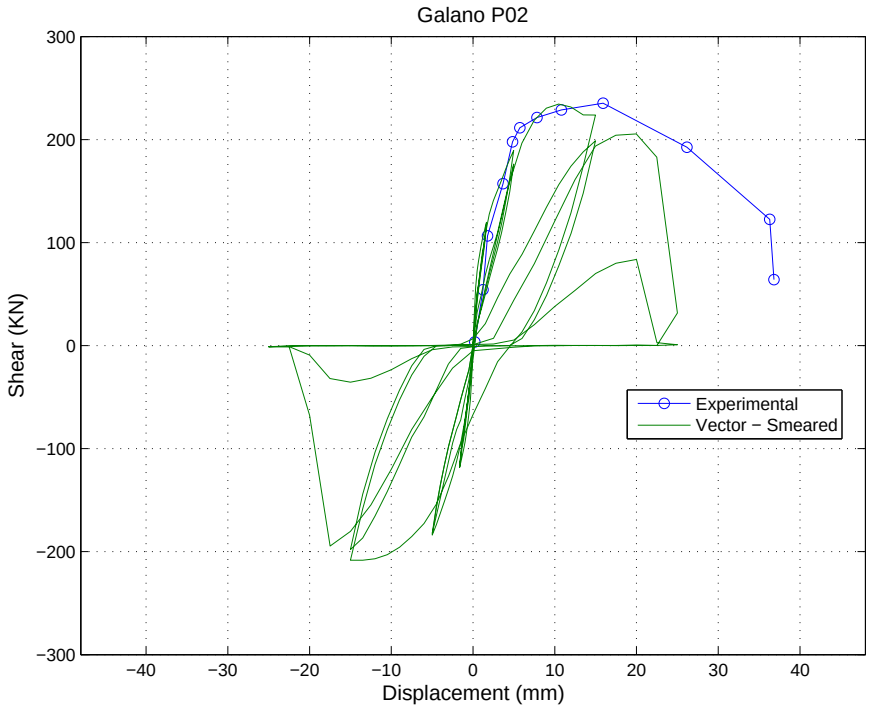

Figure A.5: Galano P02 - Vector2 Force-Disp. Smeared Reinf.

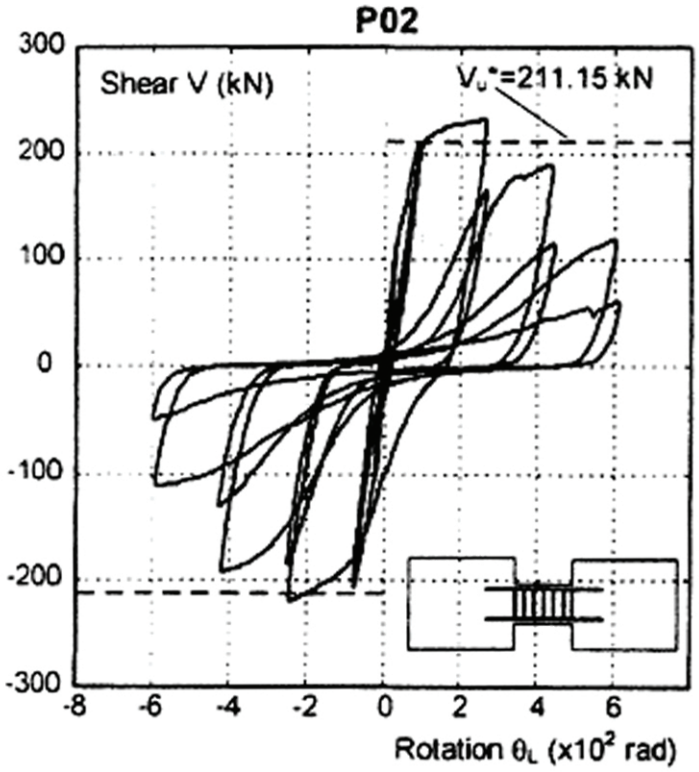

Figure A.6: Galano P02 - Experimental Force-Disp. Plot

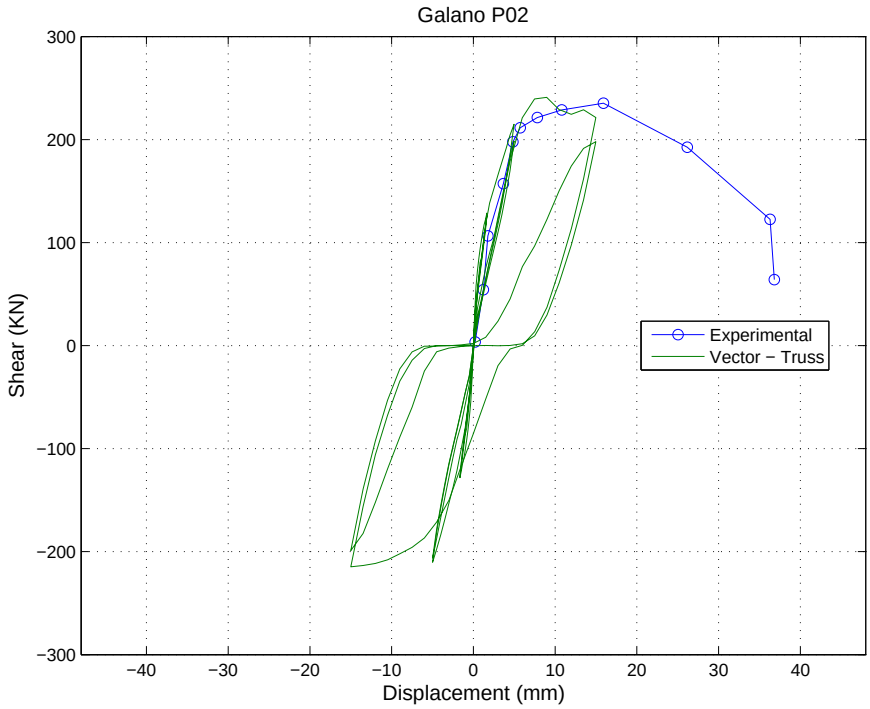

Figure A.7: Galano P02 - Vector2 Force-Disp. Truss Reinf.

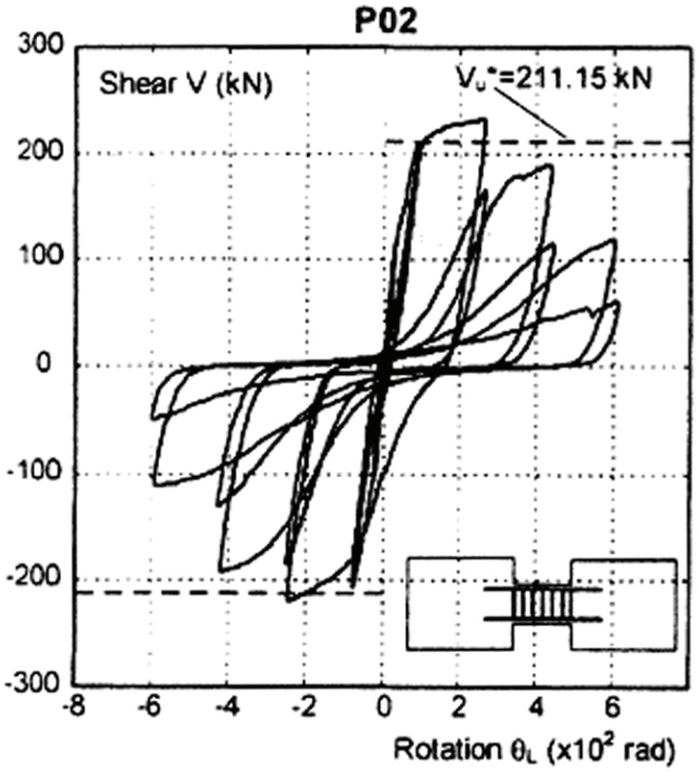

Figure A.8: Galano P02 - Experimental Force-Disp. Plot

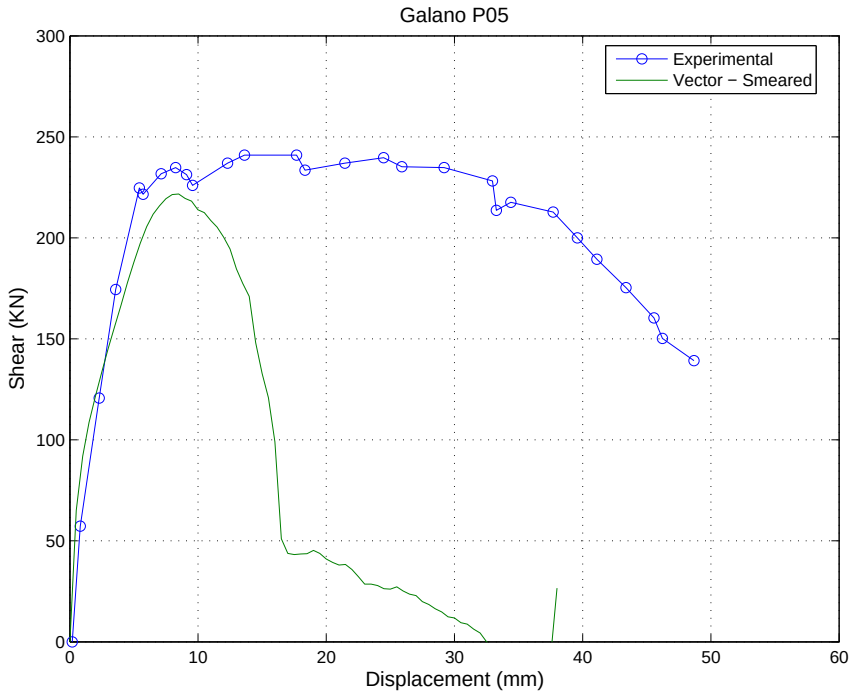

Figure A.9: Galano P05 - Vector2 Force-Disp. Smeared Reinf.

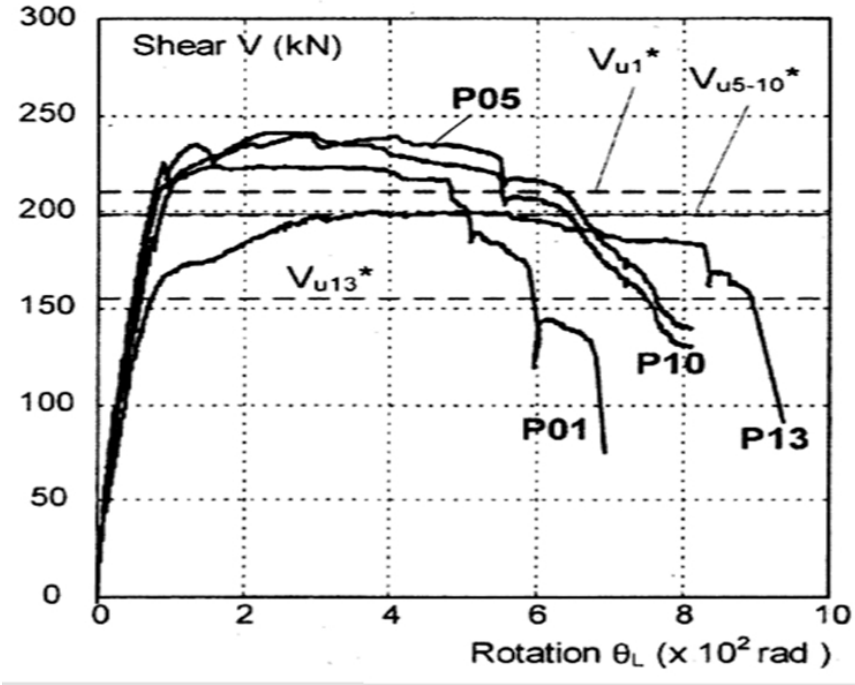

Figure A.10: Galano - Experimental Force-Disp. Plot

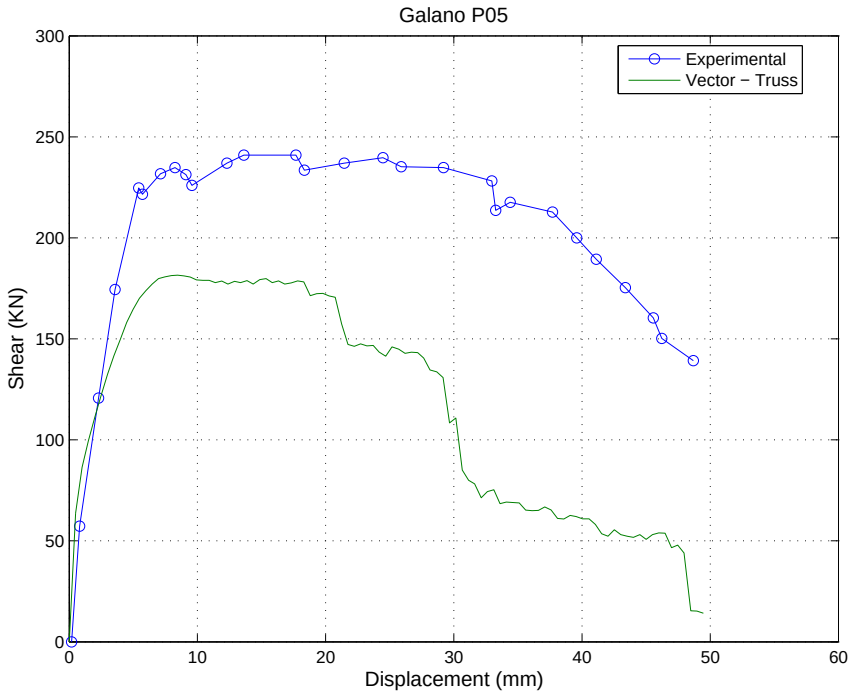

Figure A.11: Galano P05 - Vector2 Force-Disp. Truss Reinf.

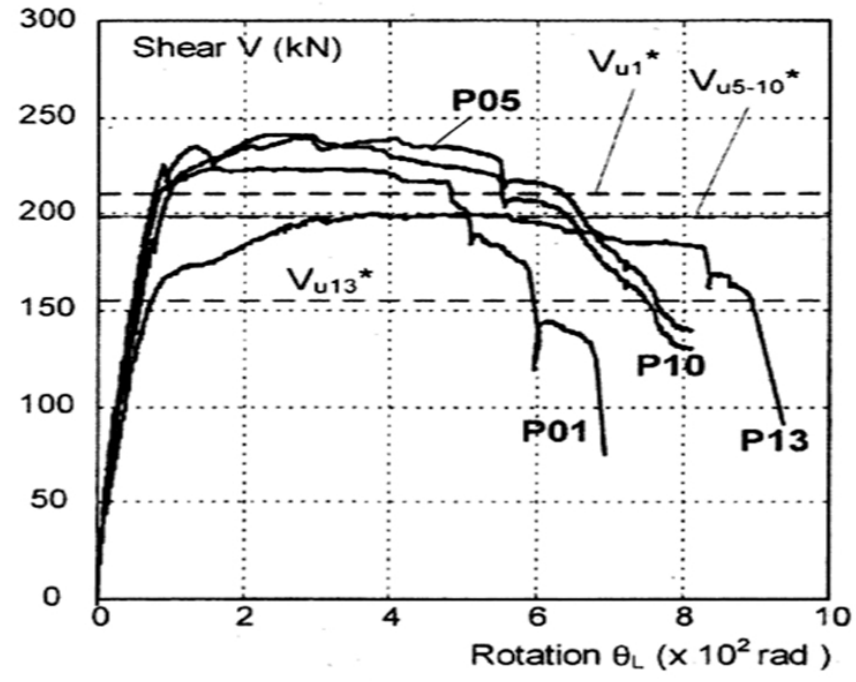

Figure A.12: Galano - Experimental Force-Disp. Plot

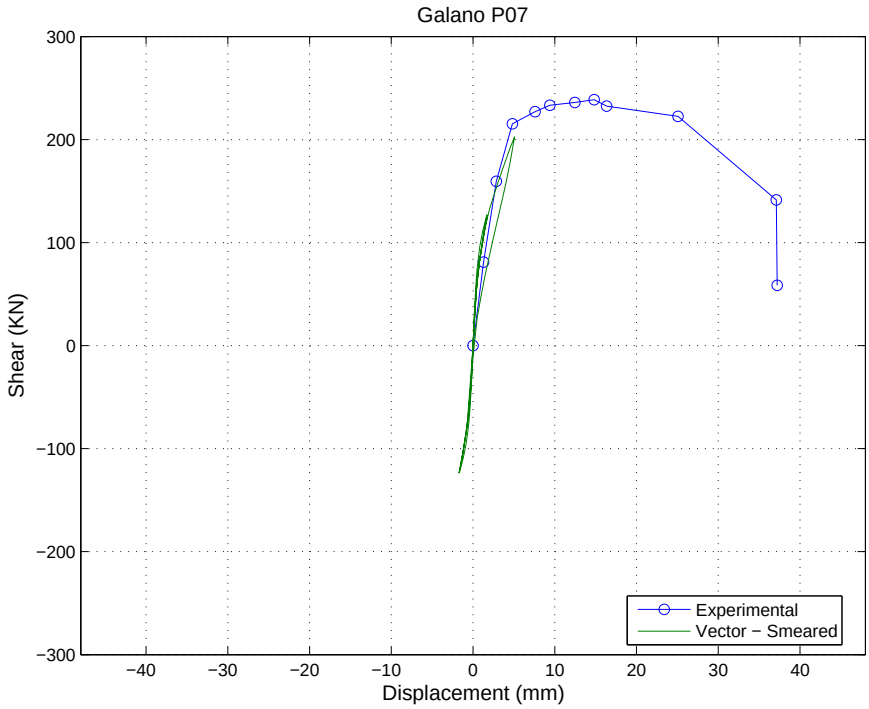

Figure A.13: Galano P07 - Vector2 Force-Disp. Smeared Reinf.

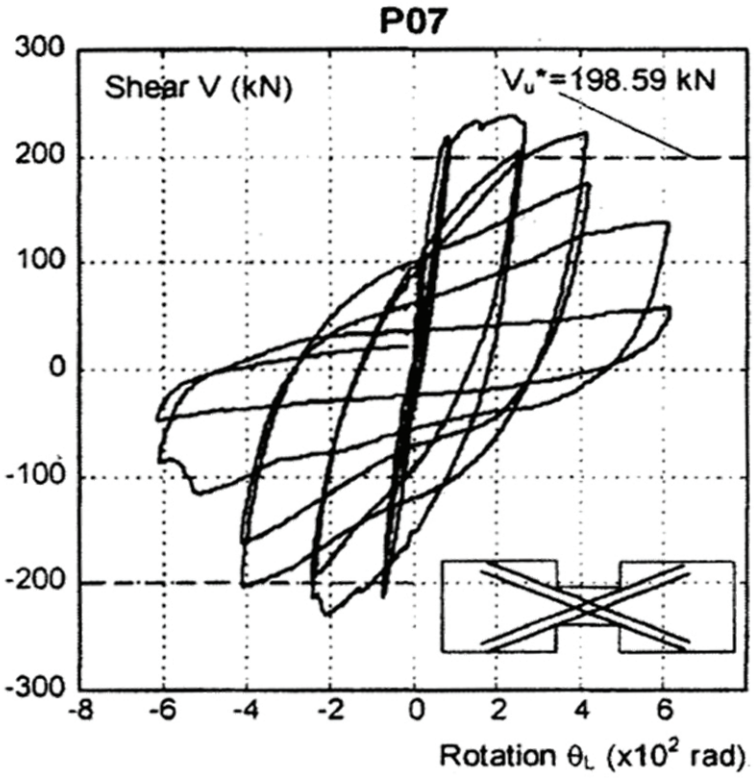

Figure A.14: Galano P07 - Experimental Force-Disp. Plot

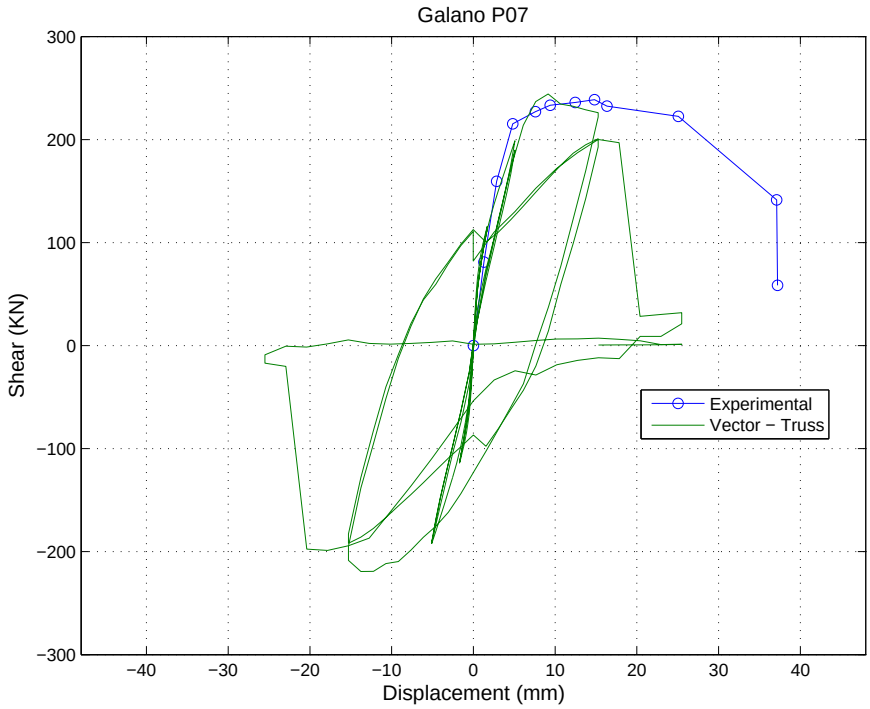

Figure A.15: Galano P07 - Vector2 Force-Disp. Truss Reinf.

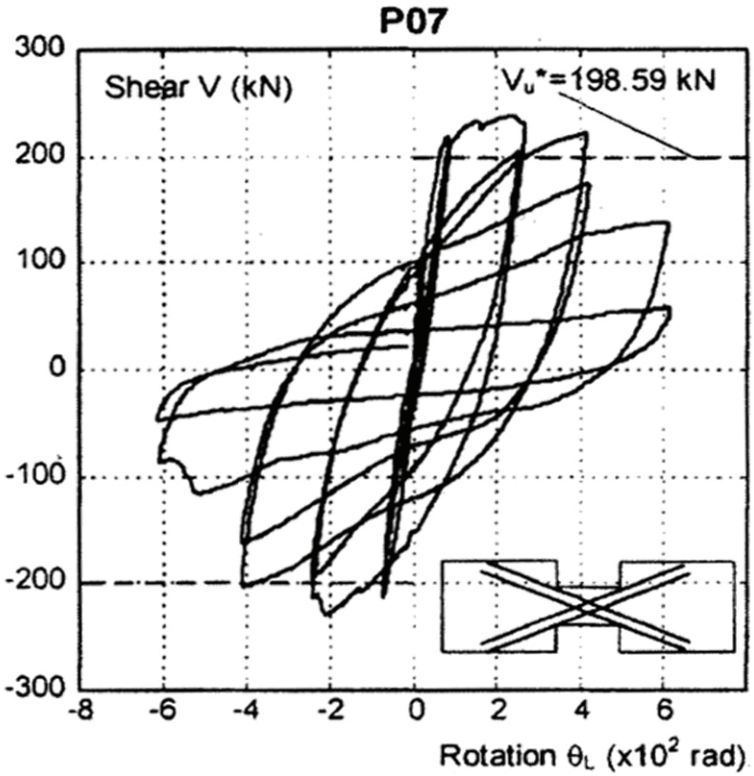

Figure A.16: Galano P07 - Experimental Force-Disp. Plot

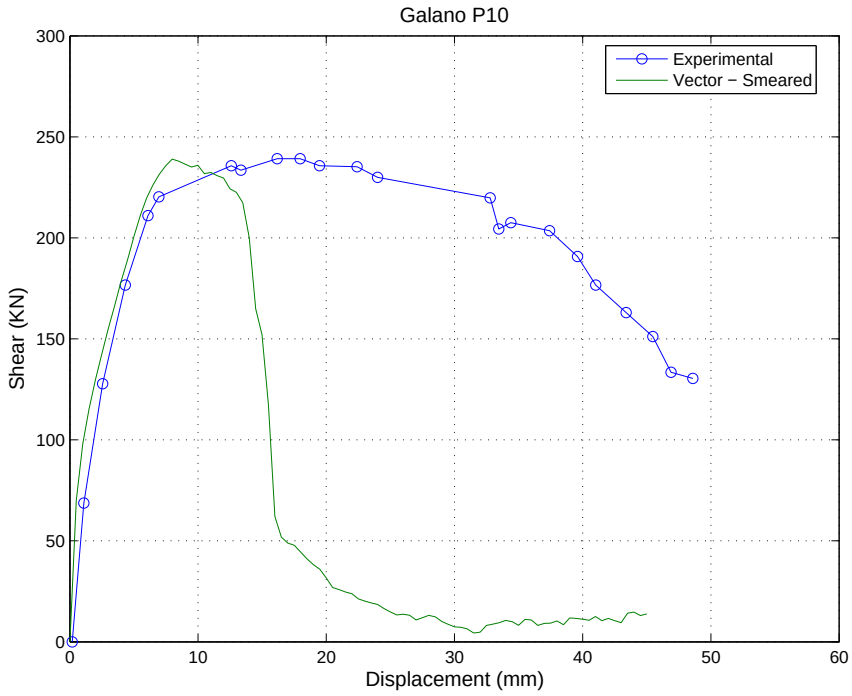

Figure A.17: Galano P10 - Vector2 Force-Disp. Smeared Reinf.

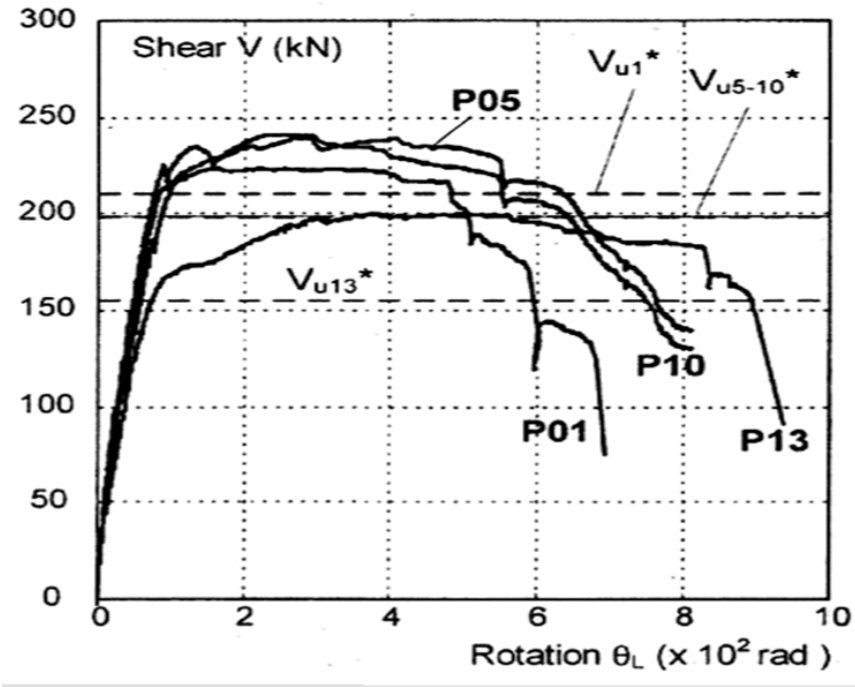

Figure A.18: Galano - Experimental Force-Disp. Plot

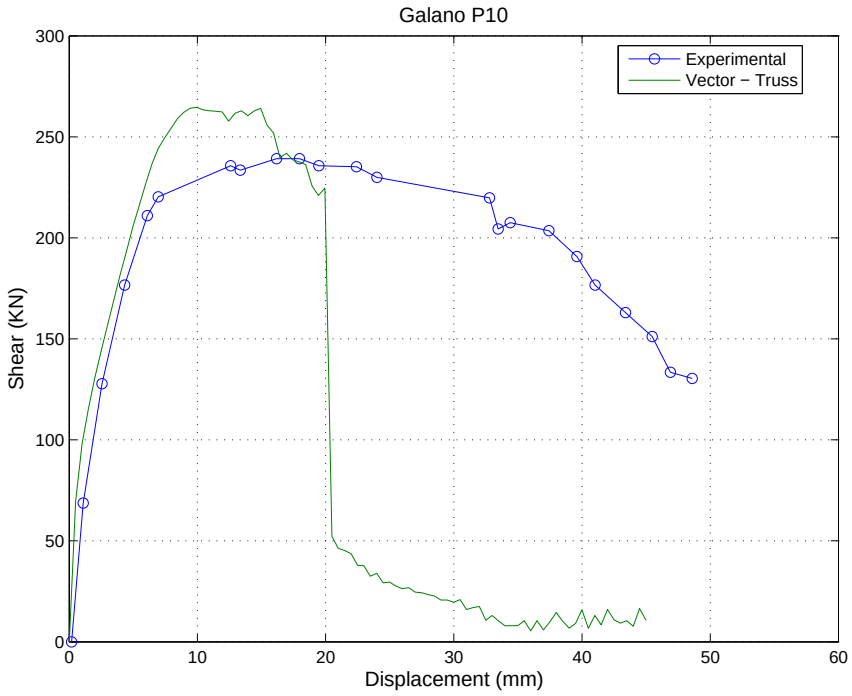

Figure A.19: Galano P10 - Vector2 Force-Disp. Truss Reinf.

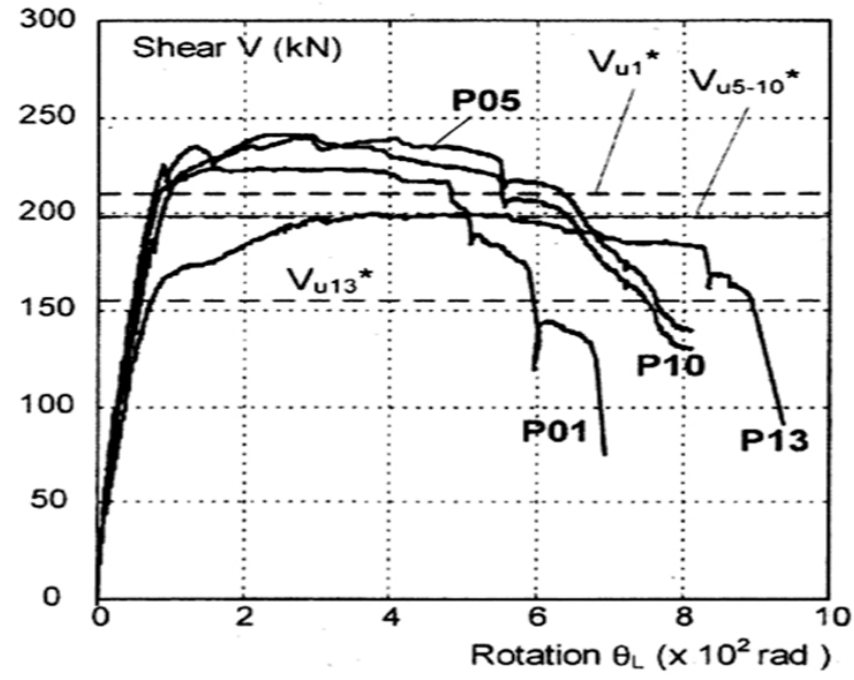

Figure A.20: Galano - Experimental Force-Disp. Plot

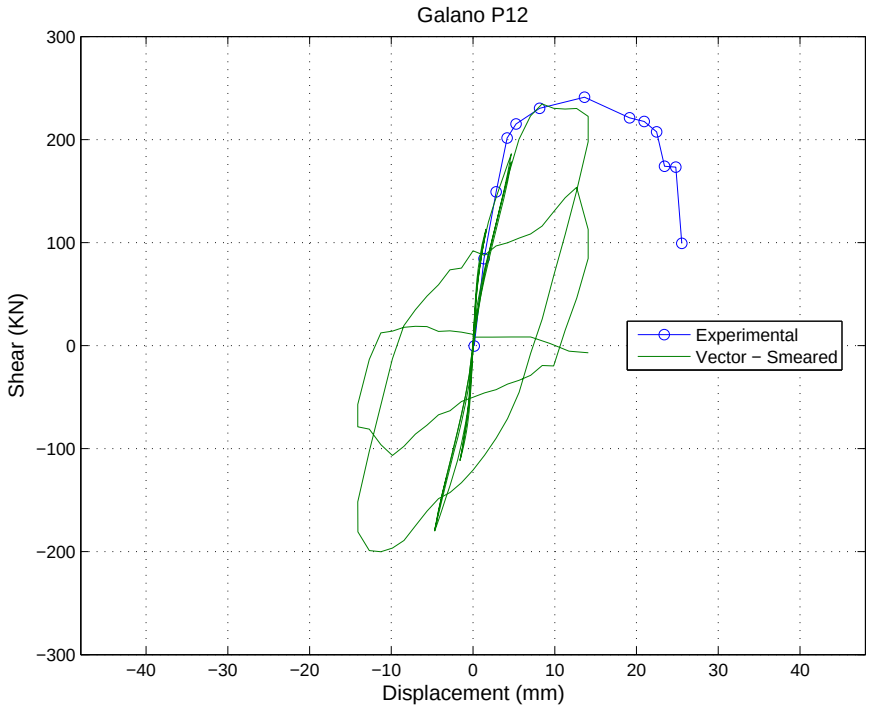

Figure A.21: Galano P12 - Vector2 Force-Disp. Smeared Reinf.

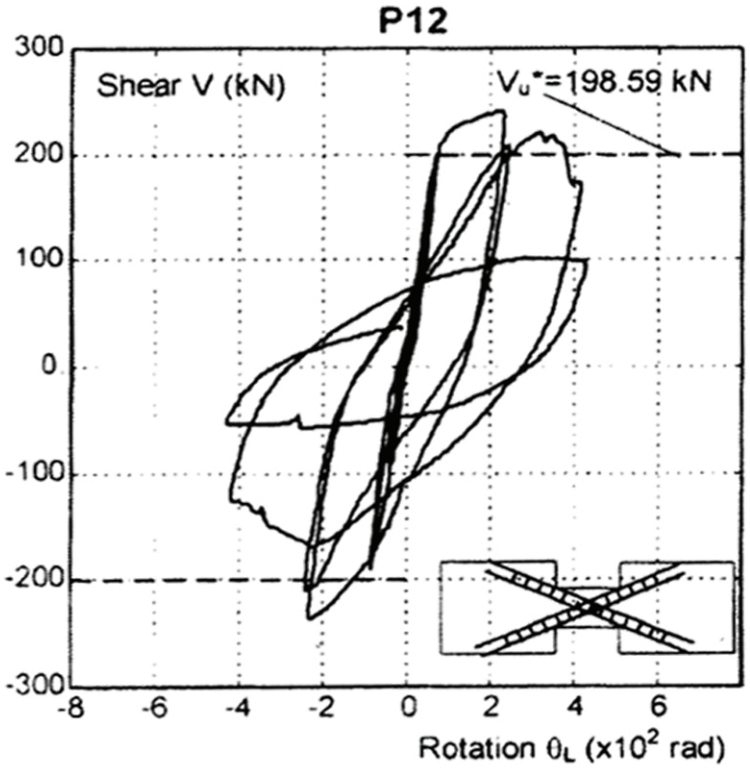

Figure A.22: Galano P12 - Experimental Force-Disp. Plot

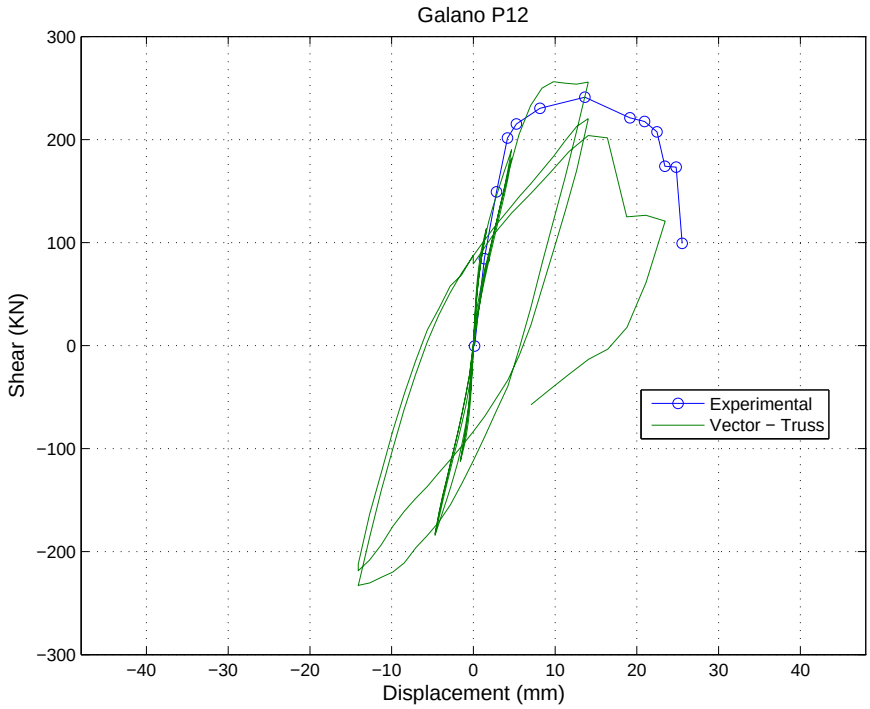

Figure A.23: Galano P12 - Vector2 Force-Disp. Truss Reinf.

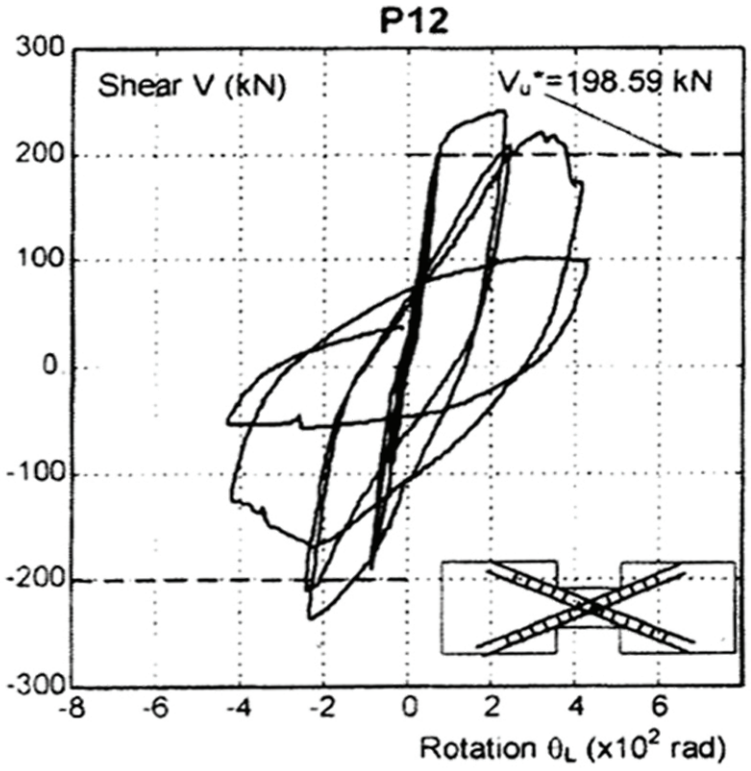

Figure A.24: Galano P12 - Experimental Force-Disp. Plot

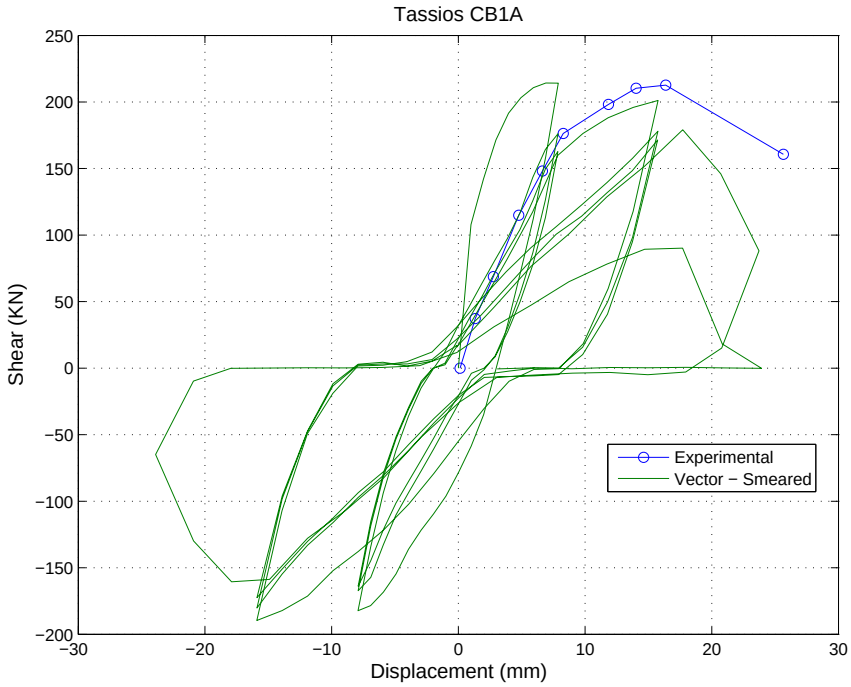

Figure A.25: Tassios CB1A - Vector2 Force-Disp. Smeared Reinf.

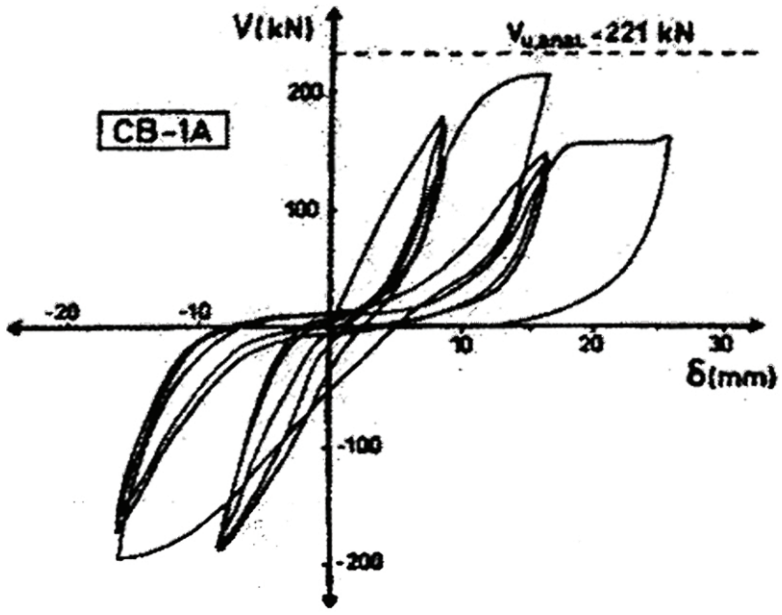

Figure A.26: Tassios CB1A - Experimental Force-Disp. Plot

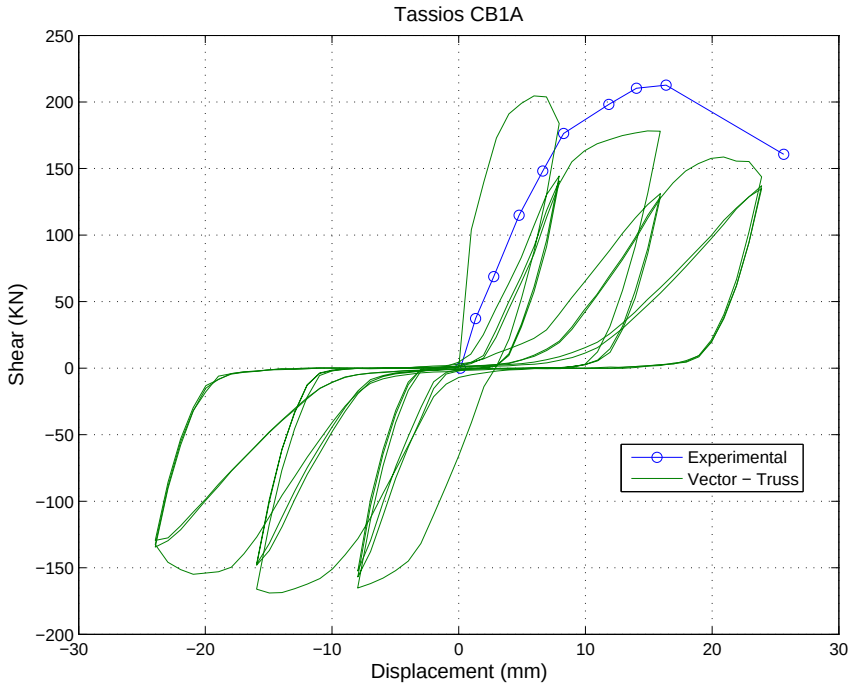

Figure A.27: Tassios CB1A - Vector2 Force-Disp. Truss Reinf.

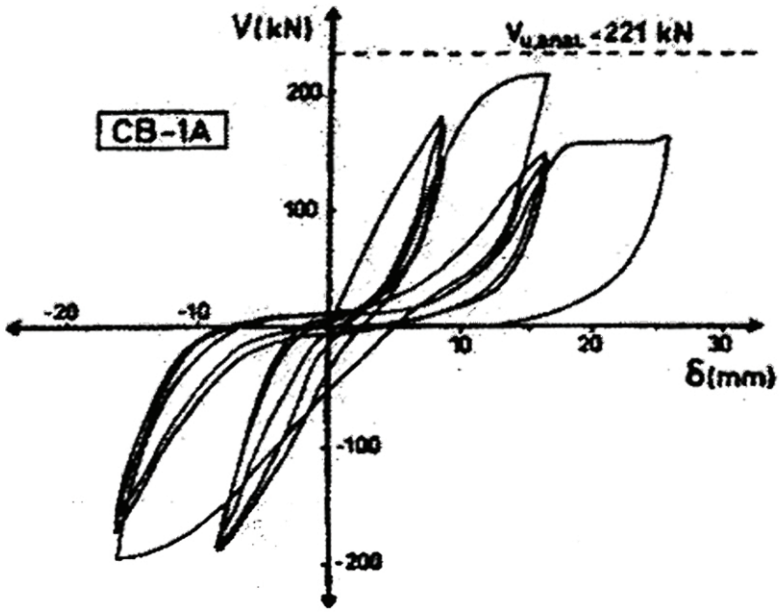

Figure A.28: Tassios CB1A - Experimental Force-Disp. Plot

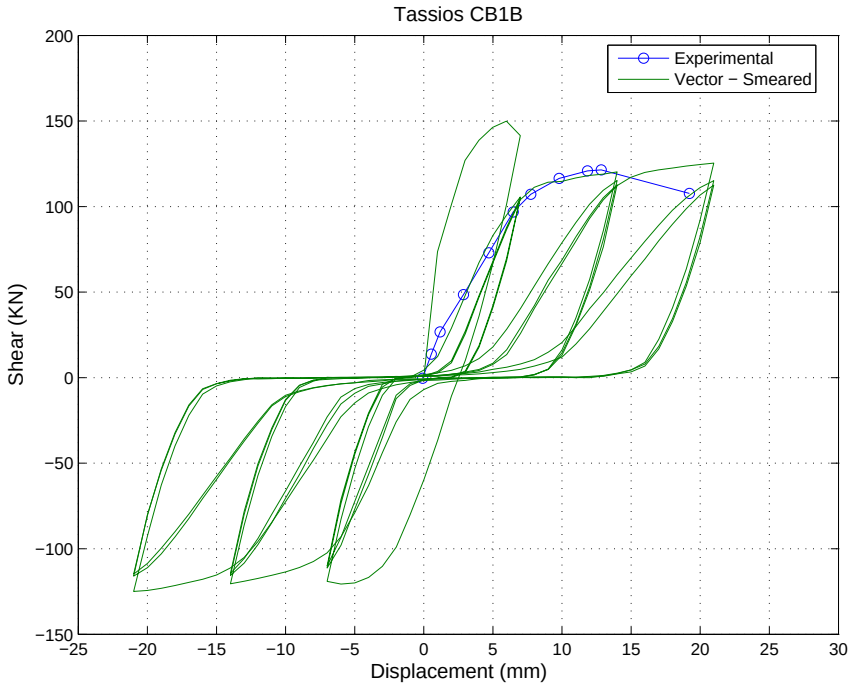

Figure A.29: Tassios CB1B - Vector2 Force-Disp. Smeared Reinf.

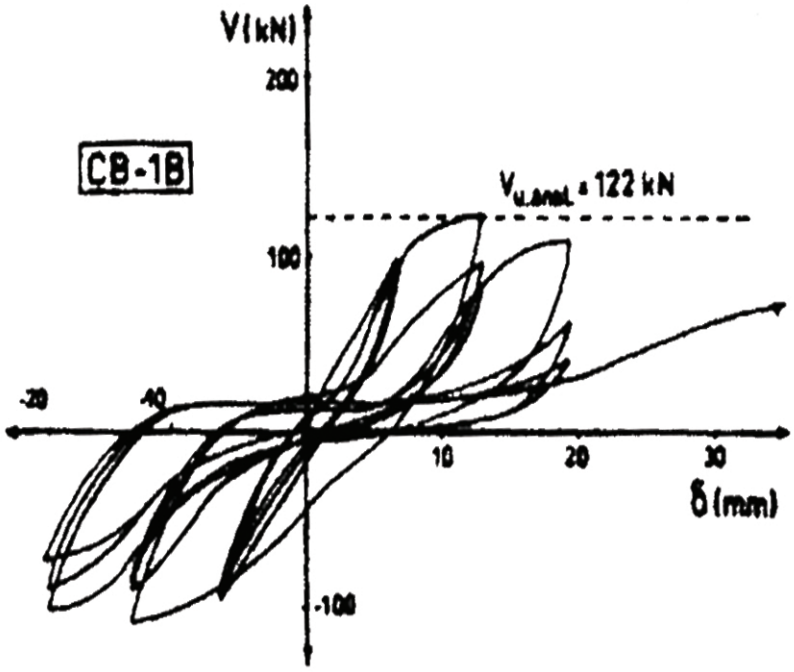

Figure A.30: Tassios CB1B - Experimental Force-Disp. Plot

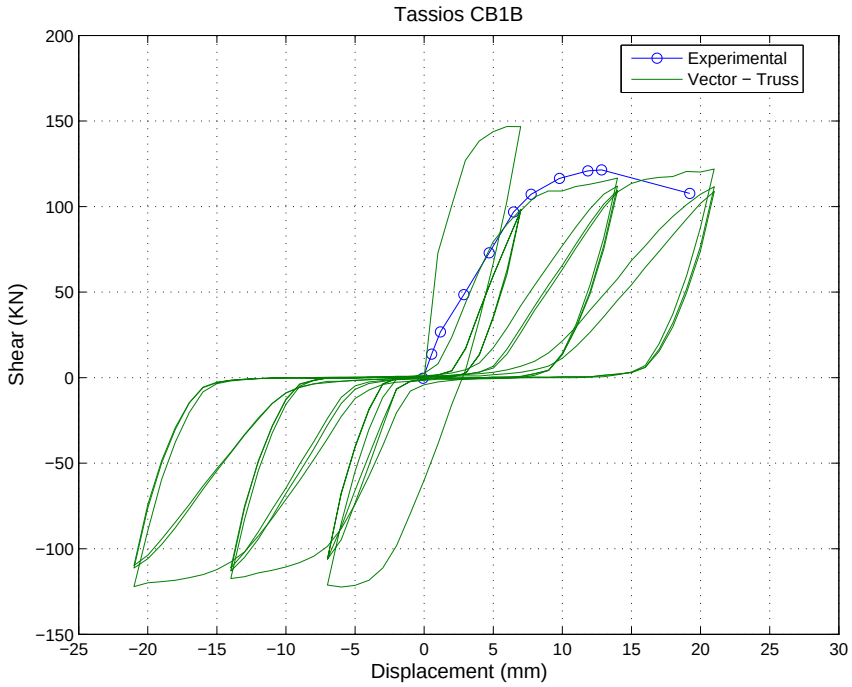

Figure A.31: Tassios CB1B - Vector2 Force-Disp. Truss Reinf.

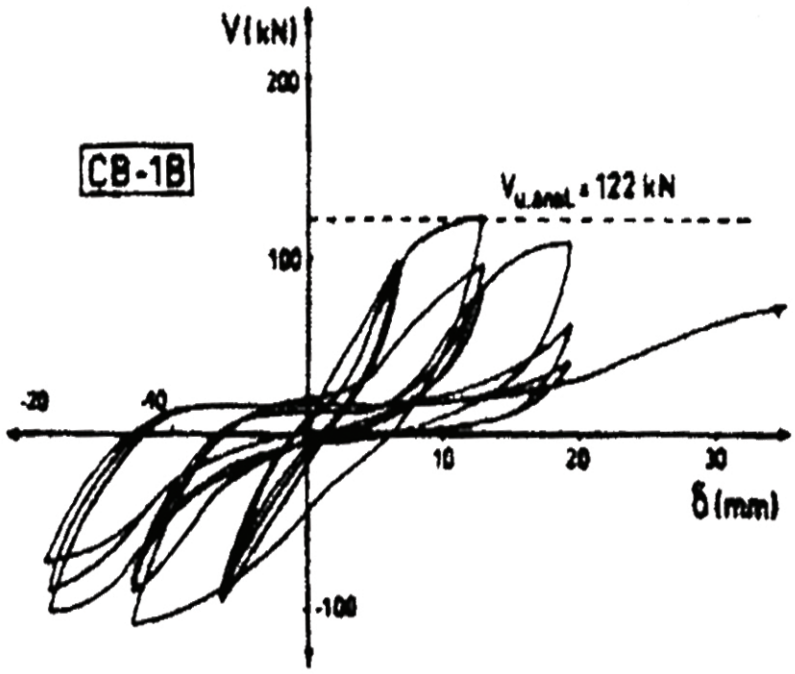

Figure A.32: Tassios CB1B - Experimental Force-Disp. Plot

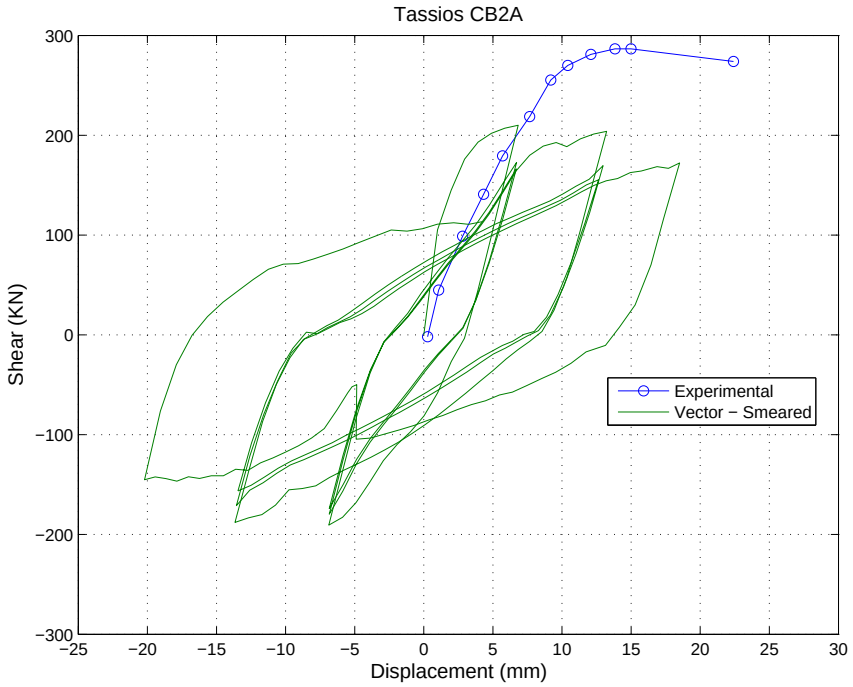

Figure A.33: Tassios CB2A - Vector2 Force-Disp Smeared Reinf.

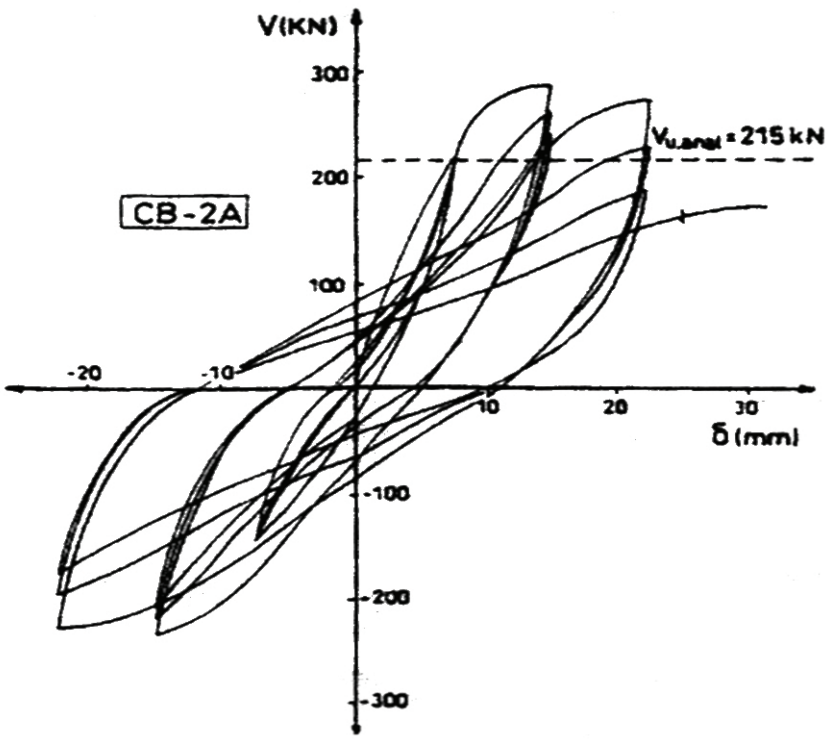

Figure A.34: Tassios CB2A - Experimental Force-Disp. Plot

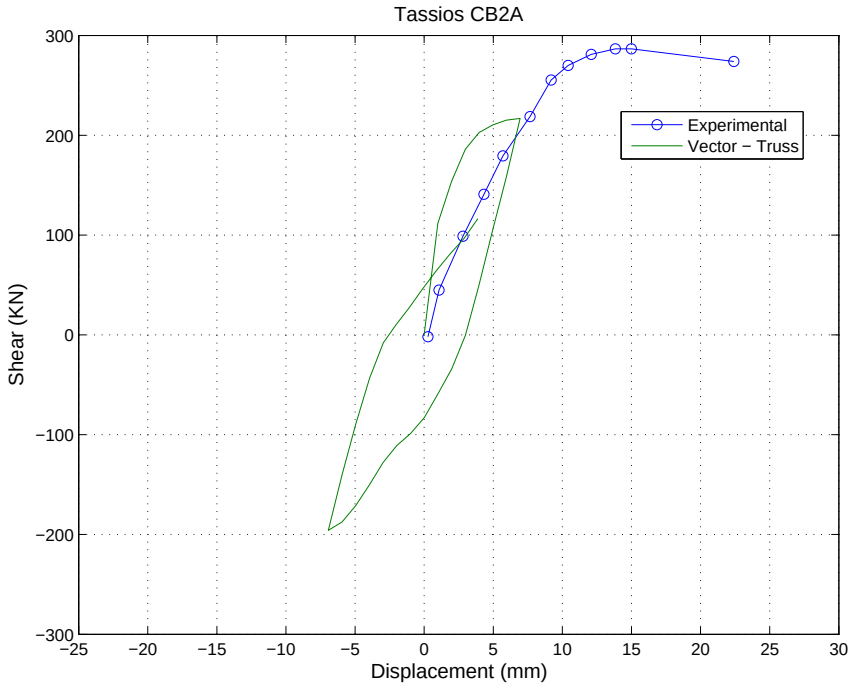

Figure A.35: Tassios CB2A - Vector2 Force-Disp Truss Reinf.

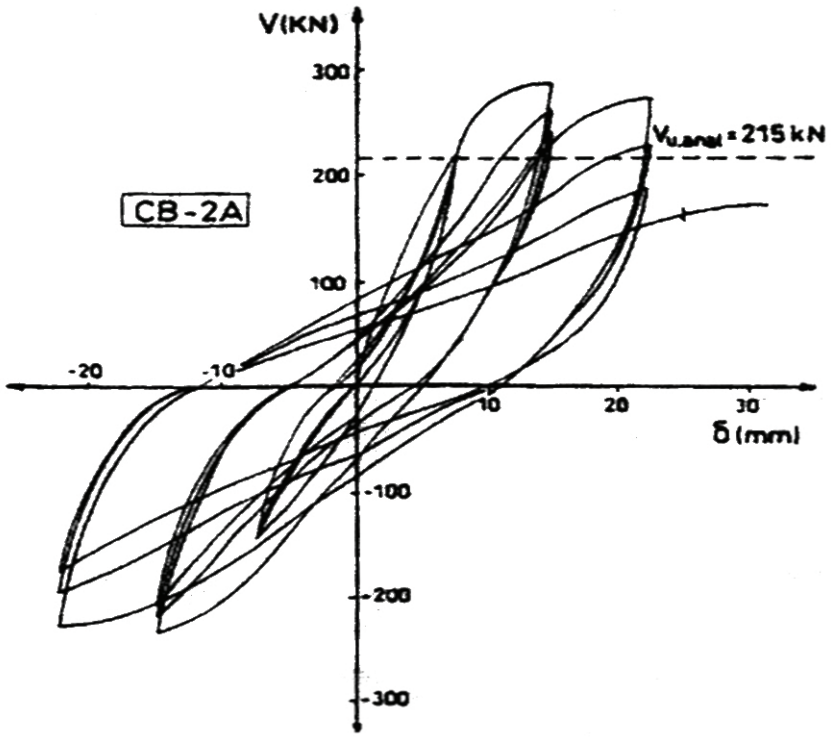

Figure A.36: Tassios CB2A - Experimental Force-Disp. Plot

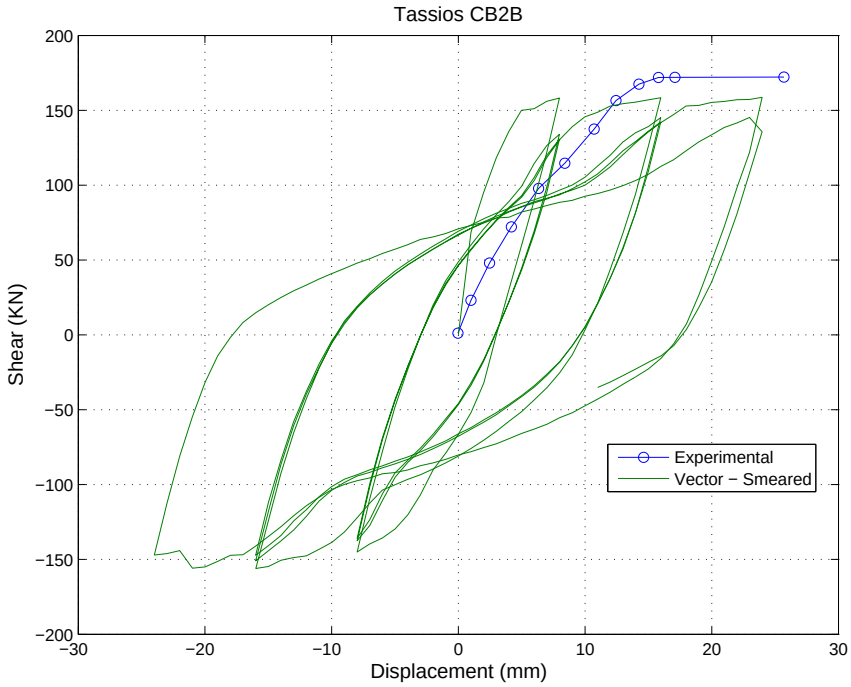

Figure A.37: Tassios CB2B - Vector2 Force-Disp Smeared Reinf.

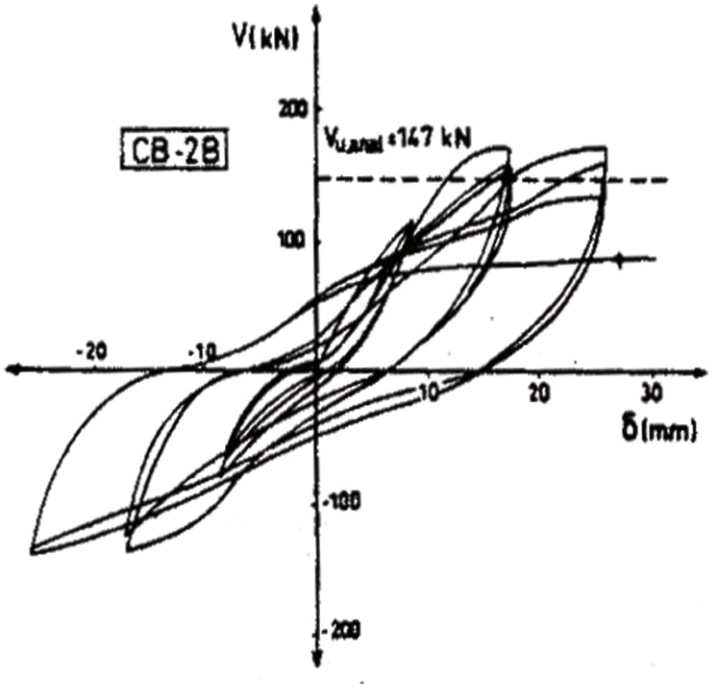

Figure A.38: Tassios CB2B - Experimental Force-Disp. Plot

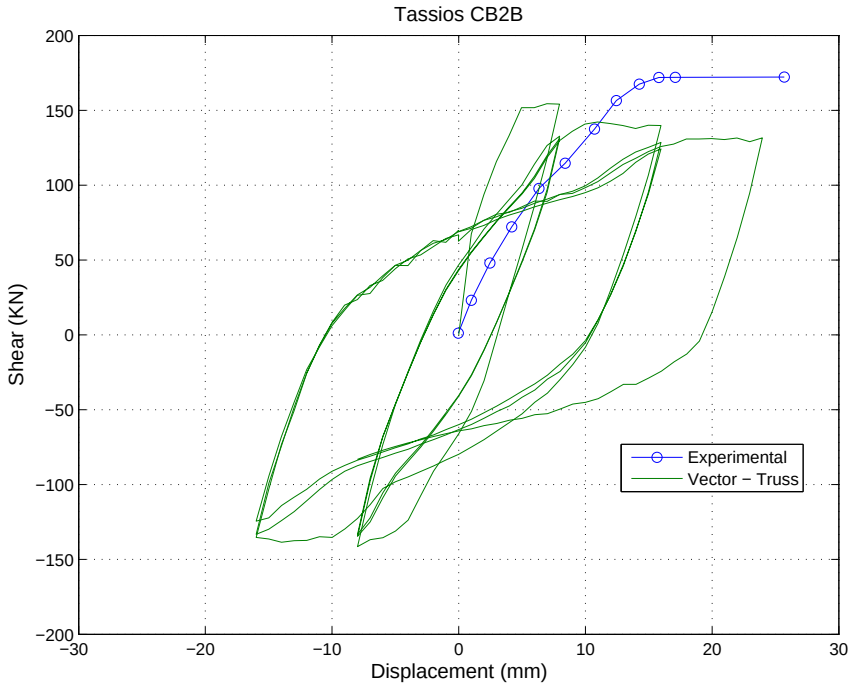

Figure A.39: Tassios CB2B - Vector2 Force-Disp Smeared Reinf.

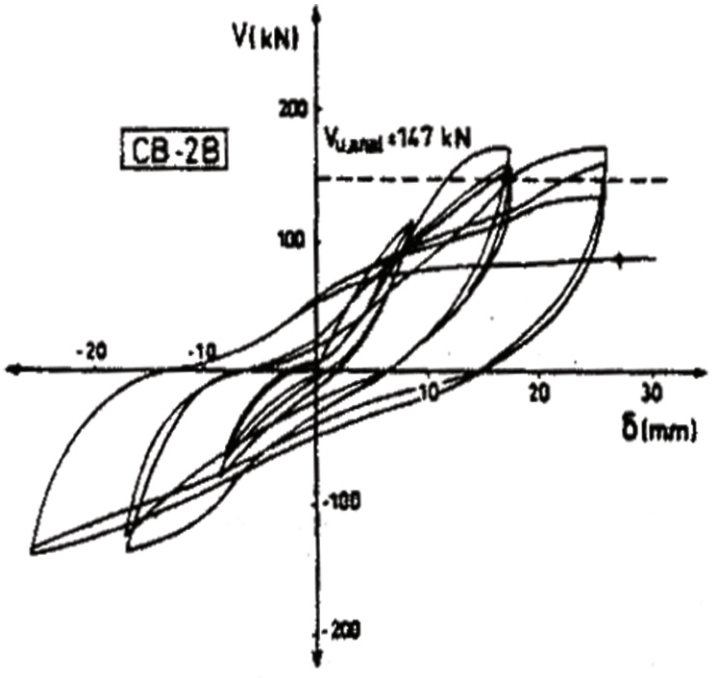

Figure A.40: Tassios CB2B - Experimental Force-Disp. Plot

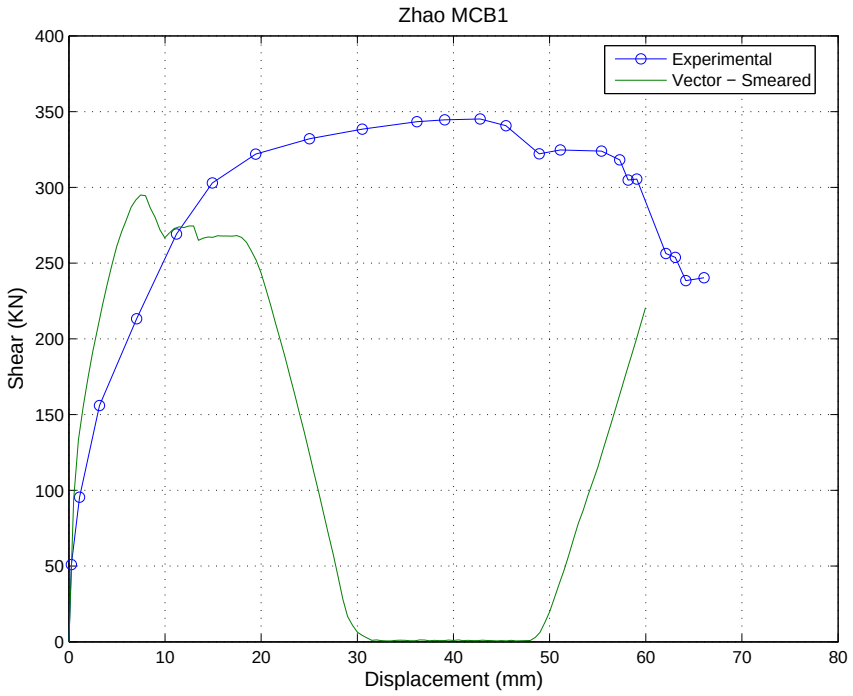

Figure A.41: Kwan & Zhao MCB1 - Vector2 Force-Disp Smeared Reinf.

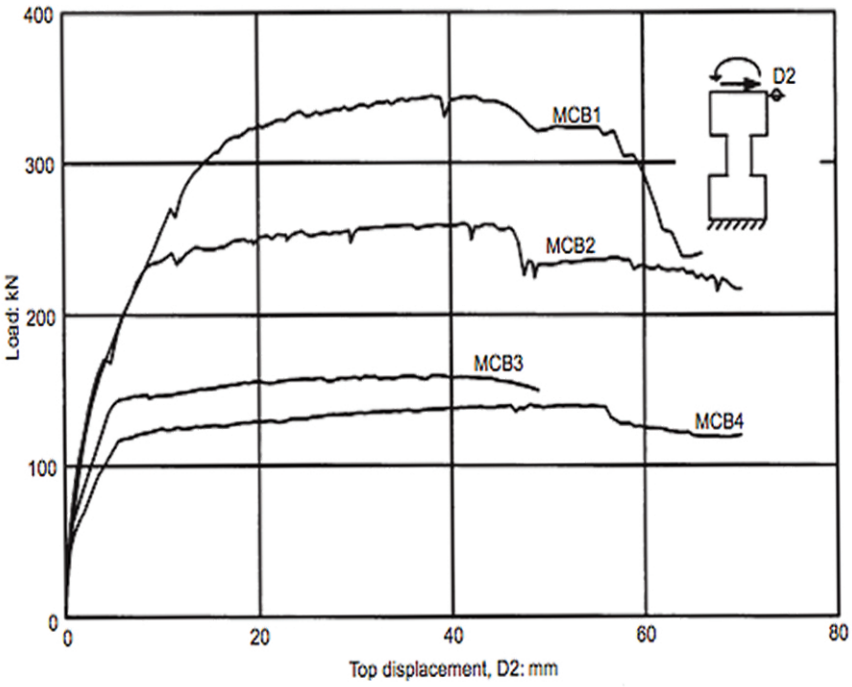

Figure A.42: Kwan & Zhao - Experimental Force-Disp. Plot

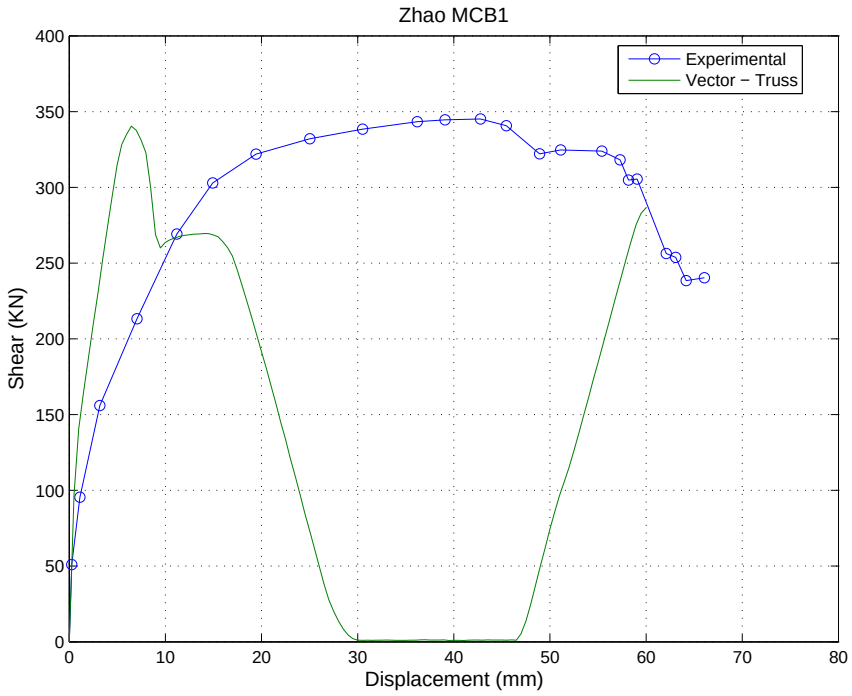

Figure A.43: Kwan & Zhao MCB1 - Vector2 Force-Disp Truss Reinf.

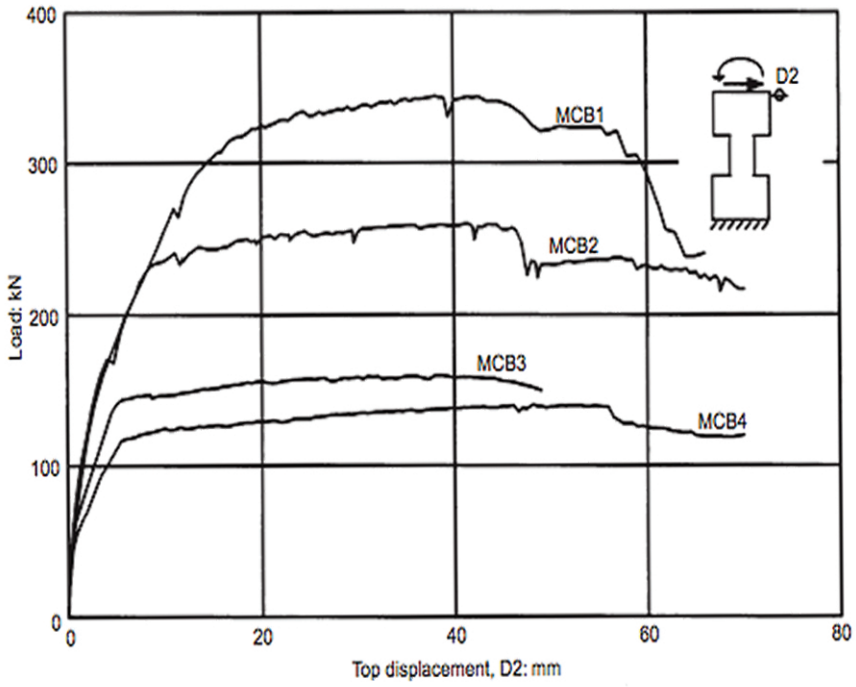

Figure A.44: Kwan & Zhao - Experimental Force-Disp. Plot

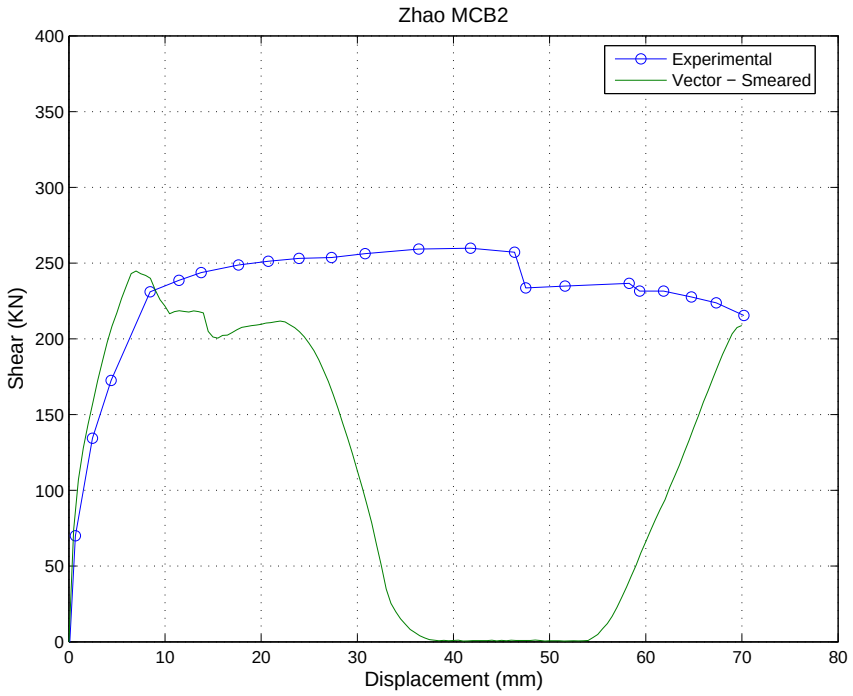

Figure A.45: Kwan & Zhao MCB2 - Vector2 Force-Disp Smeared Reinf.

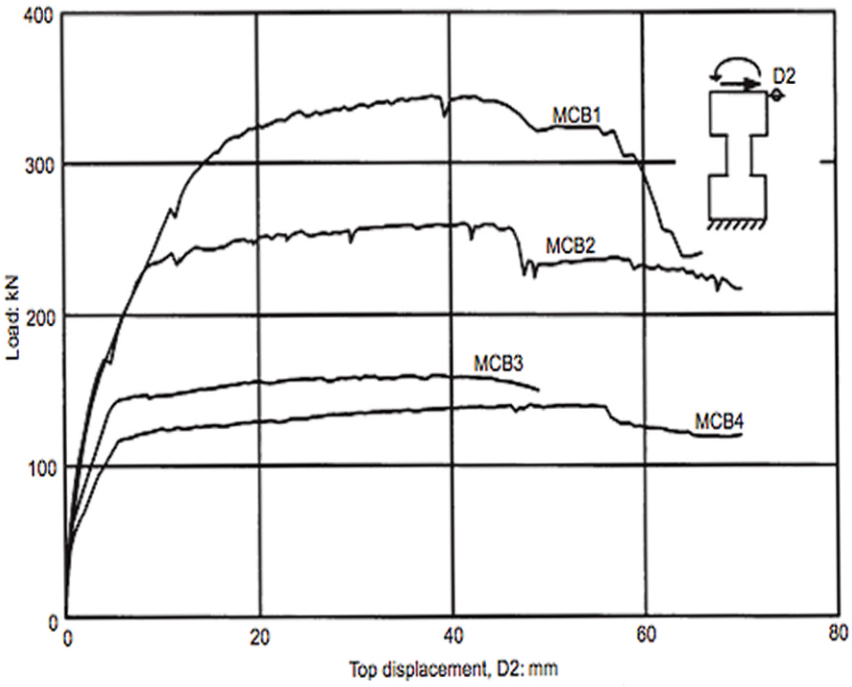

Figure A.46: Kwan & Zhao - Experimental Force-Disp. Plot

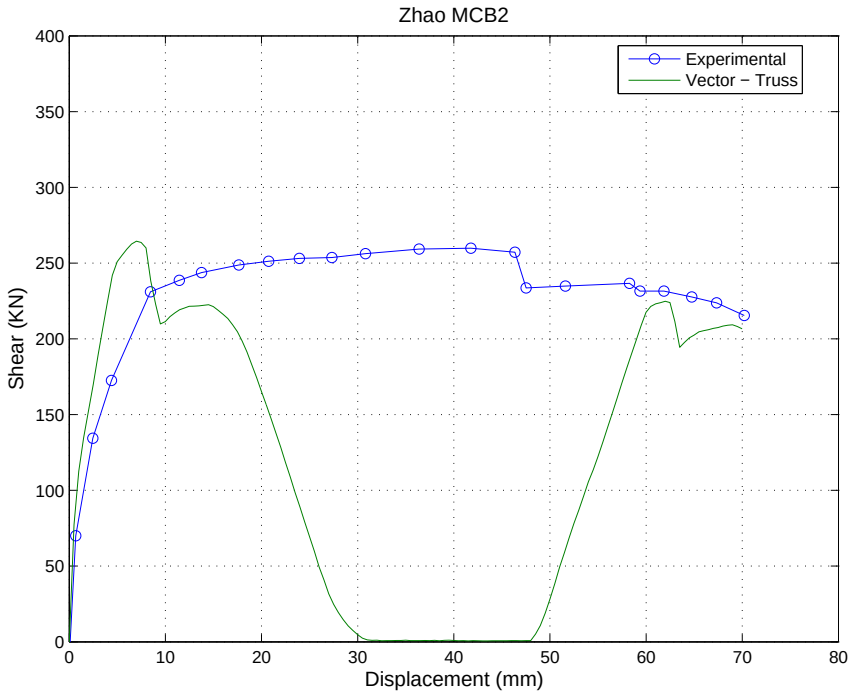

Figure A.47: Kwan & Zhao MCB2 - Vector2 Force-Disp Truss Reinf.

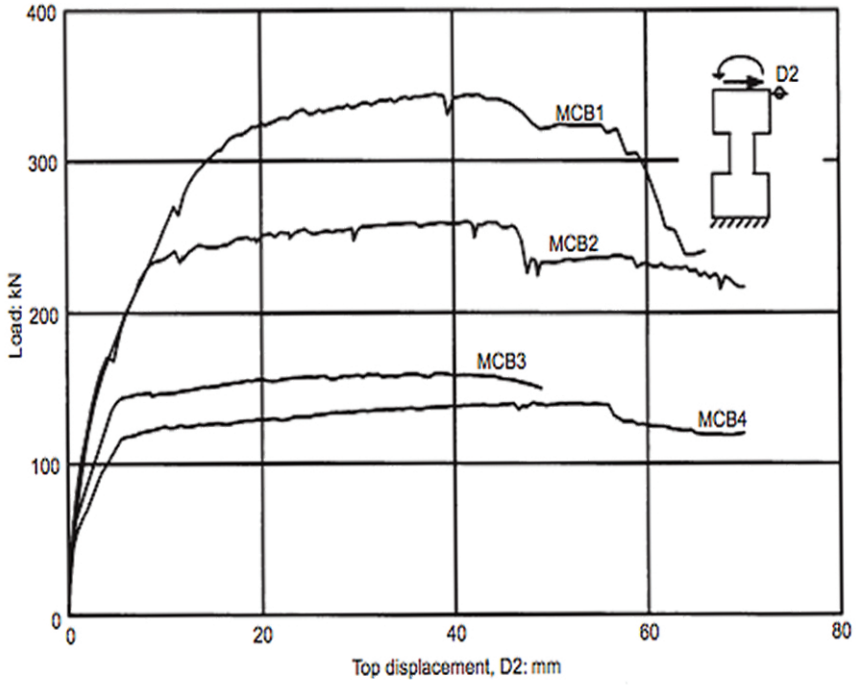

Figure A.48: Kwan & Zhao - Experimental Force-Disp. Plot

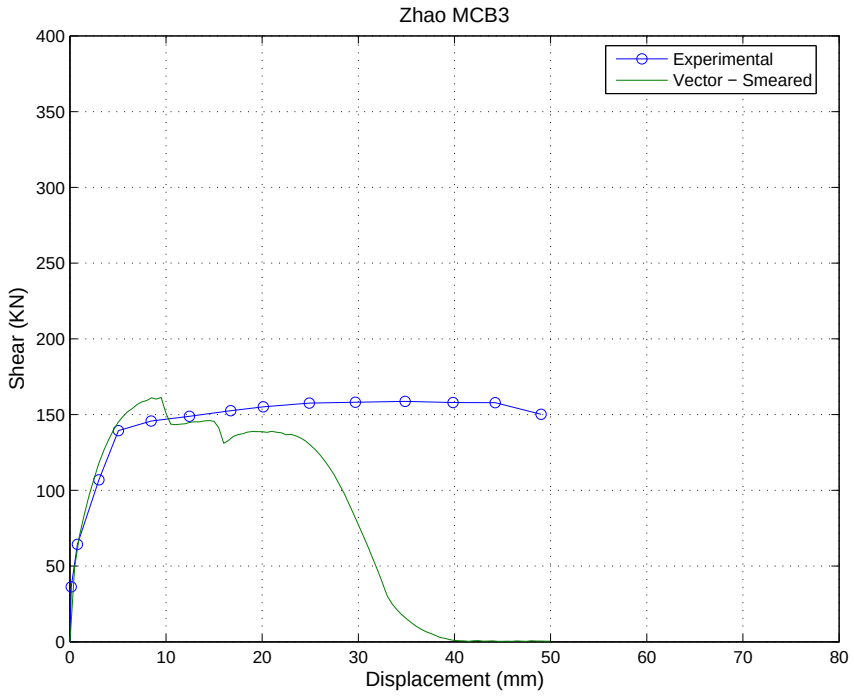

Figure A.49: Kwan & Zhao MCB3 - Vector2 Force-Disp Smeared Reinf.

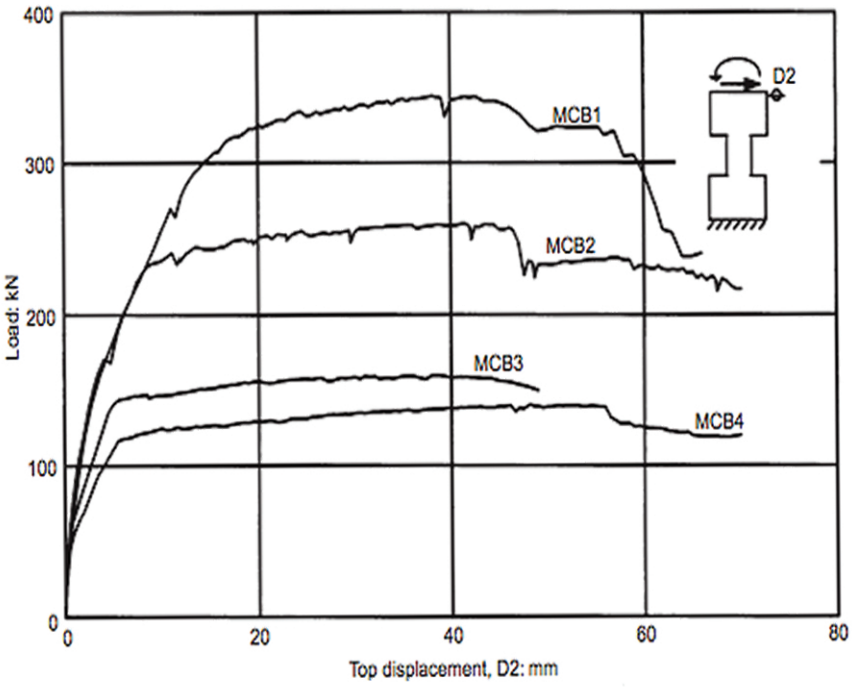

Figure A.50: Kwan & Zhao - Experimental Force-Disp. Plot

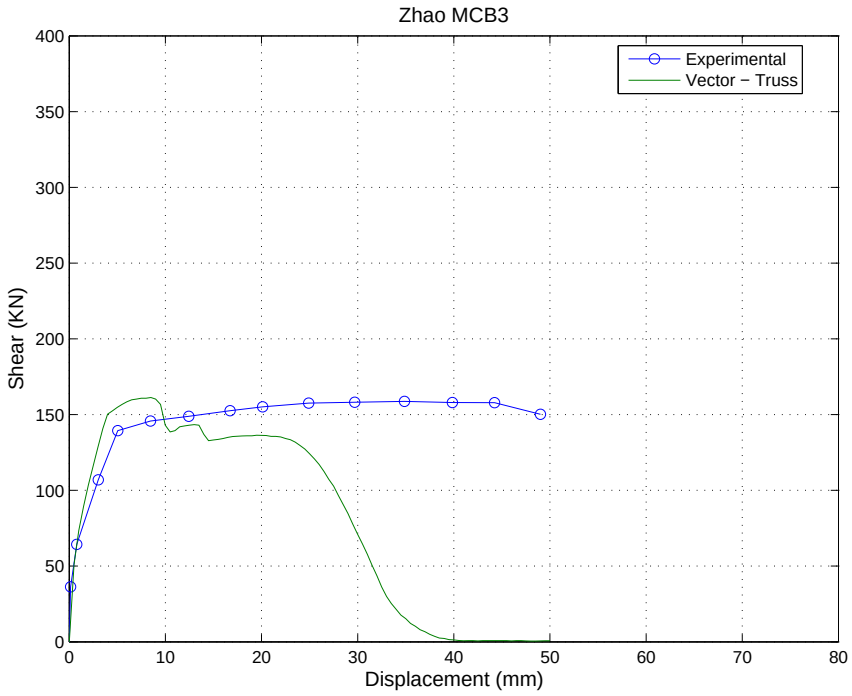

Figure A.51: Kwan & Zhao MCB3 - Vector2 Force-Disp Truss Reinf.

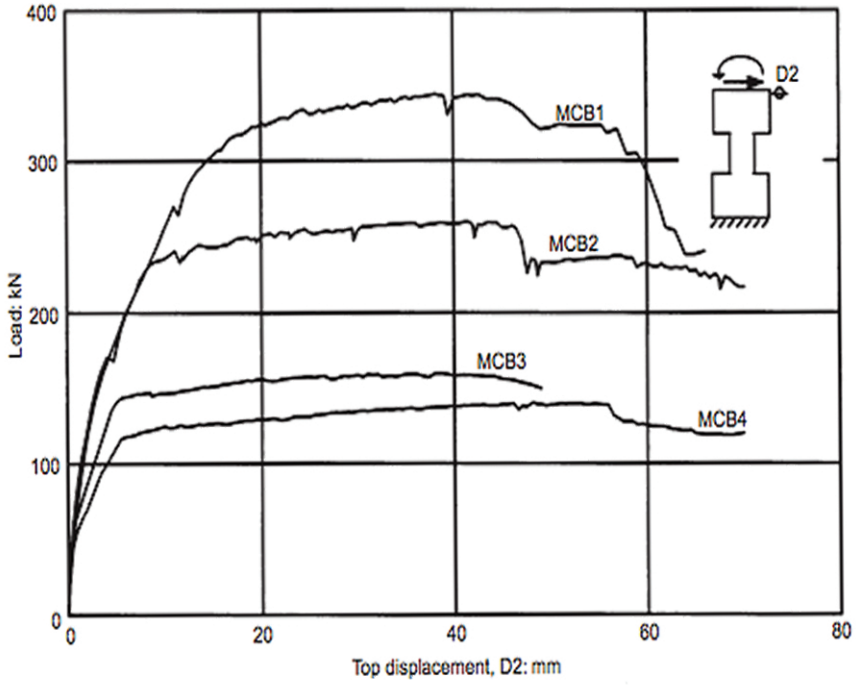

Figure A.52: Kwan & Zhao - Experimental Force-Disp. Plot

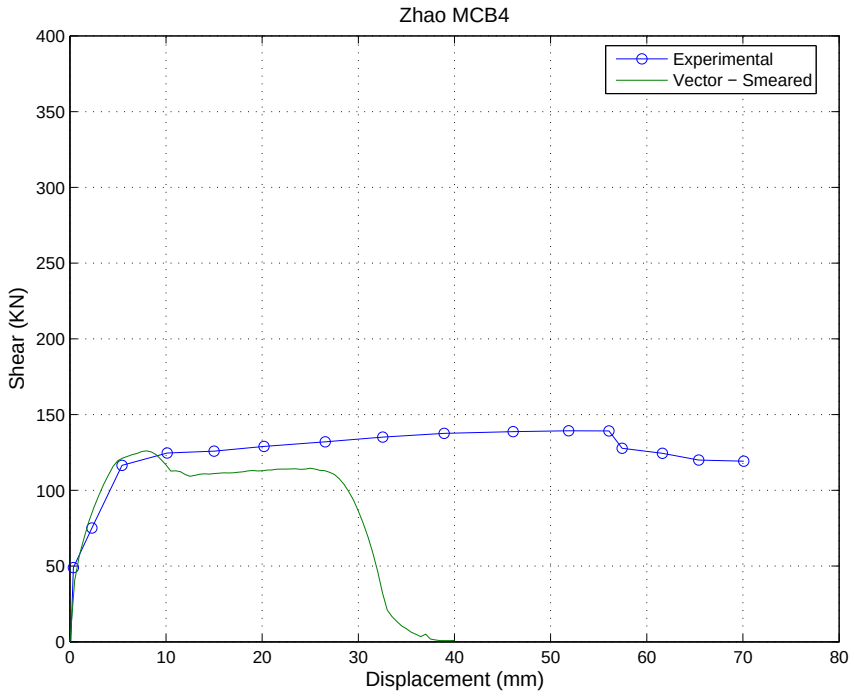

Figure A.53: Kwan & Zhao MCB4 - Vector2 Force-Disp Smeared Reinf.

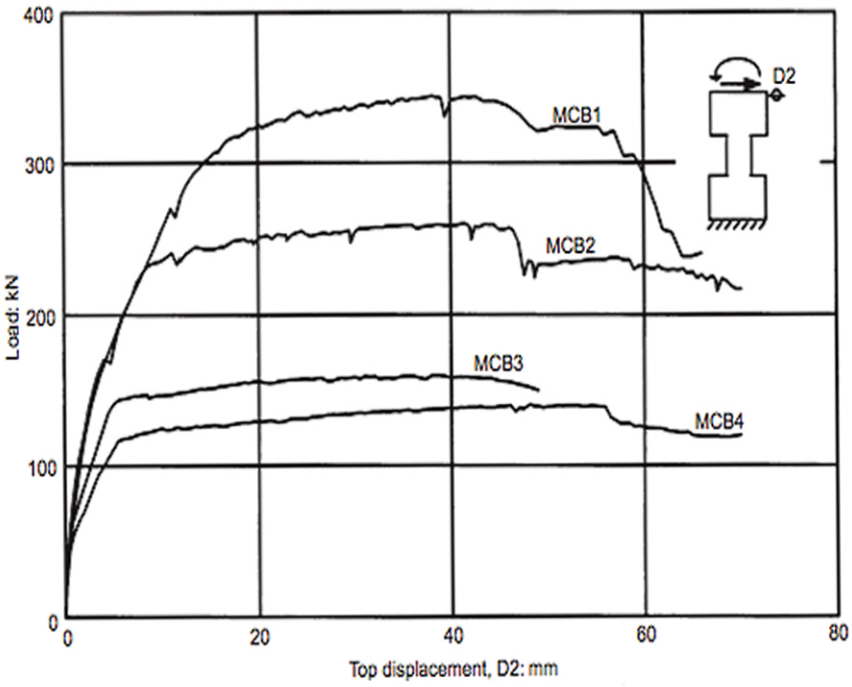

Figure A.54: Kwan & Zhao - Experimental Force-Disp. Plot

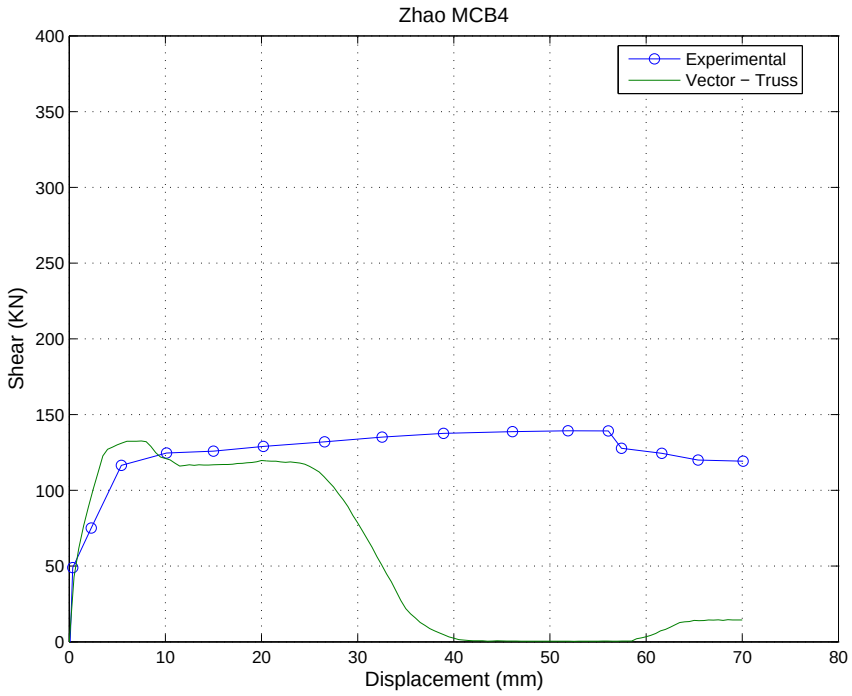

Figure A.55: Kwan & Zhao MCB4 - Vector2 Force-Disp Truss Reinf.

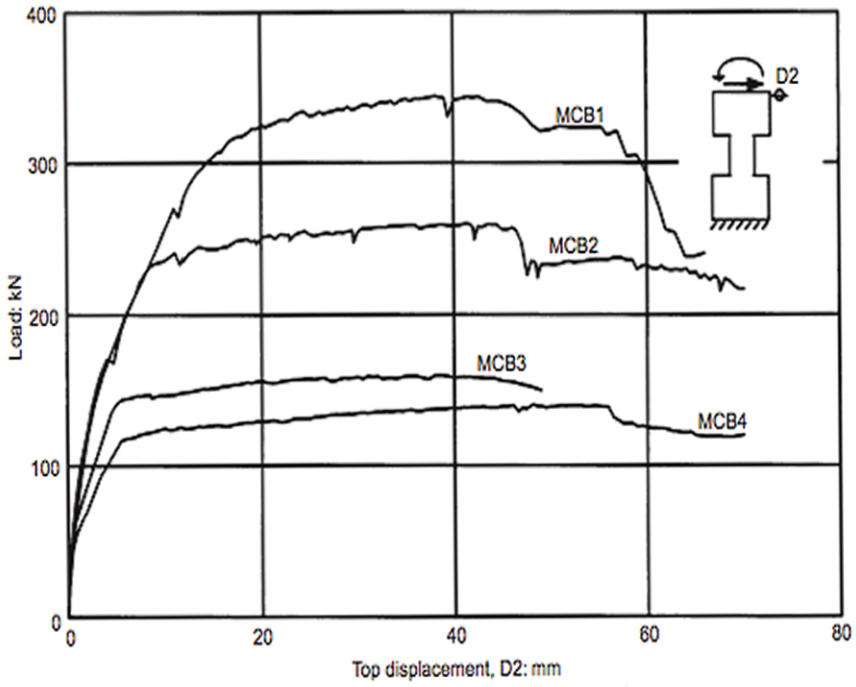

Figure A.56: Kwan & Zhao - Experimental Force-Disp. Plot

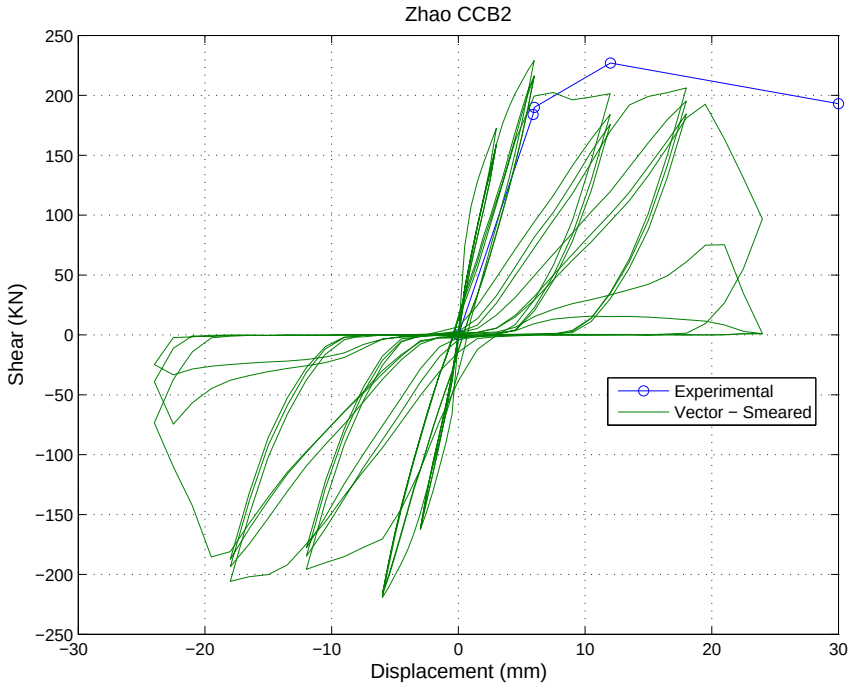

Figure A.57: Kwan & Zhao CCB2 - Vector2 Force-Disp Smeared Reinf.

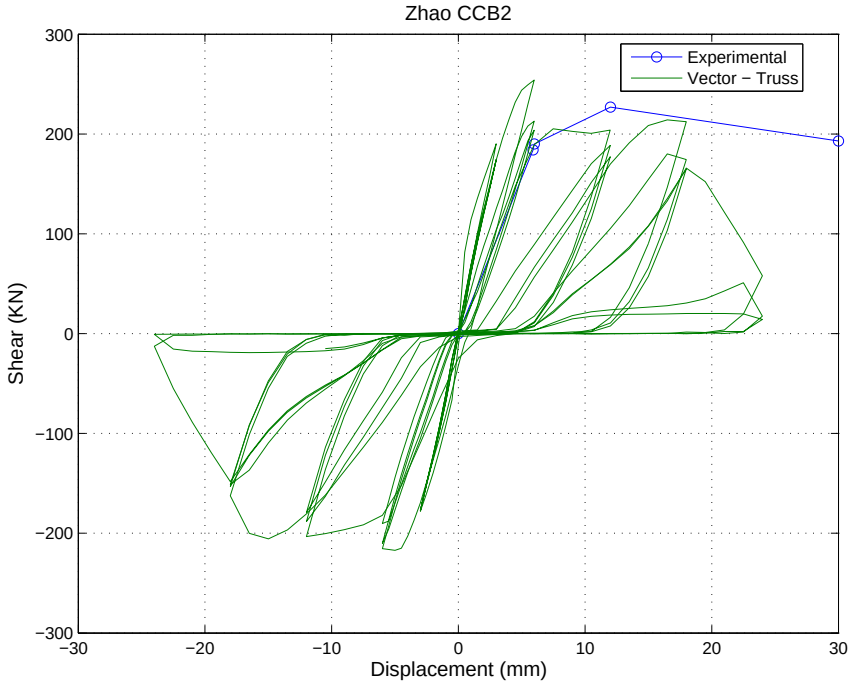

Figure A.58: Kwan & Zhao CCB2 - Vector2 Force-Disp Truss Reinf.

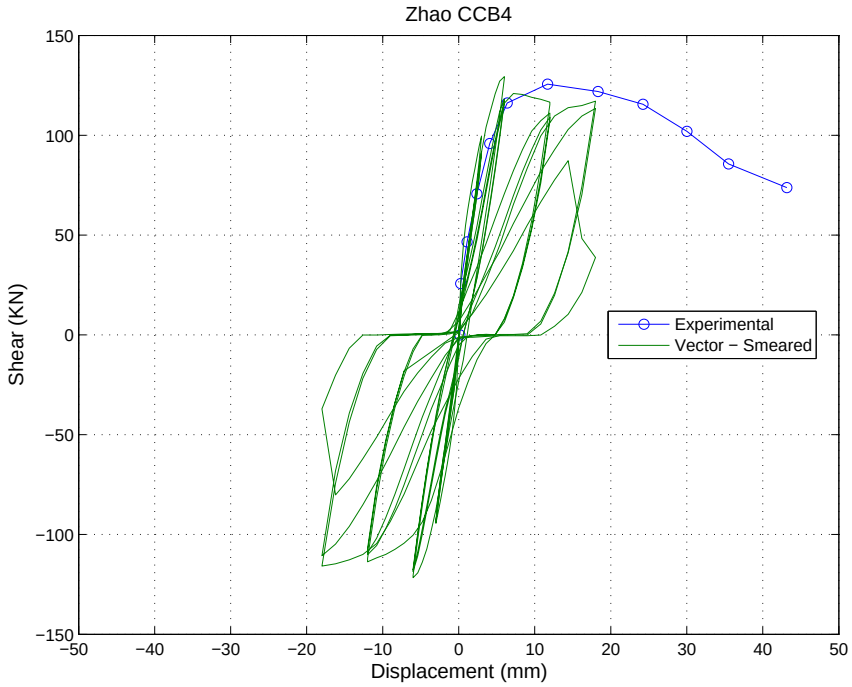

Figure A.59: Kwan & Zhao CCB4 - Vector2 Force-Disp Smeared Reinf.

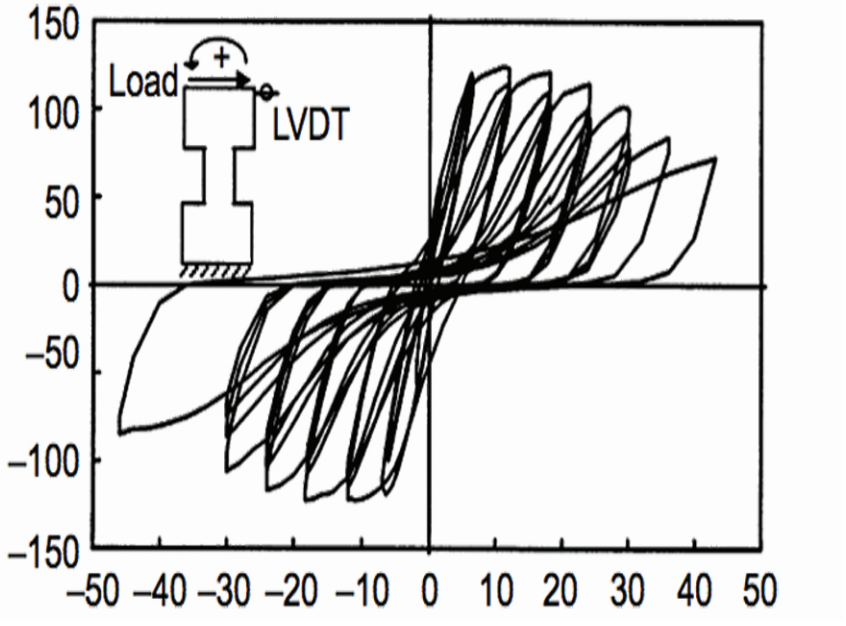

Figure A.60: Kwan & Zhao CCB4 - Experimental Force-Disp. Plot

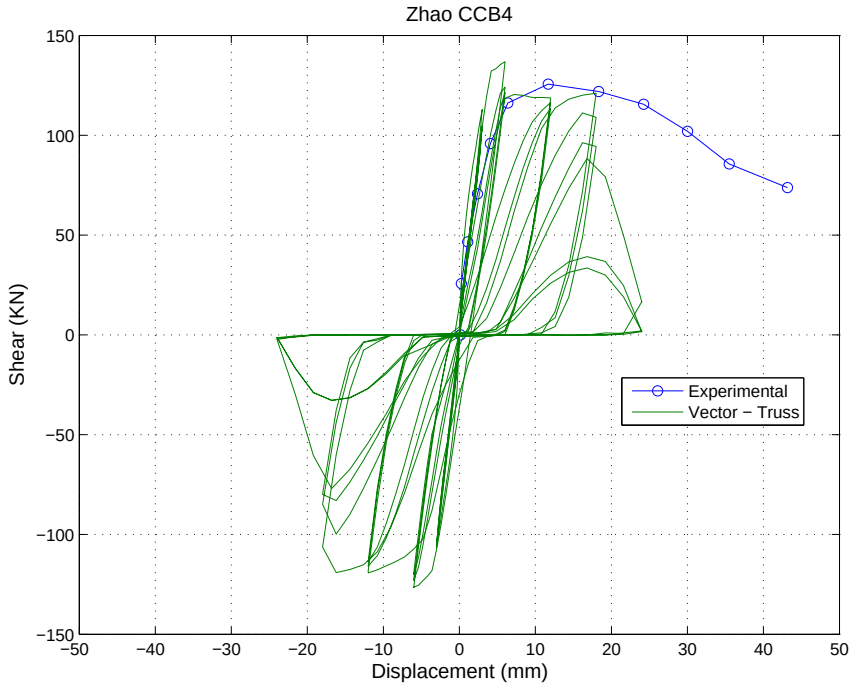

Figure A.61: Kwan & Zhao CCB4 - Vector2 Force-Disp Truss Reinf.

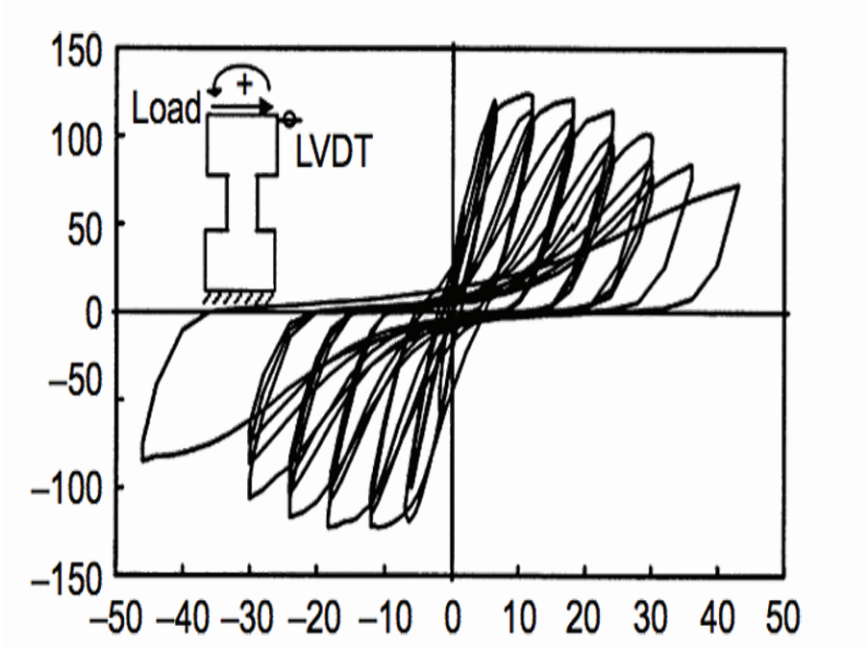

Figure A.62: Kwan & Zhao CCB4 - Experimental Force-Disp. Plot

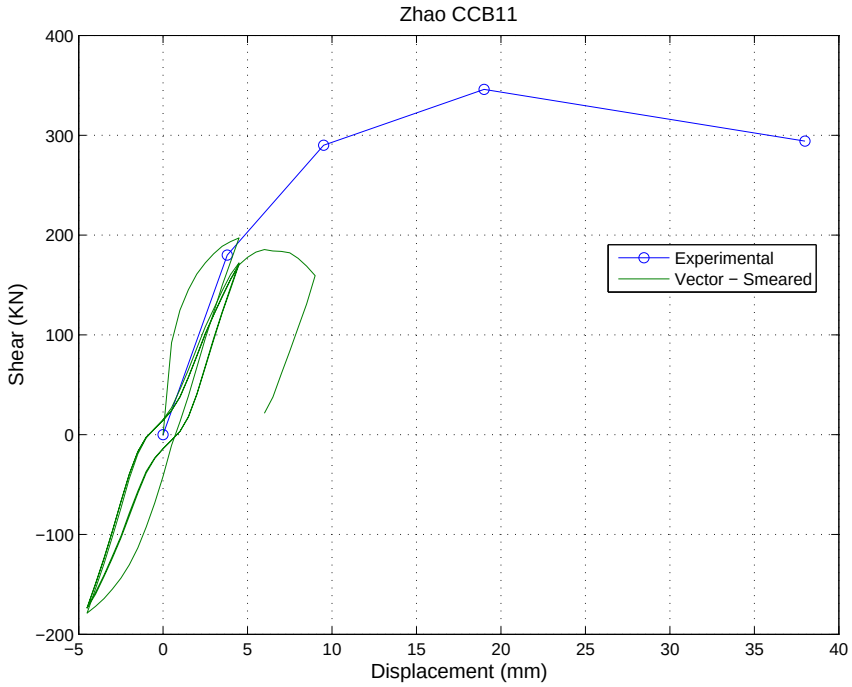

Figure A.63: Kwan & Zhao CCB11 - Vector2 Force-Disp Smeared Reinf.

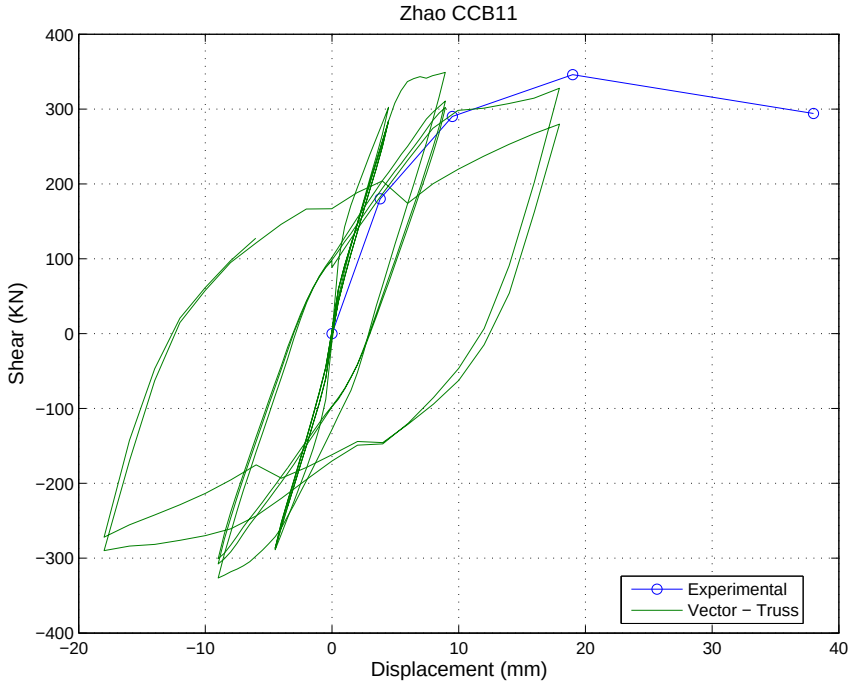

Figure A.64: Kwan & Zhao CCB11 - Vector2 Force-Disp Truss Reinf.

Appendix B

COUPLING BEAM PLOTS

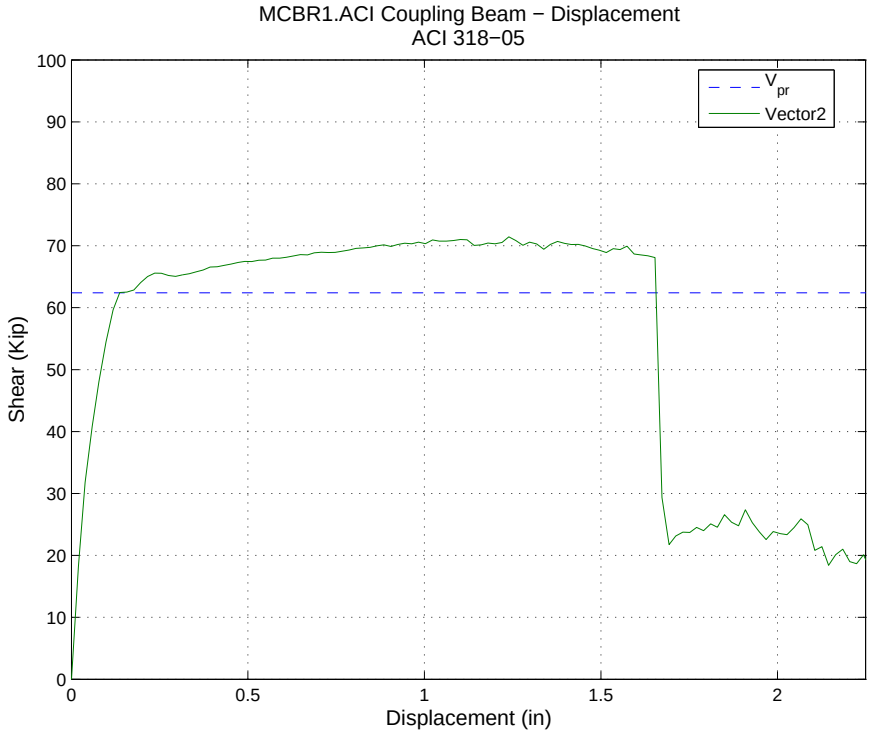

Figure B.1: MCBR1.ACI Displacement- VecTor2

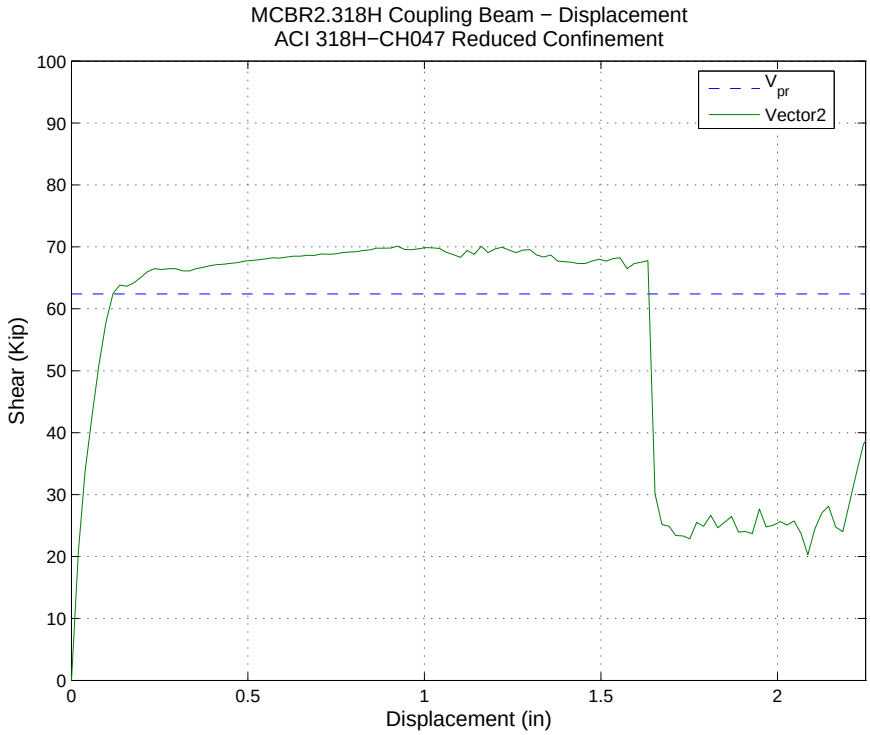

Figure B.2: MCBR2.318H Displacement - VecTor2

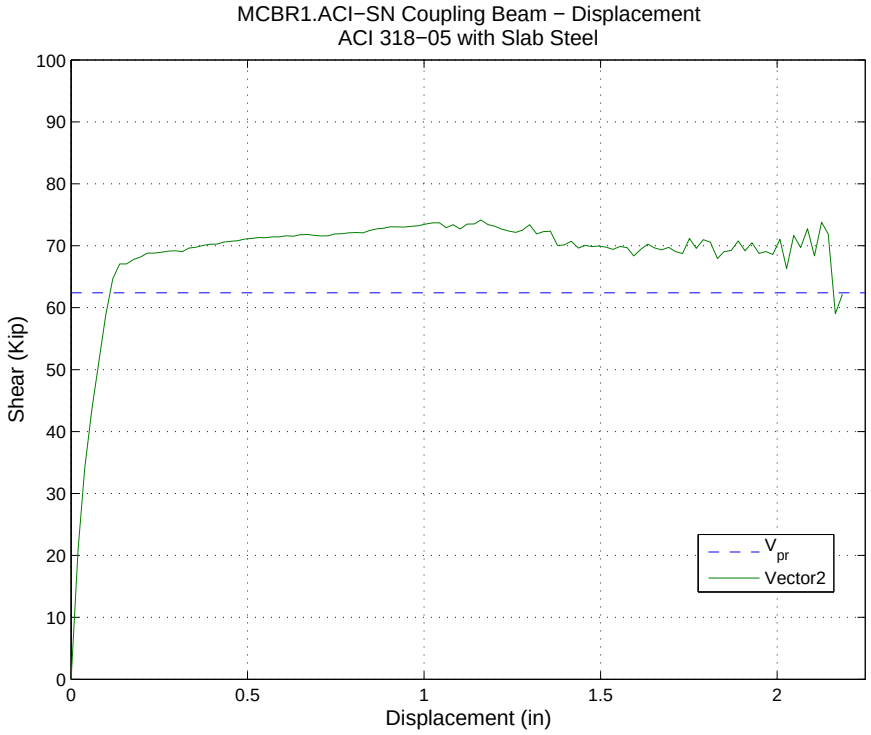

Figure B.3: MCBR1.ACI-SN Displacement- VecTor2

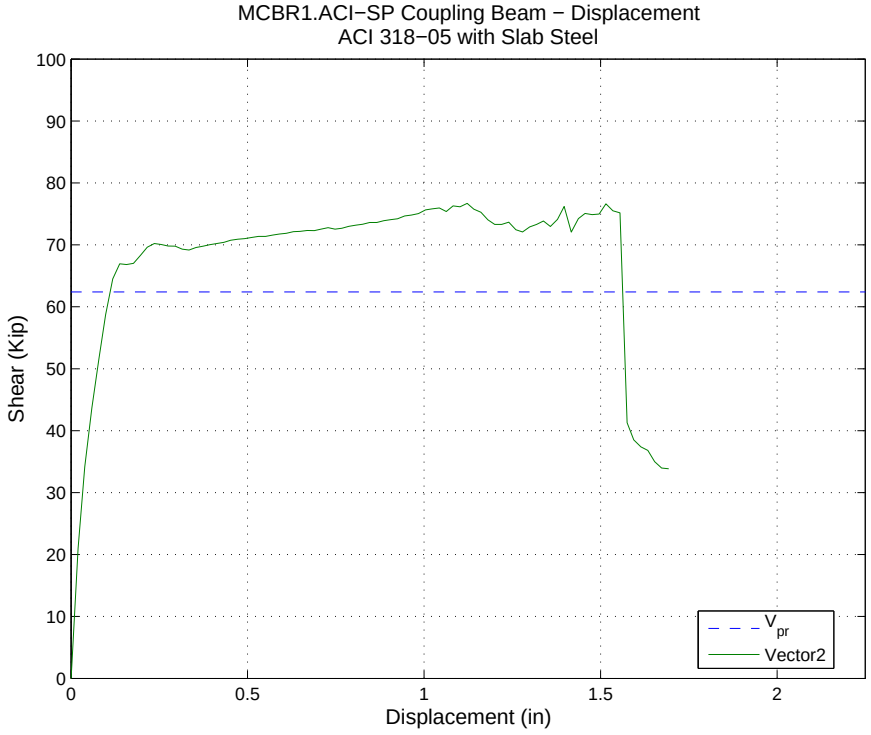

Figure B.4: MCBR1.ACI-SP Displacement - VecTor2

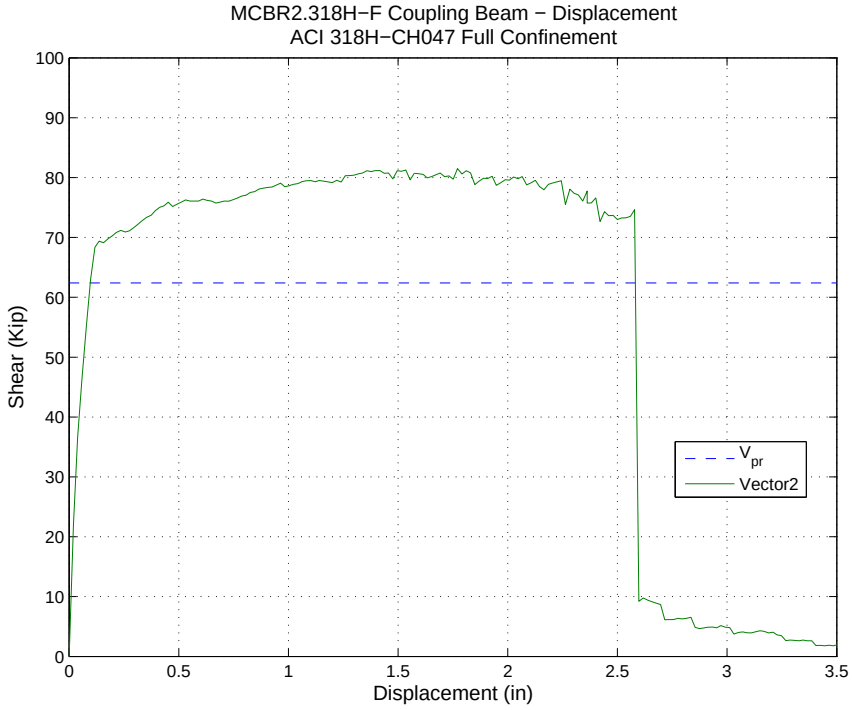

Figure B.5: MCBR2.318H-F Displacement- VecTor2

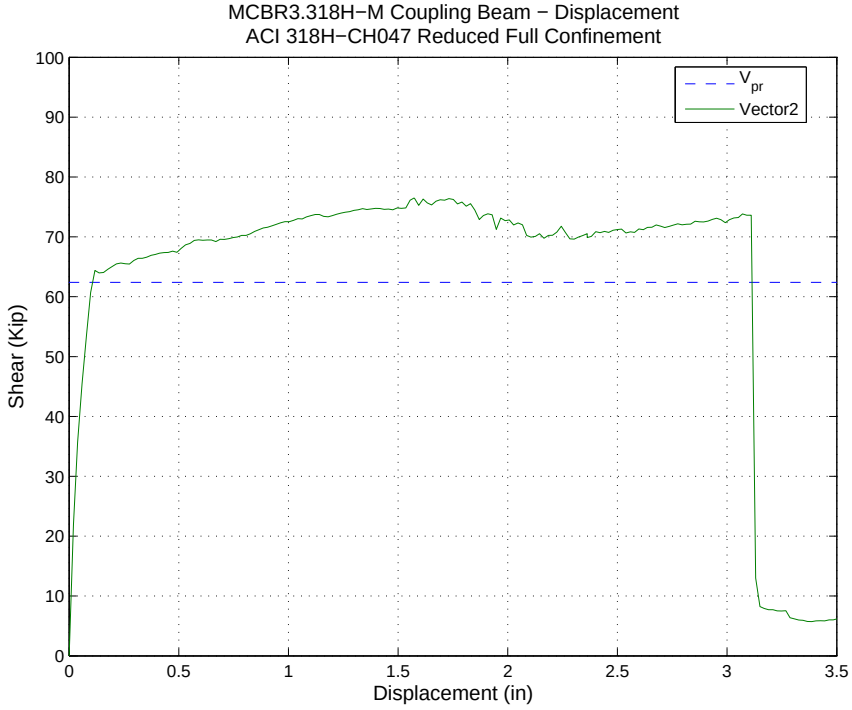

Figure B.6: MCBR3.318H-M Displacement - VecTor2

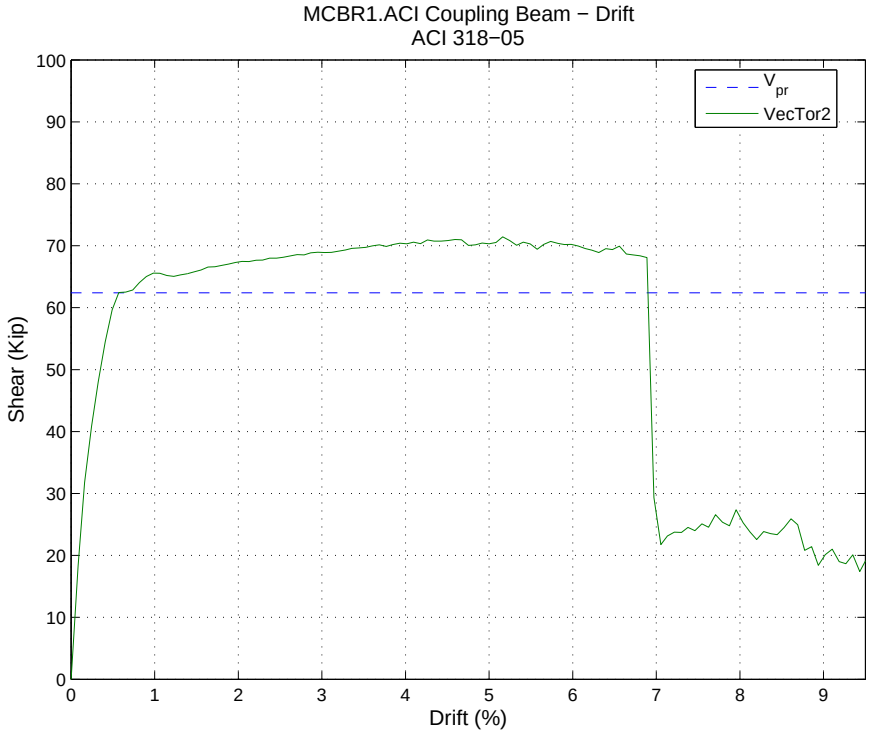

Figure B.7: MCBR1.ACI Drift - VecTor2

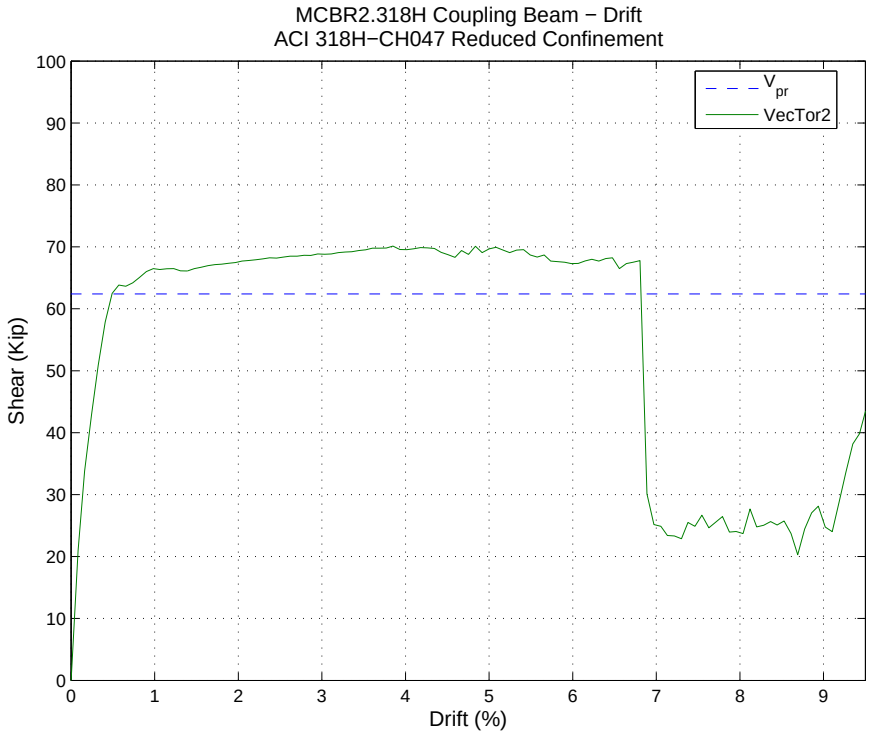

Figure B.8: MCBR2.318H Drift - VecTor2

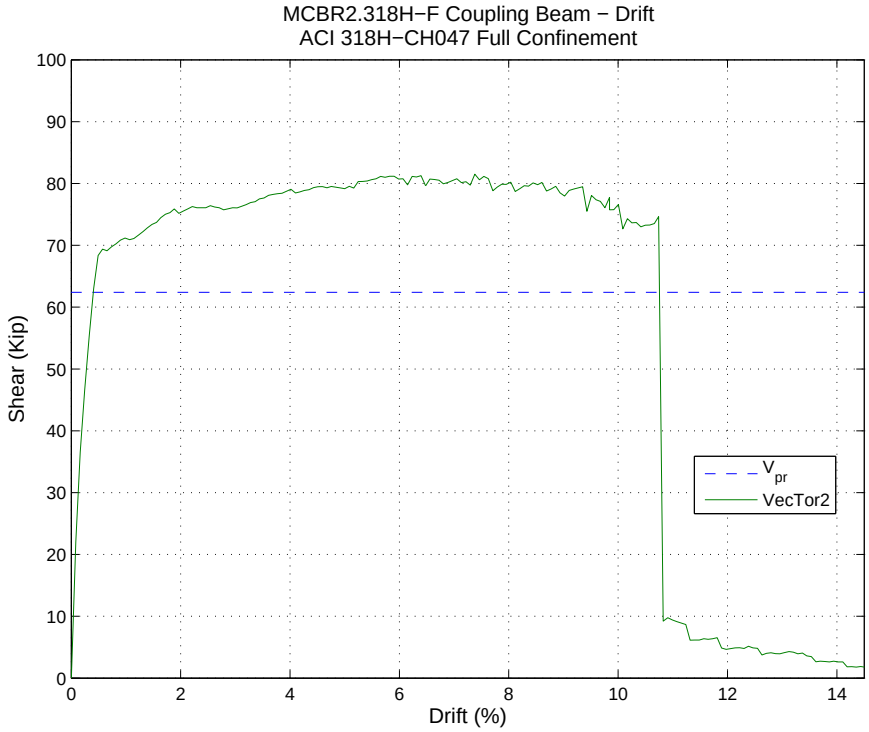

Figure B.9: MCBR2.318H-F Drift- VecTor2

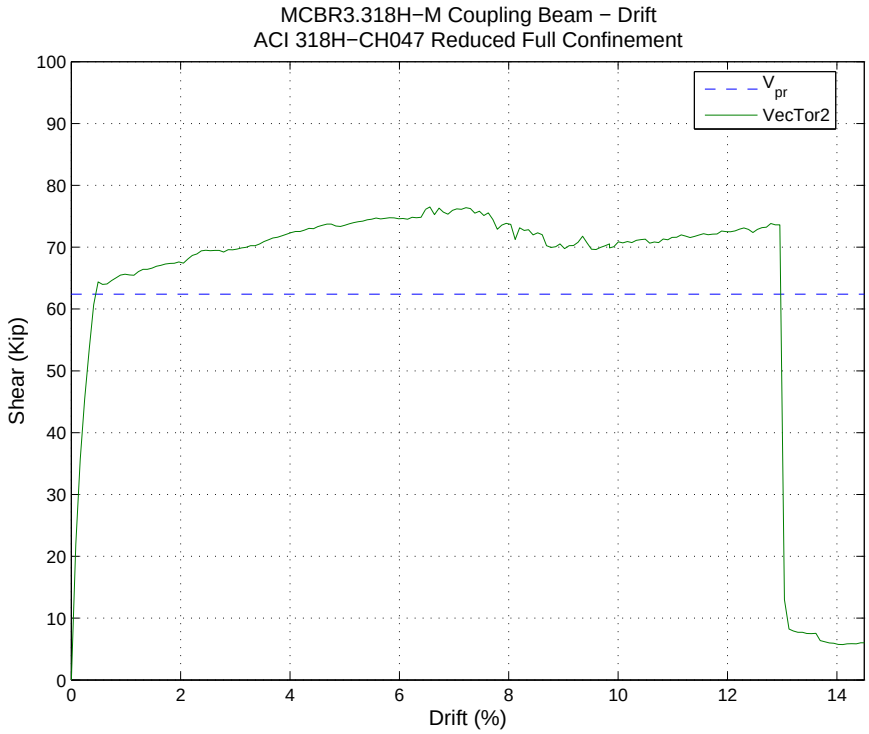

Figure B.10: MCBR3.318H-M Drift - VecTor2

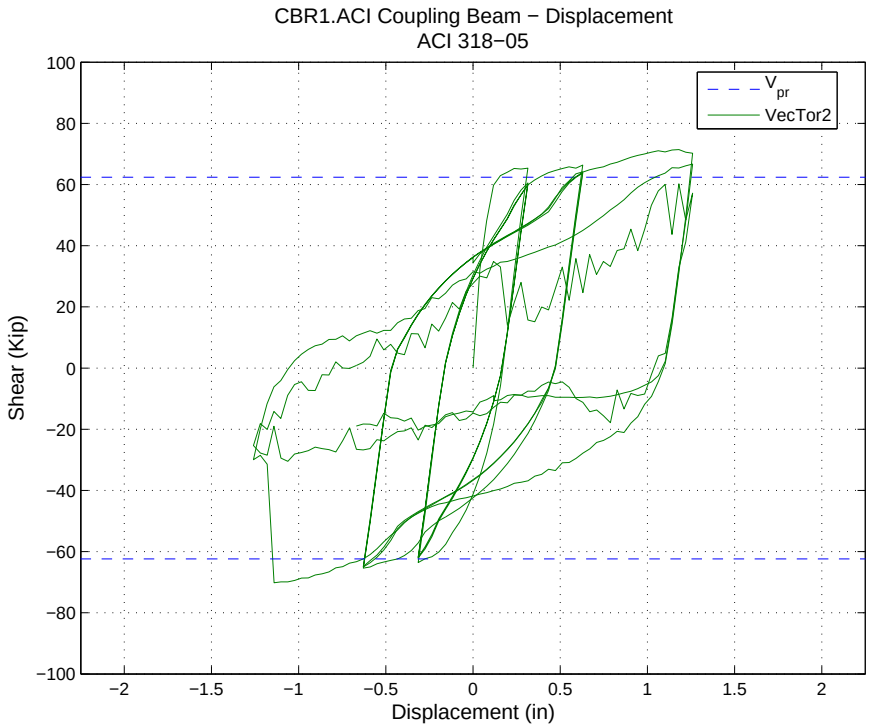

Figure B.11: CBR1.ACI Displacement- VecTor2

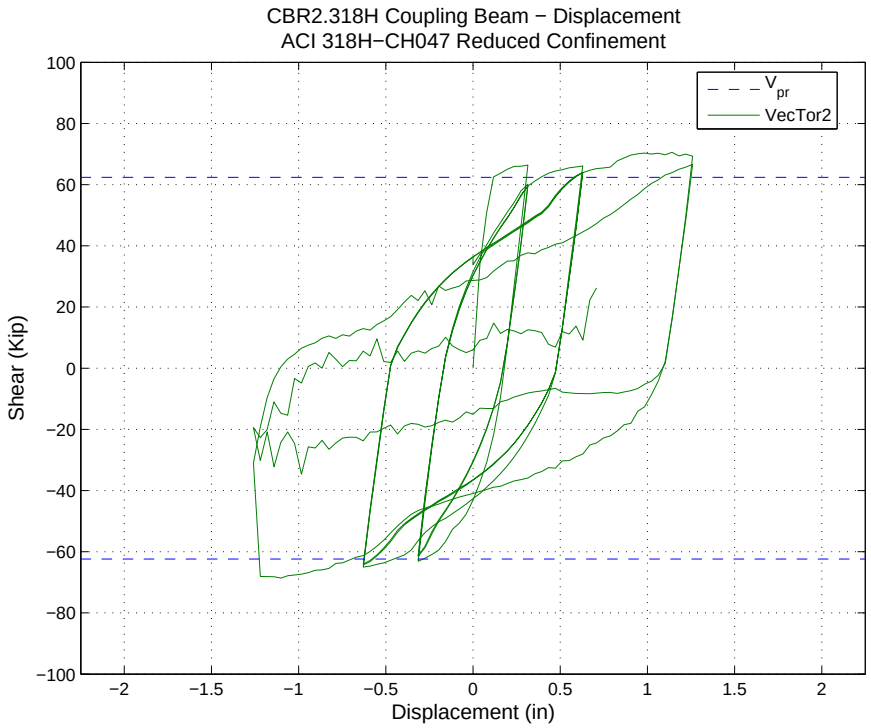

Figure B.12: CBR2.318H Displacement - VecTor2

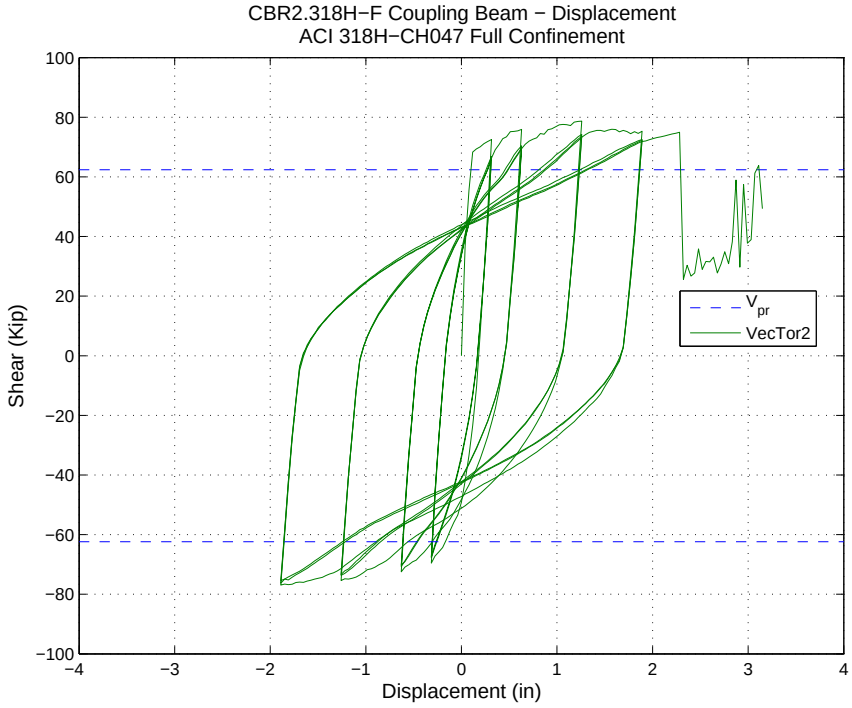

Figure B.13: CBR2.318H-F Displacement- VecTor2

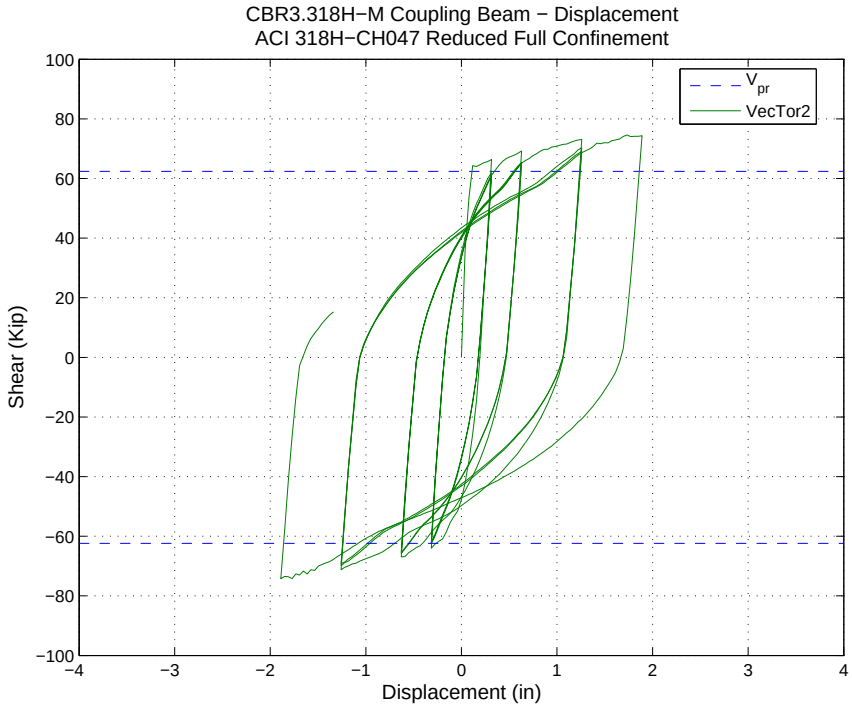

Figure B.14: CBR3.318H-M Displacement - VecTor2

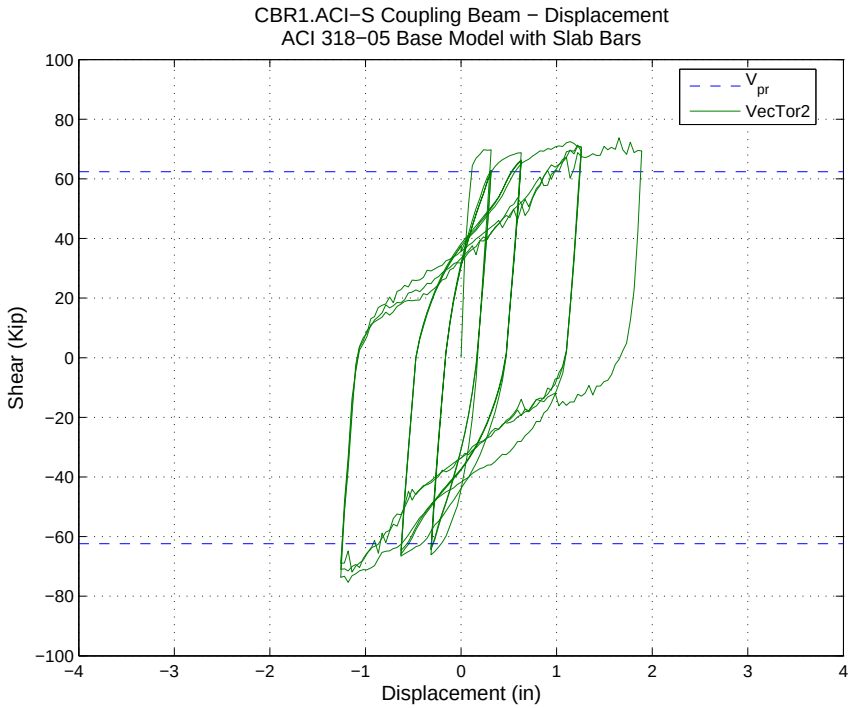

Figure B.15: CBR1.ACI-S Displacement- VecTor2

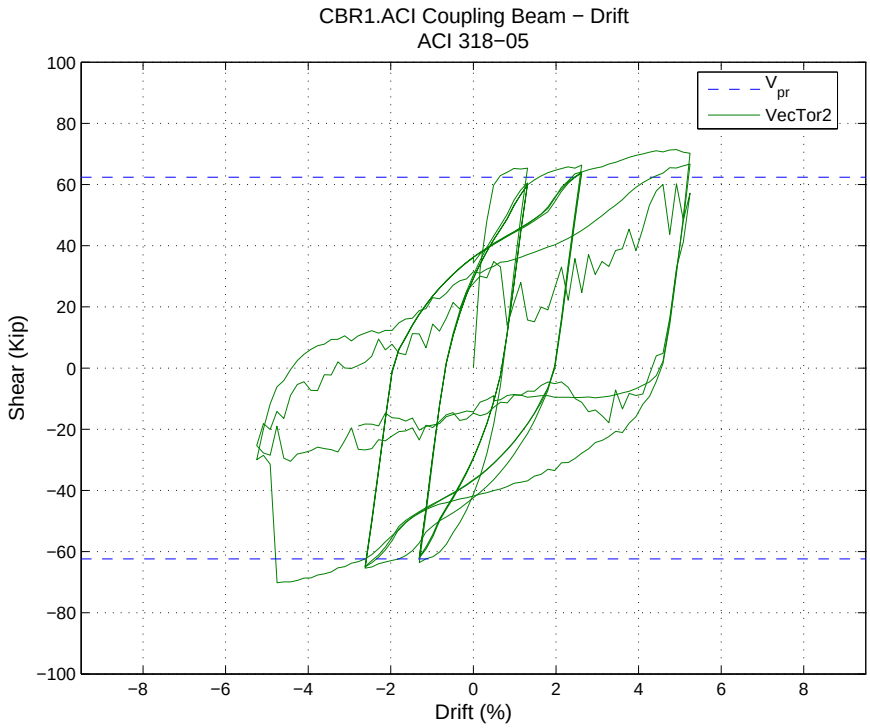

Figure B.16: CBR1.ACI Drift- VecTor2

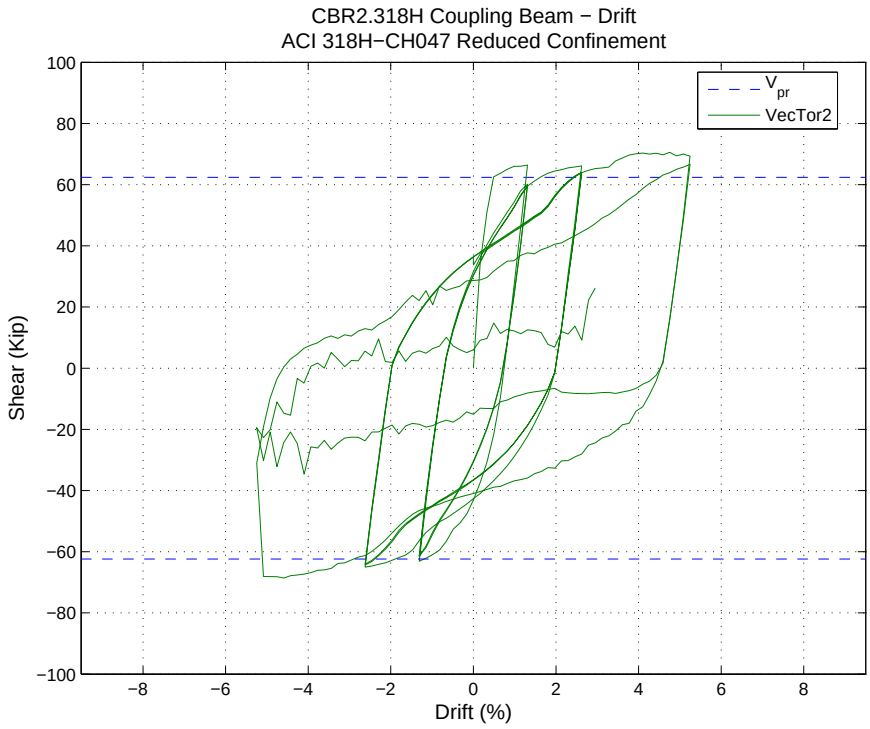

Figure B.17: CBR2.318H Drift - VecTor2

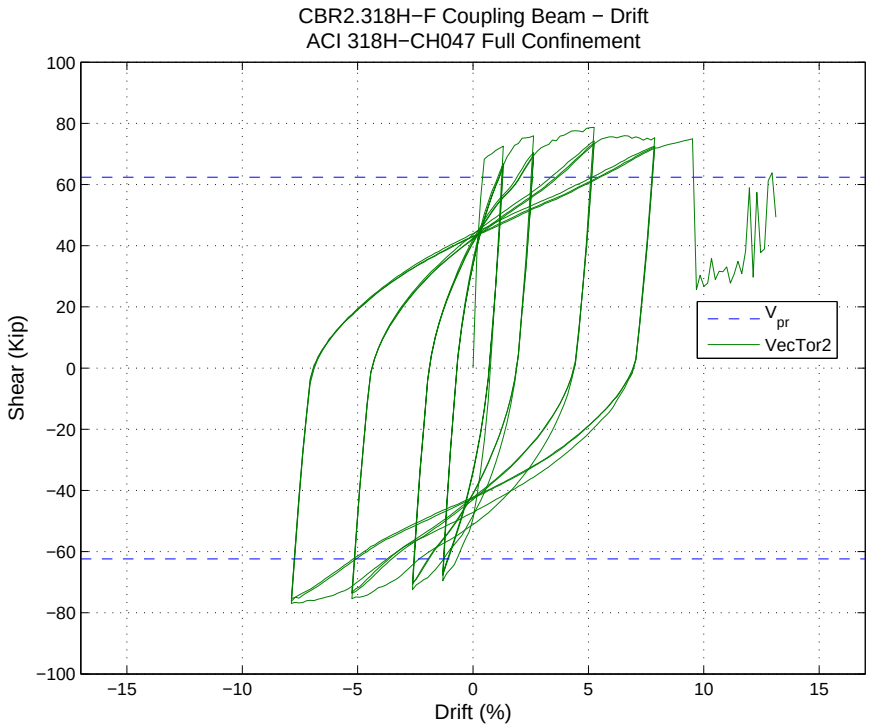

Figure B.18: CBR2.318H-F Drift- VecTor2

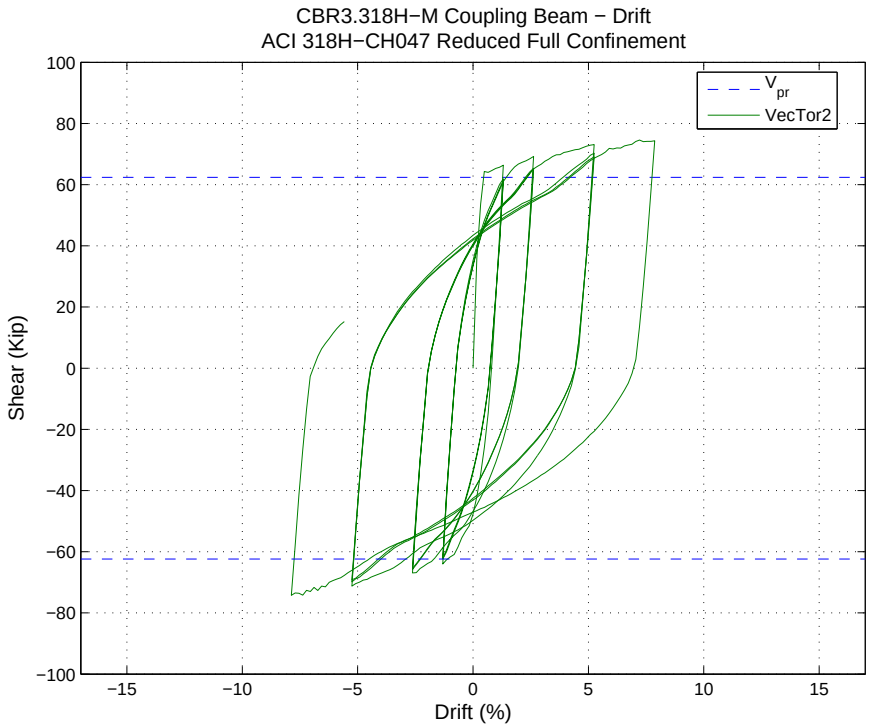

Figure B.19: CBR3.318H-M Drift - VecTor2

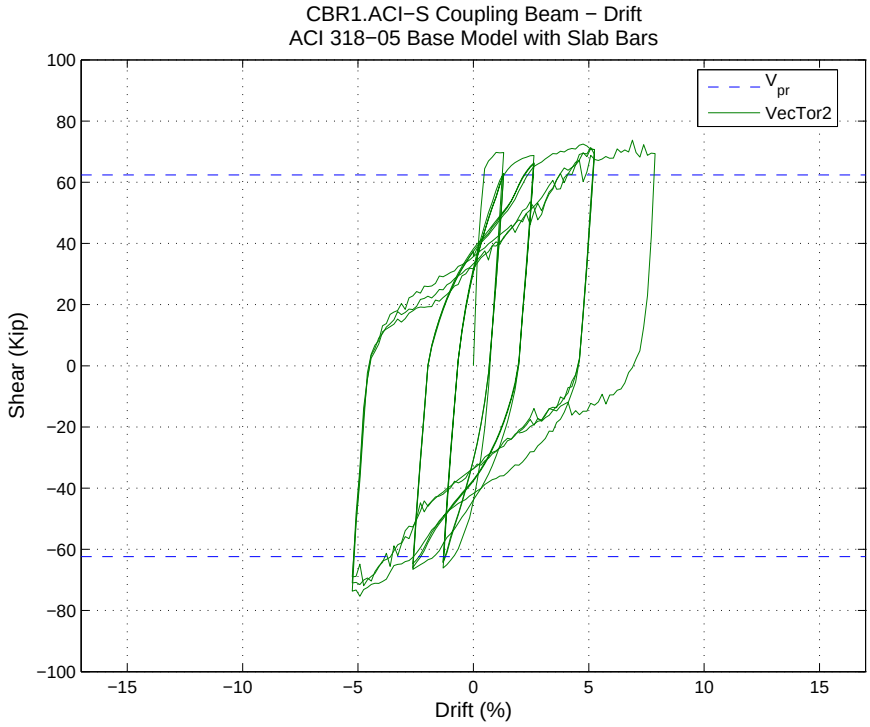

Figure B.20: CBR1.ACI-S Drift- VecTor2

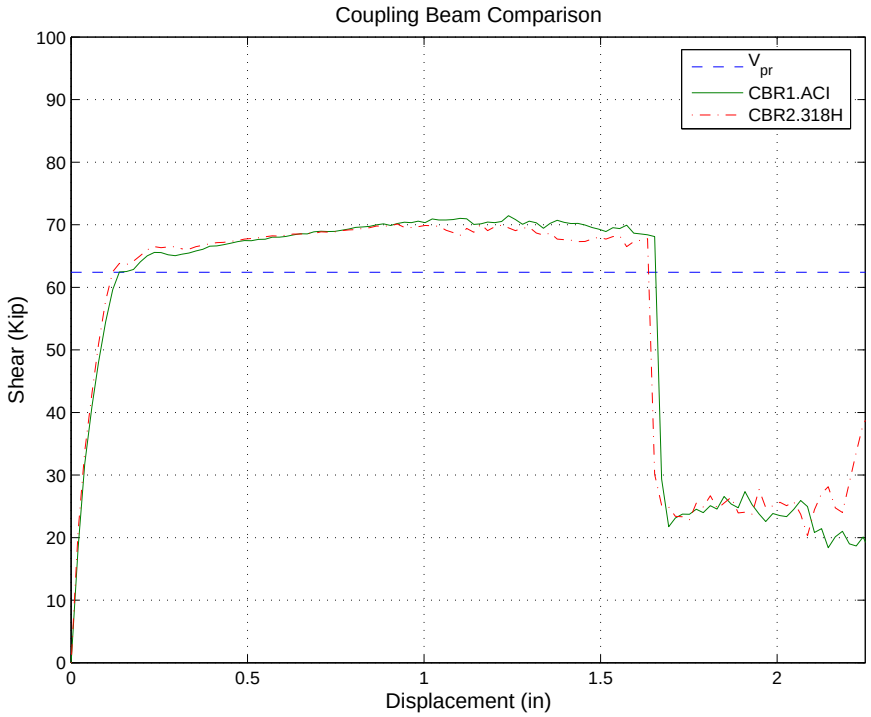

Figure B.21: MCBR1.ACI vs. MCBR2.318H - VecTor2

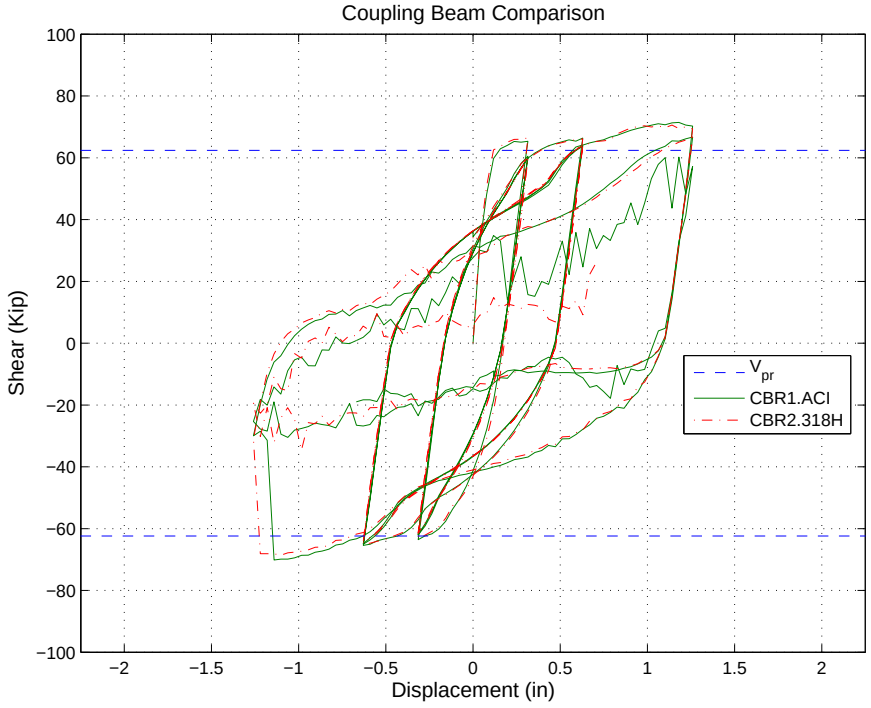

Figure B.22: CBR1.ACI vs. CBR2.318H - VecTor2

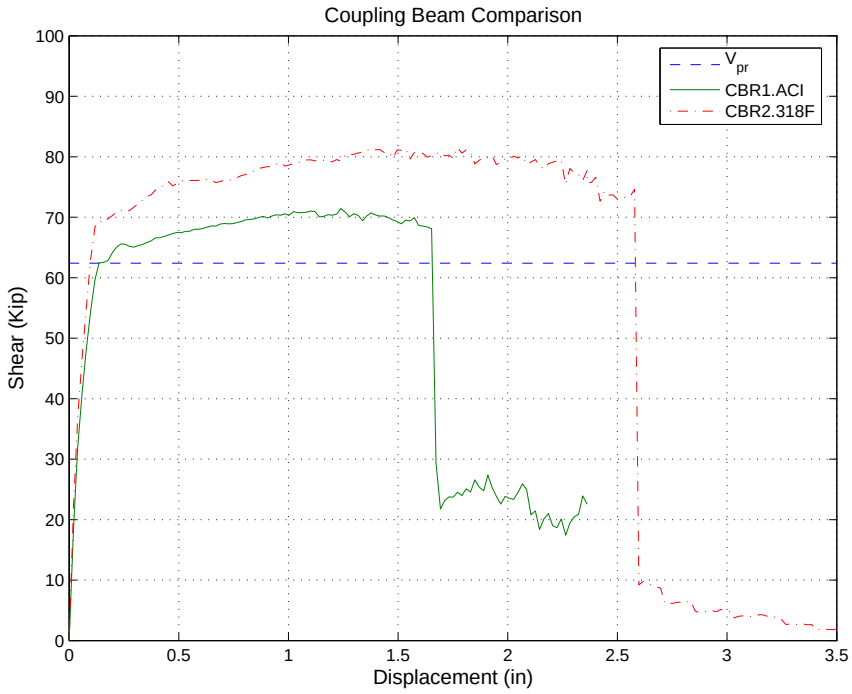

Figure B.23: MCBR1.ACI vs. MCBR2.318H-F - VecTor2

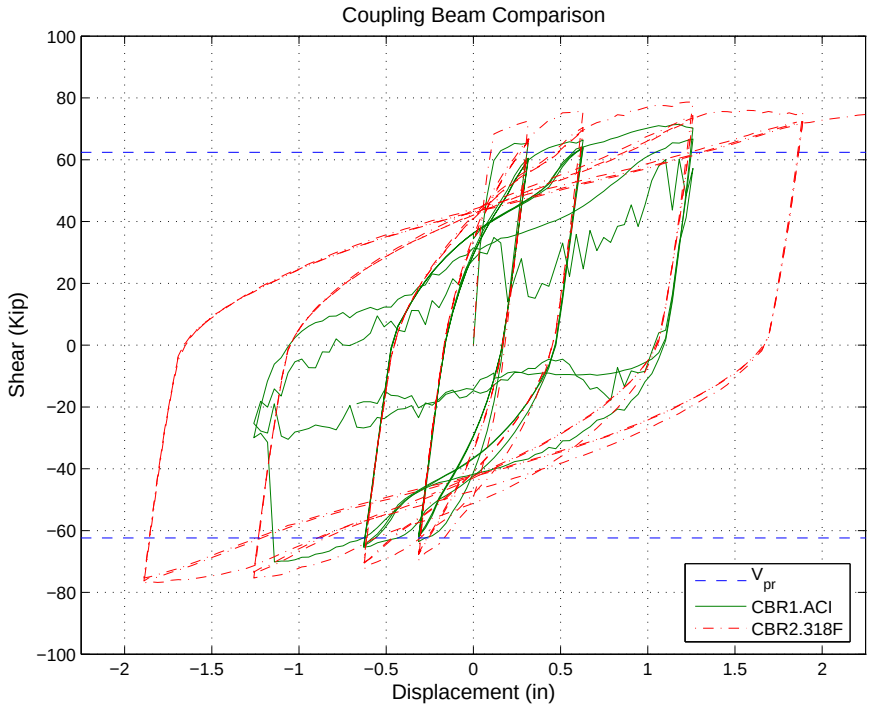

Figure B.24: CBR1.ACI vs. CBR2.318H-F - VecTor2

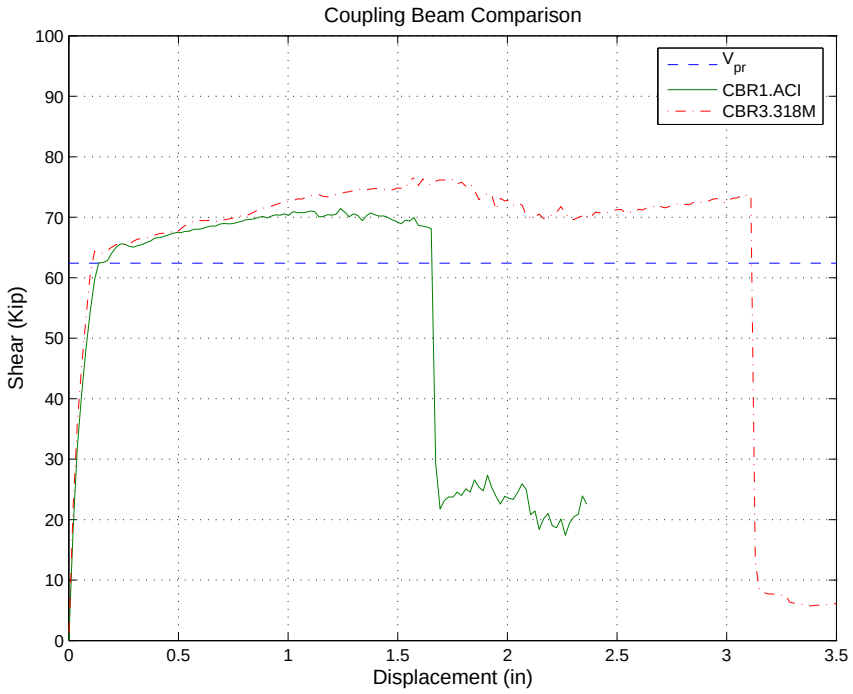

Figure B.25: MCBR1.ACI vs. MCBR3.318H-M - VecTor2

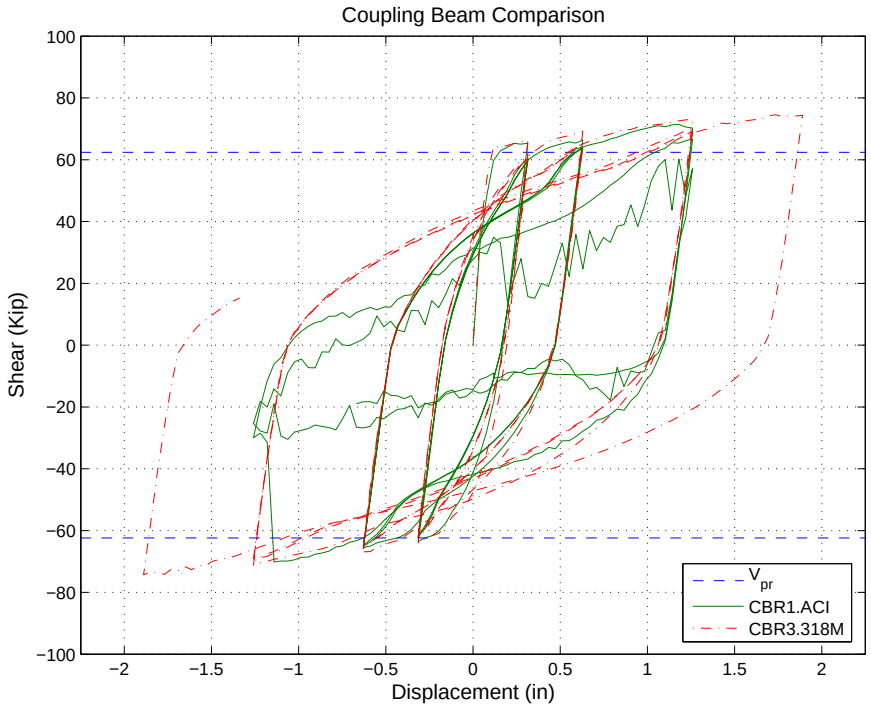

Figure B.26: CBR1.ACI vs. CBR3.318H-M - VecTor2